Spin-to-charge conversion at the LaAlO3/SrTiO3 interface Rashba state

Anas El Hamdi

Thèse de doctorat

NNT : 2021UPASP124

université PARIS-SACLAY

Spin-to-charge conversion at the $LaAlO_3/SrTiO_3$ interface Rashba state

Conversion spin-charge dans les états d'interface Rashba dans $LaAlO_3/SrTiO_3$

Thèse de doctorat de l'université Paris-Saclay

École doctorale n°564 École Doctorale Physique Île-de-France (EDPIF)
Spécialité de doctorat: Physique
Graduate School : Physique, Référent : Faculté des sciences d'Orsay

Thèse préparée dans l'unité de recherche **SPEC** (Université Paris-Saclay, CEA, CNRS) , sous la direction de Michel VIRET, directeur de recherche, le co-encadrement de Jean-Yves CHAULEAU, chercheur.

Thèse soutenue à Paris-Saclay, le 03 décembre 2021, par

Anas EL HAMDI

Composition du Jury :

Aurélien MANCHON Professeur de physique, Centre Interdisciplinaire de Nanoscience de Marseille (CINaM)	Président
Laurent VILA Chercheur, SPINTEC, URA CNRS/CEA 2512 CEA-Grenoble	Rapporteur & Examinateur
Juan-Carlos ROJAS-SÁNCHEZ Chercheur, Institut Jean Lamour (IJL) UMR 7198	Rapporteur & Examinateur
Rebeca RIBEIRO-PALAU Chercheuse, C2N (UMR 9001) CNRS / Université Paris-Saclay	Examinatrice
Jean-Marc TRISCONE Professeur de physique, Department of Quantum Matter Physics (DQMP) at the University of Geneva	Examinateur
Michel VIRET Dircteur de recherche, Service de Physique de l'Etat Condensé, CEA Saclay	Directeur de thèse

To my familly and friends.

Acknowledgements

My first thoughts go straight to my PhD supervisor, Michel Viret, without whom this work would not have been possible. Not only for the great scientific guidance over the course of my PhD but also for your generosity and all the exchanges we had will mark me forever. My second thoughts goes to Jean-Yves Chauleau, you were truly my second supervisor, your rigor and passion were a great inspiration for me. Even in the toughest moments, the positivism and the great atmosphere allowed me to overcome the most challenging periods. I would also like to thank Grégoire de Loubens, Jean-Baptiste Moussy, and our collaborators from whom I was fortunate to steal as much knowledge as I could, and in particular the people in Geneva (Margherita Boselli, Stefano Gariglio, Jean-Marc Triscone) and in the LPS (Raphaël Veil) for the amazing samples that they have made for us, and the team from Le Mans (Vincent Juvé, Pascal Ruello, Gwenaëlle Vaudel, Tadele Orbula Otomalo, Artem Levchuk) for the extensive terrahetrz measurements of our samples.

I also would like to express my gratitude to all members of the jury for their interest in my work and I would also like to thank Laurent Vila and Juan-Carlos Rojas-Sánchez who have done me the immense honor of agreeing to report this thesis. I am very grateful to them.

Since building an experimental set up is no easy task, I would like to thank Gerald Le Goff and Gregory Cannies for the amazing work they have done, behind the scenes, in manufacturing the various components for our experiments. I would also like to thank Corinne for the friendly discussions and her help when ever I faced some administrative difficulties.

To everybody I met in the SPEC, especially in the LNO group. I will miss the great environment, the jokes and funny discussions we had around the lunch table. I will never forget all the good times we spent together, our coffee breaks as well as our football matches. I am happy to have met colleagues whom I consider now my friends, even my second family.

Thanks to all the great friendships created and amazing experiences and accidental encounters with the most amazing people. To all the people with whom I shared my office during this three 3 years : Theophile, Paul, Eswara, Titiksha, Zixin ... Greetings to all current and former colleagues in the SPEC : Chloé, Julien, Nathanaël, Andrin, Fernanda, Michel, Maikane, Igor, Adel, Ramon, Amal, Nahuel, Wanissa, Omar, Ludovic, Binh, Ryhei, Anyssa, Pamella, Cyril, Marianne, François-Damien, Olivier, ...

Thanks to my parents and brother for their unfailing support throughout these three years. I hope they are proud of me. Thanks to my close friends S.,Y.,O. for all the moments spent together. May our friendship last forever.

Contents

Introduction

0.1 Motivation and future applications

Since its discovery, the transistor has been at the heart of the rapid development of our digital society. In this context, the semiconductor industry has relied on the exponential downsizing of transistors in order to increase the processing power of our digital devices. This trend lead to the doubling of the number of transistor per microchip roughly every two years, while the price per transistor was halved, leading to the miniaturization of our electronic devices. This steady down scaling process was first predicted by Gordon Moore [212], and was mainly sustained thanks to the various breakthroughs in material science and photo-lithography techniques, allowing the transistor to reach a size as small as $10nm$ or less [223]. In the last decade, Moore's prediction has no longer been the rule, since downsizing reached intrinsic limits[229, 209], partly due to the quantum mechanical effects such as tunneling which becomes non negligible at such length scales, but also because of the increase in the power density per transistor[219]. So the question that begs to be answered, is how can we keep Moore's law alive ? To answer this question, scientists have proposed new alternatives beyond the CMOS technology.

One of these alternatives, relies on the design of a new set of spin-based devices which, in contrast to their charge counterparts can be driven without the need of a charge current, leading to a higher energy efficiency, lower latency and improved integration between the memory and data processing units. These spin-based devices have been backed by multiple proposals such as the spin field effect transistor, proposed by Datta and Das back in the 1990's[218, 246], as well as the recent proposal by Intel of their MESO logic device [236], which relies on two main components: A first brick allows for the electric control of the magnetization through a magnetoelectric element coupled to a ferromagnet via exchange/strain coupling. The second element relies on the conversion of a spin current into a charge current through a highly coupled spin-orbit interface. Nevertheless, these spin-based devices still need to be integrated within the already existing semiconductor technology, raising multiple technical issues regarding their functionalities.

Thanks to their very appealing properties, oxide materials seem to be prime candidates for the design of future

oxide-based spintronic devices. These multifunctional oxides can be copper oxides based superconductors[206], or display wide range of other physical properties such as ferroelectricity, ferromagnetism or antiferromagnetism, as well as multiferroic orders. New emergent properties can also be induced through the realization of oxide heterointerfaces, such as the two dimensional electron system at the interface between $LaAlO_3$ and $SrTiO_3$[231], which displays a wide range of physical properties such as superconductivity and a gate-tuneable spin-orbit coupling [242].

In this thesis, we will investigate the spin-to-charge conversion mechanism within the two dimensional electron system at the interface between $LaAlO_3$ and $SrTiO_3$, at various times scales, using different experimental techniques such as spin pumping by ferromagnetic resonance and spin Seebeck, THz generation and second harmonic generation.

0.2 Outline of this Thesis

This thesis will be divided into five chapters. In the first chapter we introduce the basic concepts, regarding the spin and orbital degrees of freedom of the electron, as well as the various mechanisms behind the conversion of spin and orbital currents into charge currents and vice-versa, particularly at interfaces through the so called direct and inverse spin and orbital Edelstein effects.

In the second chapter, I explore the remarkable physical properties of the two dimensional electron system (2DES) at the interface of $LaAlO_3/SrTiO_3$ (LAO/STO), as well as the intriguing origin behind the existence of this 2DES. Later, I give a brief overview of the electronic band structure of the 2DES using a tight biding model.

In the third chapter, I describe in detail the first two experimental methods used to measure the spin-to-charge signal, which are the spin pumping by ferromagnetic resonance and the spin injection using the spin Seebeck effect. For each experimental technique, I provide an overview of the various spurious effects which can hinder our measurements.

In the fourth chapter, I present the measurements of the spin-to-charge conversion signal in LAO/STO using both spin pumping and spin Seebeck experiments. I first demonstrate the tunability and high efficiency of the spin-to-charge conversion. Secondly, I precisely measure the angular dependence of the spin-to-charge conversion signal and demonstrate its intimate relation with the electronic band structure of the 2DES. Finally, I demonstrate the significant orbital nature of the spin-to-charge conversion signal in LAO/STO.

In the last chapter, I attempt to unveil the dynamical response of the spin-to-charge conversion signal at very short timescales through ultrafast spin injection using the demagnetization of a ferromagnetic layer.

Chapter1

Overview of the field of spin-orbitronics

Contents

Since the discovery of the giant magnetoresistance effect by Albert Fert and Peter Grunberg [205, 211], a wide variety of applications have emerged especially in the field of magnetic memories. Lately, these rely on the magnetization switching in ferromagnetic materials, through the so-called "Spin-Transfer-Torque" (STT)[244, 208], using the injection of a polarized spin current to apply an effective torque on the magnetization. However, a new type of magnetization control based on the spin-orbit coupling has shown

to be highly efficient. It allows to perform an efficient spin injection without the need for ferromagnetic materials[237, 235, 217], as well as the detection of a spin current through the spin-to-charge conversion which can have wide variety of applications[225, 232, 241]. Very recently, a new degree of freedom has also been investigated based on the quantized orbital moment of the electrons, which like the spin can play an important role in magnetization switching[224]. Moreover, orbital-to-charge conversion effects will be discussed later in this thesis[247].

In the following, we will give a quick introduction to the charge, spin and orbital degrees of freedom of the electron. These are the building blocks of various mechanisms behind the inter-conversion of the spin and orbital information into a charge current through for example the spin-orbit coupling or sp hybridization[226], including the Spin Hall Effect[228], Spin Edelstein Effect[214] and their orbital counterpart, the Orbital Hall Effect[247] and Orbital Edelstein Effect[249].

1.1 Electron's spin and orbital angular momentum

In quantum mechanics, the total angular momentum **J**, describing the motion of an electron around its nucleus is quantized. In fact, $\mathbf{J} = \mathbf{L} + \mathbf{S}$ corresponds to the sum of two quantum operators, the first **L** being the orbital angular momentum operator, which describes the circular motion of the electron, while the second **S** is called the spin operator and it has a purely quantum mechanical origin, emerging from the Dirac equation [1]. According to the rules of quantum mechanics, the projection along all different axis x, y, z of the orbital and spin degrees of freedom are quantized and can be defined by two quantum numbers : m_l the magnetic quantum number, [2] and m_s the secondary spin quantum number, [3], through the relation :

$$L_i = \hbar m_l \qquad S_i = \hbar m_l \qquad \forall i \in x, y, z \tag{1.1}$$

Furthermore, electrons with spin **S** and orbital momentum **L**, carry a magnetic moment $\boldsymbol{\mu_s}$ and $\boldsymbol{\mu_l}$ respectively. Thus, the total magnetic moment $\boldsymbol{\mu} = \boldsymbol{\mu_s} + \boldsymbol{\mu_l}$ held by an electron has the following expression :

$$\boldsymbol{\mu} = -g_S \mu_B \boldsymbol{S} - g_L \mu_B \boldsymbol{L} \tag{1.2}$$

where $g_S \approx 2$, $g_L = 1$ and $\mu_B = e\bar{/}2m_e$ is the Bohr magnetron.

Since the electron holds various information regarding the charge, spin and orbital, one would expect that a

[1] Through relativistic corrections to the Schrodinger equation

[2] Which distinguishes the various orbitals available in the subshell (s,p,d,f,..) and it can have integer values ranging from $-l$ to $+l$ depending on the subshell occupied by the electrons

[3] It can take only two discrete values for the electron $-1/2$ and $+1/2$

flow of one degree of freedom such as charge may result into a flow of spin and orbital momentum, which will be discussed in the next section.

1.2 Charge, Spin and Orbital currents

A charge current density j_c refers simply to the flow of a density of charge carriers $n_{\sigma,L}$, for both spin σ (both spin-up $\uparrow$ or spin-down $\downarrow$) and orbital degree of freedom L (both clockwise L_z^+, and anticlockwise L_z^-), with a velocity $v_{\sigma,L}$ and it reads :

$$j_c = \sum_{\sigma,L} -en_{\sigma,L}v_{\sigma,L} \tag{1.3}$$

Therefore, one can also define from equation 1.3, the flux of spin(orbital)-polarized charged carriers j_σ (j_L) simply as :

$$j_\sigma = \sum_{L} -en_{\sigma,L}v_{\sigma,L} \tag{1.4}$$

$$j_L = \sum_{\sigma} -en_{\sigma,L}v_{\sigma,L} \tag{1.5}$$

Moreover, we can also define the so called spin current density j_s, and orbital current density j_o, as :

$$j_s = \frac{\hbar}{2e}(j_\uparrow - j_\downarrow) \tag{1.6}$$

$$j_o = \frac{\hbar}{e}(j_{L_z^+} - j_{L_z^-}) \tag{1.7}$$

where both j_s and j_o are expressed in the units of angular momentum $\hbar$.

From Figure 1.1, we notice that we can produce various types of currents, which can be either a pure charge current where $j_\uparrow = j_\downarrow$ and $j_{L_z}^+ = j_{L_z}^-$ with no net flow of angular momentum, a spin(orbital)-polarized current where $j_\uparrow \neq j_\downarrow$ or $j_{L_z}^+ \neq j_{L_z}^-$, resulting in both a flow of charges, spin and orbital momentum, and a pure spin(orbital) current where there is a net flow of spin and orbital angular momentum without any charge flow, as illustrated in Figure 1.1. The concept of pure spin and orbital currents have attracted a lot of attention lately, especially with the recent studies which have reported the detection and production of pure spin and orbital currents, through the highly efficient spin(orbit)-to-charge and charge-to-spin(orbit) inter-conversion processes[248, 243]. Indeed, a central ingredient in the conversion of charge current into a pure spin, is the spin-orbit coupling which will be introduced in the following subsection.

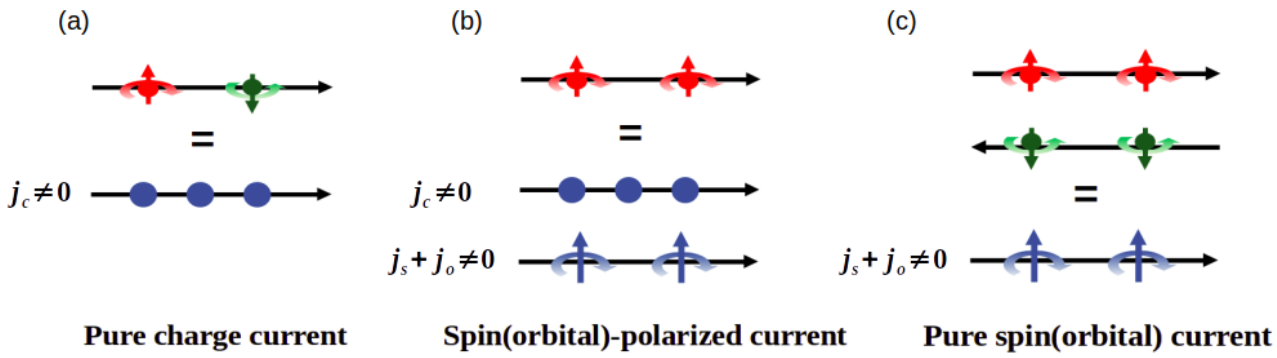

Figure 1.1: Three different types of currents. **(a)** A pure charge current where only a flow of charge carriers take place while no flow of spin or orbital moments is recorded. **(b)** Spin and Orbital polarized flow of charge carriers, where both a charge current and an angular momentum current are non zero. **(c)** A pure flow of angular momentum without any flow of charge carriers.

1.3 Atomic Spin-orbit coupling

Since an electron carries both a spin **S** and orbital angular momentum, **L** one would assume that a relation linking both degrees of freedom may exist. Indeed, in a semi-classical picture we represent the electron as an object, with an intrinsic spin angular momentum, orbiting around the nucleus with a velocity v. In the frame of the electron, the positively charged nucleus will appear to be orbiting around it, creating a time-varying electric field E which in turn produces an induction-like magnetic field B, which will interact with the spin magnetic moment of the electron $\boldsymbol{\mu_s}$ as shown in Figure 1.2. The additional Zeeman term in the Hamiltonian, which accounts for the spin-orbit coupling, reads :

$$H_{SOC} = -\frac{1}{2}\boldsymbol{\mu_s} \cdot \mathbf{B} \tag{1.8}$$

where the factor $1/2$ is the relativistic Thomas-Fermi factor, and $\mathbf{B} = (1/c^2)\mathrm{E} \times \mathbf{v}$. Thus, equation 1.8 , becomes [4] :

$$H_{SOC} = \frac{e\hbar}{4m_e^2c^2}\mathbf{E} \cdot (\mathbf{k} \times \boldsymbol{\sigma}) = \xi \mathbf{L} \cdot \mathbf{S} \tag{1.9}$$

, where $\mathbf{E} = -\nabla V(r) = (\mathbf{r}/r)(dV(r)/dr)$ is the local static electric field generated by the nucleus, $\xi = (e/2m_e^2c^2)(1/r)(dV(r)/dr)$ is the spin-orbit coupling constant, $\mathbf{L} = \mathbf{r} \times \mathbf{p}$ is orbital angular momentum and $\mathbf{S} = (\hbar/2)\boldsymbol{\sigma}$ is the spin angular momentum. The spin-orbit interaction is ubiquitous in various physical phenomena and it explains the fine structure of the Hydrogen atoms[222], it plays also an important role in the spin-dependent transport phenomena, to cite few : anistropic magnetoresistance (AMR)[233],

[4] Obtained from Lorentz transform applied to the Maxwell equations

anoumaloues Hall effect (AHE)[240] or in the spin Hall effect (SHE)[248], etc.

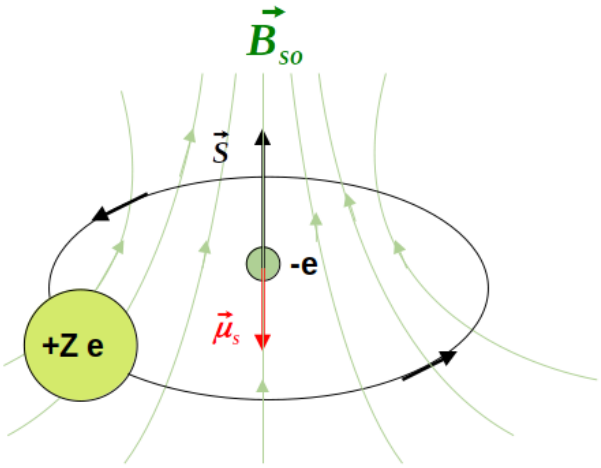

Figure 1.2: An illustration of the spin-orbit coupling, where in the frame of the electron the positively charged nucleus will generate a magnetic field which will act on the spin magnetic moment of the electron $\vec{\mu_s}$.

It is also interesting to note that since the spin-orbit coupling is proportional to **L**, one would expect no spin-orbit interaction for the s-orbitals ($L = 0$) and a maximum spin-orbit interaction for the p-orbitals compared to the d and f orbitals. This can be explained intuitively from the expression of the spin-orbit coupling constant [5] $\xi \propto -Z|e|/r^3$, where the closer the electrons are to the nucleus the larger the spin-orbit interaction is. Therefore, due to the close proximity of the p-orbitals to the nucleus compared to the d- and f-orbitals, one would expect a strong spin-orbit interaction in the 3p electron states. This was shown by Yafet[177] who reported also an increase of the spin-orbit splitting when filling the outer shell of the 3p orbitals [6], which explains the strong spin-orbit coupling in heavier elements.

1.4 Spin relaxation and dephasing mechanisms

Let's consider a single electron placed in a random fluctuating magnetic field. In this case, the electron's spin will precess around the effective fluctuating magnetic field with a Larmor frequency ω_0 and a correlation time τ_c, which represents the period for which a change of the effective dephasing magnetic field occurs, so that after multiple periods the spin information will be lost.

In order to understand the spin relaxation and spin dephasing mechanisms which are defined in the framework of Bloch-Torrey equations for the magnetization dynamics, one can resort to the toy model presented by Fabian and Wu[198] which introduces an external fluctuating magnetic field $\mathbf{B} = B_0\mathbf{u}_z + \mathbf{B}_\perp(t)$, where

[5] if we consider a simple coulomb potential generated by the nucleus with charge +Z
[6] By increasing Z from 11 to 19

B_0 is the static longitudinal component of the magnetic field and $\mathbf{B}_\perp(t)$ is a time-oscillating transverse component as sketched in Figure 1.3 a.

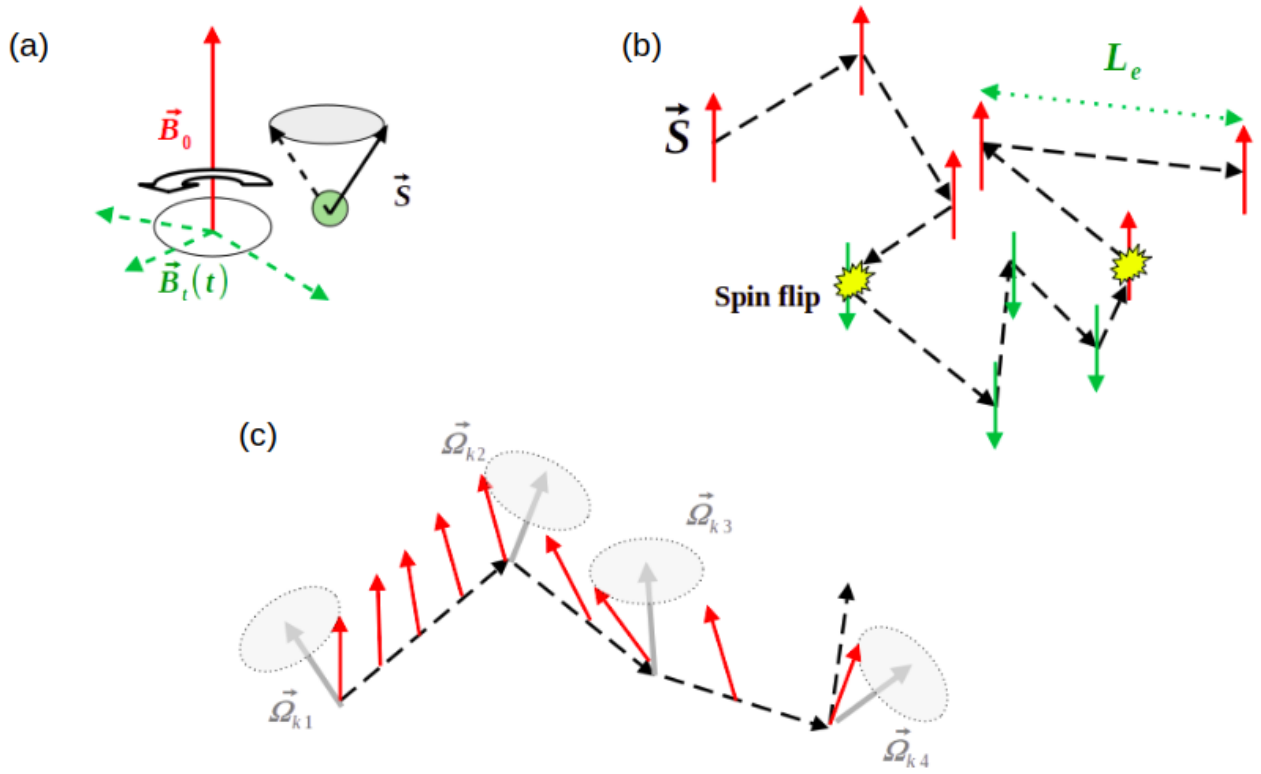

Figure 1.3: Various types of spin relaxation mechanisms. **(a)** An illustration of an electron precessing within a time oscillating magnetic field. **(b)** A sketch describing the Elliot-Yafet mechanism, where during each collision with impurities or phonons the spin may undergo a spin flip process. The distance between two collisions corresponds to the characteristic scattering length L_e. **(c)** A brief description of the D'yakonov-Perel' mechanism, where the spin undergoes a precession motion between two collisions, due to a k-dependent magnetic field, so that after multiple collisions the spin loses the information about its original phase.

Under these conditions, the dynamics of the spin S motion will be described by the following equations :

$$\frac{\partial S_x}{\partial t} = -\omega_0 S_y - \frac{S_x}{\tau_2} \tag{1.10}$$

$$\frac{\partial S_y}{\partial t} = -\omega_0 S_x - \frac{S_y}{\tau_2} \tag{1.11}$$

$$\frac{\partial S_z}{\partial t} = \frac{S_z - S_z^0}{\tau_1} \tag{1.12}$$

where S_z^0 is the thermal equilibrium value of the spin in the presence of a static magnetic field B_0. In addition, we note from equation 1.10 & 1.11 , that S_x and S_y decay with characteristic time τ_2 so-called

spin dephasing time, which describes the phase loss for the transverse components of electrons spin, which is ascribed to the time and spatial fluctuations of the precession frequencies. On the other hand, a second characteristic time constant τ_1 termed *the spin relaxation time*, appears in equation 1.12, and describes the time needed for the longitudinal spin component to reach its thermal equilibrium value S_z^0, thanks to the energy exchange between the spin system and lattice through spin-phonon coupling.

It also noteworthy to report that depending on the magnitude of the fluctuating magnetic field, two particular cases can be considered. The first case scenario, where we consider a weak fluctuating magnetic field, so that the inequality $\omega_0\tau \ll 1$ is satisfied, leads to a small spin precession frequency. Under these assumptions, in isotropic and cubic solids, the toy model described previously leads to the following relation :

$$\tau_1 = \tau_2 = \frac{1}{\omega_0^2 \tau c} \tag{1.13}$$

Thus, both the spin relaxation time τ_1 and the spin dephasing time τ_2 will represent the same quantity τ_{sf} ($\tau_{sf} = \tau_1 = \tau_2$), which is referred to as the spin-flip time or the spin lifetime. In conducting electronic systems, *the correlation time* τ_c is given by *the electron relaxation time* τ_p, which is smaller than a picosecond. Thus, keeping the relation satisfied even for magnetic fields of the order of a Tesla.

In the second case scenario, where the inequality $\omega_0\tau \gg 1$ is satisfied, the spin will precesses around B_0 several times during one period τ_c, leading to a conservation of the longitudinal component of the spin system while the transverse component to $\mathbf{u}_z$ will be averaged to zero, so that $\tau_{sf} \sim \tau_c$.

In the following section we will introduce in more detail two different scenarios that can generate a random fluctuating magnetic field, which will dive rise to different spin relaxation mechanisms.

1.4.1 Elliot-Yafet mechanism

Elliot was the first to realize that when an electron get scattered by the lattice ions, the electron spin will relax through spin-orbit coupling[176]. When considering metals with center of inversion symmetry, Elliot showed that the Bloch wavefunctions are no longer eignestates to $\boldsymbol{\sigma_z}$, but rather a linear combination of spin-up and spin-down states. Thus, the spin-state of the electron will be conserved between two collisions, and has a non-zero probability of flipping during a scattering event, as shown in Figure 1.3 b. Typically, for metals, the flipping rate equals one spin-flip in a thousand scattering events. Under these assumptions, Elliot derived a relation which links the spin relaxation time τ_{sf} to the momentum relaxation time τ_p and reads[176] :

$$\frac{1}{\tau_{sf}} = \xi \frac{(\delta g)^2}{\tau p} \tag{1.14}$$

where $\delta g = g - g_0$ stands for the variation in the g-factor from the free-electron value g_0, and ξ is a numerical factor introduced by Beuneu and Monod[180] which is related to the scattering mechanism.
In order to include the electron-phonon interaction, Yaffet extended Elliot's model, by drawing a straightforward relation between τ_{sf} and the resistivity of the materials ρ, so that the Yaffet relation reads[177]:

$$\frac{1}{\tau_{sf}}(T) \sim \rho(T) \tag{1.15}$$

Thus, Yafet was able to draw the temperature dependence for $\tau_{sf} \sim T^{-5}$ at low temperatures, just like the conductivity of various metals, which was confirmed experimentally by Monod and Beuneu. However, the Yaffet relation doesn't hold for example in the case of silicon where $\tau_{sf} \sim T^{-3}$[194]. In order to estimate τ_{sf}, both Elliot and Yaffet mechanisms should be considered, especially at low temperature where they have the same magnitude and can interfere destructively. Thus, the Elliot-Yaffet spin relaxation mechanism will link τ_{sf}^{EY} to τ_p through the following equation:

$$\frac{1}{\tau_{sf}^{EY}(\epsilon_k)} = \xi \frac{(\lambda_{SO})^2}{(\Delta\epsilon)^2} \frac{\epsilon_k}{\tau p(\epsilon_k)} \tag{1.16}$$

where λ_{SO} is the spin-orbit coupling constant, and $\Delta\epsilon$ is the average energy separation between a conduction band and nearest unoccupied (valence) band which are coupled through the spin-orbit interaction.
To conclude, one should keep in mind that the Elliot-Yaffet mechanism dominates the spin relaxation processes for centrosymmetric conductors, with center of inversion. However, when the system lacks inversion symmetry another spin relaxation mechanism should be taken into account which is the so-called D'yakonov-Perel' mechanism presented in the next section.

1.4.2 D'yakonov-Perel' mechanism

For systems lacking inversion symmetry, the spin degeneracy is lifted so that $E_{k,\uparrow} \neq E_{k,\downarrow}$, whereas the Kramers degeneracy due to time reversal symmetry $E_{k,\uparrow} = E_{-k,\downarrow}$, is preserved. This spin degeneracy lifting translates into a k-dependent magnetic field $\mathbf{B}_{SO}(\mathbf{k})$, which corresponds to an effective spin-orbit field and introduces a k-dependent Zeeman-like term to the Hamiltonian, given by :

$$H_{SO}^{DP} = \frac{\hbar e g_e}{4 m_e} \mathbf{B}_{SO}(\mathbf{k}) \cdot \boldsymbol{\sigma} = \frac{\hbar}{2} (\boldsymbol{\Omega}_{\mathbf{k}} \cdot \boldsymbol{\sigma}) \tag{1.17}$$

where $\mathbf{\Omega_k}$ represents the Larmor frequency of a single spin precessing around $\mathbf{B}_{SO}(\mathbf{k})$. In this case, for a given $\mathbf{k_1}$ the spin will precess with a frequency $\mathbf{\Omega_{k_1}}$ for an average time τ_p, after which it gets scattered and acquires a new momentum $\mathbf{k_2}$, which will change the precession frequency to $\mathbf{\Omega_{k_2}}$ as illustrated in Figure 1.3 c. In this case, the spin relaxation mechanism was derived by D'yakonov and Perel' through the following formula which links the the spin relaxation time τ_{sf}^{DP} and the electron relaxation time τ_p[179] :

$$\frac{1}{\tau_{sf}^{DP}} = \overline{\mathbf{\Omega_k^2}}\tau_p \tag{1.18}$$

Thus from equation 1.18, we notice that the spin phase changes randomly between each collision, so that during a time interval set by τ_p, it will undergo a random walk stochastic process. It is noteworthy to report that the above formula is true only in the limit where the inequality $\overline{\mathbf{\Omega_k}}\tau_p \leqslant 1$ is verified.

One should also notice that in the D'yakonov-Perel' relaxation mechanism, the spin relaxation rate $1/\tau_{sf}^{DP} \sim \tau_p$, which seems counter-intuitive because the more scattering processes there are (short τ_p) the bigger τ_{sf}^{DP} will become !

In a stark contrast, with the Elliot-Yafet mechanism, where $\tau_{sf}^{EY} \sim \tau_p$. One can explain the discrepancy between those two mechanisms simply by looking at Figure 1.3, where we observe that the faster the random changes in $\mathbf{B}_{SO}(\mathbf{k})$, the more they tend to cancel each other, thus keeping the spin phase unchanged.

As discussed previously, for systems lacking the inversion symmetry [7], both the Elliot-Yafet and the D'yakonov-Perel' mechanisms will compete. Their individual importance will depend on several parameters such as temperature, doping, crystal structure, materials composition, etc.

1.5 The interconversion of the spin, orbital and charge currents

By harnessing the spin-orbit interaction, one can manipulate the spin, orbital and charge degrees of freedom, through the various spin-momentum and orbital-momentum locking processes, which can be divided into two categories. The first corresponds to the spin Hall effect (SHE)[228] and inverse spin Hall effect (ISHE) [196] and their orbital counterpart the orbital Hall effect (OHE) [247] and inverse orbital Hall effect (IOHE) [196] which are found to exist in bulk materials. The second process, which is found at the surfaces and interfaces is driven by the Rashba spin-orbit coupling through the Direct and Inverse Rashba Eldestein effect [214, 249] which can be associated to both spin and orbital angular momentum.

[7] such as semiconductors III-V BIA and surfaces and interfaces SIA

1.5.1 In bulk materials

1.5.1.1 Direct and Inverse Spin Hall Effect

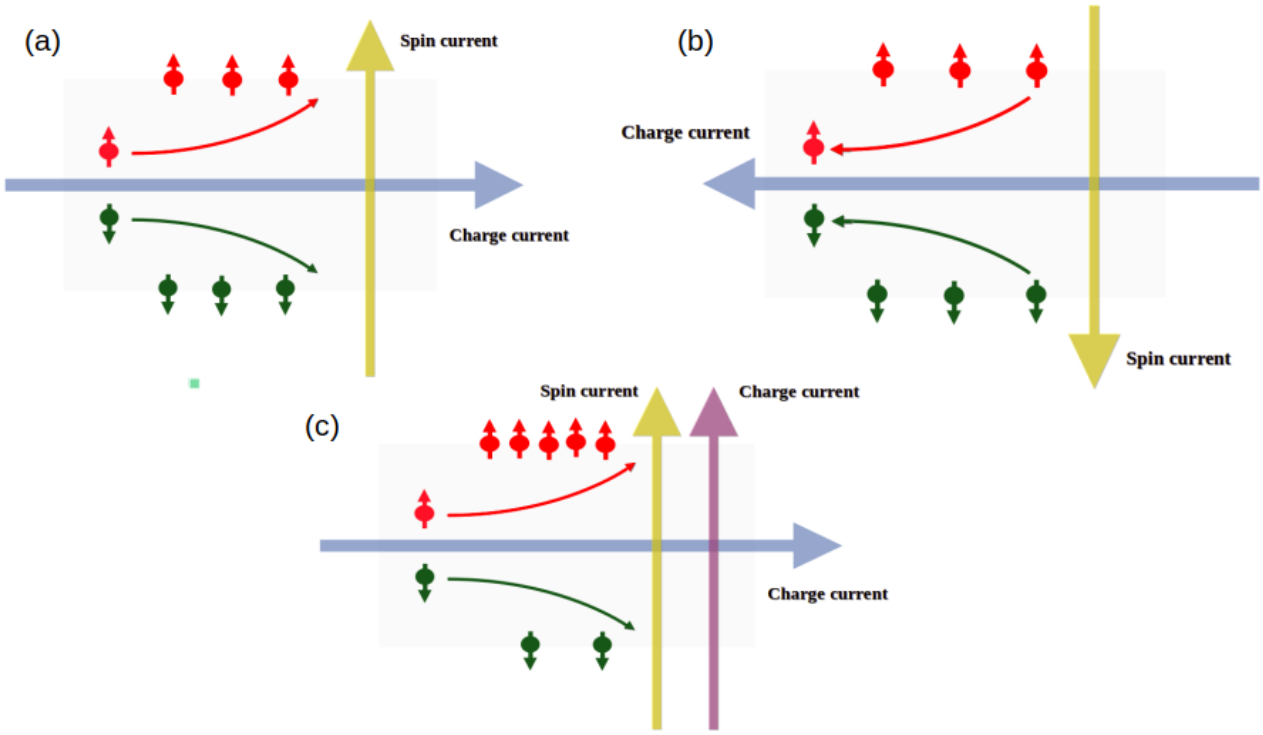

Figure 1.4: Three different Hall effects. **(a)** Direct spin Hall effect (SHE) where a charge current is converted into a spin current. **(b)** Inverse spin Hall effect (ISHE) where a spin current is converted into a charge current. **(c)** Anomalous Hall effect which occurs in magnetic materials, and corresponds to a spin-dependent mechanism where a charge current is converted into a transverse spin polarized charge current.

Since its theoretical prediction by Dyakonov and Perel' in the early 70's[178], the spin Hall effect (SHE) has played a central role in the creation of a dissipation-less pure spin current. It relies on the spin-orbit coupling allowing for the conversion of an electrical current passing through a nonmagnetic material into a pure spin current transverse to the directions of the charge current and the spin momentum as illustrated in Figure 1.4 a. Shortly after, the opposite effect referred to as Inverse spin Hall effect (ISHE) which corresponds to the conversion of a spin current into a charge current was observed in semiconductors by various groups around the world (see Figure 1.3 b). As one would expect, the experimental observation of the direct spin Hall effect has taken some time, due to difficulties encountered in order to measure a pure spin accumulation where no transverse electrical signal can be detected. The first experimental finding came from Kato et al who reported a direct spin Hall effect in GaAs using Kerr rotation microscopy[184]. It was also detected in heavy metals such as Pt or Al by Saitoh et al and Valenzuela et al[187, 248].

In order to understand the physics behind the spin Hall effect, we should recall the theory behind the

anomalous Hall effect (AHE), consequence of a spin-dependent scattering in ferromagnetic materials. Due to the spin population imbalance in the ferromagnetic material, a charge current within the ferromagnetic material creates a transverse spin accumulation at both sides of the sample. This is also associated to a charge imbalance resulting to a transverse Hall voltage, as illustrated in in Figure 1.3 c. Similarly, the spin Hall effect is the result of spin-dependent deflections in non-magnetic materials with no spin imbalance. Thus, the number of deflected carriers to opposite directions will be the same and no electrical transverse signal is detected, as illustrated in Figure 1.3 a. Therefore, in the spin Hall and inverse spin Hall experiments the spin and charge currents are connected through :

$$\mathbf{j_s^{SHE}} = -\frac{\hbar}{2e}\theta_{SHE}(\mathbf{j_c} \times \mathbf{s}) \tag{1.19}$$

$$\mathbf{j_c^{ISHE}} = -\frac{2e}{\hbar}\theta_{SHE}(\mathbf{j_s} \times \mathbf{s}) \tag{1.20}$$

where **s** is the spin polarization, θ_{SHE} is the spin Hall angle which quantifies the spin-to-charge conversion efficiency and it corresponds to the ratio of the off-diagonal spin Hall conductivity σ_{xy}^{SHE} to the conductivity of the diagonal term σ_{xx}. The value of the spin Hall angle θ_{SHE} depends on various parameters which can be divided into two main contributions. The first is intrinsic and solely related to the electronic contributions ascribed to the spin-splitted band structure in the presence of spin-orbit coupling. The second contribution is related to a spin-dependent scattering driven by impurities through the spin-orbit coupling. The latter contribution stems from two impurities-driven scattering mechanisms which are the skew scattering[227] and the side-jump scattering[207], which we will discuss in the following section.

1.5.1.1.1 Intrinsic mechanism The spin Hall effect has an intrinsic contribution, present even in the absence of impurities, that can be ascribed to the spin-split band structure due to the spin-orbit interaction. It yields an additional term to the carrier's velocity, the so-called anomalous velocity, which is related to the Berry curvature $\mathbf{C_k}$. It manifests itself as a k-dependent effective magnetic field which links the band structure to the anomalous velocity through an electric field[239, 238]. Thus, the intrinsic contribution will correspond to a spin-depend deflection of electrons of different spins in the presence of an electric field, as illustrated in Figure 1.5 a. It is also important to note that the Berry curvature $\mathbf{C_k}$, is non-zero for systems with broken-time reversal symmetry, or broken inversion symmetry. It is also well known that this intrinsic mechanism is dominant in heavy metals (Pt or Ta)[187, 235], through an intrinsic contribution to the total spin Hall conductivity σ_{xy}^{int}.

1.5.1.1.2 Extrinsic mechanisms In the presence of a charge impurity, the electrons will undergo a spin-dependent scattering due to the spin-orbit coupling on the impurity, and this in turn yields an additional term σ_{xy}^{skew} to the total transverse spin Hall conductivity. This mechanism is known as the Mott-skew scattering, and was first described by Smit[245], where both spin-up $\uparrow$ and spin-down $\downarrow$ electrons are deflected into two opposite directions due to the strong spin orbit interaction with the impurity, as illustrated in Figure 1.5 b. The skew scattering was also envisioned by D'yakonov-Perel' to be behind the spin accumulation in non-magnetic materials[220]. Another type of spin-dependent scattering was introduced by Berger[207], corresponding to a spin-dependent scattering mechanism where the trajectory of the deflected spins will be altered through a spin-dependent lateral displacement, while the electrons preserves their wave vector **k**, as illustrated in Figure 1.5 c. This scattering mechanism is referred to as the side-jump scattering, and it contributes with an additional term to the spin Hall conductivity σ_{xy}^{s-j}, so that the total spin Hall conductivity will be given as the sum all previous contributions:

$$\sigma_{xy}^{SHE} = \sigma_{xy}^{int} + \sigma_{xy}^{skew} + \sigma_{xy}^{s-j} \tag{1.21}$$

Thus the spin Hall angle θ_{SHE} will be the sum of various terms which can be tuned in order to increase the spin-to-charge conversion efficiency. However, one should recall that the electron carries also an orbital degree of freedom which can, like its spin counterpart, be converted into a charge current and vice-versa.

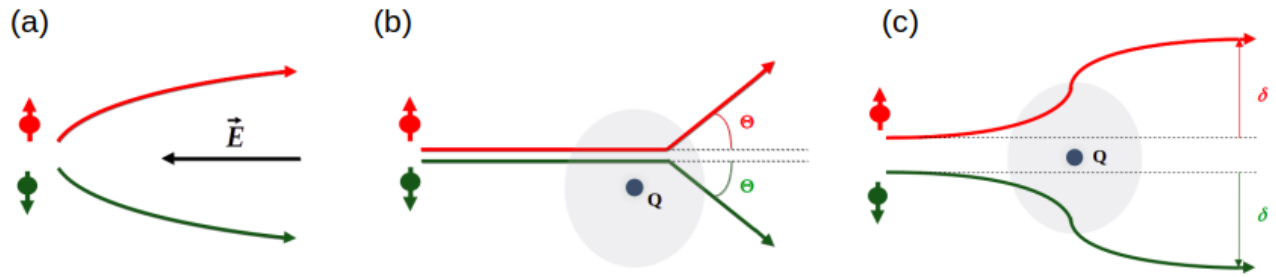

Figure 1.5: Intrinsic and Extrinsic spin contributions to the spin Hall effect. **(a)** Intrinsic electrically driven spin-dependent mechanism. The two different extrinsic mechanisms relying on spin-dependent impurity scattering are, **(b)** the skew scattering and **(c)** the side-jump scattering.

1.5.1.2 Direct and Inverse Orbital Hall effect

The orbital Hall effect refers to the counterpart of the spin Hall effect, but with the orbital momentum degree of freedom **L** instead of the spin degree of freedom. In this case, an applied external electric field induces a transverse flow of atomic orbital angular momentum (which is an orbital current), as illustrated in Figure 1.6 a. The opposite effect is also possible, where the flow of a pure orbital momentum current can

generate a transverse charge current, which is known as the Inverse orbital Hall effect. It is also noteworthy to report that the orbital degree of freedom **L** has often been taken into account in various theoretical studies[247, 192, 210]. However, the dynamical roles of **L** have been commonly ignored in the literature, until very recently with various studies by Tanaka et al [247] and Kontani et al [192] for 4d and 5d transition metals.

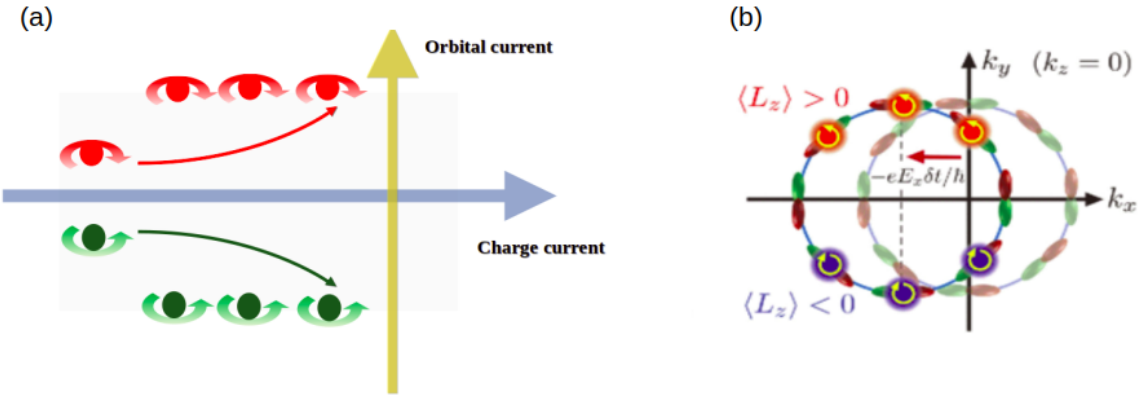

Figure 1.6: An illustration of the orbital Hall effect (OHE) and its intrinsic origin. **(a)** In the presence of an applied electric field, orbitals with opposite chiralities (clockwise or anti-clockwise) are deflected into two opposite directions which induces a pure orbital current. **(b)** An applied electric field induces a shift in the orbital contours which yields a non zero $\langle L_z \rangle$ which changes sign depending on the sign of k_y. [202]

Interestingly, it appears that the orbital Hall effect, unlike the spin Hall effect, can take place even in the absence of spin-orbit coupling, and can be converted into spin Hall effect in the presence of sizable spin-orbit coupling, meaning that the orbital Hall effect is more fundamental than the spin Hall effect in this case. It is also important to note that a strong spin-orbit coupling is not the only ingredient for a high spin Hall angle, so that it appears that in materials with low spin-orbit coupling and with a gigantic orbital Hall conductivity, one can still obtain a very high spin Hall angle, which opens the quest to seek for materials with the highest orbital Hall conductivity.

In order to investigate further the origin of the orbital Hall effect, one needs to return to a microscopic understanding based on the orbital-texture mechanism.

1.5.1.2.1 Intrinsic mechanism Upon applying an external electric field **E** along the x-direction, we observe that the k-dependent orbital texture [8](see Figure 1.6 b), will be shifted due to the Coulomb force which acts on the electrons, and will induce a momentum displacement :

[8]which unlike the spin-texture can be present in centrosymmetric media, and where the expectation value of **L** vanishes for all the eigenstates

$$\Delta k_x = \frac{-eE\delta t}{\hbar} \tag{1.22}$$

,

where δt represents the time duration of the injected charge current into the system. It appears that this k-space shift induces an interband superposition in the orbital texture which generates a non zero $\langle \mathbf{L} \rangle \propto \mathbf{E} \times \mathbf{k}$. So that in the plane $k_z = 0$, as shown in Figure 1.6, we observe that $\langle \mathbf{L} \rangle$ is aligned with the **z** direction and points in opposite directions for positive and negative k_y's. Thus, one would expect that even in the presence of orbital quenching the orbital Hall current $\sim \langle v_y L_z \rangle$ is non zero, signaling the importance of the orbital-texture which explains the intrinsic mechanism behind the orbital Hall effect. In order to further understand this mechanism, Go et al [202] have shown that by tuning the sp hybridization parameter γ_{sp}, both orbital and spin Hall conductivity (resp σ_{OH} and σ_{SH}) can be gigantic $\sim 10^3\hbar/2|e|$ $(\Omega \cdot cm)^{-1}$, for γ_{sp} above $0.1eV$, as illustrated in Figure 1.7 a. This shows that the orbital texture is not only crucial to the orbital Hall effect but also to the spin Hall effect. Furthermore, as shown in Figure 1.7 b, the orbital Hall conductivity is non zero even in the absence of spin-orbit coupling, whereas, the spin Hall conductivity increases when the spin-orbit coupling is turned on. However, the spin Hall conductivity appears to have non-monotonic dependence on the spin-orbit parameter α_{SO}, and it starts decreasing above a threshold value of $\alpha_{SO} \approx 0.1eV$. This non-monotonic dependence can be associated to a reduction of the orbital Hall conductivity σ_{OH} at higher α_{SO}, but also to the saturation of the conversion efficiency of the OHE to SHE, as shown in Figure 1.7 b in the inset.

On the other hand, some theoretical studies have shown that a giant positive orbital Hall conductivity σ_{OH} in transition metals which can be considerably larger than the spin Hall conductivity σ_{SH} can be associated to the orbital Aharanov-Bohm phase factor due to the d-orbital angular momentum[192]. In that case, the details of the band structure are irrelevant to the orbital Hall conductivity σ_{OH}, as shown in Figure 1.7 c, where it seems that the orbital Hall conductivity σ_{OH} is independent of the atomic species of the transition metals.

Consequently, the orbital Hall effect is an essential phenomenon to explain the origin of the spin Hall effect but also the anomalous Hall effect in the presence of spin-orbit coupling, so that the sign change in the spin Hall conductivity will be directly associated to the spin-orbit polarization at the Fermi level.

Finally, one would expect that in multi-orbital systems, where the orbital texture is ubiquitous, the orbital Hall effect may have a crucial role in the engineering of new materials with a strong orbital Hall conductivity leading to a highly efficient spin-to-charge interconversion.

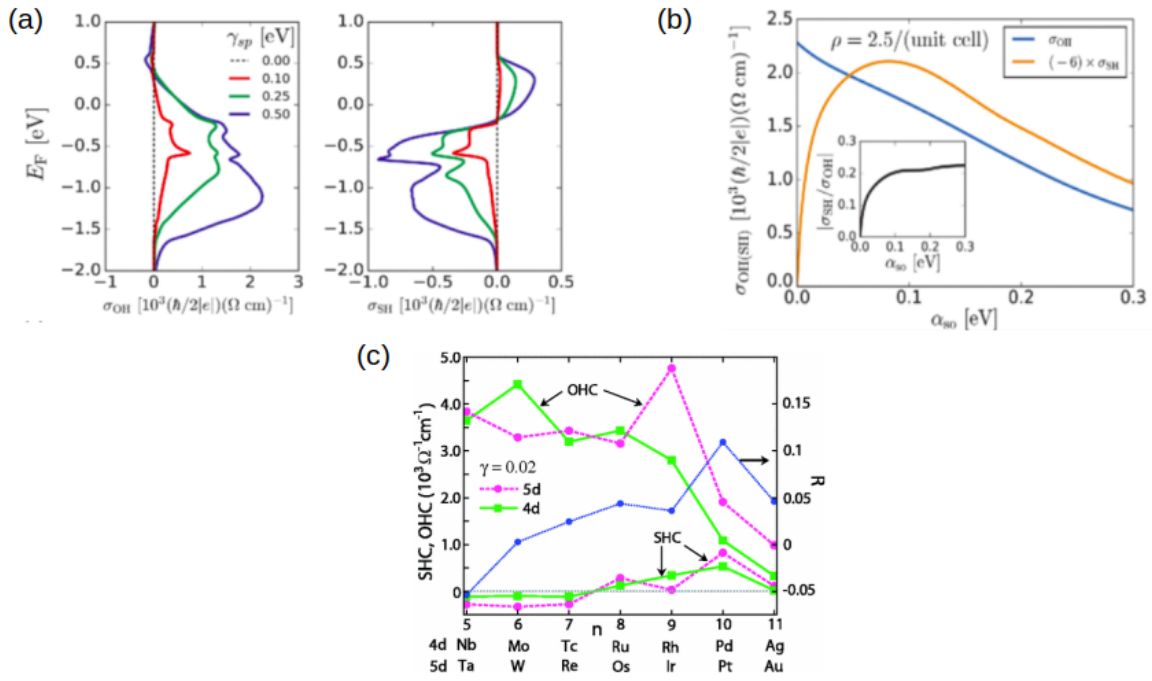

Figure 1.7: A comparison between the orbital and spin Hall effects. **(a)** Energy dependence E_f of the spin and orbital conductivity for various values of the sp hybridization term γ_{sp}.[202] **(b)** Variation of spin and orbital conductivity versus the spin orbit strength α_{SO}, for a fixed electron density $\rho = 2.5$/u.c. In inset: the ratio σ_{SH}/σ_{OH} versus α_{SO}.[202] **(c)** Left axis : variation of the spin and orbital conductivities for various 4d and 5d metals. Right axis : Spin-orbit polarization R for various 5d metals.[192]

1.5.2 At surfaces and interfaces

The lack of space-inversion symmetry in a physical system results in a non-vanishing electric field which may arise at surfaces and interfaces of various materials, such as the interface between two metals Ag/Bi or oxide interfaces like $LaAlO_3/SrTiO_3$. In this case, the electrons moving in this electric field will experience, as seen previously, a magnetic field which will act on their spin degree of freedom. In the presence of spin-orbit coupling, the magnetic field which arises indirectly from the space-inversion asymmetry (SIA) at the interface, will act on the momentum of these electrons **k** through the spin-momentum locking [9], resulting in the spin degeneracy lifting of the band structure.

In the following, we will focus in particular on the interaction between the emerging magnetic field and the spin angular momentum of electrons, at the interface of two different materials, which leads to an additional term to the Hamiltonian known as the Byachkov-Rashba spin-orbit coupling or more briefly the "Rashba coupling" .

[9] It corresponds to the configuration where the direction of the spin and the momentum which needs to be perpendicular to one another to maximize the Rashba coupling

1.5.2.1 Byachkov-Rashba spin-orbit coupling

As discussed previously, the combination of space-inversion asymmetry (SIA) and spin-orbit coupling result in the separation of the conduction bands into two branches, each with its own spin orientation, as illustrated in Figure 1.8 a. In this context, Rashba and Byachkov were the first to realize that this effect can occur at the interface of two different materials like in quantum wells in semiconductors where a two-dimensional electron gas is trapped at the interface through engineered band-gaps[213, 214]. Due to the SIA, an electric field **E** along the z-direction perpendicular to the interface results in an additional term to the Hamiltonian, the so-called Rashba Hamiltonian H_R, and is given by:

$$H_R = \alpha_R(\mathbf{z} \times \mathbf{k}) \cdot \boldsymbol{\sigma} \tag{1.23}$$

where α_R represents the Rashba coefficient , **k** is the in-plane wavevector, and $\boldsymbol{\sigma}$ is the Pauli spin matrices. From the expression of the Rashba Hamitonian (see equation1.23), a maximum contribution can be obtained if all the three vectors (**k** , **z**, and $\boldsymbol{\sigma}$) are perpendicular to one another, so that the spin $\boldsymbol{\sigma}$ will lie in the plane perpendicular to the momentum **k**, which refers to the spin-momentum locking.

In addition, Rashba coupling leads to the spin-degeneracy lifting in the band structure so that the energy dispersion of opposite spin-oriented subbands is given by :

$$E_{\uparrow,\downarrow}(k) = \frac{\hbar k^2}{2m} \pm \alpha_R k \tag{1.24}$$

So one can deduce the momentum-dependent separation between the two subbands which yields a momentum shift $k_R = \pm\alpha_R m/\hbar^2$, so that the Fermi surface will contain two inequivalent Fermi contours with opposite spin chiralities (clockwise or counter-clockwise) in the (k_x , k_y) plane. This is illustrated in Figure 1.8 b, where we chose $\alpha_R > 0$. For each **k**, the Rashba coupling can be understood in the framework of the D'yakonov Perel' mechanism where a momentum-dependent magnetic field induces a spin relaxation mechanism, so that the SIA will generate an effective Rashba field which takes the following form :

$$B_{SO}^{SIA}(k) = \frac{2\alpha_R}{\hbar}(\mathbf{z} \times \mathbf{k}) \tag{1.25}$$

Lately, the Rashba coupling has attracted a lot of attention, particularly due to the large spin-splitting of the subbands (large Rashba coefficient α_R) which is displayed by various systems like the interface between Ag/Bi[199] and also the surface states of some topological insulators such as Bi_2S_3[201], allowing for some interesting applications in spin-based transistors where a spin information can be monitored by

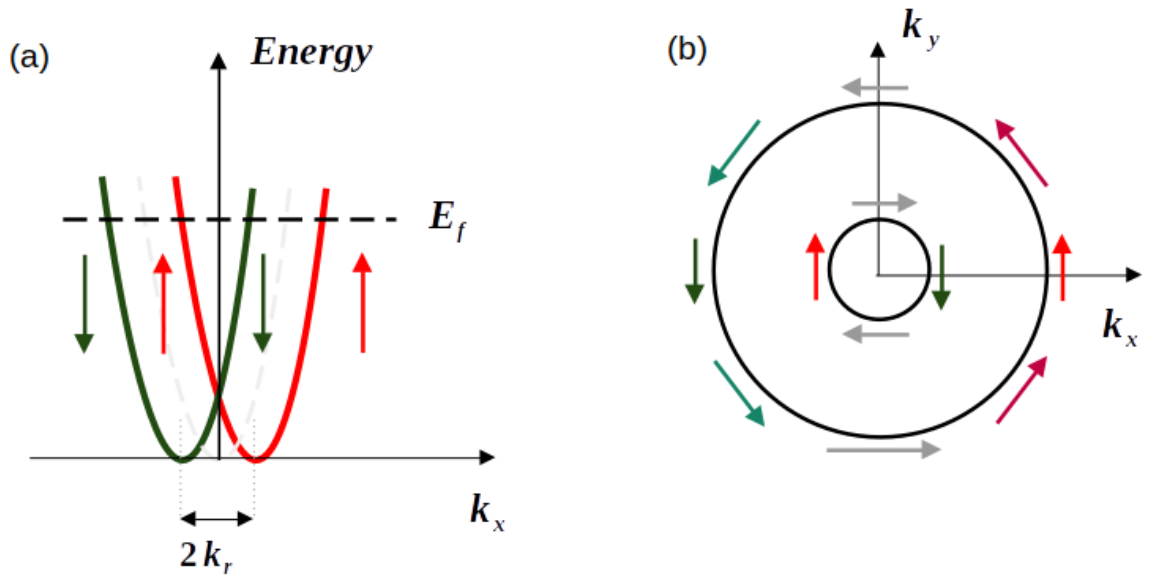

Figure 1.8: Band structure of a 2D Rashba system. **(a)** Energy dispersion for two opposite spin polarized Rashba-split bands. **(a)** The Fermi surface which contains two Fermi contours with opposite spin chiralities.

a gate voltage which tunes the strength of the Rashba coupling. Another interesting application is the spin-to-charge interconversion where the Rashba spin-orbit coupling can be harnessed to allow for a more efficient conversion compared to the classical ISHE in heavy metals.

Interestingly, the lack of a center of inversion symmetry in non-centrosymmetric bulk semiconductors like GaAs, can also yield an additional term to the Hamiltonian which was first introduced by Dresselhaus in the mid 50's and was named after her. The so the so-called Dresselhaus effect [195, 183] can thus be solely attributed to the bulk inversion asymmetry (BIA) contrary to the Rashba effect which stems from space inversion asymmetry (SIA). It is also noteworthy to report that because later in this manuscript we will consider only centrosymmetric media the Dresselhaus effect will not be taken into account so that only the Rashba effect will be considered.

In the following, we will investigate two different effects which are a direct consequence of the Rashba coupling at surfaces and interfaces and allow for an electrical control of the spin information and vice versa.

1.5.2.2 Direct and Inverse Spin Rashba Edelstein Effect (SEE)

Similarly to heavy metals which display an inverse spin Hall effect (ISHE), two-dimensional electron systems (2DES) exhibiting Rashba spin-orbit coupling[204, 230, 221] allow for the detection of a non-equilibrium spin population through the generation of a 2D charge current. It is known as the Inverse Spin Edelstein effect and sometimes referred to as the Inverse Spin Galvanic effect which was first demonstrated by Ganichev et al [182] in quantum well semiconductors. The opposite effect which is the Onsager reciprocal effect[216],

namely the Direct Spin Edelstein effect, allows for the conversion of a 2D charge current into a net spin polarization in the 2DES.

1.5.2.2.1 Fermi contours In order to understand the mechanisms behind these two effects one needs to return to the band structure for a 2D Rashba interface, containing 2 inequivalent Fermi contours with opposite spin chiralities, as shown in Figure 1.8 b.

Let us now consider the first case scenario, where we inject a 2D charge current into the Rashba interface, by applying an electric field $\mathbf{E} = E\mathbf{x}$, forcing the electrons to move in the opposite direction $-\mathbf{x}$ from the flowing charge current, due to their negative charge $q = -e$. This will induce a shift of the energy dispersion relation for these electrons in momentum space, which can be estimated in the single band picture as :

$$\Delta\mathbf{k_x} = \frac{e\mathbf{E}\tau}{\hbar} = \frac{\tau e\mathbf{j_c}}{\sigma\hbar} \tag{1.26}$$

,

where $\mathbf{j_c}$ is the charge current density and σ is the Drude conductivity of the 2DES.

If one considers the case of a Rashba interface [10], a k-space shift of both the inner and outer Fermi contours by Δk_x will occur in this case, as shown in Figure 1.9 a. Due to the spin-momentum locking, the spin degree of freedom for an electron with a momentum along the x direction will have to align along y (resp. $-y$) direction for the outer (resp. inner) Fermi contours. Therefore, a shift of both Fermi contours (with radii k_F^{inner} and k_F^{outer}) will induce a spin accumulation due to the inequivalent spin densities $\delta s_\uparrow$ and $\delta s_\downarrow$. This is shown in Figure 1.9 a, where the spin accumulation results from the hatched areas green and red colors which are proportional to $k_F^{inner}\Delta k_x$ and $k_F^{outer}\Delta k_x$ respectively. This mechanism is known in the literature as the direct spin Eldestein effect, which was first theorized by Edelstein back in the 90's.

The opposite effect is also possible and can be understood with the same schematics of the Fermi contours. When a spin population δs_y is injected along the y direction, the Fermi contours are shifted along two opposite directions, which generates a non-zero total net displacement Δk_x^{total}, proportional to the Rashba band splitting Δ_R. So, the injection of a 3D spin current in a Rashba interface results in the creation of a 2D charge current, as displayed in Figure 1.9 b. This effect is known as the Inverse spin Edelstein effect.

[10] where we have both space inversion asymmetry and the spin orbit coupling

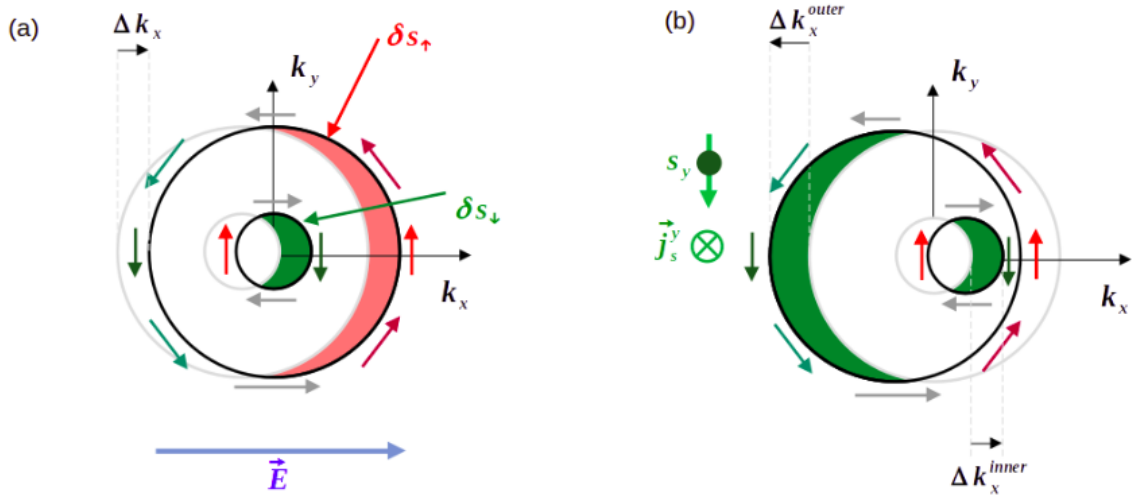

Figure 1.9: An illustration of both the direct and inverse Edelstein effects. **(a)** An applied external electric field induces a shift in the Fermi contours, which creates a spin accumulation due to the partial compensation of the of the two opposite spin polarizations ($\delta s_\uparrow$ and $\delta s_\downarrow$). **(b)** When we inject a non equilibrium spin population from the z-direction, with a spin component along the y-direction, the inner and the outer Fermi contours are shifted into two opposite directions which do not cancel each other, so that a net charge current is created.

1.5.2.2.2 The Rashba spin-to-charge conversion efficiency

Similarly to the spin Hall angle which quantifies the spin-to-charge conversion efficiency for the ISHE, one needs to calculate the conversion efficiency of the Inverse spin Edelstein effect, where we assume that a spin population polarized along the y direction $< \delta S >$ is injected within the 2D Rashba interface. This induces a displacement of the two Fermi contours as shown in Figure 1.9 b, yielding a 2D charge current $j_c^{2D} = j_{cout}^{2D} + j_{cin}^{2D}$ along the x direction. It can be written as the sum of two charge currents associated with the outer and inner Fermi contours respectively, and it is linked to the injected spin population through the (approximate) following relation :

$$j_c^{2D} = \frac{2e\hbar}{m} \frac{< \delta S >}{2} (k_F^{outer} - k_F^{inner}) \tag{1.27}$$

From the expression of the Rashba Hamiltonian (equation 1.23) one would expect that the distance between the two Fermi contours is :

$$k_F^{outer} - k_F^{inner} = \frac{2m}{\hbar^2} \alpha_R \tag{1.28}$$

Because, the injected spin population is linked to the flow of an incoming 3D spin current j_s^{3D}, one can draw the relation between these two quantities and the electron relaxation time τ in the 2DES, as :

$$j_s^{3D} = \frac{2e}{\hbar}\frac{<\delta S>}{\tau} \tag{1.29}$$

So, by combining all these equations , we can quantify the spin-to-charge conversion efficiency λ_{IEE}, which corresponds to the ratio between j_c^{2D} and j_s^{3D}, so that :

$$\lambda_{IEE} = \frac{j_c^{2D}}{j_s^{3D}} = \frac{\alpha_R \tau}{\hbar} \tag{1.30}$$

One should note that λ_{IEE} has the dimension of a length unlike the spin Hall angle which is dimensionless. Another important remark comes from the fact that λ_{IEE} depends only on the spin-independent scattering time τ contrary to the spin Hall effect related to the anomalous velocity which is a spin-dependent quantity. Therefore, from the expression of λ_{IEE}, we observe that in order to maximize the spin-to-charge conversion efficiency one needs to look for materials with high Rashba coefficient such as the interface between Ag/Bi[199] or maximize the electron relaxation time by for example isolating the 2DES form all external relaxation channels such as the 2DES at the interface of LAO/STO which displays one of the largest reported λ_{IEE} [200].

1.5.2.3 Direct and Inverse Orbital Rashba Edelstein Effect (OEE)

As shown previously, due to the spatial inversion asymmetry (SIA) an applied electric field produces a spin polarization perpendicular to the applied field, thanks to the spin-obit coupling. However, because the electrons carry both spin and orbital moments one would expect an orbital counterpart to the spin Edelstein effect, so the so-called orbital Edelstein effect. In this case, an applied electric field induces an orbital magnetization, as illustrated in Figure 1.10. The reciprocal effect is also possible where a net orbital magnetization can be converted into a charge current and this is known as the inverse orbital Edelstein effect . It is also interesting to note that the orbital magnetization can emerge from two different contributions, the first being the orbital moment generated due to the circular motion of the electrons around their nucleus which produces a net orbital moment **L**. The second contribution emerges from the self-rotation of the electron wave packets which can be represented in magnetic Bloch bands as a mechanical angular momentum $\mathbf{L} = \mathbf{r} \times \mathbf{P}$.[215]

Interestingly, the orbital Edelstein effect has not drawn enough attention when it was first predicted back in the 80's by Levitov et al[234]. It is only recently that a very strong contributions resulting from wave packet self-rotation have been predicted to appear in chiral and helical crystals[250, 249] as well as in Rashba systems[203, 113, 112]. Additionally, for noncentrosymmetric systems in the presence of spin-orbit coupling,

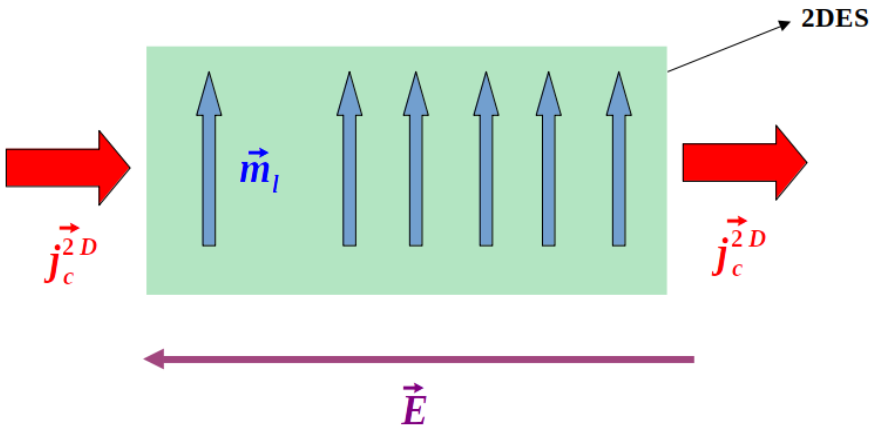

Figure 1.10: An illustration of the orbital Edelstein effect, where a transverse homogeneous orbital magnetization is induced due to an external electric field which is applied to a Rashba-split 2DES.

the electrically induced magnetization was found to originate from both spin and orbital Edelstein effects. In fact, Salemi et al [130] have shown from first principle calculations in noncentrosymmetric antiferromagnets that the electrically induced magnetization can display both Rahsba-like and Dresselhaus-like symmetries, where the magnetization have parallel and out-of plane components. More importantly, it seems that the orbital Edelstein effect does not require the presence of spin-orbit coupling, and it seems to be at least one order of magnitude higher than the spin Edelstein effect[203].

In order to further understand the underlying physics behind the orbital Edelstein effect, one needs to define an orbital counterpart to the spin Rashba Hamitonian.

1.5.2.3.1 Orbital Rashba Hamiltonian Similarly to the spin Rashba effect, which is driven by the Rashba coupling lifting the spin-degeneracy, its orbital counterpart, the orbital Rashba effect is associated with the emergence of chiral orbital textures even in the absence of the spin-orbit interaction. So, one would expect an orbital equivalent to the Byachkov-Rashba spin-orbit coupling, the so-called orbital Rashba Hamiltonian term which couples the orbital degree of freedom to the electron momentum via a Rashba constant , so it is given by[226] :

$$H_{OR} = \frac{\alpha_{OR}}{\hbar}\mathbf{L} \cdot (\mathbf{z} \times \mathbf{k}) \tag{1.31}$$

where α_{OR} is the orbital Rashba constant which depends on the surface potential associated with the spatial symmetry breaking, and the multiband effects such as sp hybridization. In that case α_{OR} will be given by:

$$\alpha_{OR} = \frac{\nu a \gamma_{sp} V_z}{\Delta E_{sp}}\Big|_{k=0} \tag{1.32}$$

where $\nu \sim 1$ is a parameter dependent on the lattice structure, a is the lattice parameter, γ_{sp} is the nearest-neighbor hopping amplitude between the $p_{x,y}$ and s orbitals, and ΔE_{sp} is the energy bandgap between p $\&$ s bands.

1.5.2.3.2 Orbital textures Similarly to the spin texture, the orbital texture is a direct consequence of the orbital Rashba coupling where the orbital moment is related to the electron momentum through equation 1.31, so in order to maximize the orbital Rashba Hamiltonian term one would expect the orbital moment to lie in the $(z = 0)$ plane and should be perpendicular to the direction of the electron momentum **k**. It is also interesting to note, that unlike the spin which has two quantum numbers $m_s = \pm 1/2$, the orbital degree of freedom has a higher number of associated quantum numbers, for example d orbitals $(l = 2)$ have five quantum numbers $m_l = 0, \pm 1, \pm 2$. This allows for larger Rashba-like splitting in the orbital textures due to the non-compensation of the antiparallel orbital moment in the inner and outer Fermi contours as shown in Figure 1.11 a. As a consequence, one would expect the orbital Rashba effect to exhibit an orbital Edelstein effect even in the absence of spin-orbit coupling, where band-resolved densities can perfectly compensate each other $\Delta k = 0$. Additionally, due to multi-orbital effects, the orbital texture can display a non-trivial **k**-dependence as shown in Figure 1.11 b, where we plot the orbital texture of the in-plane orbital moment obtained from first principle calculations for a two dimensional electron system (2DES) at $SrTiO_3$ interfaces[203]. In the next section, we will introduce the various physical properties of a quasi 2DES at the interface of two perovskite oxides which are $LaAlO_3$ and $SrTiO_3$.

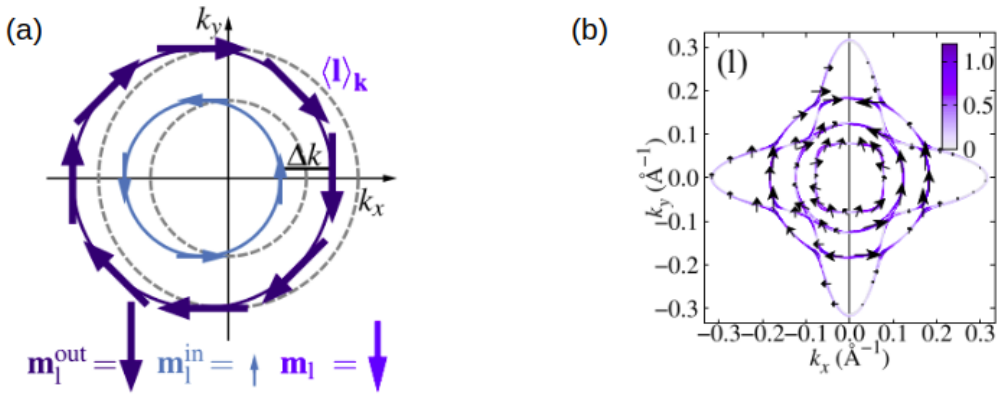

Figure 1.11: An illustration of the k-dependent orbital textures. **(a)** Two Fermi contours with opposite orbital chiralities, where the difference between the orbital moments (purple and blue arrows) in the inner and outer Fermi contours yield a finite orbital magnetization. [203] **(b)** A non-tivial orbital texture of the 2DES at the interface of $SrTiO_3$, at a Fermi energy $E_f = -14meV$.[203]

Chapter2

The interface between LAO/STO (001)

Contents

Artificially fabricated heterostructures have lead to the discovery of a variety of emerging phenomena, through parameter engineering of competing orders, leading to novel properties and functionalities. These efforts have opened up for the possibility to study a new set of physical phenomena at the boundary of two different materials, which lead to great discoveries in semiconductor physics[181], and more recently, in

complex oxide physics[186]. A first breakthrough, came from the heterointerface of two perovskite oxides of $LaAlO_3$(LAO) and $SrTiO_3$(STO), which were shown to harbor a 2 dimensional electron system at the vicinity of their interface[186]. Since then multiple studies have been published in this regard, demonstrating the coexistence of a superconducting phase [190] with a ferromagnetic order in the 2DES [197]. Thus, opening the door for various exotic physical phenomena. Furthermore, another appealing property of the 2DES, which is the Rashba coupling due the spatial symmetry breaking at the heterointerface was demonstrated very recently[193], leading to the creation of a spin-to-charge conversion signal in LAO/STO interface, paving the way for novel spin-based devices[218, 246, 236]. In this context, this thesis will follow these efforts, and demonstrate that this system still hold many amazing properties. The first part of this chapter will focus on the recent experimental studies regarding the emerging properties of the LAO/STO hetrointerface. Later, we will discuss the various mechanisms at play, when it comes to the emergence of the conductivity at the interface, which will give us a hint into it's origin. Then, a theoretical study of the electronic structure of the 2DES at the interface will be presented in order to uncover the complex band structure which is a landmark to the multi-band effects at play in complex metal-oxides . Finally, a quick review of the pulsed laser deposition technique used for the growth of LAO/STO and the structural characterization and transport properties which were realized in collaboration with Triscone's group in Geneva.

2.1 The LAO/STO intreface

2.1.1 A surprising interfacial conductivity

In 2004, Ohtomo and Hwang have been the first to report the metallic behavior of LAO/STO interface[186]. Indeed, by growing a band gap insulator of LAO , $E_{gap}^{LAO} = 5.6eV$, on top of a 001-oriented STO substrate [1] , $E_{gap}^{STO} = 3.3eV$, a high mobility 2 dimensional electron system (2DES) have been reported, to the great surprise of the research community. This discovery have been considered as a breakthrough for multiple application for oxide-based devices, particularly for beyond CMOS applications for future computer electronics. It is noteworthy to report that LAO was deposited on top of an STO substrate using a pulsed laser deposition technique. The growth process was controlled to an atomically thin film precision using reflection high energy electron diffraction (RHEED), where each period in Figure 2.1 a, represents a grown unit cell of LAO. Surprisingly, the metallic behavior shown in Figure 2.1 b, where we observe a decrease in the sheet resistance when lowering the temperature down to $\approx 2K$, is solely observed when LAO is deposited

[1] Under the conditions of [186]

on top TiO_2-terminated STO. On the other hand Nishimura et al, have reported a sudden metal-insulator transition where an insulating behavior was observed when the STO interface is purely SrO-terminated[185], while we observe a slow transition in the conducting sheet resistance at low temperature when changing the gradient of SrO coverage θ_{SrO}[2] (see Figure 2.1 c).

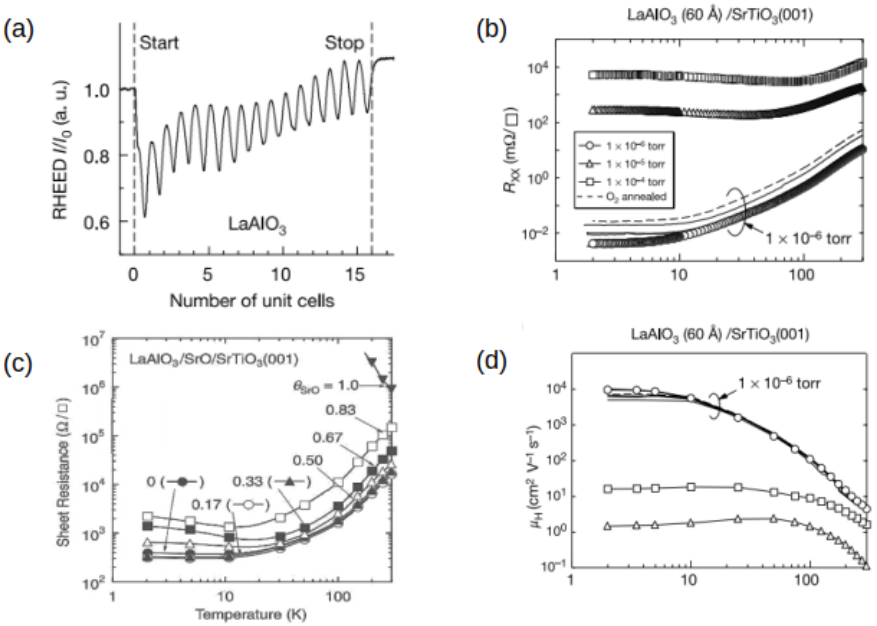

Figure 2.1: Discovery of the metallic behavior at the interface of LAO and TiO_2-terminated STO. **(a)** Reflection high-energy electron diffraction profile after the growth of 16 u.c of LAO on top of TiO_2-terminated STO substrate.[186]**(b,d)** Temperature dependence of the longitudinal resistance R_{xx}, and carrier mobility μ_H of a sample of 60 $\AA$ of LAO on top of TiO_2-terminated STO for different oxygen partial pressures during the PLD growth ranging from 10^4 to 10^6 Torr.[186] **(c)** Temperature dependence of the sheet resistance of a sample of LAO/STO with various SrO atomic layer coverage θ_{SrO}, where a metal-insulator transition is observed for a SrO-terminated STO ($\theta_{SrO} = 1$).[185]

Furthermore, the growth process can be greatly influenced by the oxygen pressure in the deposition chamber. We report that at low oxygen pressure below $10^{-6}mbar$, the STO substrate can be highly sensitive to defect formation particularly at high temperature, $T = 800K$. Indeed, from Hall measurements at low temperature, $T = 10K$, we report a high carrier mobility of $10^4 cm^2 \cdot V^{-1} \cdot s^{-1}$, and also a high carrier density n_s in the range of $10^{16} - 10^{17} e^-/cm^2$, signaling a bulk conductivity in the STO substrate. However, for the samples grown in lower oxygen pressure, around $10^{-4}mbar$, or annealed in oxygen tend to display a much lower carrier mobility, at least 3 order of magnitudes lower $50cm^2 \cdot V^{-1} \cdot s^{-1}$, and carrier density $10^{13} - 10^{14} e^-/cm^2$. In the light of these experimental findings, Thiel at al have been the first to report a the metal-insulator transition at around 4 u.c[188] of deposited LAO as illustrated in Figure 2.2.

This important finding have been supported by various measurements done in multiple research groups

[2]The gradient of SrO coverage θ_{SrO} was obtained by a sliding a mask technique where SrO layer was deposited on top of TiO_2-terminated STO.[185]

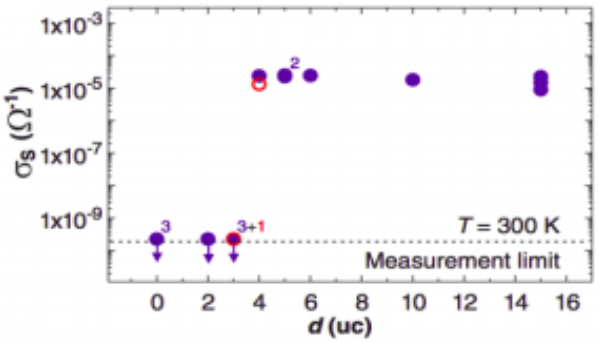

Figure 2.2: Universal critical thickness n_c for a conducting LAO/STO. The sheet resistance versus the thickness of LAO layers show a clear insulator-to-metal transition around $n_c = 4u.c$ of LAO.[188]

around the world[189, 191]. In this regard, the conduction regime in LAO/STO cannot be attributed to the diffusion of oxygen vacancies in the bulk of STO substrate, but rather to a special conduction regime, which can be referred to as a 2D regime, as the name suggest, in this regime the electrons will be trapped within the top surface of STO at the vicinity to the interface, forming what it's called quasi 2DES. The demonstration of this conduction regime did not take long before it was proved by the work of Basletic et al and Copie et al, who used a scanning method to visualize the lateral resistance of LAO/STO (CT-AFM), through the estimation of the electron density distribution within the interface[189, 191]. In this case, they have demonstrated that the conduction regime can be either in the bulk of STO, if the the sample is grown at a high temperature without any annealing, this leads to the creation of highly doped STO substrate due to the diffusion of oxygen vacancies in the bulk crystal (see Figure 2.3 a), whereas, in the case where the sample is annealed in an oxygen-rich environment, we observe the appearance of a 2D conduction regime (see Figure 2.3 b), where a quasi 2D conducting sheet spanning inside the the STO crystal within a thickness of several nm, which varies when changing the temperature, and ranging from $12nm$ at $T = 8K$ to $3nm$ at $T = 300K$. These results where supported by various other experiments using for example infrared ellipsometry, and photoelectron spectroscopy[44, 139].

It is also interesting to note that the two-dimensional electron system (2DES) can display a variety of different emerging properties, which makes LAO/STO a gold mine for the discovery of a variety of novel exotic phenomena in metal-oxides physics.

2.1.2 Emergence of superconductivity

Since its discovery in 2004, the 2DES at LAO/STO interface has taken a central role as the playground of various exotic phenomena. The most intriguing of these phenomena is the existence of a superconducting phase, which brought LAO/STO under the spotlight for the recent years. Indeed, Reyren et al have been

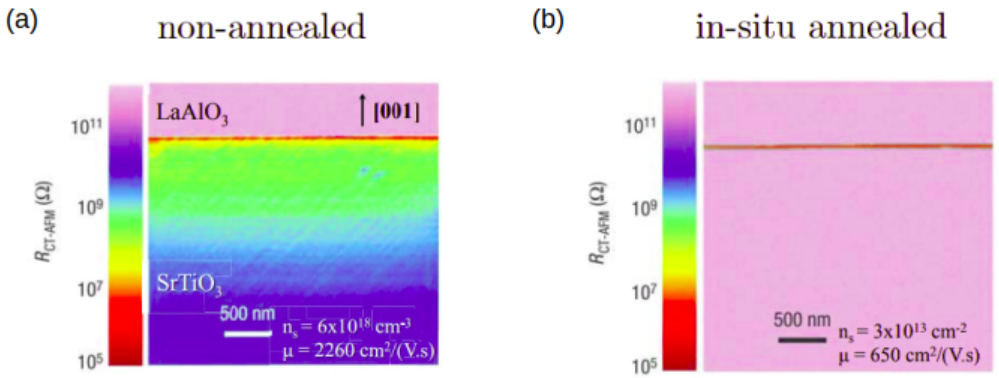

Figure 2.3: A resistance scan of a transverse cut of LAO/STO heterointerface using an atomic force microscope mounted with a conducting tip showing the effect of oxygen partial pressure and annealing process on the transport properties of the sample, **(a)** the sample is prepared under $P_{O_2} = 10^{-5}$ mbar and not annealed, and **(b)** the sample is annealed in an oxygen-rich environment and grown at $P_{O_2} = 10^{-6}$ mbar.[189]

the first to observe the superconducting phase in LAO/STO below $200mK$[121], as illustrated in Figure 2.4 a, where we observe a clear metal-to-superconductor phase transition around $200mK$. Moreover, the superconducting phase have been reported to span along a width of $10nm$ far below the superconducting coherence length equal to $70nm$, demonstrating the 2D character of the superconducting phase transition, which corresponds to the topological phase transition of Berezinskii-Kosterlitz-Thouless (BKT). Quickly after, Caviglia et al have shown that the superconducting phase can be modulated by an electrostatic doping using a backgate voltage[30]. As illustrated in Figure 2.4 b, the phase diagram associated to the superconducting phase has a dome-like shape, with the highest T_C recorded at around $300mK$.

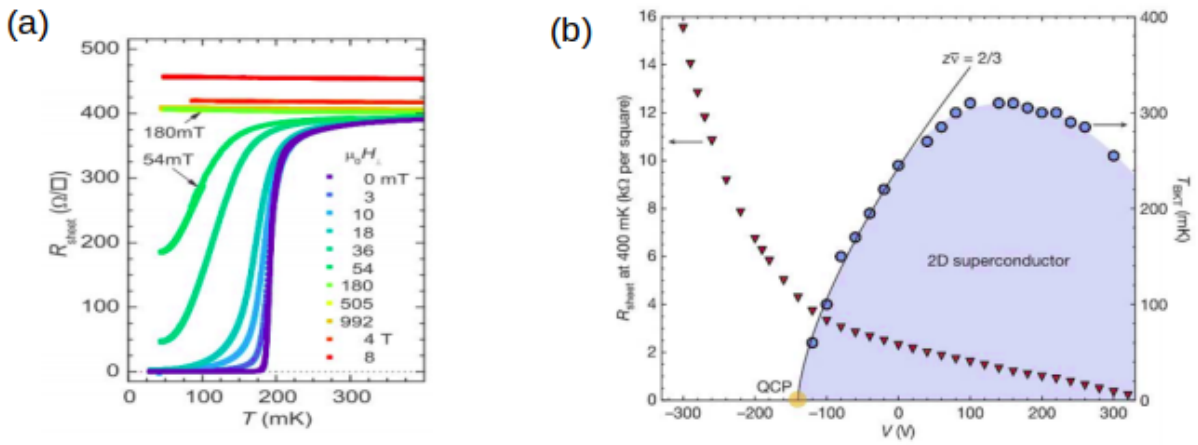

Figure 2.4: LAO/STO interface displays both superconductivity and magnetism. **(a)** The temperature dependence of the sheet resistance, various out-of-plane applied magnetic field, a superconducting phase transition is observed around 200mK.[121] **(b)** Phase diagram showing a critical temperature T_c which can be tuned using a gate voltage V_g, which allows for an electrostatic doping.[30]

2.1.3 A Strong Rashba coupling

A key ingredient in LAO/STO physics, resides in the Rashba spin orbit coupling, stemming form the spatial symmetry breaking at the interface due the strong confining potential, thus lifting the spin degeneracy at the Γ point as shown in Chapter 2. In addition, a bulk contribution to the atomic-spin orbit coupling in STO crystal will also help lift the spin degeneracy as it will be shown later. Recently, a strong Rashba spin orbit coupling at LAO/STO interface was reported by Caviglia et al, using magnetotransport measurements, he observed the appearance of a weak anti-localization regime taking place at positive electrostatic doping[31], as illustrated in Figure 2.5 a. Similarly, Ben Shalom et al have demonstrated the coexistence of a strong Rashba spin orbit coupling with the highest T_C transition temperature as shown in the phase diagram[137] (see Figure 2.4 b), which opens up the door for possible experimental observations of Mejorana-like quasi-particles.

These exciting developments have also had an important impact on the emerging field of spintronics, with the recent developments lead by the work of Reyran et al who have been the first to report the spin injection into LAO/STO interface[242]. Therefore, paving the way for the exploration of the spin transport in these complex systems, which will be an important part of this thesis, so far we will not give more details.

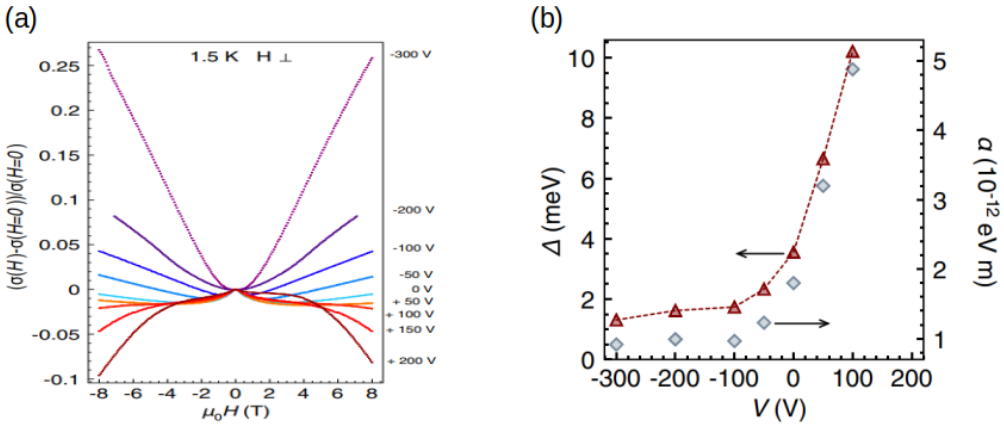

Figure 2.5: A gate tunable spin-orbit coupling. **(a)** The magneto conductance of a sample of LAO/STO for various back-gate voltages at $T = 1.5K$ and in perpendicular magnetic field. **(b)** Left axis, red triangles: field effect modulation of the Rashba spin splitting Δ. Right axis, gray diamonds: field effect modulation of the Rashba coupling constant α.[31]

2.2 Origin of the 2DES

After the surprising discovery of the two dimensional electron system (2DES) at the interface of LAO/STO, many theoretical explanations regarding the origin of the 2DES have been proposed. However, a unified theory explaining the origin of the 2DES is still lacking, until now various explanations are still debated. In

the following, we will review the various scenarios that have been proposed as potential candidates as to the formation of the 2DES. First, we will present the electronic reconstruction mechanism which is based on the polar catastrophe scenario. Then, we will review other plausible scenarios based on defects and interface intermixing.

2.2.1 Polar catastrophe

Initially proposed by Ohmoto and Hwang in their seminal work, the polar catastrophe scenario have been under the spot as a potential candidate for the origin of the mobile charge carriers at LAO/STO interface[186]. As a matter of fact, one should recall the ionic picture for the charge distribution along the [001] direction for the perovskite crystals of LAO and STO. As shown in Figure 2.6 a, the STO crystal displays two neutral planes, $(SrO)^0$ and $(TiO_2)^0$, due to the valence states of $+2$ (resp. $+4$) for Sr (resp Ti), whereas the LAO has two oppositely charged planes, $(LaO)^{+1}$ and $(AlO_2)^{-1}$, due to the valence state of Al and La equal to $+3$, leading to the creation of a non zero polarization inside the LAO crystal. Therefore, when growing LAO on top of 001-oriented STO, a strong polar discontinuity at the interface will occur, giving rise to an electrostatic instability proposed back in the 70's by Tasker et al[111]. A simple explanation to this electrostatic instability, can be viewed in the picture of plate capacitors, where in each unit cell (u.c) of LAO we have $+1$/-1 charges planes. Thus, when increasing the number of LAO deposited on STO, an electric field will arise inside the LAO layer, leading to an electrostatic potential V build-up which will diverge with the LAO thickness, so the name *"polar catastrophe"*. In order to avoid this instability, Nakagawa et al have proposed an electronic reconstruction mechanism, which could explain various experimental observations[104]. In fact, due to the electric potential build up within the LAO layer, its valence band will be tilted, as illustrated in Figure 2.6 c.

As the number of LAO layer is increased a Zener breakdown occurs at a critical thickness of LAO, for which the top valence band of LAO is at the level of the bottom conduction band of STO, then a charge transfer takes places where 0.5 e^- per u.c is transferred from the surface of the LAO layer (O 2p) to the TiO_2-terminated STO at the interface with LAO (where Ti 3d change their valence from Ti^{+4} to Ti^{+3}), creating a 2DES at the interface, and canceling the electrostatic potential build up within the LAO layer. On the other hand, for an SrO-terminated STO, a similar mechanism takes place, where "hole" charge carriers are transferred to the interface. Nevertheless, no free charge carriers have been observed in this case[186], mainly because Ti cannot have a valence states higher than $+4$, and the Oxygen atoms have an ionization energy twice that of Ti atoms, ruling out the charge transfer mechanism in this type of heterostructures. The validity of this reconstruction mechanism have been supported by various experimental findings. Indeed,

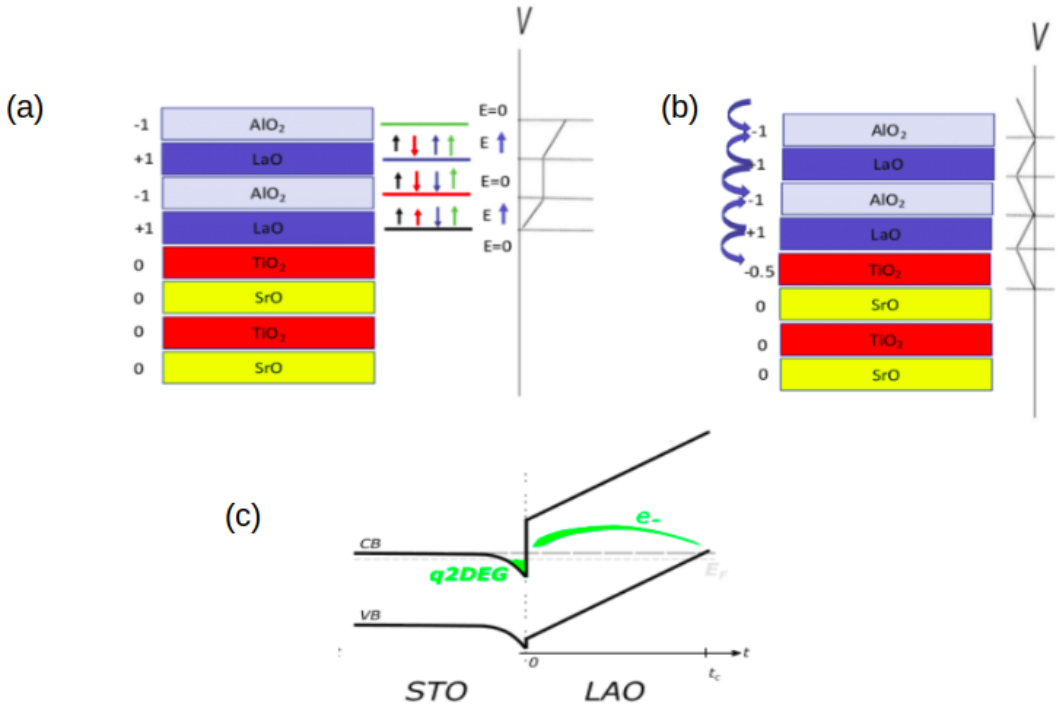

Figure 2.6: The polar catastrophe scenario. **(a)** Schematics representing the polar discontinuity at the interface of the LAO/TiO_2 interface, where the the system can be considered as a stacking of capacitor planes, with a diverging potential, **(b)** at a certain critical thickness of LAO a charge transfer mechanism takes place transferring $0.5\ e^-/u.c$ from the surface to the interface with STO.[64] **(c)**Sketch of the LAO/STO energy band diagram where a Zener breakdown occurs at a critical tickness t_c of the LAO layer allowing for the creation of 2DES.[158]

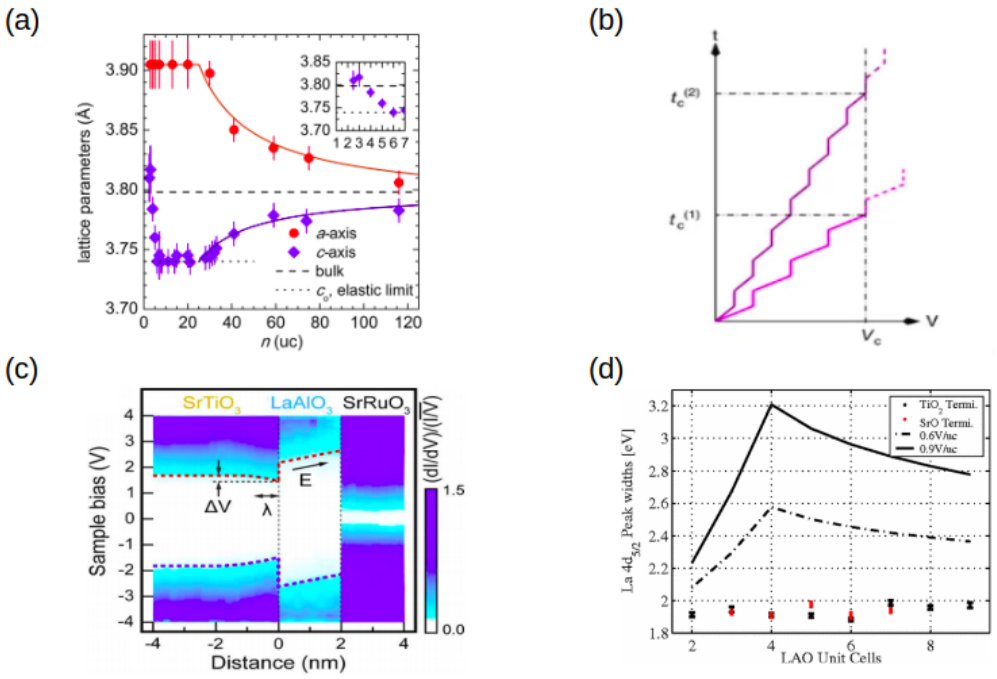

Figure 2.7: **(a)** a-axis (red dots) and c-axis (purple dots) parameters of the LAO layer as a function of the film thickness, the solid lines are guide to the eye, and the dashed horizontal line shows the pseudo-cubic bulk lattice constant and the inset shows the c-axis parameter for the low film thicknesses.[24] **(b)** Schematics represent the potential build-up as a function of the thickness of LAO layers for two different samples: a pure LAO (pink curve) and a diluted LAO with 50% of STO (purple curve), we observe that by changing the chemical composition of the LAO layers we can change the critical thickness $t_c^{(1)}$ (resp. $t_c^{(2)}$) due to the modulation of the polarization P_0.[120] **(c)** An experimental measurement of the band alignment of LAO(5u.c)/STO, where the color map represents the normalized differential conductance with respect to the general total conductance background.[66] **(d)** FWHM of La $4d_{5/2}$ peak for an annealed sample, where the lines follow the peak-broadening in the case of the polar catastrophe scenario for TiO_2-terminated STO. However, we observe no peak broadening across the film where neither the thickness nor the termination dependence is observed (red and black dots).[135]

Thiel et al, have been the first to report a critical threshold in the film thickness of LAO layer, where a conducting LAO/STO was observed only for an LAO thickness above 3 u.c, as illustrated in Figure 2.2, where various research groups around the world reported similar findings[93, 57]. In addition, Cancellieri et al have investigated the elastostriction of LAO layer along the c-axis[24], as illustrated in Figure 2.7 a, we report a large c-axis deformation below 5 u.c thick LAO film, 2% deformation , which can be attributed to the electrostatic buildup within the LAO layer, whereas above 5 u.c this deformation vanishes demonstrating that the charge transfer mechanism is at play. Similarly, Reinle-Schmitt et al have shown the possibility to tune the critical film thickness of the polar LAO layer by changing its polarization[120] (see Figure 2.7 b).

Furthermore, Huang et al have directly measured the band deformation of LAO layer, by a tunneling microscopic technique indicating the polar catastrophe scenario in the LAO/STO[66] (see Figure 2.7 c).

On the other hand, Segal et al using a core-level photoemission spectroscopy, have found no evidence

of energy shift of atomic levels of La and Al as function of the film thickness grown on both TiO_2- or SrO-terminated STO[135] (see Figure 2.7 d). In addition, several inconsistencies regarding the polar catastrophe scenario were raise by Tikazawa et al who found an electric field at least 10 times smaller than the one predicted by the polar catastrophe scenario, whereas the polarity of the field seemed to be independent of the STO termination[142]. Another study by Sing et al have shown that both Ti^{4+}/Ti^{3+} components have been spotted below the critical thickness, demonstrating the coexistence of localized and mobile charge carriers below the critical thickness[139]. In the same direction, Hall effect measurements yield values of the charge carrier density in the range of $2-5\times10^{13}\ e^{-}/cm^{-2}$ at low temperature, far below the value of $3.3\times10^{14}\ e^{-}/cm^{-2}$, which is expected from the reconstruction scenario. Therefore, supporting the spectroscopic studies introduced previously, which divide the electrons population into mobile charge carriers which are responsible for the transport measurements and located far from the interface in the bulk STO, and a population of localized electrons which is trapped at the interface due to impurities and defects.

2.2.2 Oxygen vacancies

Recently, number of studies have reported that oxygen vacancies can play an important role in the creation of the 2DES at the LAO/STO interfaces. In fact, from photemission and X-ray absorption spectroscopy, Siemons et al have reported a large Ti^{+3} signal, which was shown to depend on the partial oxygen pressure during the growth process

and was substantially diminished after a post-growth annealing under high temperature , $T\geq530°C$, and in high oxygen pressure, 0.2 bar[138] . Siemons et al have also shown that thin films of LAO, 1 to 3 u.c, grown under low oxygen pressure , $P\sim10^{-6}$ Torr, display a conducting behavior, whereas under the same conditions a bare STO substrate was found to be insulating. This demonstrates that an oxygen deficient LAO layer can lower the energy barrier of the formation of oxygen vacancies at the interface with STO during the growth process[138]. Similarly, Bristowe et al have reported that the presence of oxygen vacancies in ultra thin films of LAO can localize the charge transfer carriers to the interface, thus inducing a metal to oxide transition depending on the thickness of the LAO layer.[21]

Until recently, Cen et al have been able to induce a metal to oxide transition in the buried 2DES using an AFM tip, which was used to "write" or "erase" conduction paths in the LAO/STO interface[32] (see Figure 2.8 c). This was possible by reducing the film thickness of the LAO layer at its threshold value of 3 u.c. Therefore, the AFM tip can alter the chemical and electrostatic properties at the surface of the LAO layer, inducing a charge transfer to the interface due to the creation of oxygen vacancies at the surface of

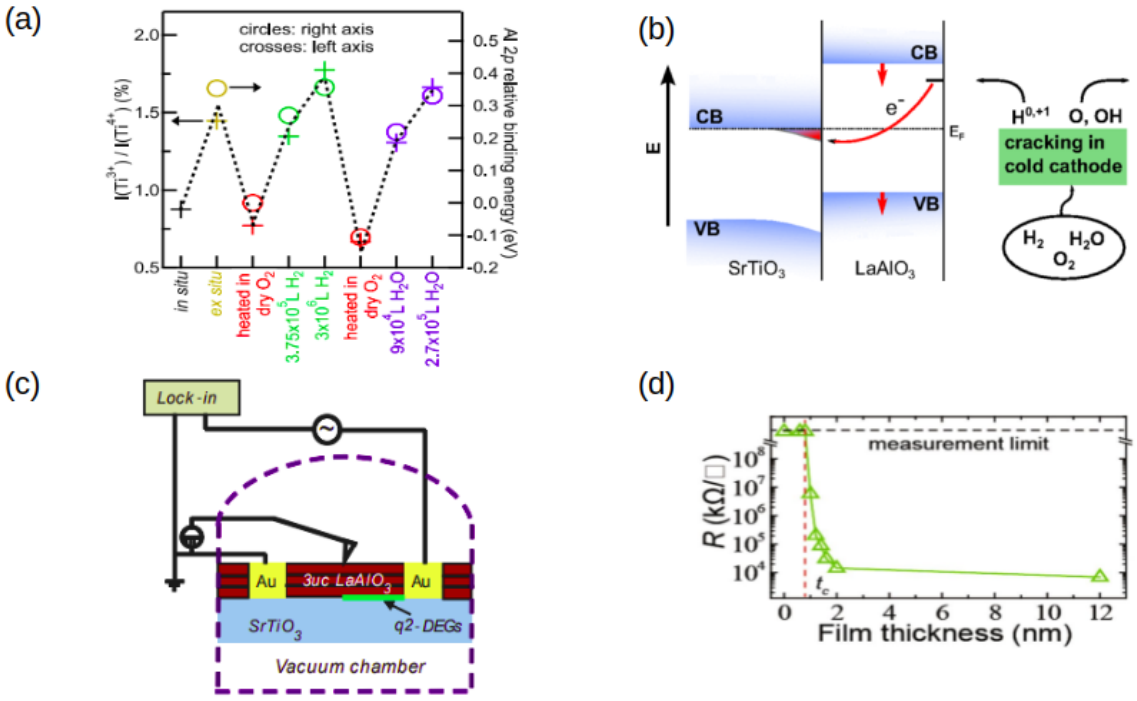

Figure 2.8: The validity of the oxygen vacancies scenario.**(a)** Ti^{+3}/Ti^{+4} spectral weight ratio and relative Al 2p core level shift for the complete set of experiments (the x-axis represent the chronological order of measurements). **(b)** A schematic summarizing the absorption process on the energy diagram of LAO/STO. We observe that the hydrogen species bind to the surface of LAO generating one electron which moves to the interface (STO CB) accompanied by a shift of LAO bands to lower energies (red arrows).[133] **(c)** A sketch of the experimental set-up used to write/erase 1D conducting channels in LAO(3 u.c)/STO sample, using AFM tip.[180] **(d)** The film thickness dependence of interfacial resistance for a sample a-LAO/STO, where the dashed red line represents the critical thickness t_c.[89]

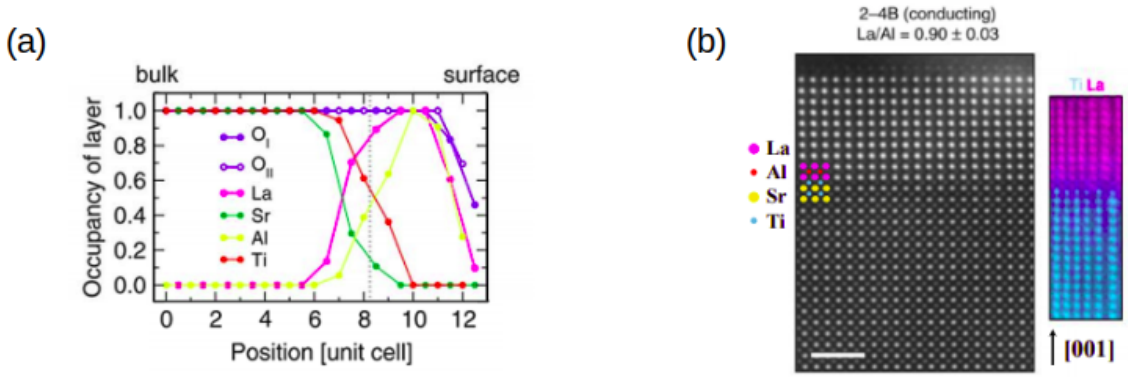

Figure 2.9: **(a)** The relative position of various chemical species O,La,Sr,Ti and Al at the interface of LAO/STO highlighting the interdiffusion at the interface.[165] **(b)** Right: High-angle annular dark-field STEM image of a conducting LAO/STO heterointerface grown by MBE, Left: EELS scan where very little interdiffusion occurs at the interface.[164]

LAO. This was described by Bi et al as the "water cycle", due to the presence of OH^- and H^+ species, as a result of the dissociated molecules of water at the LAO surface.[9] Thus, creating oxygen vacancies at the surface, which will release electrons that will be transferred to the interface through the polar LAO. This agrees with the findings of Sheiderer et al, who reported a Ti^{+3} signature from X-ray photoelectron spectroscopy (XPS), when introducing H or H_20 into the measurement chamber[133] (see Figure 2.8 a&b). Additionally, Li et al have deposited various thicknesses of amorphous LAO on STO substrate and have show that a 2DES can appear at $t_c \approx 0.8nm$, demonstrating the importance of the electron transfer from the a-LAO to the STO side through the formation of oxygen vacancies at the surface of a-LAO resulting in insulator-metal transition[89] as shown in Figure 2.8 d.

2.2.3 Cation intermixing

As seen previously, polar discontinuity at the interface can be source of instability, which can be avoided by introducing a reconstruction mechanism based on atomic reconstruction. Indeed, this mechanism can be at the source of the conducting behavior of the LAO/STO interface, where the atoms at the interfacial planes of LAO and STO intermix, in order to compensate for the potential build-up within the LAO layer. In fact, the interface between LAO and STO can be rougher as one expect from the measurements probing the interface using x-ray diffraction (SXRD), medium-energy ion spectroscopy (MEIS), and electron energy loss spectroscopy (EELS),[165, 77, 104] as shown in Figure 2.9. We observe an interdiffusion of La, Sr, Al, Ti cations, leading to a substitution of La and Sr atoms at the interface. Thus, creating a conducting layer of $La_{1-x}Sr_xTiO_3$ at the STO side, which can be at the origin of the 2DES (see Figure 2.9 a).

However, Warusawithana et al have shown that when growing LAO/STO sample using molecular beam

epitaxy (MBE), where a smoother interfaces were obtained ruling out any cation interdiffusion[164] as shown in Figure 2.9 b, they still observed a conducting behavior of the LAO/STO samples. Furthermore, the precise thickness dependence can be hardly reconciled with the cation interdiffusion mechanism, which undermines the consistency of this scenario.

2.2.4 Polarity-induced defects

Despite, the abundance of theories regarding the origin of the 2DES at the interface of LAO/STO, no one have been able to present simultaneously a unified theory that reckon for all the puzzling experimental observations in the LAO/STO interface. However, in 2014 Yu and Zunger have succeeded to provide a unified explanation for wide variety of experimental findings, by addressing the effects of cation substitutions, cation vacancies and oxygen vacancies all together, for both n-type and p-type interfaces.[171] By considering the polar discontinuity at the interface, which is a key ingredient in their formulation, Yu and Zenger have proposed a mechanism which compensate for the electrostatic build-up within the polar LAO layer [3], by considering only the formation of thermodynamically stable deep and shallow donors and deep acceptor states, ruling out the pure electrostatic and defect-free scenarios. In the case of an n-type interface, below the critical thickness ($t_{LAO} < 4$ u.c), one observes the formation of energetically favorable charge defects, due to the Fermi energy lying within the STO band gap. Thus, we observe the onset of Ti-on-Al substitutions on the surface of LAO (Ti^{+}_{Al}(S)) yielding a deep electron donors to the interfacial deep acceptor states formed by Al-on-Ti substitutions Al^{-}_{Ti}(I) at the STO surface near the interface with LAO[171] (see Figure 2.10 a). Typically, these acceptor states are located within the STO band gap (where the Fermi energy lies) ruling out any mobile carriers, which agrees with the insulating behavior below the critical thickness of 4 u.c . Furthermore, this charge transfer towards deep acceptor states may explain the weaker internal electric field within the LAO layer. Additionally, form Figure 2.10 c&d, it appears that oxygen vacancies seem to have a high formation energy, which explains the absence of mobile charge carriers in this regime. On the other hand, above the critical thickness ($t_{LAO} > 4$ u.c), the formation energy of oxygen vacancies V_O(S) at the LAO surface, becomes favorable as illustrated in Figure 2.10 c, we observe a linear decrease in the formation energy of V_O(S), with the film thickness t_{LAO}. Thus, due to the internal electric field in polar LAO, the shallow charge carriers $V_O^{+/++}$(S), will be transferred to the interface, where they will be primarily trapped in the in-gap Al^{-}_{Ti}(I) defect states (see Figure 2.10 b). However, the Fermi energy will be within the bottom of the conduction band of STO, thus leaving a smaller proportion of these shallow states to form the 2DES, which explains the mysterious "missing charge " problem reported by various

[3] Which increases linearly with the LAO thickness

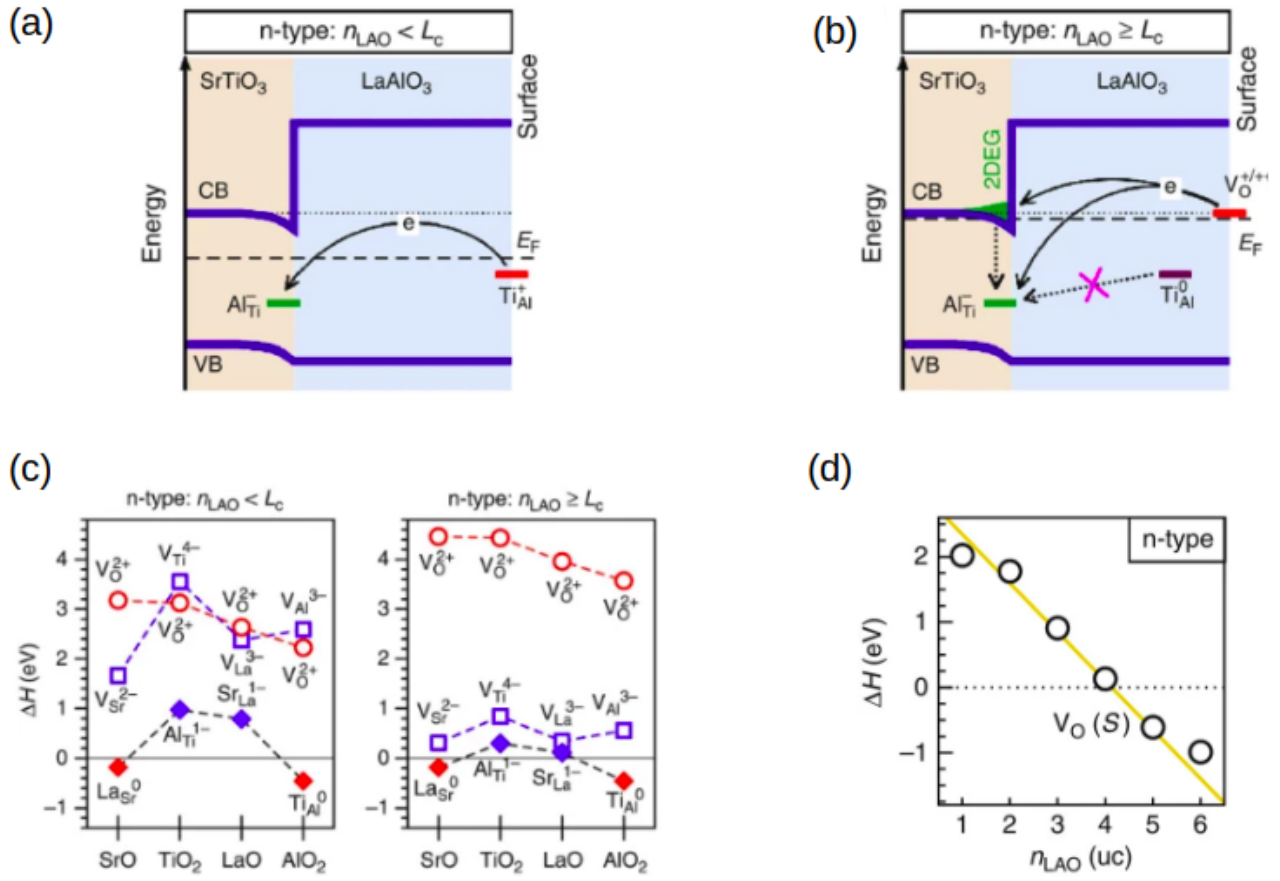

Figure 2.10: **(a)** Schematics band diagram showing the charge transfer among defect at LAO/STO interface, where for $n_{LAO} < L_c$ all charge are trapped in the in gap states Al_{Ti}^-, whereas **(b)** at $n_{LAO} \geqslant L_c$ the $V_O(S)$ at rhe surface of LAO allow for a charge transfer to the in gap states but also to the CB of STO allowing for the creation of the 2DES. **(c)** Formation energy of the interfacial point defects at the thermodynamical equilibrium for both $n_{LAO} < L_c$ and $n_{LAO} \geqslant L_c$. **(d)** First principle calculations of the energy formation of oxygen vacancies in oxygen-rich environment versus the the film thickness of LAO.[171]

experimental studies[137, 30, 128]. However, in the case of a p-type interface, an insulating behavior was reported regardless of the LAO thickness, which can be explained by the absence of shallow donors which are thermodynamically unfavorable in this case. Indeed, below critical thickness ($t_{LAO} < 4$ u.c), we observe the creation of deep electron donors at the interface due to the onset of La-on-Sr substitutions (La^{+}_{Sr}(I)) defect states, and thanks to the internal polar field within the LAO layer, these charge carriers will be transferred towards deep acceptor states at the surface of LAO, where they will be trapped within the Sr-on-La substitutions (Sr^{-}_{La}(S)) defects and La vacancies V^{-}_{La}(S) at the surface of LAO.

As a summary, we have presented in this section, a wide variety of possible scenarios which seem to point towards the polar-induced defect mechanism as a very plausible explanation for the origin of the 2DES at the LAO/STO interface. Subsequently, due to the complex mechanism giving rise to the 2DES, one needs a simpler way to understand the physics behind the LAO/STO interface, which can be unveiled through the study of the band structure of the confined interfacial 2DES.

2.3 Structural and electronic properties

In this section we will give an introduction to the surprising properties of bulk STO, both in its stoichiometric form and in its doped state, then we will provide a brief description of the tight biding model, which takes into account the conduction bands at the surface of STO, where the charge carriers are injected thanks to the polar-induced defect mechanism.

2.3.1 Bulk STO : A versatile insulator

STO is considered as one of the most surprising complex oxides, due its versatility and the wide range of interesting properties it can display. Indeed, in its stoichiometric form, STO is a wide band gap insulator with a large band gap $E_{gap} = 3.2eV$, separating the oxygen 2p dominated valence bands (p_x, p_y, p_z), form the Ti 3d dominated conduction bands ($d_{xy}, d_{xz}, d_{yz}, d_{3z^2-r^2}, d_{x^2-y^2}$). Therefore, the conduction bands in STO, can be reduced to the 3d orbitals of an isolated Ti atom with $+4$ valence state, lying in a cubic crystal field due to the surrounding oxygen octahedron, which lifts the degeneracy of the empty 3d orbitals[175], as illustrated in Figure 2.11 a, separating them into a degenerate triplet t_{2g} which is composed of orbitals pointing at 45° angle with respect to the oxygen atoms (d_{xy}, d_{xz}, d_{yz}), and a higher energy doublet, which lies at $2eV$ above the t_{2g} triplet, with the orbital lobes pointing towards the oxygen atoms ($d_{3z^2-r^2}, d_{x^2-y^2}$). Below a transition temperature $T_c = 105K$, STO undergoes a structural phase transition, from a cubic to a tetragonal phase, accompanied with an antiferrodistortive (AFD) rotation, which is characterized by

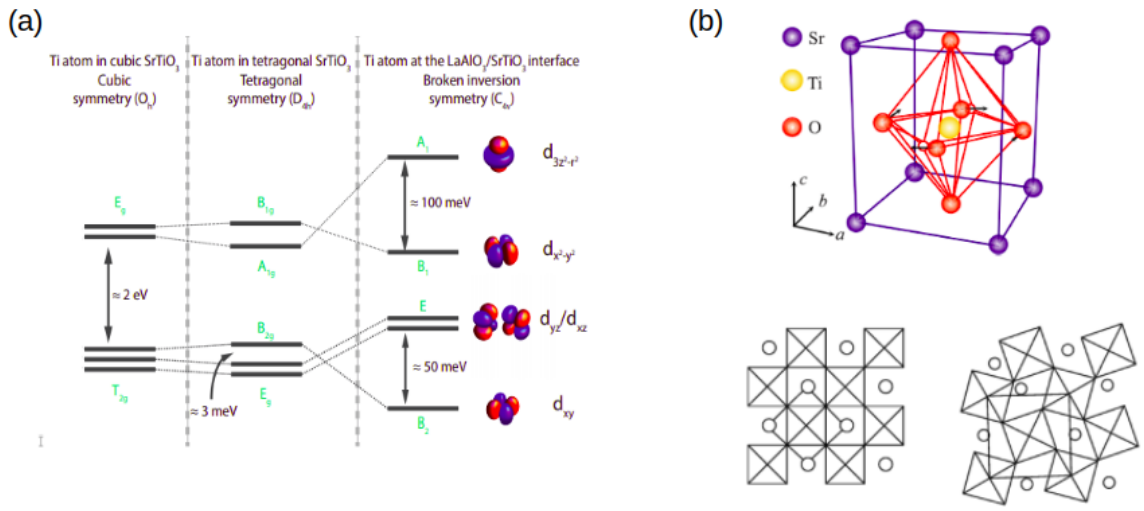

Figure 2.11: **(a)** Energy levels of Ti 3d orbitals in the presence of cubic, tetragonal and non-inversion symmetric tetragonal crystal fields, the values of the energy splittings was determined using both experimental and theoretical studies. The green labels refer to the irreducible representations of the symmetry point group to which each orbitals belong.[175] **(b)** On the top : crystal structure of STO. In the bottom : AFD phase transition. On the left: $T \geqslant 105K$ before the phase transition and on the right: $T < 105K$ after the phase transition where the TiO_6 octahedral rotate in opposite directions.[46]

the rotation of the oxygen octahedra [46] (as shown in Figure 2.11 b), and an elongation of the c axis ($c/a \approx 1.001$ at $T = 4K$). This phase transition drives the d_{xy} orbitals to higher energies $\Delta_T \approx 3meV$ above the d_{xz} and d_{yz} orbitals , as illustrated in Figure 2.11 a. One should also note, that the ferroelastic distortion of Ti atoms do not drive the STO into a ferroelectric phase, due to opposite displacement of two adjacent Ti atoms. Indeed, STO is know to stay in its paraelectric phase at all finite temperature, albeit at low temperatures (below 20K), STO becomes a "quantum paraelectric", where a ferroelectric-like instability driven by quantum fluctuations competes with the AFD distortions. Thus, driving STO close to a ferroelectric phase, which is manifested by a large increase in the dielectric constant ϵ_{STO}, from $\epsilon_{STO}(300K) \approx 200$ to $\epsilon_{STO}(4K) \approx 20000$,[101] which will have an important application as it will be discussed in Chapter 5. However, a ferroelectric phase can be induced in STO, through various methods such as : strain induced ferroelectricity, oxygen deficiency, cation substitution, or by applying large electric fields.

Furthermore, an electron-doped STO can undergo a metal-insulator transition at carrier densities as low as $\sim 8.5 \times 10^{15} cm^{-3}$, orders of magnitude lower compared to semiconductors like silicon ($\sim 10^{18} cm^{-3}$) or germanium ($\sim 10^{17} cm^{-3}$). This can be explained by recalling the Mott criterion which links the Bohr radius a_B^* to the critical electron density of the metal-insulator transition n_c, through the relation $n_c^{1/3} a_B^\star \sim 0.2$, and since the a_B^* is proportional to the dielectric constant which was shown to increase dramatically, this should explain the low carrier densities of conducting STO. It is also noteworthy to report that bulk STO

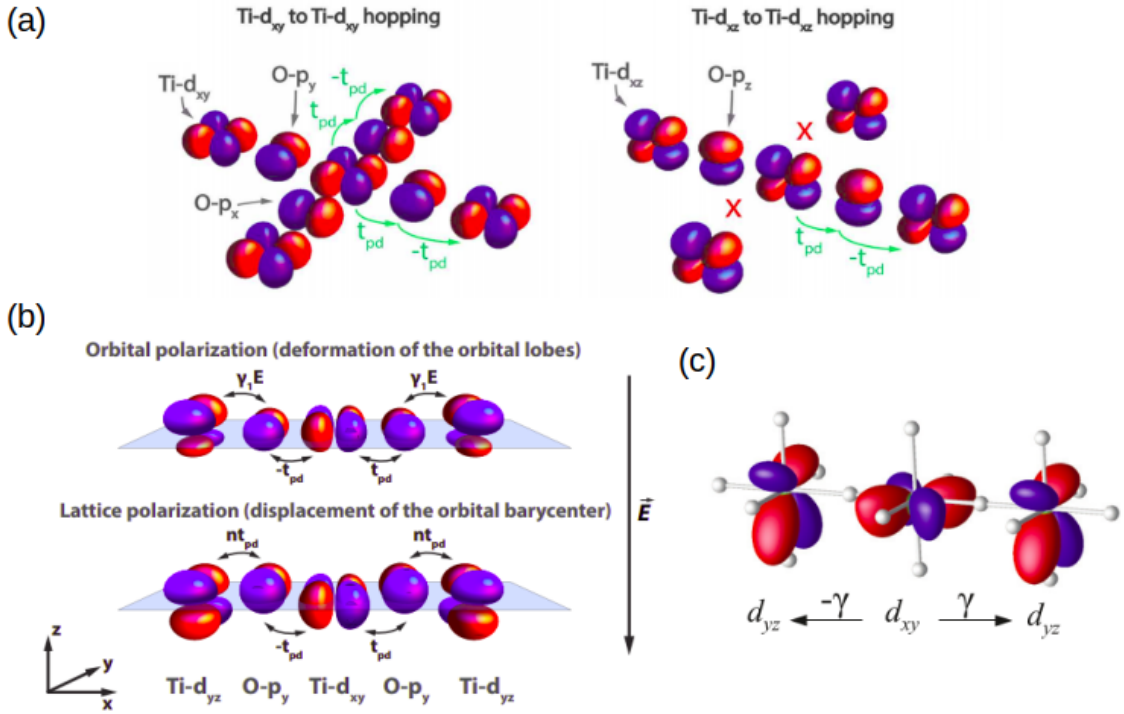

Figure 2.12: **(a)** Hopping contributions to the Ti-d$_{xy}$ (on the left), and Ti-d$_{xz}$ (on the right) orbitals in the nearest neighbor approximation, where similar conclusion can be drawn for the Ti-d$_{yz}$ orbitals.[79] **(b)** Orbital and lattice deformation due to a strong confining electric field at the LAO/STO interface, we observe that the hopping between the Ti-d$_{yz}$ and O-p$_y$ orbitals is allowed in this case.[80] **(c)** Schematics representing the orbital deformation at the interface allowing for an antisymmetric hopping with a γ term.[172]

exhibits a superconducting phase at critical temperature around $300mK$, displaying a dome-shaped like phase diagram, with carrier densities as low as $\sim 5.5 \times 10^{17} cm^{-3}$, which make STO one of the most dilute superconductors in the market.[190]

Despite all those surprising properties of bulk STO, low dimensional transport channels that occur at the surface of STO, have attracted a lot of interest from the research community, particularly after the discovery of the conducting 2DES at the interface of LAO/STO. In the next section will give a brief review of the "three subband model" which takes into account the lowest energy conduction bands in LAO/STO.

2.3.2 Band structure of LAO/STO interface

Upon adding a confining potential, the 3d orbitals of Ti atoms do not undergo any additional degeneracy lifting. However, the splitting between the in-plane and out-of-plane orbitals of the t_{2g} and e_g bands are completely modified, as illustrated in Figure 2.11 a. Indeed, From X-ray absorption spectroscopy measurements, Salluzzo et al have reported a $50meV$ splitting between the d_{xy} and the d_{xz}/d_{yz} orbitals, and a higher energy splitting of $100meV$ between $d_{x^2-y^2}$ and $d_{3z^2-r^2}$.[131]

A way to move from this crystal field picture to the bottom conduction bands of LAO/STO is through the tight binding model, which quantifies the relevant hopping terms between the nearest neighbors along the x and y directions, while no hopping along the z-direction is taken into account due the strong confining potential along the z axis [4]. In the following we will present the "three sub-band" model proposed by Zhong et al and Kim et al,[172, 80] which takes into account only the t_{2g} lowest energy conduction bands, with a degenerate d_{xz}/d_{yz} sub bands, and a lower energy d_{xy} sub band laying at ΔE below d_{xz}/d_{yz} sub bands. In Figure 2.12 a, we show the relevant hopping processes, for only the t_{2g} orbitals[79]. We observe that the hopping between two d_{xy} orbitals, proceeds though the oxygen p_y orbitals in the x-direction and oxygen p_x orbitals in the y-direction, with the same hopping integral $t_1 = 0.277eV$ obtained from Wannier projection method, so that the first diagonal term of the tight biding Hamiltonian $H^{TB}_{0,2D}$ is given by :

$$< xy|H^{TB}_{0,2D}|xy >= \epsilon_1 - 2 \times (t_1 cos(k_x) + t_1 cos(k_y) + 2t_3 cos(k_x) cos(k_y)) \tag{2.1}$$

where $\epsilon_1 = eV$ is the local energy term for all three t_{2g} orbitals, while $t_3 = 0.076$ corresponds to the diagonal hopping term along the (110)-direction, giving a smaller hopping integral [5]. On the other hand, the hopping term between the d_{yz} (resp. d_{xz}) orbitals is given by :

$$< yz|H^{TB}_{0,2D}|yz >= \epsilon_2 - 2 \times (t_2 cos(k_x) + t_1 cos(k_y) + t_3 cos(k_y)) \tag{2.2}$$

where $\epsilon_2 = eV$ and the same expression holds for d_{xz} orbitals.

Another important ingredient that needs to be taken into account to describe the physics at the LAO/STO interface is the spin-orbit coupling. Indeed, an additional term which includes the atomic spin-orbit coupling H^{TB}_{SOC} needs to be taken into account, and can be expressed as :

$$H^{TB}_{SOC} = \frac{2\Delta_{SO}}{3} \mathbf{L} \cdot \mathbf{S} \tag{2.3}$$

where $\mathbf{L} = \overrightarrow{r} \times \overrightarrow{p}$ is the angular momentum operator, $\mathbf{S}$ is the spin operator, and Δ_{SO} is the energy splitting due to spin orbit interaction in bulk STO. In the original t_{2g} basis ($|i, s >$ where $i = yz, xz, xy$ respectively and s is the spin state $|\uparrow>$ or $|\downarrow>$) H^{TB}_{SOC} reads :

[4] k_z is quantized in this case !

[5] One should also remark that there is no hopping term along the z-direction due to the confining potential.

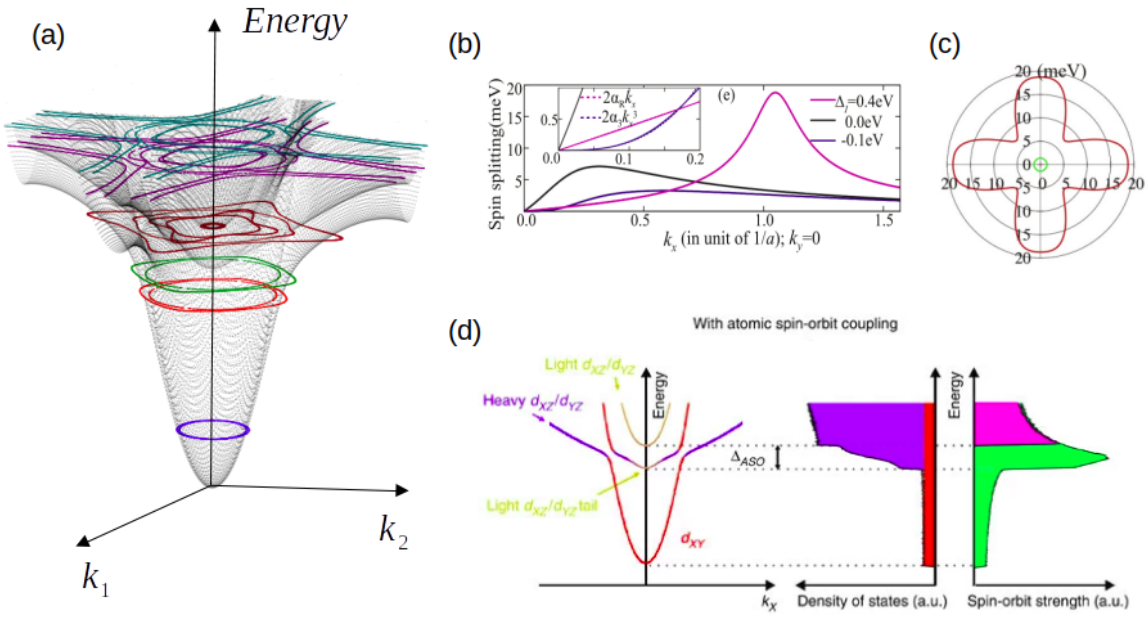

Figure 2.13: **(a)** 3D band structure of LAO/STO, the figures in different colors represent the Fermi surfaces at different Fermi levels. (*Our calculations of the band structure*) **(b)** Calculated spin splitting for the lowest band of the 6 $\times$ 6 TB Hamiltonian for various energy splitting Δ_I which quantify the vanishing hopping term of the Ti-d$_{yz}$/Ti-d$_{xz}$ along the z-direction due to the symmetry breaking at the interface, the figure in the inset shows k-linear (resp. k-cubic) for $\Delta_I > 0$ (resp. $\Delta_I < 0$).[172] **(c)** angular dependence of the Rashba coefficient at the anticrossing points (red curve) and at lower Fermi energy (in d_{xy} bands) green curve.[172] **(d)**On the left : calculated band structure of LAO/STO along $[100]$-direction and on the right: we map the density of states and the strength of the spin-obit coupling to the corresponding energy levels in the band structure.[75]

$$H_{SOC}^{TB} = i\frac{\Delta_{SO}}{3}\begin{pmatrix} 0 & \boldsymbol{\sigma_z} & -\boldsymbol{\sigma_y} \\ -\boldsymbol{\sigma_z} & 0 & \boldsymbol{\sigma_x} \\ \boldsymbol{\sigma_y} & -\boldsymbol{\sigma_x} & 0 \end{pmatrix} \tag{2.4}$$

with $\boldsymbol{\sigma_x}, \boldsymbol{\sigma_y}, \boldsymbol{\sigma_z}$ the Pauli matrices. The SO energy splitting Δ_{SO}, have been estimated by Zhong et al form DFT calculations in bulk STO to be equal to $29meV$. However, experimental studies seem to have some difficulties at estimating Δ_{SO}, which is not clearly defined according to Bistritzer et al.[15].

At this stage, one should observe that both Hamiltonians $H_{0,2D}^{TB}$ and H_{SOC}^{TB}, conserve their inversion symmetry which is in stark contrast with the symmetry breaking at the interface of LAO/STO. Therefore, we need to take into account the effects of the strong confining field at interface, on the 3d Ti orbitals. In fact, two main effects result from this confining potential. The first results into an orbital polarization, due to the deformation of the orbital lobes of Ti and Oxygen atoms, sending the electrons closer to the interface. While , the second effect consists of the so-called "buckling" of the TiO_2 planes, which was observed by Pauli et al.[114]. It is caused by the displacement of Ti atoms away from the interface, while the Oxygen atoms are attracted closer to the interface, leading to a lattice polarization as illustrated in Figure 2.12 b. An important consequence of the orbital and lattice polarization is the creation of new hopping channels between t_{2g} orbitals, allowing for the hopping between the d_{xy} and d_{yz} orbitals along the Oxygen p_y orbital which is forbidden in the case of bulk STO. As a matter of fact, an additional Hamiltonian which takes into account the symmetry breaking at the interface, thus the Rashba coupling at the interface, can be expressed as[6] :

$$H_R^{TB} = \gamma\begin{pmatrix} 0 & 0 & -2isin(k_x) \\ 0 & 0 & -2isin(k_y) \\ 2isin(k_x) & 2isin(k_y) & 0 \end{pmatrix} \tag{2.5}$$

where $\gamma =< xy|H^{TB}|yz >$ represents the anti-symmetric hopping between d_{xy} and d_{yz} orbitals which changes sign upon symmetry inversion as shown in Figure 2.12 c. In fact, Zhong et al estimated $\gamma \approx 20meV$ for all n-type interfaces. Lastly, to obtain the band structure of LAO/STO, a diagonalization of the combined 6×6 Hamiltonian $H_{0,2D}^{TB} + H_{SOC}^{TB} + H_R^{TB}$, which contains all the contributions described above.[172] In Figure 2.13 a, we plot the band structure and the Fermi surfaces of the t_{2g} orbitals at the LAO/STO interface. The first observation comes from the Figure 2.12 a, where the lower energies bands conserve their d_{xy} nature, displaying an isotropic (circular) Fermi surface. Furthermore, the effect of SOC on the d_{xy}

[6] In the same orbital basis as equation 3.4

orbitals can be seen from the Fermi surface, which contains two circular Fermi contours with opposite spin chiralities. Zhong et al have shown that the SOC results into a dominant k-linear and k-cubic contributions in the t_{2g} orbitals, where the highest spin-splitting occurs at the band crossing of the d_{xy} and d_{xz}/d_{yz} bands, at a value of $18meV$ as illustrated in Figure 2.13 b. Joshua et al have reported a maximum atomic spin orbit ($\mathbf{L}\cdot\mathbf{S}$) strength at the avoided band crossing points[75] (see Figure 2.13 d), which was confirmed by various experimental studies. He also argued that the atomic SOC has the strongest effects on the band structure of 3d degenerate orbitals. From Figure 2.13 c, we observe that the Fermi surface at the band crossing is highly anistropic, giving rise to a four-fold symmetric Rashba coefficient, which we will discuss in more details in Chapter 5.

A more realistic band structure for STO interfaces was calculated by Johansson et al using an 8×8 tight biding model[203]. In Figure 2.14 a, the band structure displays multiple avoided band crossings, which are either topologically trivial or non-trivial, leading to a sign changes and extremas in the conversion efficiency for the spin-dependent Eldenstein Effect (SEE), which was confirmed experimentally by Vaz et al.[29] (see Figure 2.14 d). However, another strong contribution to the conversion efficiency can be attributed to the orbital Eldenstein Effect (OEE), which can be associated to the strongly uncompensated orbital moments among band pairs, as shown in Figure 2.14 b&c, where a no sign change have been reported below $(0.02eV)$, and a strong contribution at the first avoided band crossing, dominating the SEE contributions.[203, 81] In Chapter 5, we will shed more light into these fascinating complex multi-band effects, by taking into account both the SEE and OEE contributions to the spin-to-charge conversion signal in the 2DES.

2.4 Sample Growth and characterization

In this section we will give a short review of the Pulsed Laser Deposition (PLD) technique used in the fabrication process of the LAO/STO heterostructures, and we will also present the structural and the electronic properties which were realized through the characterization of the LAO/STO samples using various measurements.

2.4.1 PLD growth

The LAO layers were deposited at the University of Geneva in the group of Jean-Marc Triscone, using Pulsed Laser deposition (PLD), which relies on a short and intense laser pulse ($\approx 50mJ$, $25ns$, produced by an Eximer laser), which is focused on the target which contains the desired material to be deposited, and it is placed inside a vacuum chamber. Due to the absorption of the laser power, the material is ablated and

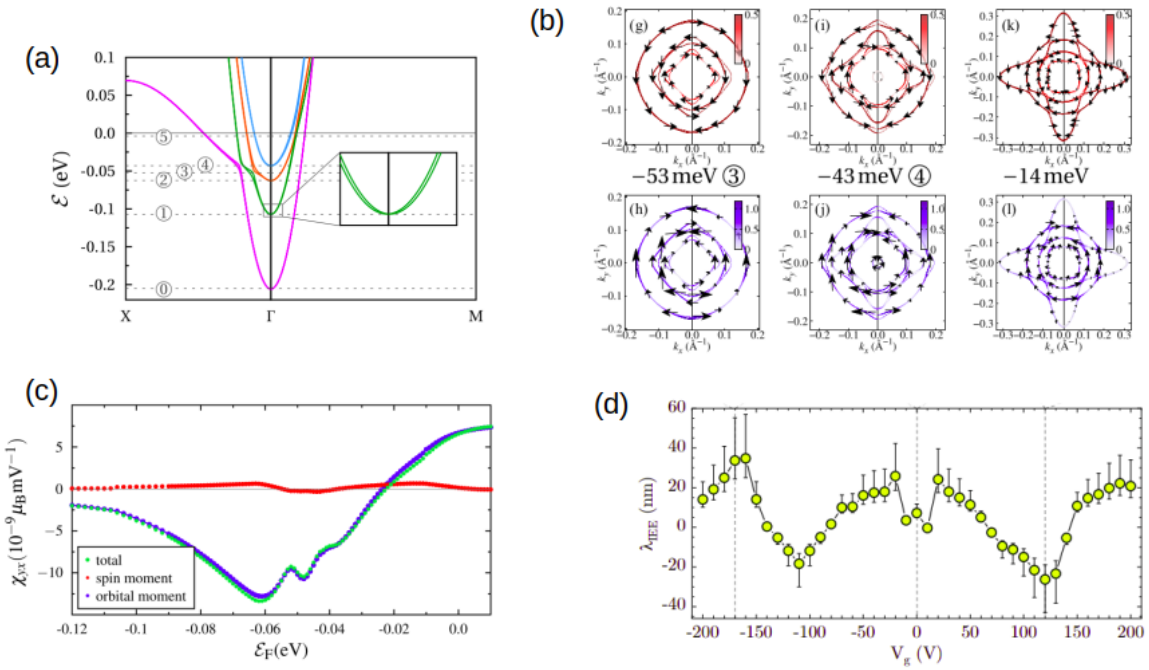

Figure 2.14: **(a)** Band structure of STO interface 2DEG using 8 × 8 TB Hamiltonian. In the inset: A zoom of the band structure picturing a Rashba-like spin-plitting. **(b)** The 6 figures represent the Fermi surface at 3 different Fermi levels, where we plot the expectation values of the spin (red) and orbital (blue) momentums in units of $\hbar$, and each arrow represents the in the left (right) panel represents the direction of the outer (inner) bands moments. **(c)** Spin and orbital Edelstein effects efficiencies dependence on the Fermi energy.[203] **(d)** Inverse Eldelstein characteristic length measured for a sample of AlO_x/STO versus a back-gate voltage.[29]

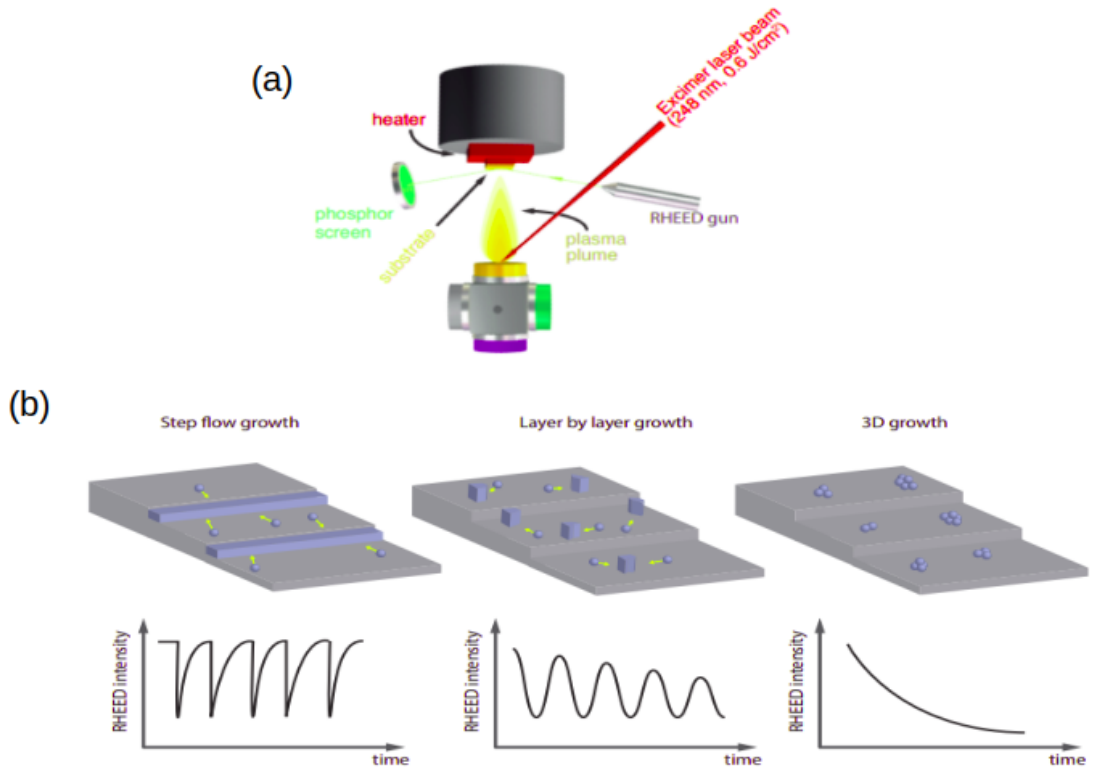

Figure 2.15: **(a)** Scheme describing the different elements of the pulsed laser deposition set up. **(b)** Three different growth modes are represented (from left to right) step flow, layer by layer and 3D growth mode. The bottom figures represent the associated RHEED intensity profile versus time for three different growth modes (here the time axis is not at the same scale for all the three figures).[47]

forms a plasma "plume" which propagates perpendicularly with respect to the target surface, as illustrated in Figure 2.15 a. Usually a substrate is placed in front of the target, allowing for the deposition of the species within the plume, through a stoichiometric transfer. Since the deposited ad-atoms will diffuse on the substrate, several factor should be taken into account [7], which could modify the diffusion length of the ad-atoms, creating three different growth modes : step flow growth, layer by layer growth and a 3D growth, as illustrated in Figure 2.15 b. Additionally, one can monitor the growth process *in-situ* by using Reflection High-Energy Electron Diffraction (RHEED). This technique relies on an accelerated electron beam ($21kV$) which is sent in a grazing incidence angle ($< 2°$) on the surface of the substrate, so that it is reflected by only the top layers of the growing material, and create a constructive interference pattern on a fully crystalline surface, thus by looking at the maximum intensity in the interference pattern we can keep track of the growth order during the deposition. In Figure 2.12 b, we plot the RHEED intensity for all three different growth modes. In the layer by layer mode we observe that the RHEED diffraction pattern presents oscillations which testify for the layer by layer growth. On the opposite, the RHEED signal in the step flow

[7] Such as the temperature of the substrate, surface binding energy,etc.

growth presents sharp oscillations representing the pulse count for each diffusion cycle. Lastly, the RHEED signal in the 3D growth mode decreases exponentially with time presenting no oscillations.

2.4.2 Samples characterization

In order to check the quality of the fabricated samples. The LAO/STO samples where characterized at the University of Geneva, using various techniques such as the Atomic Force Microscopy (AFM), and transport measurements. In the Figure 2.16 a, we plot the RHEED oscillations obtained for 9 u.c LAO layer deposited on top of the TiO_2 terminated STO, we observe clearly the 9 oscillations in the RHEED diffraction pattern testifying for the thickness of the LAO layer. On the other hand, the samples were also characterized using AFM surface topography imaging, which is shown in Figure 2.16 b. We observe that the deposited LAO layer, in this case 10 u.c LAO, reproduces clearly the steps and terrace structure of the STO substrate, with 1 u.c steps. The samples were also characterized electrically, by measuring the sheet resistance of the LAO/STO samples, while decreasing the temperature, we observe a net decrease in the sheet resistance, as illustrated in Figure 2.16 c, demonstrating the metallic behavior of the LAO/STO samples, for TiO_2 terminated STO substrates as expected from previous studies[188, 93, 57]. In the next chapter we will present the various experimental techniques used to characterize the LAO/STO samples by measuring the spin-to-charge conversion signal.

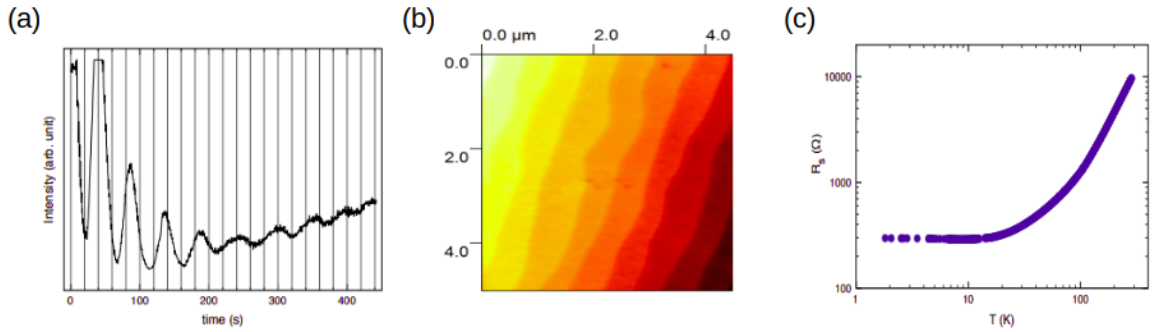

Figure 2.16: Characterization of the LAO/STO samples at the university of Geneva, **(a)** RHEED oscillation profile for a sample of LAO(9 u.c)/STO. **(b)** 2D topography map of the surface of a sample of LAO(10 u.c)/STO, where we observe flat terraces followed by abrupt unit call steps. **(b)**Sheet resistance versus the temperature, we observe a decrease of the resistance at low temperature signalling a metallic behavior in the LAO/STO sample.[47]

Chapter3

Spin-to-charge conversion at LAO/STO interface states

Contents

After the prediction of the direct and inverse spin Hall effect by Dyakonov et al.[179], various experimental studies have demonstrated the possibility to convert a spin current into a charge current, particularly in heavy metals like Pt, Ta, and Au which display a large spin Hall angle, thanks to the strong atomic spin orbit

coupling which is supposed to increase with the atomic number Z as $\sim Z^4$ in the case of a hydrogen-like atom[122, 169, 109].

Recently another type of spin orbit coupling have been discovered in 2D systems without inversion symmetry, relying on the Rashba interaction[1], which stems from a joint action of the spin orbit coupling and an electric field built-in at the interface of two different materials as described by Byachkov and Rashba[214]. Various Rashba systems have displayed a promising spin-to-charge conversion efficiency, such as the interfaces of 2D quantum wells in doped semiconductor, such as AlGaN/GaN [91] or InGaAs/InAlAs [84]), metallic surface alloys, such as Ag/Bi(111)[200], 2DES oxide interfaces, such as LAO/STO [199] or more recently in some topological insulators, to cite few α-Sn[124], and HgTe[108].

In this chapter, we will give an overview about the variety of systems which display highly efficient spin-to-charge conversion efficiency, such as 2DES oxide-based interfaces which are considered as one of the best converters in the literature, particularly LAO/STO, which displays a variety of very interesting properties [2]. In the following we will introduce the technical details regarding the spin pumping technique which is driven by the ferromagnetic resonance, then we will present the spin injection mechanism and an estimation of the conversion efficiency, and later we will give a quick review of our experimental setup. Lastly, we will present a different technique to perform spin injection, which relies on the spin Seebeck effect.

3.1 Highly efficient spin-to-charge conversion

3.1.1 Spin Hall effect in heavy metals

Heavy metals with 4d or 5d incomplete orbital shells such as Pt, Ta, and W display a large intrinsic spin orbit coupling[134, 56, 162]. On the other hand, metallic systems doped with heavy impurities like Cu doped with Ir or Bi can also display a strong extrinsic spin orbit coupling[174, 107, 106, 118]. Taking advantage of the strong SOC in these materials, multiple studies have been performed using ISHE in heavy metals such as Pt, which displays positive spin Hall angle, contrary to Ta or W which display negative spin Hall angle. This was shown by the study performed by Hahn et al. and Castel et al. [56, 28] (see Figure 3.1 a), where a complete study of the ISHE in both Ta and Pt with respect to the film thickness, allowing for an estimation of transport parameters such as the spin diffusion length for $YIG|Pt$ and $YIG|Ta$ samples, giving $\lambda_{sd}^{Pt} = 3.0 \pm 0.5nm$ and $\lambda_{sd}^{Ta} = 1.8 \pm 0.7nm$ [128] , and spin Hall angle $\theta_{SH}^{Ta} \approx -0.02$ and $\theta_{SH}^{Pt} \approx 0.03$. Indeed, from these parameters, we can estimate the spin to charge conversion efficiency in Pt (resp Ta)

[1] See Chapter 2 for more details
[2] See Chapter 3 for more details

which is evaluated to be $\lambda_{eff}^{Pt} \approx 0.09nm$ (resp $\lambda_{eff}^{Ta} \approx 0.036nm$), which is quite significant. In the quest to fetch for highly efficient spin to charge converters, it seems that heavy metal are not the ideal candidates for various reasons.

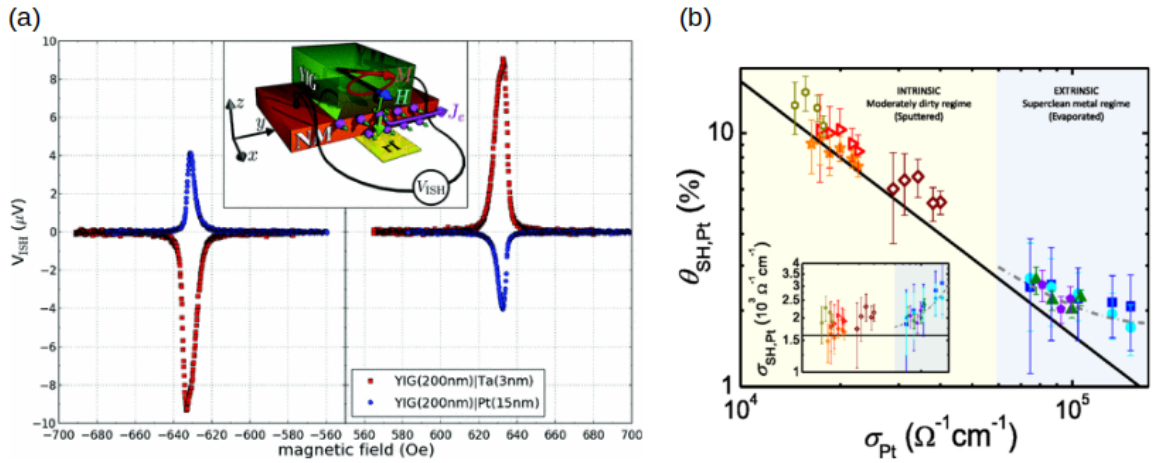

Figure 3.1: Spin Hall measurements in heavy metals. (a) Inverse spin Hall voltage measured at 3.5 GHz for two samples YIG|Pt (blue) and YIG|Ta (red), in the inset we plot a sketch of the experiment.[56] (b) Spin Hall angle versus the longitudinal conductivity of Pt, the black solid line corresponds to the intrinsic contribution. In the inset we plot the spin Hall conductivity for the same data, and the horizontal axis is the same as in the main panel.[128]

First, Sagasta et al. have shown that the spin relaxation mechanism in Pt is dominated by the Elliot Yaffet mechanism, owing to the fact that the measured spin diffusion length is proportional to the conductivity of the Pt layer[128]. Interestingly, the spin Hall angle was reported to decrease with respect to Pt conductivity as shown in Figure 3.1 b. We observe that in order to increase θ_{SH}, from 0.02 to 0.17, the resistivity of Pt should be increased from ~ 7 to $70\mu\Omega \cdot cm$, which is quite inefficient with respect to the dissipation effects that limit the current density that could be sent through these devices. Nevertheless, there are interesting ideas to work around this issue, by combining both intrinsic and extrinsic SOC in order to optimize the θ_{SH}, without increasing the resistivity , like in AuW alloys as shown by Laczkowski et al. who reported a large spin diffusion length $\lambda_{sd}^{AuW} = 1.2nm$ and $\theta_{SH} = 0.1$, which is at least one order of magnitude higher than gold.[86] It is also interesting to note that the reported large extrinsic spin Hall effect in heavy metal alloys, such as AuW[87] or AuTa[86], is still much lower compared to other systems such as 2D topological insulators (TI), as shown by Jiang et al who reported a spin-to-charge conversion signal in $(Bi_{0.24}Sb_{0.76})_2Te_3/YIG$ ten times larger than in Pt/YIG.[72]

To summarize, we have shown that heavy metal alloys, which rely on large extrinsic SOC, can be good candidate for spin-to-charge conversion. However, new types of 2D systems with large Rashba coefficient have been showing very promising properties which we will discuss in the next subsections.

3.1.2 Edelstein effect in various systems

3.1.2.1 Metallic surfaces and interfaces

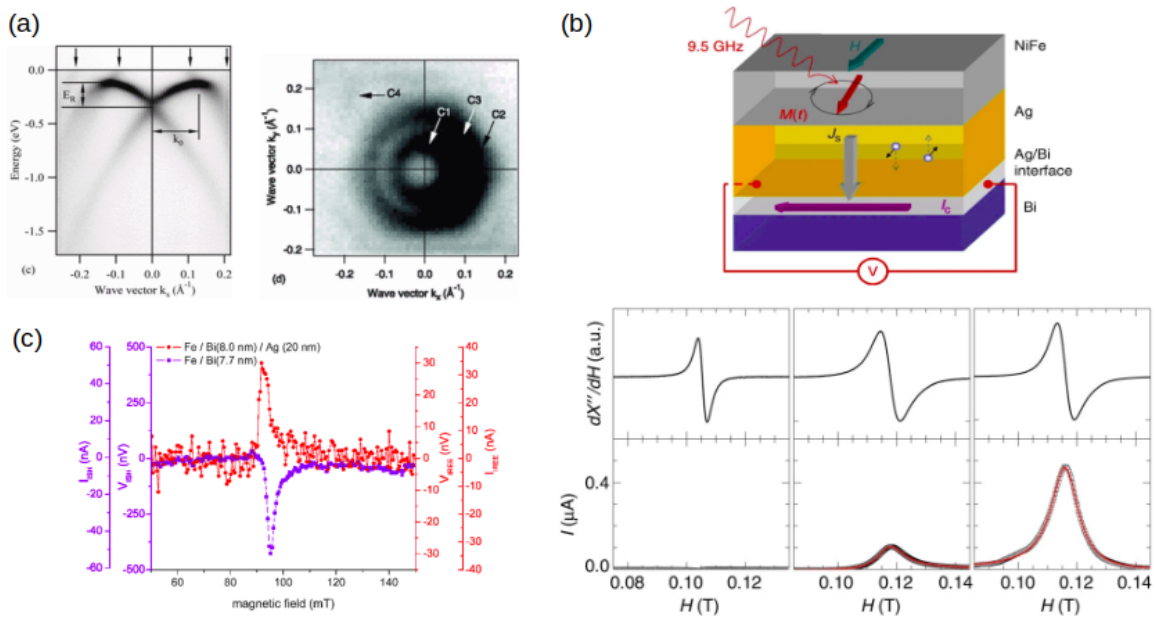

Figure 3.2: The Rashba-Edelstein effect at the Ag|Bi metallic interface. (a) The Rashba-split band structure of Ag|Bi.[3] (b) A sketch of the spin pumping experiment applied to NiFe|Ag|Bi heterostructure, where the spin current J_s is converted into a charge current J_c, which is detected as a voltage drop at both ends of the sample.[199] (c) Spin-to-charge conversion signal measured at 8.5 GHz for two different samples Fe|Bi and Fe|Bi|Ag.[132] (d) Spin pumping experiment applied to two reference samples (from left to right) NiFe|Ag and NiFe|Bi, and the Rashba system NiFe|Ag|Bi (figure to the right). FMR signal (top panel) and the spin-to-charge conversion current (bottom panel).[199]

After the theoretical prediction of the Rashba splitting at metallic surface states by Bihlmayer et al.[12], different experimental studies, relying on surfaces sensitive spectroscopy techniques such as the angle resolved photo-emission spectroscopy (ARPES), have reported a band splitting in a variety of different metallic surfaces including Au(111)[151], Ag(111)[167], Cu(111)[143]. Indeed, metallic surface states break the inversion symmetry and involve a finite effective electric field which allows for spin-manipulation. Similarly, metallic interfaces can also display a large spin-to-charge conversion efficiency as shown by Rojas Sanchez et al using Ag/Bi(111) interface[199]. Indeed, it displays a higher Rashba splitting compared to Ag(111) or Bi(111) surface states, due to a drastic change in the orbital character at the interface between Ag and Bi, as calculated by Bihlmayer et al.[13], thus leading to an increase in the Rashba splitting (see Figure 3.2 a). This large spin-to-charge conversion efficiency was evidenced, using a spin pumping technique, which injects a spin population into the Ag/Bi interface, leading to the creation of a charge current, thanks to the IEE ,which translates into a voltage peak measured along two electrical contacts (

see Figure 3.2 b). The measured IEE current, which was reported for three different systems NiFe/Ag, NiFe/Bi and NiFe/Ag/Bi, is the highest in the Ag/Bi interface followed by Bi, which can be attributed not only to the interface with NiFe layer, but also to a bulk contribution due the ISHE[199]. As a matter of fact, Sangiao et al have reported a sign change, when comparing the IEE signal in Fe/Bi/Ag and ISHE signal in Fe/Bi, respectively[132] (see Figure 3.2 c). This underlines the IEE nature of the signal in Fe/Bi/Ag, which is of opposite sign to the signal reported by Rojas Sanchez et al in NiFe/Ag/Bi with reverse stacking order. Even though some metallic surface and interface states display a very a strong Rashba coupling, they are far behind in term of conversion efficiency compared to more exotic materials like oxide interface states[200, 29].

3.1.2.2 2DES oxide-based interfaces

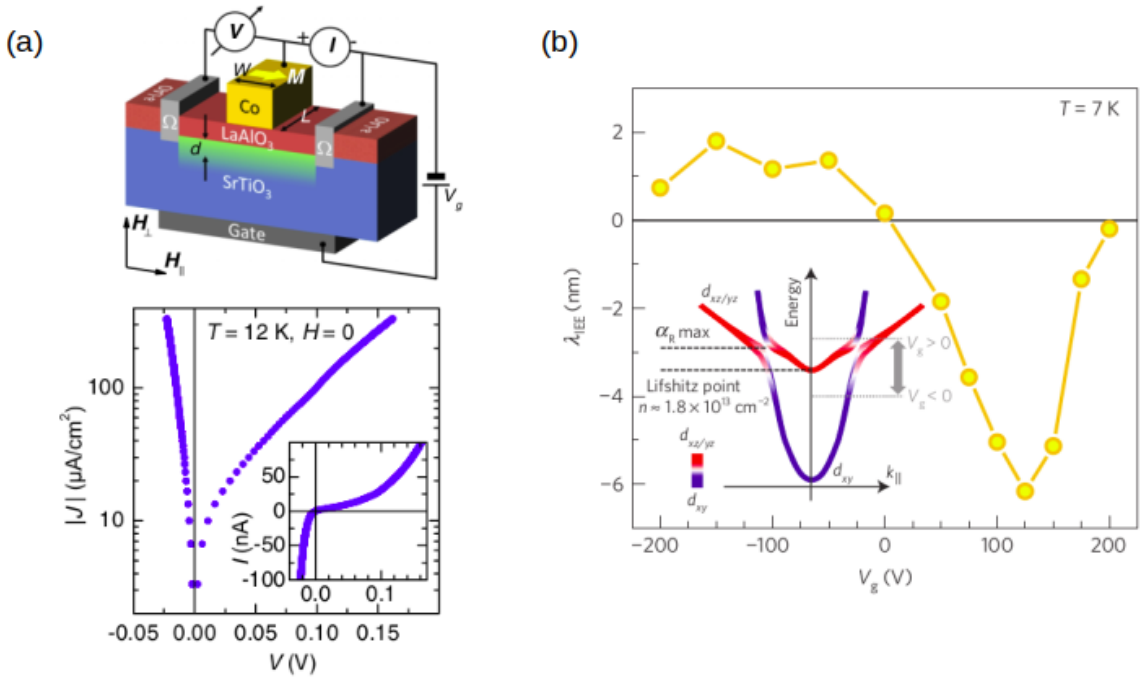

Figure 3.3: The Rashba-Edelstein effect at the LAO|STO interface. (a) Top panel : a sketch of a 3-T Hanle measurement applied to the Co| LAO|STO heterostructure, where the magnetic field is applied either perpendicular or parallel to the sample plane. Bottom panel: the I-V characteristic curve of the sample at $T = 12K$.[242](b) Spin-to-charge characteristic length λ_{IEE} versus backgate voltage, where a maximum conversion efficiency is recorded at around $V_g = 125V$, corresponding to the band anti-crossing region.[200]

Oxide interfaces have drawn a lot of attention these last few years, especially with the discovery of the 2DES at the interface of LAO/STO [3], by Ohtomo et al.[186] This 2DES has been studied extensively, owing to the fact that it displays variety of interesting physical properties, such as superconductivity reported below

[3]See Chapter 3 for more details

300mK [121], magnetism [8] and a gate tuneable strong spin-orbit coupling as demonstrated by Caviglia et al.[31] (see Figure 2.5), which can be very appealing for spin manipulation in spintronic applications[4]. Reyren et al. have been the first to report the possibility to inject a spin current through the LAO barrier , which can be tuned using electrostatic in a backgate geometry[242]. They also demonstrated the possibility to reach a resonant tunneling regime by applied a backgate voltage (see Figure 3.3 a). As a matter of fact, spin-to-charge conversion in LAO/STO can benefit greatly from the tuneability of the transport parameters [5] using electrostatic doping. The first evidence of this highly tuneable spin-to-charge conversion signal, was reported by Lesne et al, who measured a high conversion efficiency $\lambda_{IEE} \approx 6.4nm$[200], which is 1 order of magnitude higher than recorded in Ag/Bi(111) $\lambda_{IEE} \approx 0.3nm$[199], by Rojas Sanchez. This high efficiency in spin-to-charge conversion in LAO/STO is mainly due the multi-orbital nature of the interfacial 2DES at some specific points of the Fermi surface (see Figure 3.3 b), but also to the very large electron relaxation time ($\tau_{LAO/STO} \approx 1.4 \times 10^{-12}s$)[50, 193]. It is at least 3 orders of magnitude higher than in Ag/Bi ($\tau_{Ag/Bi} \approx 5 \times 10^{-15}s$)[199], due to the fact that the electrons at the interface in LAO/STO are very well isolated from relaxation channels [6]. Furthermore, Chauleau et al reported a high spin-to-charge conversion efficiency in LAO/STO, $\lambda_{IEE} \approx 1nm$ at $T \approx 77K$, which seems to decrease when increasing the temperature, to reach $\lambda_{IEE} \approx 0.15nm$ at room temperature[34] (see Figure 3.4 a), which can be explained by a 2 orders of magnitude decrease in the electron mobility of the 2DES when heated to room temperature ($\mu \sim 1000 - 5000cm^2 \cdot V^{-1} \cdot s^{-1}$ at low temperature[49]). A consistent increase of $\lambda_{IEE} = +3.9nm$ at $T = 20K$ [110] was reported by Ohya et al., in complete opposition to the results of Song et al and Wang et al, who reported an increase of λ_{IEE} while increasing the temperature, which was associated to the decrease of spin transparency through the LAO barrier[140, 163]. Chauleau et al, also reported anisotropic angular dependence of λ_{IEE}[34] (see Figure 3.4 b), which can be associated to spin polarized angular dependence of the Rashba coefficient or the electron relaxation time. Recently, a highly efficient spin-to-charge conversion has been reported by Vaz et al[158] in the SrTiO3 based 2DES formed through the deposition of Al layer on top of STO, which was first discovered by Rodel et al[127]. This 2DES has the particularity of having a higher carrier density compared to LAO/STO, leading to a more complex interplay between different t_{2g} sub-bands, and specially to a topological band inversion yielding a high spin-to-charge conversion efficiency $\lambda_{IEE} \approx -20nm$. Despite being very promising candidates for spintronic applications, these SrTiO3 based 2DES have not been studied extensively when it comes to their highly efficient orbital Edelstein effect which was predicted to dominated the spin Edelestein effect. As a matter of fact, we need to uncover the

[4] particularly in spin-FET applications[218, 246]
[5] Rashba coefficient, electron mobility, electron relaxation time[193, 50]
[6] Contrary to Ag/Bi the electrons relax quickly in the metallic layer

orbital and spin nature of the spin-to-charge conversion signal in $SrTiO_3$ based 2DES, in order to elucidate the exotic physics behind complex oxides, which we will investigate further in Chapter 5. Furthermore, in the following subsection, we will introduce some technicalities with respect to the experiments that where undertaken in order to study spin-to-charge conversion signals in LAO/STO. The first experiment relies on ferromagnetic resonance using the spin pumping technique, which will be presented and we will give an overview of the experimental setup that was developed in this context. Secondly, we will give a brief introduction to the spin Seebeck effect, which was used in the second experimental setup in order to measure the spin-to-charge conversion signal.

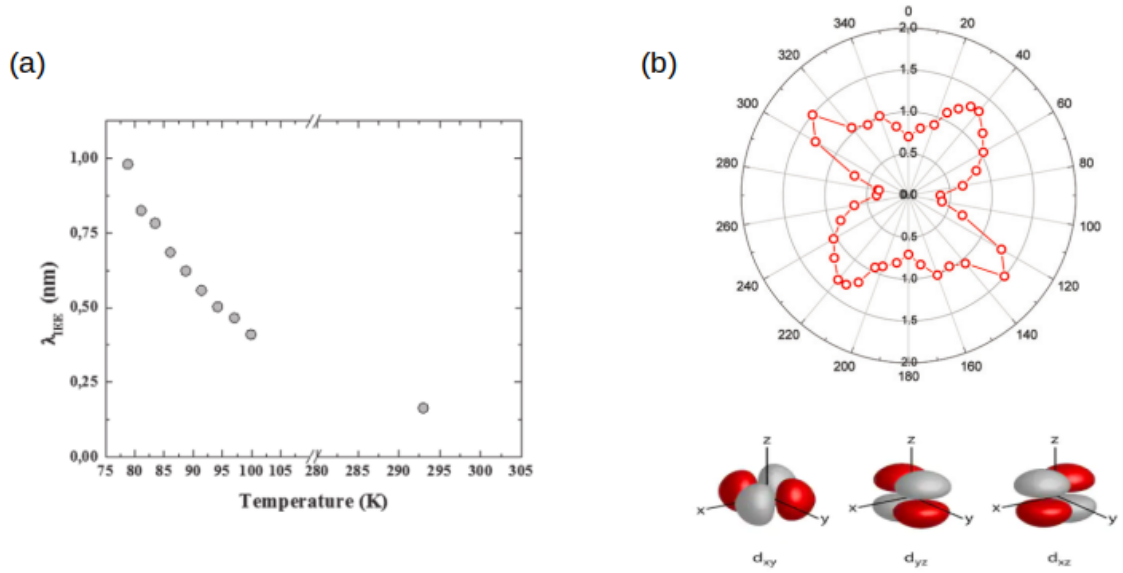

Figure 3.4: (a) Temperature variation of λ_{IEE} for a sample of NiFe|LAO(4u.c)|STO, showing an activation-like behavior. (b) Non-trivial angular dependence of λ_{IEE} for the same sample at $T = 77K$, attributed to the non-trivial symmetry of d-orbitals (bottom panel) which participate in the conduction bands.[34]

3.2 Spin injection using various techniques

The basic idea behind the spin-to-charge conversion effect relies on the conversion of a pure spin current into a charge current. Thus, the necessity to create a pure spin current driven via a spin transfer mechanism into a highly efficient spin-to-charge converter. For this reason, we need a very effective technique, which will inject a spin population without any charge injection, in order to avoid any spurious effect on the detected charge signal. In this regard, two very efficient techniques have been applied to study the spin-to-charge conversion signal. The first technique, is based on spin pumping by ferromagnetic resonance which was first introduced by Saitoh et al and various other research groups[129, 38]. This technique has been used extensively to study spin-to-charge conversion in plenty of different systems, ranging from heavy metals,

topological insulators to semiconductor heterostructures. The second technique rests on the spin Seebeck effect, first reported experimentally by Uchida et al in which a spin voltage was detected on permalloy layer submitted to a temperature gradient[152]. This technique has been also studied using a variety of heat sources in order to generate a pure spin current, which opens up the door for various thermo-spintronic applications like a thermo-electric power generator or temperature gradient sensors.

In the following section, we will present the theoretical description of the ferromagnetic resonance, and its application into spin pumping first introduced by Tserkovniak et al[150, 20]. Then we will give a brief overview of the spin injection mechanism, followed by a quantification of spin-to-charge conversion efficiency, and later we will present the experimental apparatus for the spin pumping experiment. Secondly, we will give a quick introduction to the spin Seebeck effect, where we will present the theoretical framework behind it, which was first introduced by Johnson and Silsbee[73]. In addition we will present some results and give a brief analysis on spurious effects encountered when using this technique. Lastly, we will put forward the technical details regarding the experimental set up used for thermal spin injection.

3.2.1 Spin pumping experiment

3.2.1.1 Magnetization dynamics : Phenomenological description

In the following, we will refer to ferromagnetic materials (FM), as particular systems displaying a spontaneous magnetization below a certain critical temperature, called the Curie temperature T_c. This phase transition takes place due to a spontaneous symmetry breaking, driven mainly by the exchange interaction which couples the spin degree of freedom of the system leading to a net magnetization which can be represented by a single vector $\overrightarrow{M} = M_s\overrightarrow{m}$, where M_s is the saturation magnetization and $\overrightarrow{m}$ is a unit vector . The first phenomenological description of magnetization dynamics was proposed by Landau and Lifschitz and later generalized by Gilbert[88, 53]. It is also notable, to inform the reader that throughout all the following discussion we will consider the magnetization to be uniform or slowly varying in space.

3.2.1.1.1 Landau-Lifschitz-Gilbert equation The equation of motion of the magnetization $\overrightarrow{M}$ is governed by the effective field $\overrightarrow{H_{eff}}$ which couples to $\overrightarrow{M}$, by exerting a torque $\overrightarrow{T}$ on the magnetization given by :

$$\overrightarrow{T} = \overrightarrow{M} \times \overrightarrow{H_{eff}} \tag{3.1}$$

this yields the following equation of motion, also called the Landau-Lifschitz equation :

$$\frac{\partial \overrightarrow{M}}{\partial t} = -\frac{g\mu_b}{\hbar}\overrightarrow{M} \times \overrightarrow{H_{eff}} \tag{3.2}$$

where g is the Landé factor which is close to 2, μ_b is the Bohr magnetron, the expression $-g\mu_b/\hbar$ is denoted γ and it is called the gyromagnetic ratio which denotes the collective motion of magnetic moments , whereas $\overrightarrow{H_{eff}} = -\partial H_m(\overrightarrow{M})/\partial \overrightarrow{M}$ is the effective field, which is determined by the magnetic Hamiltonian of the FM system $H_m(\overrightarrow{M})$. This effective field is given as the sum of different contributions, mainly:

$$\overrightarrow{H_{eff}} = \overrightarrow{H_{ext}} + \overrightarrow{H_d} + \overrightarrow{H_{anis}}, \tag{3.3}$$

where $\overrightarrow{H_{ext}}$ is the external applied magnetic field, $\overrightarrow{H_d}$ is the demagnetization field created by the magnetization itself and $\overrightarrow{H_{anis}}$ is the anisotropy field, which can be associated to magneto-crystalline anisotropy, surface anisotropy or magneto-elastic coupling. It is important to note that this equation ensures the conservation of the norm of the magnetization vector, which can be easily verified by multiplying both sides of equation , which gives :

$$\frac{\partial}{\partial t}\|\overrightarrow{M}\|^2 = 0 \tag{3.4}$$

In this regard, the equation 3.2 predicts a uniform precession of the magnetization, also known as the Larmor precession, which implies a dissipationless perpetual precession of the magnetization which seems unrealistic in nature, due to the existence of some dissipation channels which are going to transfer the energy of the uniform precession mode into incoherent energy modes via the coupling of the magnetization to different degrees of freedom, like magnons, conduction electrons and phonons. In order to cover those relaxation mechanisms, the equation needs to be extended, which can be complicated if one wants to include these coupling mechanisms explicitly. Gilbert proposed a phenomenological damping term corresponding to a viscous "friction" torque which is proportional to the magnetization and to a damping constant α, which force the magnetization to precess in a spiral motion and return to its equilibrium position after a time $\tau = (\alpha\gamma H_{eff})^{-1}$, this equation is given by[53] :

$$\frac{\partial \overrightarrow{M}}{\partial t} = -\gamma\overrightarrow{M} \times \overrightarrow{H_{eff}} + \frac{\alpha}{M_s}\overrightarrow{M} \times \frac{\partial \overrightarrow{M}}{\partial t} \tag{3.5}$$

This equation is called the Landau-Lifschitz-Gilbert equation (LLG), which contains two different terms. The first term is equivalent to equation 3.2 , which describes the precession of the magnetization around $\overrightarrow{H_{eff}}$, while the second term corresponds to a damping torque which is proportional to the cross product of the magnetization and the "magnetization velocity", which forces back the magnetization to its equilibrium

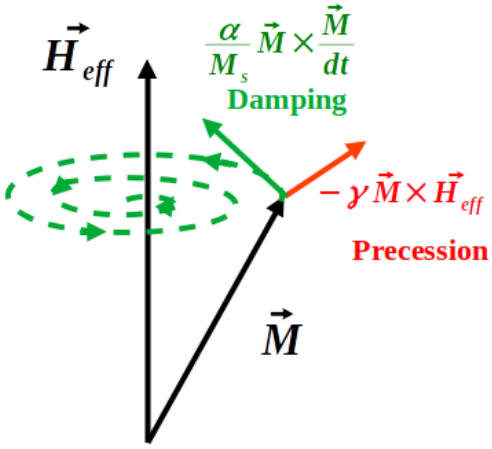

Figure 3.5: Magnetization dynamics, which is driven by two different contributions: a precession torque which rotates the magnetization around its effective field $\overrightarrow{H_{eff}}$, and a Gilbert damping torque which aligns the magnetization with $\overrightarrow{H_{eff}}$.

position as shown in Figure 3.5 .

In addition, if the damping term α is small enough, the equation can be written using the Landau-Lifschitz damping term, given by :

$$\frac{\partial\overrightarrow{M}}{\partial t} = -\gamma\overrightarrow{M}\times\overrightarrow{H_{eff}} + \frac{\alpha}{M_0}\overrightarrow{M}\times(\overrightarrow{M}\times\overrightarrow{H_{eff}}) \tag{3.6}$$

It is also interesting to note that both equations 3.5 $\&$ 3.6, ensure the conservation of the norm of the magnetization vector as shown in equation 3.2 .

In the next section, we will introduce an additional external field which will not be static but dynamic this time, in order to study the ferromagnetic resonance in thin films.

3.2.1.1.2 Ferromagnetic resonance In order to study the ferromagnetic resonance in thin films, we need to apply an oscillating excitation field $\overrightarrow{h}$ which will drive the magnetization precession out of equilibrium. When applying $\overrightarrow{h}$ perpendicular to the external effective field $\overrightarrow{H_{eff}}$, the resulting torque driving the magnetization will counterbalance the damping torque as represented in Figure 3.6 a, where we observe that the torque induced by $\overrightarrow{h}$ will point outward, counteracting the inward motion of the magnetization set by the damping torque which point toward $\overrightarrow{H_{eff}}$. When the resonance condition is reached by tuning the frequency of $\overrightarrow{h}$ so that it coincides with the resonance frequency f_{res}, which can be calculated from the magnetic properties of the sample and the external applied field. It will be quantified later, using Kittel's formula[83]. Under these conditions, the oscillating field $\overrightarrow{h}$ induced-torque will rotate at the same frequency as the magnetization, therefore it will perfectly cancel the damping torque, leading to a steady precession

state of the magnetization. This corresponds to the resonant absorption of a photon by an electron in the ferromagnet, thus creating a magnon which will reduce the longitudinal component of the magnetization by $\gamma\hbar$, this phenomenon is known as the Ferromagnetic Resonance (FMR).

To gain further insight into the physics behind the ferromagnetic resonance, we will try to give a a very brief review of the main calculation steps, in order to extract the expression of the magnetic susceptibility response for a sinusoidal oscillating external field. For more details involving those calculations we will refer the reader to the book of Gurevich and Melkov[55], which gives a detailed solution of equation . In the first step we need to linearize and solve the equation of motion , by considering a sinusoidal driving field $\overrightarrow{h}$. We assume that the magnetic field and magnetization in equation 3.6 , can be written as the sum of a steady and alternating contributions :

$$\overrightarrow{H} = \overrightarrow{H_0} + \overrightarrow{h} \ , \ \overrightarrow{M} = \overrightarrow{M_0} + \overrightarrow{m} \tag{3.7}$$

under the assumption of very small excitation :

$$\| \overrightarrow{h} \| << \| \overrightarrow{H_0} \| \ , \ \| \overrightarrow{m} \| << \| \overrightarrow{M_0} \| \tag{3.8}$$

Then, after the linearization of equation 3.6 , we get :

$$i\omega \overrightarrow{m} + \gamma \overrightarrow{m} \times \overrightarrow{H_0} + \frac{i\alpha\omega}{M_0} \overrightarrow{m} \times \overrightarrow{M_0} = -\gamma \overrightarrow{M_0} \times \overrightarrow{h} \tag{3.9}$$

After projecting the linearized equation 3.9 , we can retrieve the magnetization response which is proportional to the driving field $\overrightarrow{h}$ through:

$$\overrightarrow{M} = \overline{\overline{\chi}} \overrightarrow{h} \tag{3.10}$$

where $\overline{\overline{\chi}}$ is the susceptibility tensor, which has the following expression[7][115, 161] :

$$\overline{\overline{\chi}} = \begin{pmatrix} \chi & i\chi_a & 0 \\ -i\chi_a & \chi & 0 \\ 0 & 0 & \chi_{\parallel} \end{pmatrix} \tag{3.11}$$

where χ, χ_a and $\chi_{\parallel}$ are the various susceptibility components of the susceptibility tensor, we should also note that the FMR absorption power will be proportional to the imaginary part of $\chi = \chi' + i\chi''$, through

[7] for a detailed expression of $\overline{\overline{\chi}}$ see Appendix A

the expression :

$$P = \omega\chi''\|h\|^2 \tag{3.12}$$

with :

$$\chi'' = \frac{\alpha\gamma M_0\omega(\omega_H^2 + (1+\alpha)^2\omega^2)}{(\omega_H^2 - (1+\alpha)^2\omega^2) + 4\alpha^2\omega^2\omega_H^2} \tag{3.13}$$

where $\omega_H = \gamma H$. The expression of χ'' corresponds to a lorentizian curve, of the form $1/(1+\beta^2)$, where $\beta = (H - \omega/\gamma)/(\alpha\omega)$. In Figure 3.6 b , we plot the lorentzian absorption line, with a width $\Delta\beta$, corresponding to intervals between f or H at the points where $\chi'' = \chi''_{max}/2$, given by :

$$\Delta H = \frac{4\pi\alpha f}{\gamma} \ , \ \Delta f = 2\alpha f \tag{3.14}$$

When the resonance condition is reached in equation 3.13 , the resonance frequency, f_{res} ,can be extracted by taking into account the geometry of the sample which yields the Kittel's formula[83] for an ellipsoidal sample:

$$f_{res} = \frac{\gamma}{2\pi}((H + (N_y - N_z)M_s)(H + (N_x - N_z)M_s))^{1/2} \tag{3.15}$$

where N_x, N_y, N_z are the demagnetization factors along the 3 different direction of the ellipsoid (see Figure 3.6 c), in the case of a thin film with an in-plane magnetization, the equation can be re-written as :

$$f_{res} = \frac{\gamma}{2\pi}\sqrt{H(H + 4\pi M_s)} \tag{3.16}$$

Thus, linking the resonance frequency to the saturation magnetization M_s, and to the static component of the magnetic field H.

On the other hand, we measure usually the derivative of the lorentzian $\partial\chi''/\partial\beta$, either sweeping the magnetic field H , while $f = cste$, or sweeping the frequency f, while $H = cste$. In the former case, the peak-to-peak linewidth $\Delta H_{pp} = (2\Delta H)/\sqrt{3}$, can be rewritten using equation 3.14, as:

$$\Delta H_{pp} = \frac{2}{\sqrt{3}}\frac{\alpha\omega}{\gamma} \tag{3.17}$$

this expression links the linewidth of the FMR signal ΔH_{pp} to the Gilbert damping parameter α. An additional term ΔH_0 can be added to the expression above, to account for the contribution stemming from the inhomogeneities of the FM layer, leading to a further broadening of the FMR spectra. These local inhomogeneities can be attributed to the local variations in the properties of the FM layer, such as

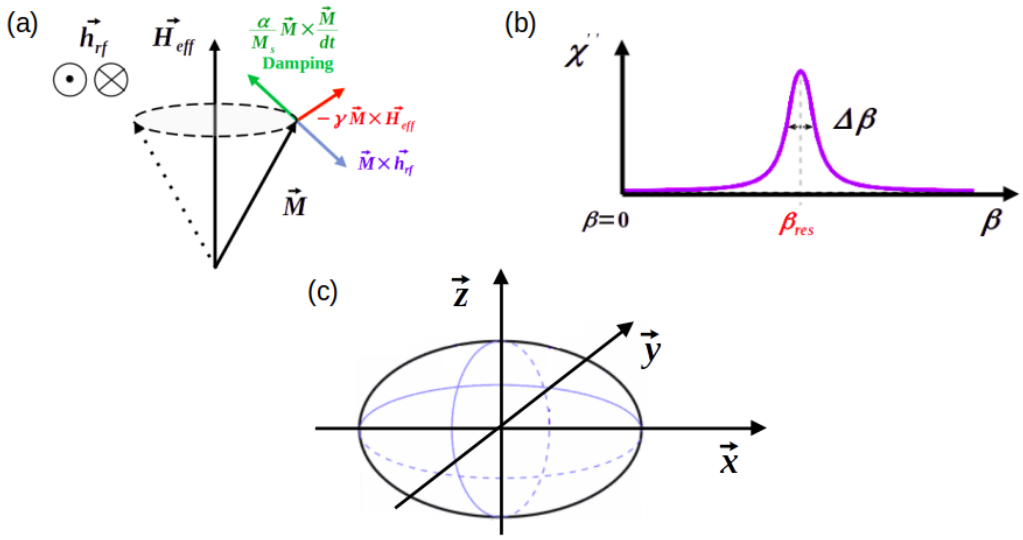

Figure 3.6: The ferromagnetic resonance in FM material. (a) a sketch of the magnetization dynamics in the presence of rf excitation $\overrightarrow{h_{rf}}$ which drives the auto-oscillation of the magnetization, so that the Gilbert damping term is canceled at the resonance.(b) The imaginary pat of the susceptibility response function versus the free parameter β (which represents either the field H or the frequency ω).(c) Ellipsoidal sample with three axis defining the three different directions of the sample.

the magnetization, external magnetic field or the anisotropy. Indeed, local differences in the resonance fields between different parts of the sample will lead to a wider resonance peak resulting from the sum of individual resonance peaks for each region of the sample.

As a matter of fact, the FMR is a powerful tool to characterize some magnetic properties of our sample, but it can also be used to do a spin pumping experiment through a mechanism called spin injection, in order to do spin-to-charge intreconversion. In the following we will introduce the mechanism of spin injection, then we will quantify the spin-to-charge conversion efficiency. We will end with a review on the multiple spurious effects that can hamper the detection of the spin-to-charge signal.

3.2.1.2 Spin pumping mechanism

Since the late 80's, Johnson and Silsbee have demonstrated the possibility to perform spin injection using magnetization precession at ferromagnetic resonance[74, 73], which was explained later by Tserkovnyak and Brataas using spin-dependent reflection and transmission coefficients forming the scattering matrix and allowing for the evaluation of the non-equilbrium charge and spin currents flowing through a ferromagnet/normal metal junction[150, 2]. After the experimental demonstration by Saitoh et al of a spin-to-charge conversion signal in Platinum at room temperature[129], the door was open for a wider application of the spin-pumping technique, which has been used since to characterize the spin-to-charge conversion in a variety of different systems. To further gain a deeper understanding of the origin of the spin injection mechanism,

we will give in the next subsection a brief review of the main arguments presented in a study of Tserkovnyak and Brataas[2], [8]. Then we will quantify the spin current injected into the normal metal, which will allow us to evaluate the spin-to-charge conversion efficiency.

3.2.1.2.1 Spin injection At the ferromagnetic resonance, the magnetization precesses around $\overrightarrow{H_{eff}}$, at frequency ω, inducing a spin-imblance as demonstrated by Tserkovnyak et al[150, 2] who have shown that when the magnetization's motion is taken into account by the scattering matrix (in the spin space), this will induce a non-equilibrium spin current, which translates into an emission of angular momentum into the neighboring nonmagnetic metal. To understand qualitatively this phenomenon, Brataas and Tesrkovnyak gave various analogies such as the concept of a spin battery which has similar features as the charge battery including the maximum voltage in the absence of a load as well as a maximum spin current that can be drawn from the battery[2]. The latter can be estimated in the assumption that the ferromagnet is thicker than the spin coherence length (few $\mathring{A}$ in transition metal such as Co, Ni, or Fe) leading to the emission of a spin current which is determined by the spin mixing conductance, $g_{\uparrow\downarrow}$ [9], and it can be expressed by :

$$\boldsymbol{J}_s^{pump} = \frac{\hbar}{4\pi}(\Re(g_{\uparrow\downarrow})\overrightarrow{m} \times \frac{\partial \overrightarrow{m}}{\partial m} - \Im(g_{\uparrow\downarrow})\overrightarrow{m}) \tag{3.18}$$

Thus the first term in the equation 3.18 , corresponds to an additional torque which can be added into the LLG equation , by considering $\overrightarrow{m} = \overrightarrow{M}/M_s$:

$$\frac{\partial \overrightarrow{m}}{\partial t} = -\gamma \overrightarrow{m} \times \overrightarrow{H_{eff}} + \alpha \overrightarrow{m} \times \frac{\partial \overrightarrow{m}}{\partial t} + \frac{g\mu_B}{4\pi M_s t_{FM}} \Re(g_{\uparrow\downarrow}) \overrightarrow{m} \times \frac{\partial \overrightarrow{m}}{\partial m} \tag{3.19}$$

where t_{FM} is the thickness of the FM layer. The spin pumping term can be seen as an additional damping mechanism , which can be added to the intrinsic Gilbert damping coefficient of the FM layer, leading to an effective damping parameter α_{eff}, expressed as :

$$\alpha_{eff} = \alpha + \Delta\alpha \tag{3.20}$$

where,

$$\Delta\alpha = \frac{g\mu_B}{4\pi M_s t_{FM}} \Re(g_{\uparrow\downarrow}) \tag{3.21}$$

Hence, one can estimate the $\Re(g_{\uparrow\downarrow})$, from the slope of the linewidth $\Delta\omega$ versus ω plot, which will be

[8] For more details regarding the nonlocal magnetization dynamics in ferromagnetic heterostructures we refer the reader to the review of Tserkovnyak et al.[150]

[9] Which corresponds to a complex quantity, that quantifies the spin transparency at the interface between the ferromagnet and non magnetic metal[2].

calculated in Chapter 5 for a Permalloy layer .

In reality equation 3.18 is incomplete, for example when a non equilibrium spin accumulation $\boldsymbol{\mu}_{spin}$ builds up in the normal metal due to a spin relaxation rate smaller than the spin injection rate, inducing a "back flow " of spin current density $\boldsymbol{J}_s^{back}$, that opposes the total spin current density $\boldsymbol{J}_{tot} = \boldsymbol{J}_s^{pump} + \boldsymbol{J}_s^{back}$ (see Figure 3.7 a). Thus, reducing the spin mixing conductance at the interface $g_{\uparrow\downarrow}$ and the damping coefficient of the ferromagnet α. Interestingly, the parallel component of $\boldsymbol{J}_s^{back}$ to $\overrightarrow{m}$ is cancelled by the incoming flow from the ferromagnet when the FMR frequency ω, and the spin-flip rate τ_{sf}^{-1} is much smaller than the spin injection rate τ_i^{-1}, so that only the perpendicular component to $\overrightarrow{m}$ survives, and is given by :

$$J_s^{back} = -\frac{\Re(g_{\uparrow\downarrow})}{4\pi}\overrightarrow{m} \times \boldsymbol{\mu}_{spin} \times \overrightarrow{m} \tag{3.22}$$

Lastly, we can estimate the static component of the spin current density by averaging the z component of equation 3.18 over one precession period, such calculation has been performed by Yoshino et al[170], which gives:

$$\begin{aligned} J_s &= \omega\frac{\hbar}{4\pi}(\Re(g_{\uparrow\downarrow}) < \overrightarrow{m} \times \frac{\partial\overrightarrow{m}}{\partial m} >_z \\ &= \frac{\hbar}{4\pi}\Re(g_{\uparrow\downarrow})\Omega \end{aligned} \tag{3.23}$$

where Ω is the solid angle of the magnetization precession $\Omega = S/M_s^2$, S is the area defined by the magnetization precession which can be derived as $S = \pi\,|M_x|\,|M_y|$, where M_x & M_y are the minor and major radiuses of the magnetization trajectory (see Figure 3.7 b). Aditionally, Ando et al extracted a more general expression for the spin current density in the coherent precession regime under the assumption of small precession angle in order to linearize the LLG equation[196] , this leads to the following expression :

$$J_s = \frac{\Re(g_{\uparrow\downarrow})\gamma^2\hbar h_{rf}^2}{8\pi\alpha^2}[\frac{\mu_0 M_s sin(\theta)^2 + \sqrt{(\mu_0 M_s sin(\theta)^2)^2 + 4\omega^2}}{(\mu_0 M_s sin(\theta)^2)^2 + 4\omega^2}](\frac{2e}{\hbar}) \tag{3.24}$$

we observe that $J_s \propto h_{rf}^2$, thus the injected spin current density is proportional to the absorbed microwave power.

Thanks to the equation 3.24, one can now estimate the spin current density flowing towards the interface of 2DES/ NM. Thus, a charge current will be created, thanks to IEE/ISHE, and in order to quantify the effectiveness of this spin-to-charge conversion signal we will need to evaluate, in the next subsection, the spin-to-charge conversion efficiency, for both the IEE/ISHE signals.

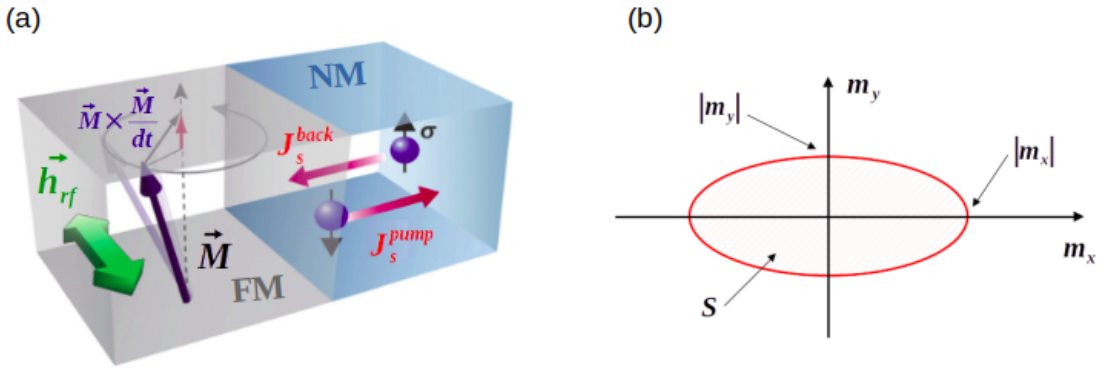

Figure 3.7: Principle behind a spin-pumping experiment.(a) Schematic illustrating the spin-pumping experiment, where we observe that the damping term of the magnetization motion will correspond to the emission of a pure spin current J_s^{pump} to the nearby NM layer, and due to the spin diffusion and spin-flip in the NM layer a net spin accumulation occurs in the NM accompanied with a backflow of pure spin current J_s^{back}.(b) The magnetization-precession trajectory when $\overrightarrow{H_{eff}}$ is in the sample plane.[129, 196]

3.2.1.2.2 Spin-to-charge conversion efficiency If one combines the knowledge of the spin current density created at the ferromagnetic resonance with the theory of spin diffusion where a spin-dependent scattering in NM/2DES, takes place due to a strong spin orbit coupling, or interfacial electric field, leading to a spin-momentum locking. As presented previously, at the ferromagnetic resonance (see Figure 3.5), the magnetization precesses around its effective field $\overrightarrow{H_{eff}}$, generating a spin accumulation at the interface with 2DES/NM. The generated spin current density will then be converted into a charge current thanks to ISHE/IEE effect. This charge current $\overrightarrow{J_c^{2D}}$ is perpendicular to both $\overrightarrow{\sigma}$ and $\overrightarrow{J_s^{3D}}$, and is measured through the 2 ohmic contacts at the ends of the film in an open circuit condition (see Figure 3.8 a). So the IEE/ISHE charge current will correspond to the measurement of a voltage V_{IEE}/V_{ISHE}, which can be linked to the charge current I_c by Ohm's law, $I_c = \frac{V_{IEE/ISHE}}{R_{sample}}$. It is also important to note that I_c needs to be normalized with respect to the microwave power, in order to compare between signals corresponding to various FMR absorption spectra. Indeed, we have seen that the injected spin current density is proportional to the rf power P_{rf} which in turn is also proportional to $\propto h_{rf}^2$, where h_{rf} is the microwave field generated by our antenna, given by:

$$h_{rf} = \frac{\mu_0}{w}\sqrt{\frac{P_{rf}}{2Z}} \tag{3.25}$$

where $Z = 50\Omega$ is the antenna's impedance, $w = 1cm$ is the width of the antenna, leading to $h_{rf} = 0.8$ mT for an input power $P_{rf} = 20dBm$. Thus one needs to normalize I_c with respect to h_{rf}^2 as shown in Figure 3.8 b, we observe I_c/h_{rf}^2 has a Lorentizan shape which is expected because the injected spin current will follow the shape of the FMR signal.

In order to calculate the spin-to-charge conversion efficiency, we need to distinguish between the IEE and ISHE, where in the former the conversion efficiency is evaluated by the inverse Eldestein characteristic length λ_{IEE}, while the latter is related to the spin Hall angle and the spin diffusion length.

First, one can compute easily λ_{IEE}, which can be interpreted from equation 1.30 in Chapter 2, as the characteristic length travelled by an electron in a 2DES/NM before spin memory loss. It can have quite high values if the electron relaxation rate is very low, and it is given by :

$$\lambda_{IEE} = \frac{J_c^{2D}}{J_s^{3D}} = \frac{V_{IEE}}{w J_s^{3D} R_{sample}} \tag{3.26}$$

this characteristic length can also be extended to ISHE where it corresponds to the effective length $\lambda_{eff} = \Theta_{SHE}\lambda_{sd}$.[122]

In the case of ISHE, a more complex derivation for V_{ISHE} needs to take into account the spin diffusion in the NM across the interface FM/NM. The calculation has been performed by Castel et al.[28] who have shown a strong dependence of the V_{ISHE} to the NM thickness, magnetization precession and other relevant parameters, and it takes the form :

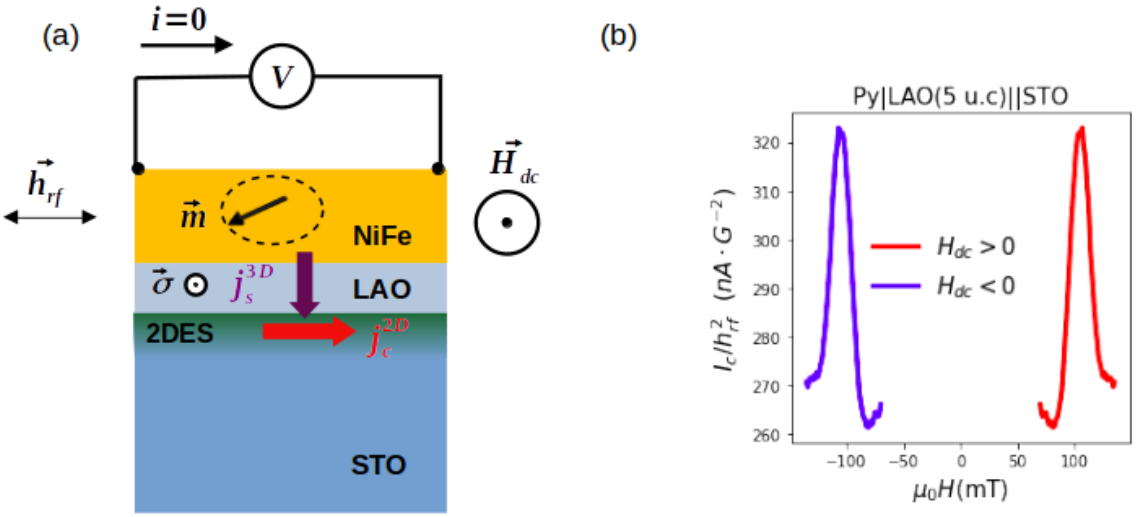

Figure 3.8: Spin-to-charge conversion at LAO(5u.c)|STO interface.(a) Schematic of the spin-pumping experiment, showing the open circuit conditions where a voltage drop is recorded at both ends of the sample. (b) Normalized charge current measured for both a positive (red) and negative (blue) dc magnetic field H_{dc}.

$$V_{ISHE} = \Theta_{SHE}\lambda_{sd} f(t_{NM}, \theta, h_{rf}, w, , \lambda_{sd}, \sigma, g_{\uparrow\downarrow}) \tag{3.27}$$

where ϵ is the ellipticity correction factor, θ is the angle of precession, σ is the conductance of the NM , and f is a function which depends on various parameters related to the FM properties and the magnetization

dynamics, a more detailed expression of V_{ISHE} is given in Appendix A .

It is interesting to note, that this evaluation of the spin-to-charge conversion efficiency is incomplete, because we assume that the measured dc voltage drop is purely due to spin-to-charge conversion, which is not quite the case because of various spurious effects which can add to the dc voltage at resonance. In the next section, we will give a brief introduction to one of these effects, which is the spin rectification effect.

3.2.1.2.3 Spin rectification effects In the presence of a non zero microwave excitation $h_{rf} \neq 0$ [10], a conducting ferromagnetic material exhibits a dc voltage drop in the absence of any dc current source. This effect has been explained by Egan and Juretschke[45, 76], and observed in various experiments[45, 37]. Indeed, when shining h_{rf} on the FM layer, it creates an induced rf current $I_{rf} = I_0 sin(\omega t + \beta)$, where β is the angle between the magnetization and rf current lines. This rf current will be coupled through Ohm's law to the resistivity of our FM layer, that varies depending on the magnetization direction through the magnetoresistance effects such as the Anisotropic magnetoresistance effect (AMR) or Hall effects such as the Anomalous (AHE) and Planar Hall effects (PHE). For example , let's take the case of the AMR effect for which one can write the variation of the resistance due to AMR as $\Delta R_{AMR}(t) = \Delta R_{AMR}(0) cos(\omega t)$, following Ohm's law the AMR voltage reads (see Figure 3.9 a) :

$$V_{AMR} =< \Delta R_{AMR}(t) I_{rf} >_t = \frac{\Delta R_{AMR}(0) I_{rf} cos(\beta)}{2} \tag{3.28}$$

The spin rectification effect was measured by Egan et al in the early 60's[45], who reported a dc voltage at resonance in Nickel plates with a particular angular dependence in the in-plane geometry which was ascribed to the magnetoresistance and hall effects (see Figure 3.9 b). More recently, Rojas Sanchez et al have reported a dc voltage in a CoFeB layer which was attributed to the AMR effect[123]. In order to avoid the spin rectification effects which add to the spin-to-charge conversion signal, one should find a way to disentangle those two contributions.

In order to separate both contributions, measurements of the signal in both parallel and antiparallel configurations with respect to H_{dc}, should be performed, in addition to a normalization of the signal with respect to h_{rf}^2. In the case of a dc voltage purely due to spin-to-charge conversion, one expects two lorentzian curves, with the same amplitude and opposite sign, because $j_c \propto \sigma \times j_s$. This is a first step to disentangle both contributions, although this technique has some limitations, based of the fact that the SRE signal can also be antisymmetric with respect to H_{dc}, as demonstrated by various studies.

An additional step needs to be undertaken in order to be certain of the nature of measured signal, so in

[10] h_{rf} is in the GHz range

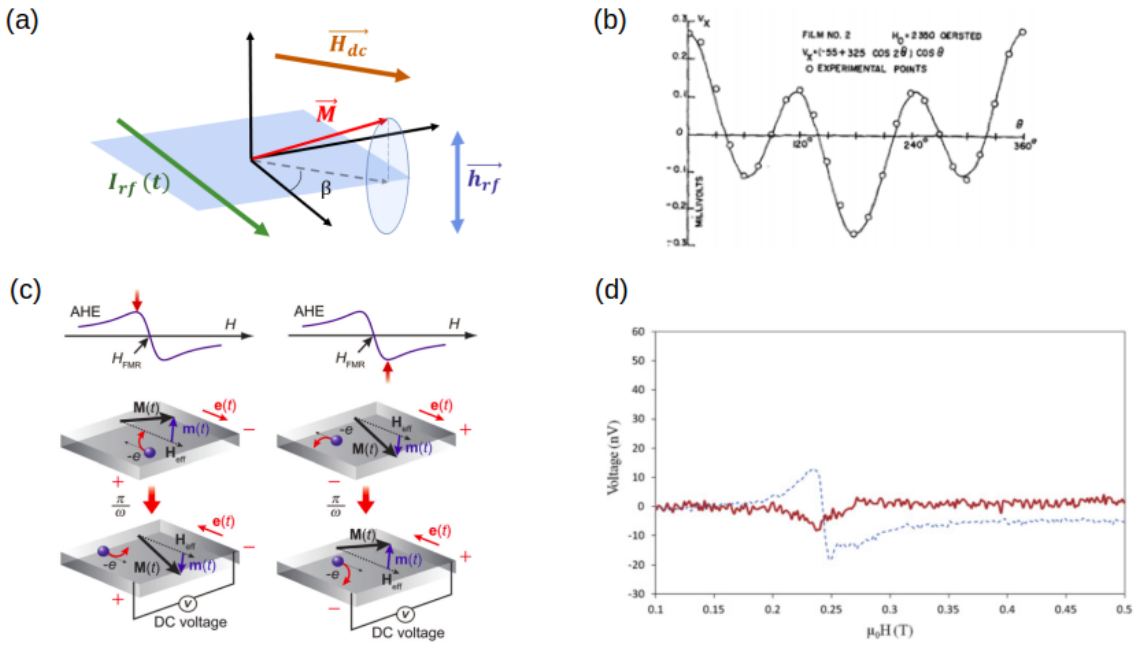

Figure 3.9: Spin rectification effect in FM layer.(a) a sketch illustrating the varying rf induced current I_{rf}, which couples to any change in the resistance at the same frequency to produce a dc voltage.(b) Angular dependence of the dc voltage corresponding to the SRE signal in Nickel plates, the solid line corresponds to the fitting of the data.[45](c) Schematic illustrating the Anomalous Hall effect (AHE) signal for both $H < H_{FMR}$ (left panel) and $H > H_{FMR}$ (right panel).[196] (d) Transverse field dependence of the measured dc voltage for a sample of Au|NiFe at 15 GHz, where the solid curve corresponds to the ISHE signal (odd contribution), while the dashed curve corresponds to the AMR signal (even contribution).[126]

the next step we performed measurements on a reference sample without an adjacent layer of NM/2DES, which when compared to the original sample, which allows us to draw a conclusion on the existence or not of the IEE/ISHE signal in the sample, which is a strong evidence for ISHE/IEE signal.

Another way to separate the two contributions, was proposed by Ando et al.[196] which relies on a symmetry argument which states that the IEE/ISHE signal should be purely symmetric because it should be maximum at maximum FMR absorption intensity, on the other hand the spin rectification signal should be antisymmetric due to a phase shift of $\pi/2$ at the resonance (see Figure 3.9 c). Even though, this argument seems to be true for a perfect resonator (without loses), in the case of non zero losses in our rf antenna, which is our case, the AMR signal is no longer antisymmetric, due an arbitrary phase shift at resonance ($\neq \pi/2$), as demonstrated by Rojas Sanchez et al who ascribed both a symmetric and antisymmetric components to the AMR signal in a CoFeB layer. To further separate the two contributions, Costache et al. and Azevedo et al.[38, 5] proposed to perform an out of plane angular dependence of the dc voltage with respect to H_{dc}, which can be very efficient to separate those two contributions. It is also interesting to mention, that we can separate the two contributions using a different geometry where we apply an out of plane rf field h_{rf}, while keeping the dc field in plane. As discussed previously, the spin-to-charge conversion signal should be

antisymmetric with respect to H_{dc}, while the AMR contributions in this particular geometry should have only a symmetric contribution. This symmetry argument was proposed by Rousseau et al.[126], who have shown that an out of plane h_{rf} leaves the precession angle of the magnetization $\theta(t)$ unchanged upon a reversal of H_{dc}, leading to a symmetric contribution to the AMR signal, this argument allows for a perfect separation of the spin-to-charge signal versus the spin rectification effects, as illustrated in Figure 3.9 d.

Unfortunately for us, we can neither perform an out of plane angular dependence of our signal nor apply an out of plane rf field h_{rf} due to the geometry of the cryostat and the rf antenna which is not designed to apply out of plane h_{rf}.

3.2.1.3 Experimental setup

As discussed previously Ferromagnetic resonance can be used to characterize the magnetic response of the FM layer, but it is also a very interesting tool to perform spin pumping experiments, in order to study for example the spin-to-charge conversion signal in a variety of different materials. In this subsection, we will introduce the experimental apparatus of a broadband FMR set up, which was used in order to characterize the samples in both the field and frequency domains, where the resonance condition was attained either by a magnetic field sweep or an rf frequency sweep. In the following, measurements using both of these approaches will be presented and compared.

3.2.1.3.1 Frequency and Field dependent FMR A broardband FMR set up is used to characterize the ferromagnetic resonance at various rf frequencies. In general, it is used with a micro-stripline, which contains a main metallic strip, and a ground plane composed of an electrode which is connected to the ground, and separated by a dielectric material as shown in Figure 3.10 . The various parameters of a micro-stripline have to be tuned in order to adapt the impedance of the micro-stripline to the frequency of the rf signal we want to convey, so as to minimize the impedance mismatch between the antenna and the coax cables. The rf signal is sent from an rf power generator through a coax cable, which transfers the signal to the micro-stripline through the top conductor. This generates an electromagnetic wave giving rise to an rf magnetic field $\overrightarrow{h_{rf}}$, which is perpendicular to the rf current lines, and to the rf electric field $\overrightarrow{e_{rf}}$, as shown in Figure 3.10.

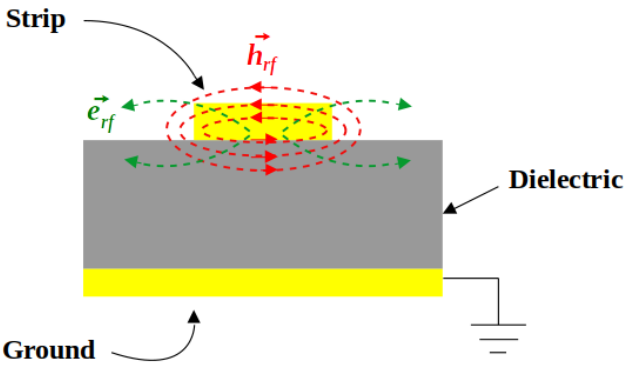

Figure 3.10: A sketch representing the geometry of the microstripline where we plot the generated rf magnetic and electric fields when a microwave current is sent through the stripline.

Thus, by placing the sample close to the micro-stripline while applying $\overrightarrow{H_{dc}}$, through the electromagnets one can perform FMR measurements. To measure the FMR signal, we use a lock-in technique which is highly sensitive to the variations of our signal, giving us a high signal-to-noise ratio. In Figure 3.11 , we plot a sketch of the lock-in amplifier based FMR set up. The rf signal is sent through a circulator which is then transferred to the micro-stripline, where it is reflected back to the circulator which conveys the signal to a photodiode where it is converted into a voltage [11]. This voltage is then measured by a lock-in amplifier, which demodulate the signal at the same reference frequency of the modulation coils used to modulate $\overrightarrow{H_{dc}}$. At resonance, the sample absorbs the rf power leading to a variation in the reflected signal which is measured by the lock-in amplifier.

Therefore, the measured signal will be proportional to the derivative of the absorbed microwave power, giving it the form of a derivative of a lorentzian curve as shown in Figure 3.12 , where we measure the FMR signal of NiFe sample at various microwave frequencies. This technique allows us to extract the main magnetic properties of the FM layer using equations 3.16 & 3.17. For more details regarding the extraction of the various magnetic propeties for a NiFe layer such as $g-factor$, M_s, $\mu_0\ \Delta H$, α, we refer the reader to Chapter 5 . Even though the micro-stripline antenna's geometry seems to be one of the best options for broadband FMR, one should recall that the main strip lateral size in our case does not exceed $2mm$, leading to an inhomogeneous h_{rf} shined on our sample, whose dimensions are much greater $5 \times 5\ mm^2$. The voltage signal in a spin pumping experiment being proportional to the lateral dimension of the pumping, it is thus more appropriate to maximize the area on which the RF field is applied. Therefore, we have designed a U-shaped rf antenna, that produces an homogeneous h_{rf} over the entire sample surface.

In order to carry out FMR-driven spin pumping experiments, the sample is glued to an alumina substrate [12],

[11] The measured voltage is proportional to the reflected power $V \propto P_{refl}$

[12] In order to transfer the heat to the sample from the cryostat

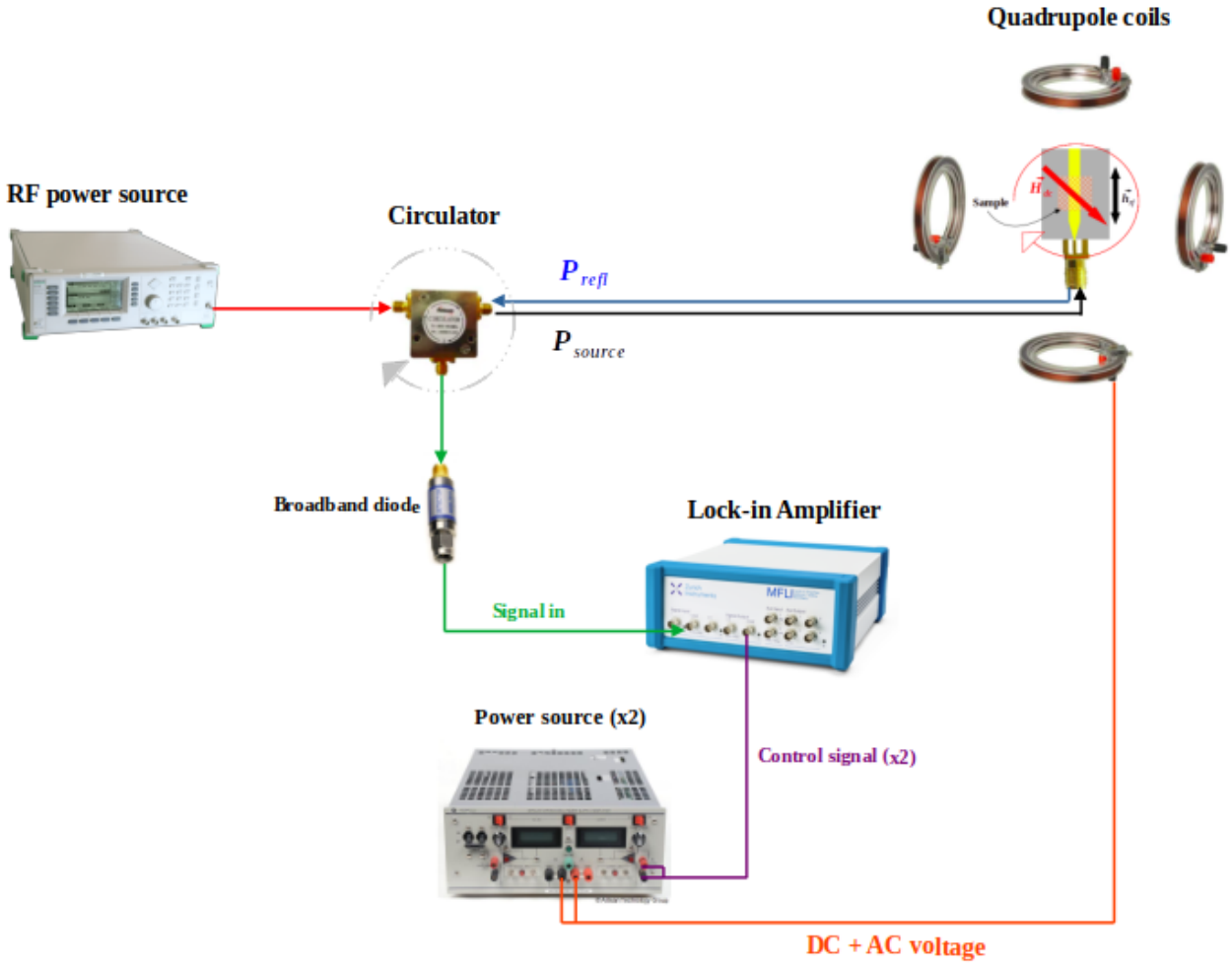

Figure 3.11: A schematic illustrating the main elements used for a Lock-in broadband FMR set up, where the magnetic field is rotated using 4 coils in the quadrupole geometry.

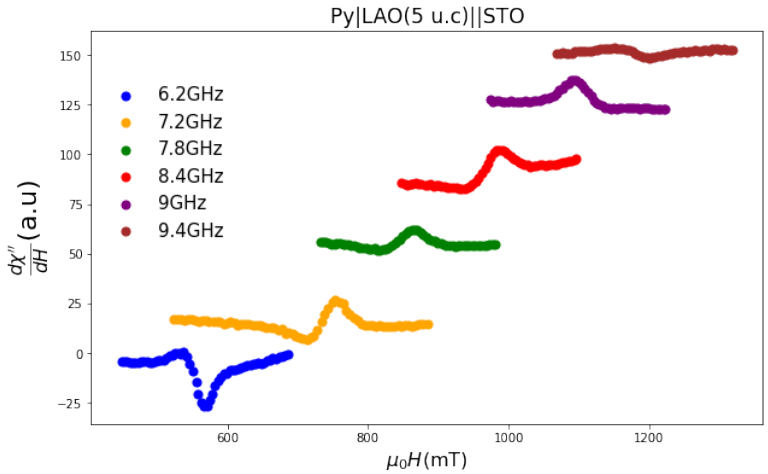

Figure 3.12: The FMR signal of a sample of NiFe|LAO(5u.c)||STO for various rf frequencies at room temperature.

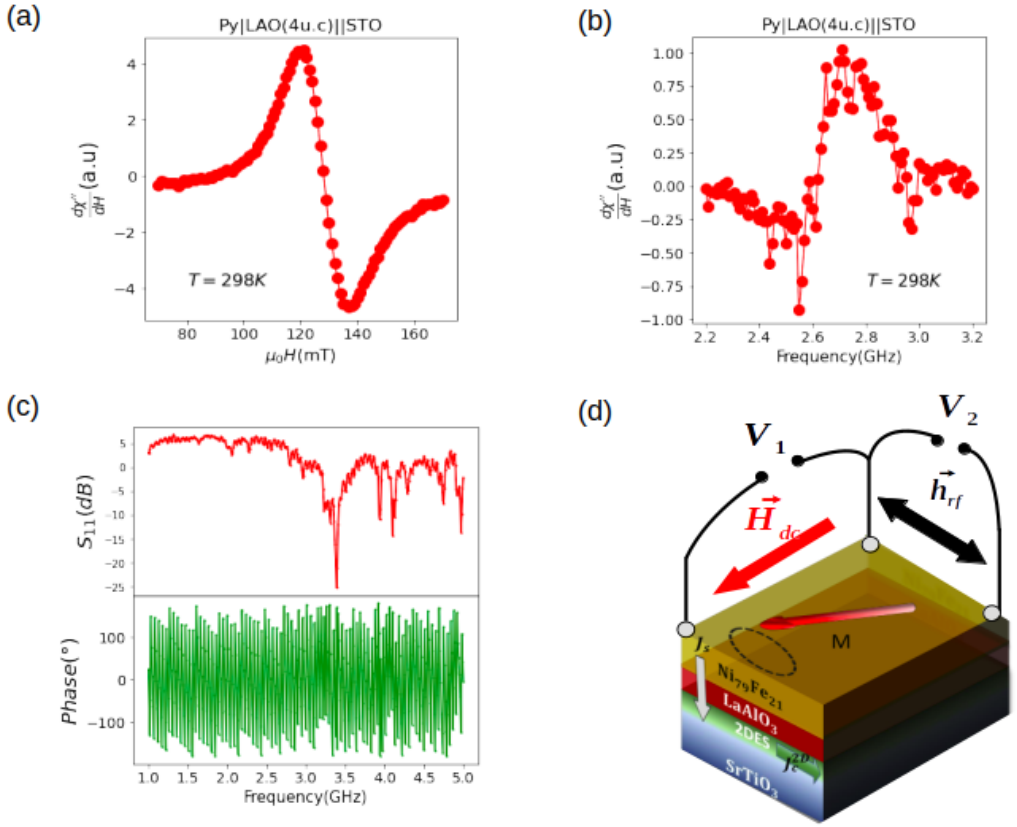

Figure 3.13: Comparison between frequency and field swept FMR signals.(a) The variation of the imaginary part of the susceptibility factor versus the dc magnetic field at room temperature and fixed frequency 3 GHz, (b) same but while changing the frequency and at fixed magnetic field $\mu_0 H_{dc} = 170G$.(c) The response function of the microwave line in reflection geometry, where the top panel represents the gain S_{11} and the bottom panel we plot the phase, while changing the frequency of the microwave excitation. (d) A sketch illustrating the 3 contacts measurement, where the signal is measured in open circuit conditions along two perpendicular directions V_1 & V_2.

through a thin layer of silver paste which plays the role of the backgate. Then, the sample is connected to three copper wires bonded to the top of the sample using silver paste, probing the voltages along two perpendicular directions, thus allowing for a complete reconstruction of the angular dependence of the IEE/ISHE signal. The sample is then placed inside the U-shaped rf antenna which is then connected to the cryostat, through a thin layer of Teflon and GE varnish, in order to transfer the heat flow to the sample, while keeping the antenna electrically isolated from the cryostat. As visible in equation 3.14 , one can meet the resonance conditions either by fixing the rf frequency ω, and sweeping H_{dc}, or inversely by fixing H_{dc} and sweeping the frequency. We have performed both measurements on a FM layer of NiFe.

In Figure 3.13 a & b , we plot the FMR signal obtained by both an H_{dc} and an rf frequency sweeps, so one should expect to see a signal of similar form, corresponding to the derivative of a lorentizian, with some differences related to the linewidth which are addressed in Appendix B. However, we observe that the FMR signal versus ω is more noisy, and exhibits many artifacts appearing in the baseline of the FMR curve (see

Figure 3.13 b), compared to the same FMR signal versus H_{dc}. To understand, this difference on needs to study the spectrum of the reflected power coefficient S_{11} using a Vector Network Analyser (VNA), shown in Figure 3.13 c, exhibiting a very complex landscape which is due to the various spurious absorptions and reflections along the whole rf line. In other to avoid this complexity, we have been constrained to sweep the magnetic field in the plane of the sample, which was achieved by designing an electromagnet with four coils arranged to resemble a quadrupole coils scheme, which allowing us to study the FMR signal by sweeping H_{dc}, but also to rotate H_{dc} in the plane of the sample in order to study the angular dependence of IEE/ISHE signal.

On the other hand, the dc voltage was measured along both directions (see Figure 3.13 d) in an open circuit conditions, through a lock-in amplifier. The signal is further disentangled from the spin rectification as explained in the previous subsection.

In order to avoid the spurious effects due to spin rectification, one can perform a spin injection experiment using another technique, which relies on a temperature gradient-driven spin current, called the Spin Seebeck Effect (SSE). This technique presents several advantages compared to the spin pumping experiment, where we avoid all the unwanted effects related to magnetization dynamics in the FM layer such as the ac spin currents or the spin rectification effects.

3.2.2 Thermal spin injection

In the 19th century, Thomas Seebeck have reported that thermal gradients can generate an electromotive force across two points of an electrically conducting material, an effect now known as the "Seebeck Effect"[159]. More recently, Johnson and Silsbee have theorized the possibility to include the spin transport into the interfacial thermoelectric effects, thus proposing a spin analog to the Seebeck Effect known as the spin-dependent Seebeck effect[73]. In 2008, Uchida et al have reported the possibility to inject a spin population from a NiFe layer into a Pt layer using a temperature gradient, where they measured a charge voltage at the ends of Pt wire deposited on top of the NiFe layer in a non local geometry[152]. This evidences a non zero electromotive force in Pt wires at length scales of several millimeters, far exceeding the spin-flip diffusion length of conduction electrons, signaling that conduction electrons in the FM are irrelevant to this phenomenon. Subsequently, the spin Seebeck effect has also been reported in various ferromagnetic insulators such as $Y_3Fe_2O_{12}$ (YIG)[70, 1] or $LaY_2Fe_5O_{12}$[155], suggesting that a non conventional spin transport is driving the spin Seebeck effect. Until now, several research groups have suggested that the spin Seebeck effect is driven by localized spins through an interplay of non equilibrium magnons and phonons in the FM with conduction electrons in the NM[1, 60, 17]. For more details regarding the theoretical

description of the spin Seebeck effect we refer the reader to the work of Hoffman et al.[60]

In the following we will give a brief theoretical description of the spin Seebeck Effect in the longitudinal geometry for a conducting FM using a spin drift model. Later, we will present in more detail the two different ways to realize thermal spin injection, using both local and a non-local geometries.

3.2.2.1 The Origin of the Spin Seebeck Effect

In a spin Seebeck experiment a temperature gradient is applied to a FM layer, thus generating a non zero spin voltage, which can be attributed to the spatial variation of the spin-dependent chemical potentials[152]. To further clarify the link between the temperature gradient and the spin degree of freedom, we will consider FM/NM bilayers subjected to a temperature gradient applied in a direction normal to the FM/NM interface, while applying a $\overrightarrow{H_{dc}}$ in the plane of the sample, as illustrated in Figure 3.14

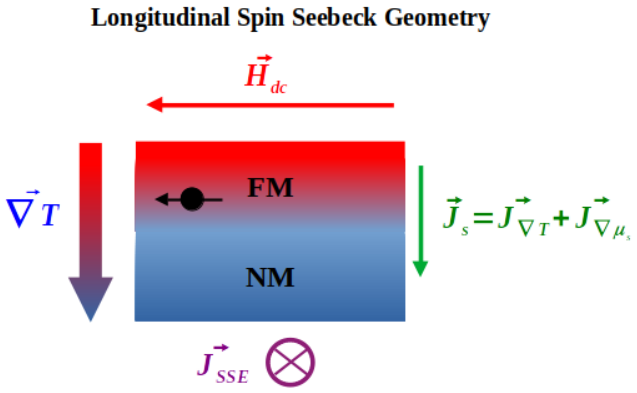

Figure 3.14: A schematic illustrating the Longitudinal spin Seebeck geometry, where the temperature gradient ∇T is parallel to the injected spin current $\overrightarrow{J_s}$, and results from the sum of two separate contributions.

Here, we will consider a metallic FM, such as NiFe, where the spin current can be carried either by conduction electrons but also by magnons. It is also important to recall that the magnon lifetime in NiFe is two order of magnitude smaller than that in FM insulators such as YIG, thus in the following only the electronic contribution to the thermoelectric transport will be considered. Using the Boltzman transport equation, Holanda et al.[61] were able to extract the expression of the electronic distribution $f^{\sigma}(\overrightarrow{k}, \overrightarrow{r})$ in the presence of an electric field $\overrightarrow{E}$, temperature gradient ∇T and random scattering, which reads [13] :

$$f^{\sigma}(\overrightarrow{k}, \overrightarrow{r}) \approx f_0(\epsilon_k) - \tau^{\sigma}(\frac{\partial f_0}{\partial T})\overrightarrow{v}_k \cdot \nabla_r T + \frac{\hbar e \tau^{\sigma}}{m}(\frac{\partial f_0}{\partial \epsilon_k})\overrightarrow{k} \cdot \overrightarrow{E}^{\sigma} - \mu^{\sigma}(\overrightarrow{r})(\frac{\partial f_0}{\partial \epsilon_k})_{\epsilon_F)} \tag{3.29}$$

where τ^{σ} is the transport relaxation time, $\overrightarrow{E}^{\sigma} = \overrightarrow{E} +_r \mu^{\sigma}(\overrightarrow{r})/e$ is the spin-dependent effective electric field, and $\overrightarrow{v}_k = (1/\hbar)\nabla_k \epsilon_k$ is the electron velocity.

[13] Here σ represents the spin degree of freedom like in equation 1.3

From this electronic distribution, we are able to compute various quantities, such as the spin current density which is given by the sum of two quantities :

$$\overrightarrow{J}_s = \overrightarrow{J}_{\nabla T} + \overrightarrow{J}_{\nabla \mu_s} \tag{3.30}$$

where $\overrightarrow{J}_{\nabla T}$ represents the contribution emerging from the thermally induced drift of electrons due the temperature-dependent spin splitting, while $\overrightarrow{J}_{\nabla \mu_s}$ corresponds to the spatial variation of the spin accumulation.

Upon considering the right boundary conditions, we can retrieve the expression of the injected spin current density at the FM/NM interface, which is given by :

$$J_s = -\frac{g_{eff}^{\uparrow\downarrow}\lambda_{sf}}{3\pi n_e}(-\frac{\partial\Delta}{\partial T})\beta\frac{cosh(\beta)-1}{sinh(\beta)}\partial_z T N(\epsilon_F)\epsilon_F \tag{3.31}$$

where $\beta = t_{FM}/\lambda_{sf}$ is the ratio of FM thickness t_{FM} and spin-flip diffusion length λ_{sf}, Δ is the temperature-dependent exchange splitting.

Indeed, this spin current density once injected in NM will be converted into a charge current thanks to the ISHE/IEE, the measured charge current I_{SSE} is linked to the temperature gradient $\partial_z T$ through the Seebeck coefficient $S_{SEE} \propto I_{SSE}/\partial_z T$, which is given by :

$$S_{SEE} = \frac{2g_{eff}^{\uparrow\downarrow}\lambda_{sf} w \lambda_N e \Theta_{SH}}{3\pi n_e \hbar} tanh(t_N/2\lambda_N)(-\frac{\partial\Delta}{\partial T})N(\epsilon_F)\epsilon_F \tag{3.32}$$

where λ_N is the spin diffusion length inside the NM, w is the width of the sample and t_{NM} is the thickness of the NM layer. For more detail regarding those calculations, we refer the reader to the paper of Hollanda et al.[61]

To sum up, we have computed the spin current density and the spin Seebeck coefficient in a longitudinal geometry in a metallic FM. So in the next section, we will present the two different ways to perform a thermal spin injection, using either the longitudinal spin Seebeck effect (LSSE) or the transverse spin Seebeck effect (TSSE).

3.2.2.1.1 Longitudinal Spin Seebeck Effect (LSEE) In the longitudinal geometry of the spin Seebeck effect, the thermal spin injection is parallel to the temperature gradient as illustrated in Figure 3.14. As a matter of fact this configuration is best suited for ferromagnetic insulators (FMI) that do not generate the parasitic anomalous Nernst effect[99], which can produce a non negligible contribution to the signal in this

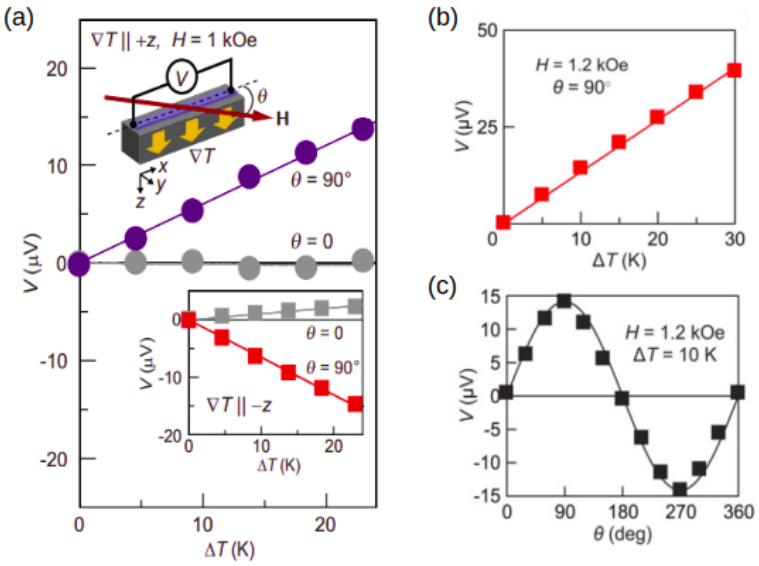

Figure 3.15: The longitudinal spin Seebeck effect in a YIG|Pt sample.(a) DC voltage drop at both ends of the sample while changing the temperature difference between the top and bottom and for two $\overrightarrow{H_{dc}}$ angles (0° & 90°). The inset : same as the main figure whereas the temperature gradient is applied in the opposite direction. (b) DC voltage drop while changing the temperature difference at both ends of the sample of YIG|Pt, and for $\overrightarrow{H_{dc}}$ at 90° angle. (c) Angular dependence of the dc voltage drop at both ends of the sample, for a fixed temperature difference $\Delta T = 10K$.[154]

configuration.

Some research groups, have successfully observed a longitudinal spin Seebeck signal in metallic ferromagnets such as NiFe or CoFeB, or in half-metals such as LSMO[61, 52, 166]. The first observation of LSSE was realized in 2010 by Uchida et al, who measured a voltage at both ends of a Pt strip that has been evaporated on the top of a YIG layer[154]. By heating the sample using a Peltier module, a temperature gradient $\nabla_z T$ was established inside the FMI, leading to a magnon heat flux due to phonon drag or magnon conductivity, thus generating a spin current density in the FMI. The measured voltage has been reported to change sign upon reversing the direction of the temperature gradient as illustrated in Figure 3.15. It appears also to be linear with respect to the temperature difference ΔT, and it evolves with respect to the applied magnetic field H_{dc} as $\propto sin(H_{dc})$, hence with the symmetry of ISHE induced by LSSE, which agrees with 1.20

The LSEE, can be understood quantitatively in a FMI layer through a linear-response approach which was developed by Adachi et al[1]. Here we can explain qualitatively the thermal spin injection mechanism in FMI, using a phenomenological approach linking the LSSE to an imbalance between thermal noise of the in FMI and the thermal noise of conduction electrons in the NM. This thermal noise imbalance induces a non compensation of two opposite effects. The first one is a spin injection in the NM due to the magnonic thermal noise, while the second effect, expels the spins from the NM, due to the conduction electron thermal noise. Therefore, this thermal noise imbalance, will lead to an effective spin injection/ejection into/from

the NM.

Finally, the LSEE was chosen in our case to perform thermal spin injection in LAO/STO because it is the simplest configuration in which a bulk ferromagnet can be used, and it relies on a local spin injection similar to the spin pumping configuration presented in section 4.2.1 . In the next subsection, we will introduce another interesting method to do thermal spin injection, which relies on Transverse Spin Seebeck Effect (TSSE).

3.2.2.1.2 Transverse Spin Seebeck Effect (TSEE) The transverse Spin Seebeck effect (TSEE), was first reported in 2008 by Uchida et al.[152] in a sample of NiFe/Pt, which like the LSEE, is driven by a thermal gradient applied to a spin-polarized material (such as a FM), thus pushing the spins out of equilibrium. When depositing a Pt wire in contact with the NiFe layer a net spin current will diffuse to the Pt acting as a spin sink, as illustrated in Figure 3.16 a . In this case, the generated spin current (along the z-direction) is perpendicular to the direction of the applied temperature gradient (along the x-direction). Surprisingly, Uchida et al have reported a considerable variation in the spin current density $j_s^z(x)$ as a function of x, leading to opposite signs of $j_s^z(x)$ at both ends of the FM layer, between the hot region ($j_s^z(0) > 0$) and the cold region ($j_s^z(L) < 0$), and a zero contribution in the middle of the FM layer $j_s^z(L/2) = 0$ (see Figure 3.16 b)[152]. The scale of this variation, which corresponds to the length of the sample $L = 1cm$, is orders of magnitude higher than the spin diffusion length. Shortly after, Jaworski et al.[71] clarified this long-range spin injection mechanism, using a sample of GaMnAs, which was sliced along the y-direction, as illustrated in figure 3.16 c . The x -dependence of the resulting signal was unaffected by the slicing of the FM layer(see Figure 3.16 d), thus highlighting the phonon transport in GaAs, to be behind the x-dependence of the measured signal. This result was later verified by Uchida et al.[153], who showed that the x-dependence disappears when depositing the FM layer on top of an amorphous substrate in which the phonons are more localized. In order to explain theoretically this long-range x-dependence, Tikhonov et al.[147] have proposed an explanation to this non-local behavior, which arises from the fact that the thermal phonons, which store thermal energy, and the subthermal phonons which transfer the energy to the magnons are located in different parts of the spectrum and have different kinetics. Thus, the interacting phonons develop a spectral phonon distribution that deviates from the local equilibrium, leading to longer mean free paths compared to the thermal phonons, and can be sensitive to the boundary conditions.

It is interesting to note that the TSSE corresponds to the spin analog of the non-local electrical spin injection, and similarly to the non-local electrical spin-injection, which eliminates parasitic charge transport effects such as AMR and AHE (see section 4.2.1), the TSSE also eliminates the spurious thermal transport

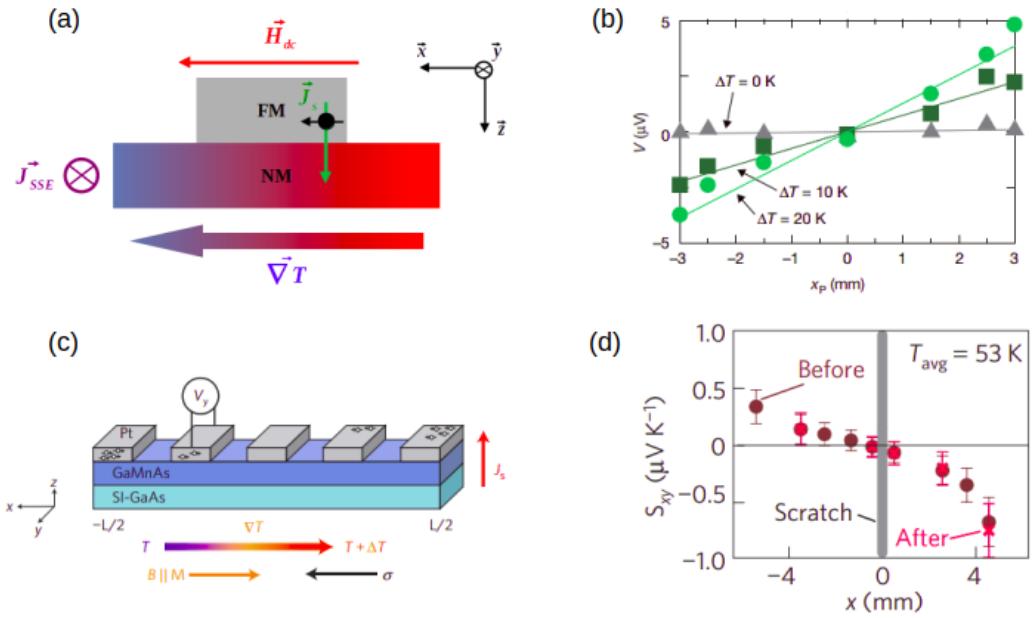

Figure 3.16: The transverse spin Seebeck effect.(a) Schematic illustrating the Transverse Spin Seebeck experiment where the applied temperature gradient ∇T is perpendicular to the direction of the injected pure spin current $\vec{J_s}$.[152](b) The variation of the dc voltage V versus the position of the Pt wires which where placed perpendicular to the x-direction, and were saturated at $H = 100Oe$.[152](c) A sketch representing the measurement geometry of the spin-Seebeck effect in GaMnAs using strip contacts of Pt.[71] (d) The spatial dependence of the spin Seebeck coefficient S_{xy}, before and after the scratch which is represented by the shaded area.[71]

signals such as the Anomalous and planar Nernst effects (ANE and PNE), and intrinsic spin-dependent thermal transport signals. These parasitic effects will be discussed briefly in the next subsection.

3.2.2.2 Spurious effects

Like the spin pumping experiment, the thermal spin injection exhibits various parasitic signals, which emerge from the magneto-thermoelectric effects. As a matter of fact, in magnetic conductors, an anisotropic thermoelectric voltage depending on the angle between the magnetization and the temperature gradient is induced by spin-orbit coupling. Therefore, the thermal counterparts to the magnetoresistance and Hall effects through the Onsager reciprocity, are manifested, leading to what is called the Anomalous Nernst Effect (ANE) and the Planar Nernst Effect (PNE). In the following, these two spurious contributions to the thermal voltage will be introduced.

3.2.2.2.1 Anoumaloues Nernst Effect (ANE) The Anomalous Nernst Effect has been observed in a FM material in both the LSSE and TSSE configurations. Like the spin Seebeck effect, the ANE is related to a temperature gradient, which generates through magneto-thermoelectric coupling an electric field given

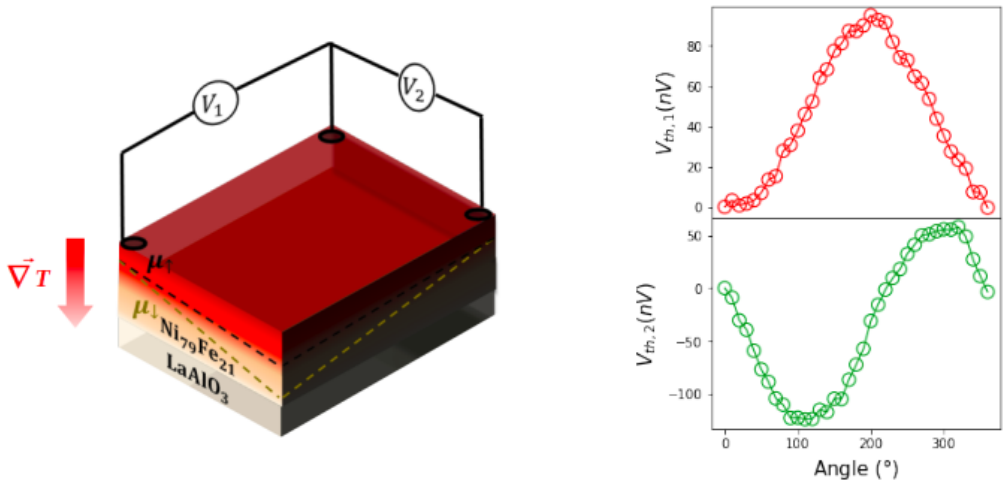

Figure 3.17: Left panel: sketch representing the LSSE experiment on a reference sample of NiFe|LAO, while recording the voltage drop along two perpendicular directions. Right panel : thermal voltage along the two different directions V_1 & V_2, while changing the direction of $\overrightarrow{H_{dc}}$ in the sample plane.

by :

$$\overrightarrow{E_{ANE}} = -\alpha_N \vec{m} \times \overrightarrow{\nabla_\perp T} \tag{3.33}$$

where α_N is the anomalous Nernst coefficient, $\vec{m}$ is the direction of the magnetic polarization of the FM, and $\overrightarrow{\nabla_\perp T}$ the temperature gradient perpendicular to the sample plane. This effect is ubiquitous to SSE experiments, particularly in the LSSE geometry, where the temperature gradient is parallel to the injected spin current. This effect have been reported in various ferromagnetic materials, particularly by Miyasato et al.[100] who showed a crossover behavior with three different regimes in the AMR and ANE signals in various materials like transition metals, oxides and chalcogenides. Hollanda et al.[61] have measured the ANE in NiFe/MgO samples, by which he estimated the exchange bias field due the a NiO(100) crystal. Similarly, Pu et al have reported ANE in (Ga,Mn)As semiconductor[116]. Recent studies by Huang et al and Bosu et al have shown that in the TSSE geometry, a thermal conductivity mismatch between the FM layer and the substrate, generates a parasitic ANE signal[67, 19].

In this regard, we have measured a thermal voltage V_{th} in a sample of NiFe/LAO, as illustrated in Figure 3.17, the signal possess a $\propto sin(\theta)$ angular dependence, where θ is the angle between the direction of H_{dc} and the electrical contacts. We report also $\pi/2$ phase shift which is merely due to the difference between V_1 and V_2, as shown in Figure 3.17 . Consequently, this thermal voltage V_{th} measured in NiFe layer can be well accounted for by the ANE effect, owing to the fact that the temperature gradient was applied perpendicularly to the plane of the sample (xy-plane) (see the experimental set up section for more details),

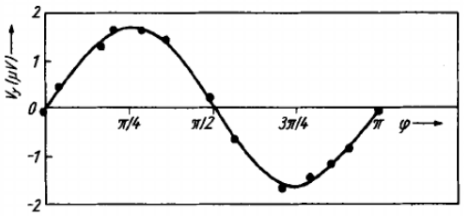

Fig. 1. The planar Nernst voltage in permalloy films as a function of φ (1390 Å, 83%Ni-17%Fe, |∇T| = 15 deg/cm)

Figure 3.18: The angular dependence of the thermal voltage measured at both ends of a NiFe film along the y-direction while applying a perpendicular temperature gradient ∇T along the x-direction in the TSSE geometry.[85]

while rotating θ in the xy-plane. Thus, from equation 3.33 , $\overrightarrow{E_{ANE}}$ will be in the xy-plane at an angle of $\pi/2 - \theta$. Therefore, both V_1 and V_2 have a sinusoidal dependence on θ, with a phase shift of $\pi/2$.

3.2.2.2.2 Planar Nernst Effect (PNE) Unlike the anomalous Nernst effect, the planar Nernst effect (PNE) originates from a planar temperature gradient $\nabla_{\parallel} T$ applied in the xy-plane of the sample. Thus, this parasitic effect is only relevant in the TSSE geometry. Vu Dinh Ky has attributed this effect to the following term from the thermomagnetic equation[85]:

$$\overrightarrow{E_{PNE}} = \alpha_P \overrightarrow{m} \times (\overrightarrow{m} \times \overrightarrow{\nabla_{\parallel} T}) \tag{3.34}$$

where α_P is the planar Nernst coefficient. Therefore, in the case of $\overrightarrow{\nabla_{\parallel} T} = \|\nabla_{\parallel} T\| \hat{x}$, and $\overrightarrow{m} = \|m\|(cos(\theta)\hat{x} + sin(\theta)\hat{y})$, where θ is the angle between $\overrightarrow{m}$ and $\hat{x}$ direction, equation 3.34 gives :

$$\overrightarrow{E_{PNE}} = \alpha_P \|\overrightarrow{m}\|^2 \|\overrightarrow{\nabla_{\parallel} T}\| \begin{bmatrix} -sin(\theta)^2 \\ cos(\theta)sin(\phi) \end{bmatrix} \tag{3.35}$$

The PNE has been reported since the 60's by Vu Dinh Ky[85] in NiFe films, where he reported a $sin(2\theta)$ dependence, as illustrated in Figure 3.18 . Since then, the PNE has been studied extensively in various materials. Bui et al.[22, 23], have reported a PNE signal in half-metallic LSMO, and in Fe-doped III-V semiconductors such as n-type (In,Fe)Sb.

Since we have chosen to measure the thermal voltage using the LSSE configuration the PNE effect is irrelevant in our case. Thus, only the ANE effect will be considered. In the next subsection, we present our thermal spin injection experimental set up, which generates a thermal gradient perpendicular to the sample plane, using an optically-induced heating technique.

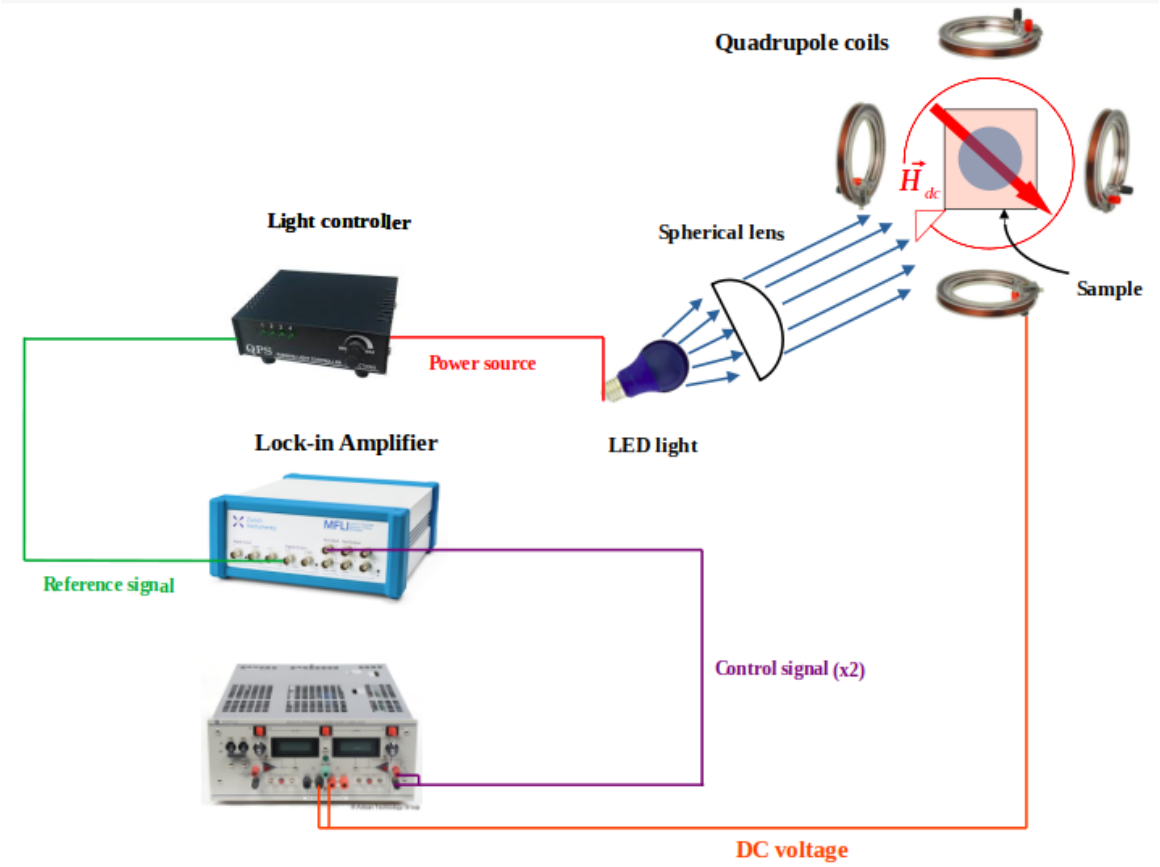

Figure 3.19: Schematic illustrating the main elements used for a LSEE experiment, using a dc light source (blue LED), while rotating the magnetic field using quadruple coils.

3.2.2.3 Experimental setup

An optically generated thermal gradient was achieved using a dc light source, corresponding to a 2 Watts blue light emitting diode ($\lambda \sim 450nm$), which was shined upon a sample of NiFe/LAO/STO (see Figure 3.19), leading to the creation of a pure spin current in an NiFe layer, through the LSSE and ANE effects. As a matter of fact, the spin current flowing through the NiFe layer will generate two charge current contributions, from either the spin-to-charge conversion at the interface of LAO/STO and from the intrinsic contribution of the NiFe layer through the ANE effect. Similarly to the experimental set up seen in section 4.2.1.3, we connected the sample to three electrical contacts though copper wires, as illustrated in Figure 3.20 a.

The sample was cooled down using a He-flow cryotstat, which was connected to a substrate of allumina onto which the sample was glued using a layer of silver paste which plays the role of the backgate. Identically to section 4.2.1.3, a dc magnetic field H_{dc} was rotated in the plane of the sample, in order to obtain a complete angular dependence of the charge signal, which was measured in both directions V_1 & V_2 using a lock-in amplifier locked on the reference frequency used to modulate the intensity of the dc light source. In Figure 3.20 b, we plot the angular dependence of the measured signal in a LAO/STO sample at room

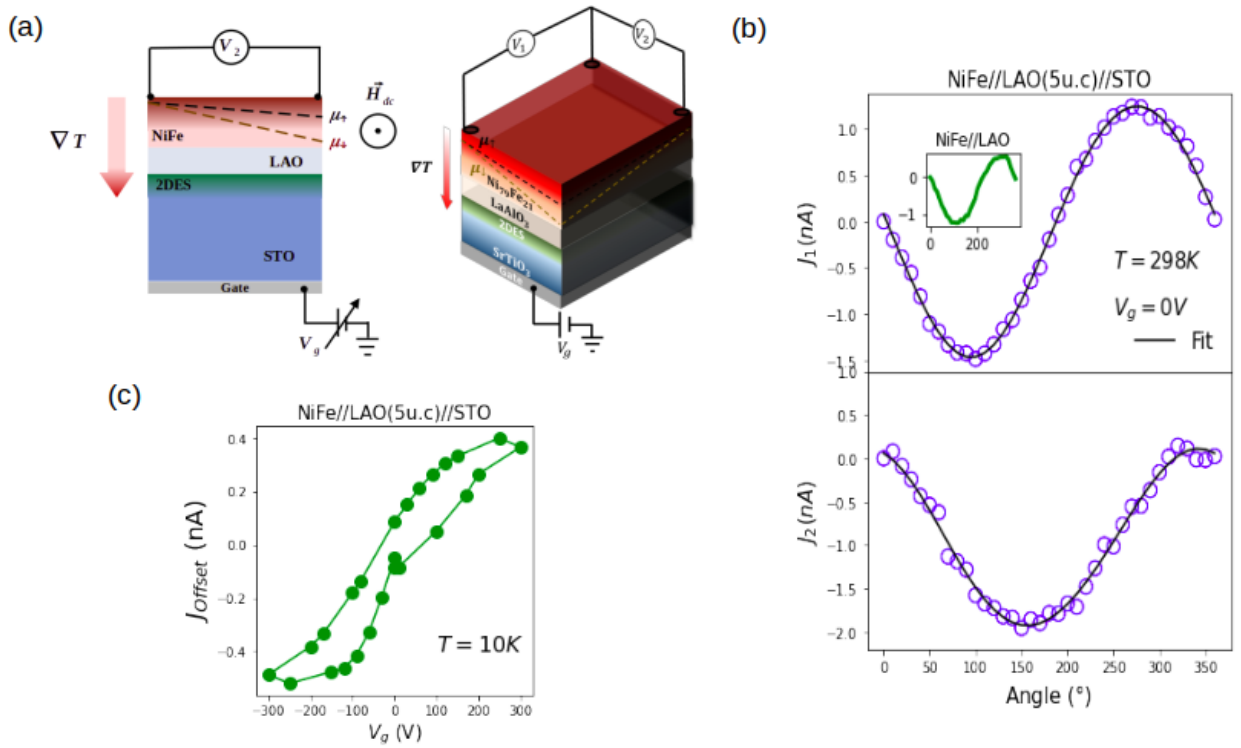

Figure 3.20: (a) Sketch representing the LSSE experiment applied to a sample of NiFe|LAO(5u.c)|STO, while measuring the voltage drop along two perpendicular directions. A backgate volatge is applied to the bottom of the STO layer.(b) we plot the angular dependence of the charge current along both directions (1) & (2), while changing the direction of the magnetic field in the sample plane. Inset: same as the main plot but for the refence sample NiFe|LAO.(c) Hysterisis loop for the offset current versus the backgate voltage at $T = 10K$.

temperature. We observe that the signal is dominated by the ANE effect when comparing to the signal measured in the NiFe/LAO sample, which agrees with previous studies .

Furthermore, due to thermoelectric coupling and a transverse thermal gradient on the contacts, another dc signal is added. So a simple way to reduce this thermoelectric signal is to prevent the ohmic contacts from heating up, by covering them with a flexible polymide film based copper laminate which can withstand high temperature environment up to 400 C°. At low temperature, due to the rise of the dielectric constant in STO (see Chapter 5), photoelectric effects may appear leading to the generation of a dc signal which adds to the spin-to-charge conversion signal, as illustrated in Figure 3.20 c. Typically, a way to reduce these photoelectric effects is to increase the thickness of NiFe layer, which minimizess the light reaching the 2DES and thus the photocurrent signal. Because this also increases the thermal gradient in the NiFe layer, it leads to a higher spin-to-charge signal and ANE.

Chapter4

Anisotropic and tunable spin-to-charge conversion signal at LAO/STO interface states

Contents

In the present chapter, we present the results obtained for the spin-pumping and the spin Seebeck experiments at the LAO/STO interfaces, using electrostatic field-effect modulation while mapping the total angular dependence of our signal for various spin polarizations. The spin-to-charge conversion signal was

measured thanks to the Inverse Rashba Eldenstein Effect, which exhibits a large conversion efficiency at the LAO/STO interface. The strong back gate dependence can be attributed to the complex multi-band effects that appear in particular in transition metal-oxides[81, 172, 203]. It appears that the spin-to-charge conversion signal in LAO/STO can be attributed not only to the spin but also to orbital contributions[203], giving rise to an anisotropic angular dependence resulting from the orbital mixing at the band crossing of t_{2g} orbitals.

4.1 IEE signal at the interface of LAO/STO

4.1.1 Spin pumping measurements

In order to study the Inverse Edelstein effect (IEE) in LAO/STO interfaces, we used a spin pumping technique which relies on ferromagnetic resonance (FMR) experiment at 7K [1], on a sample of AlOx/NiFe/LAO(5u.c)/STO. The NiFe(15nm)/AlOx(3nm) bilayer was deposited by evaporation in a different chamber after the PLD growth of the LAO/STO. The role of the Al capping layer is to protect the NiFe layer from oxidation, so as to avoid any widening of the spectral shape of our ferromagnetic resonance signal. Then the sample was placed in a broad band stripline where the rf magnetic field $\overrightarrow{hrf}$ is (roughly) homogeneous over the whole surface of our samples ($5 \times 5\ mm^2$). At resonance a spin current is expelled, which is then converted into charge, thanks to the Inverse Eldestein Effect (IEE). Here we measure the resulting voltages along two different directions, as shown in Figure 3.13 where we plot a sketch of the geometry used in the spin pumping experiment.

4.1.1.1 Sample characterization

The figure of merit for the spin-to-charge conversion signal in LAO/STO is λ_{IEE} is the ratio between the 3D spin current density j_s^{3D}, and the 2D charge current density j_c^{2D}, which is equal to a length λ_{IEE} called the Inverse Eldestein Effect characteristic length[2] $\lambda_{IEE} = j_c^{2D}/j_s^{3D}$. The charge current density was estimated from dc voltage measurements V_{dc}, of our sample of LAO/STO divided by the stack resistance R_s of the sample and the unit cell parameter w, considering that our electron system is purely two dimensional. The spin current density j_s^{3D}, depends on a variety of different parameters like the spin mixing conductance $g_{\uparrow\downarrow}$, the Gilbert damping coefficient α, and the effective magnetization of our ferromagnetic layer M_s, which can be estimated using equation 3.16. In Figure 4.1 a, we plot the peak-to-peak linewidth ΔH_{pp}

[1] For more detail see Chapter 4 section 4.2.1
[2] For more details see Chapter 1 section 2.5.2.2

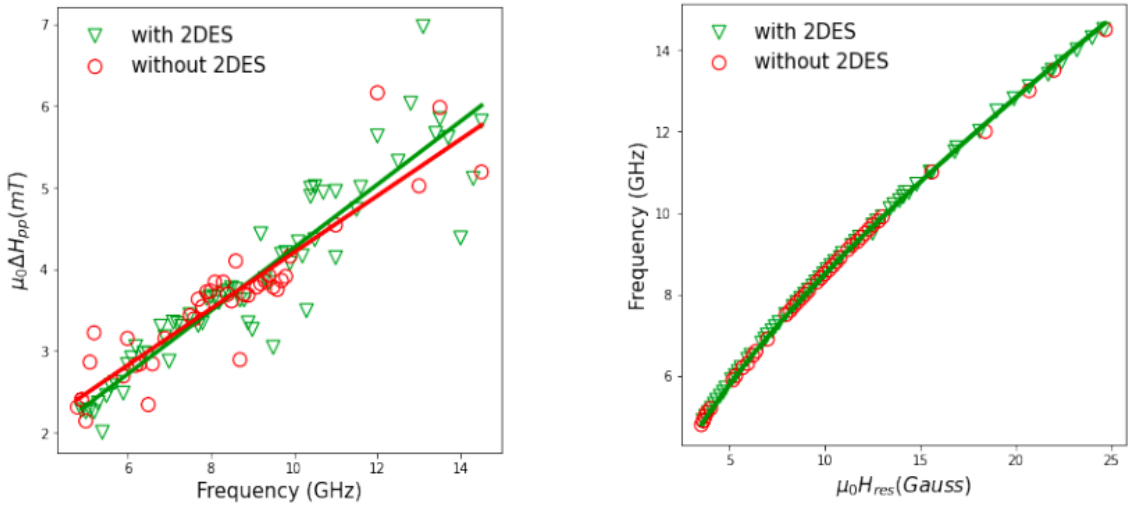

Figure 4.1: On the left: the linewidth of the FMR signal versus the frequency of the rf field. On the right: the resonance frequency versus the magnetic field at the ferromagnetic resonance for both samples of Py|LAO(5u.c)|STO and at room-temperature in the presence and absence of the 2DES at the interface.

with respect to the frequency ω for both a sample of AlOx/NiFe/LAO(5u.c)/STO, where the STO is TiO_2-terminated, and a reference sample where the STO is SrO-terminated [3] , so that we can retrieve the Gilbert damping coefficient for both samples which give roughly the same damping coefficient of both samples at room temperature, $\alpha_{NiFe/2DES} \simeq \alpha_{NiFe} \simeq 6.01 \cdot 10^{-3}$, by using the equation 3.17. In order to retrieve the static magnetization of our sample, we plot in Figure 4.1 b, the resonance field H_r versus the rf frequency ω, and using the Kittel formula (equation 3.16), we can extract the effective magnetization which can be estimated to be equal $M_s \approx 1T$. In addition, by subtracting the Gilbert coefficient for both samples of LAO/STO with and without the 2DES, we can retrieve the value of the spin mixing conductance $g_{\uparrow\downarrow} \simeq 10^{-19}\ m^{-2}$, which actually quantifies the spin transparency of the interface between the NiFe layer and the LAO/STO two dimensional electron system (2DES) at the interface of LAO/STO. Thus, using equation 3.24, we can estimate the spin current density $j_s^{3D} \simeq 1 \cdot 10^5 A \cdot m^{-2}$, which appears to be in the range of previous reported values[34, 200]. From the obtained value of j_s^{3D} and j_c^{2D}, we can compute the Inverse Eldestein characteristic length λ_{IEE}, which quantifies the spin conversion efficiency of our sample of LAO/STO[4]. In Figure 4.2,we show that the ferromagnetic resonance signal $d\chi''/dH$ is linear with respect to the absorbed power. This is consistant with equation 3.13, where χ'' is proportional to h_{rf}^2 which is in turn is proportional to P_{rf}. Similarly, we observe that the measured V_{dc} along both directions (Figure 4.2) are also linear with respect to P_{rf} which is in accordance with equation 3.24 .

[3] So the 2DES is not present at the interface in this case !
[4] For more datails see Chapter 4 section 4.2.1.2.2

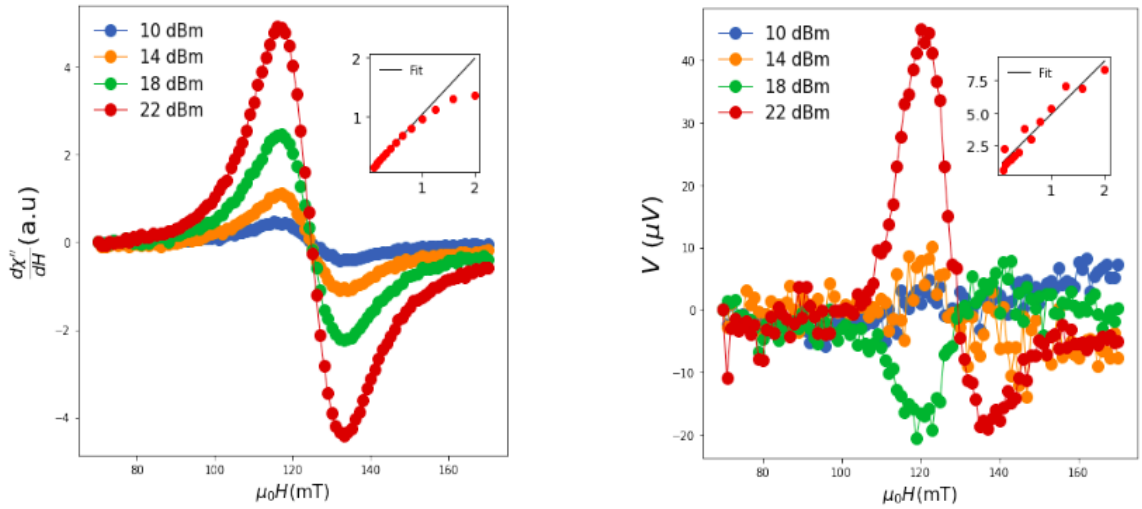

Figure 4.2: FMR signal and measured voltage in a sample of AlOx|Py|LAO(5u.c)|STO for various powers of the exciting rf field. Both figures in the inset represent the amplitude of the signal versus the applied power of the rf field.

4.1.1.2 Evidence for IEE signal

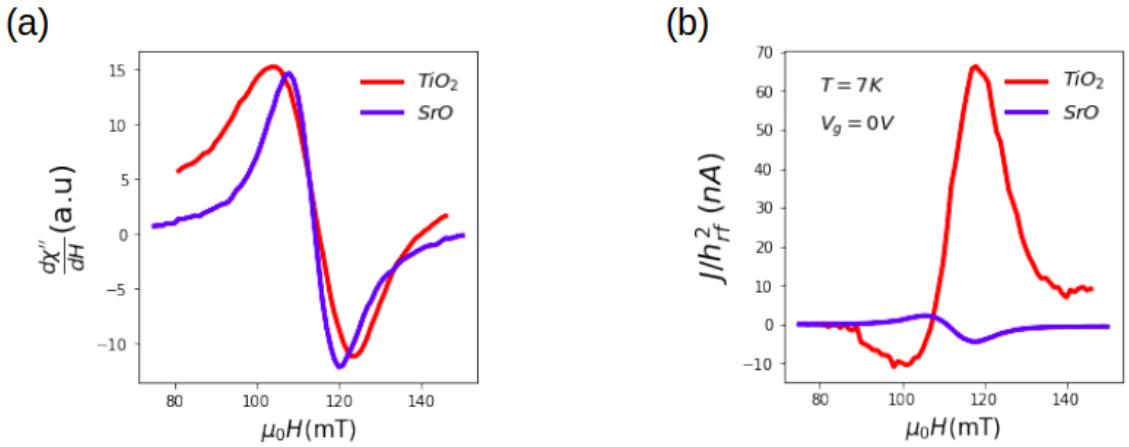

Figure 4.3: Comparison between two different AlOx[NiFe|LAO|STO samples in the presence (TiO_2-terminated STO) and absence (SrO-terminated STO) of the 2DES. We plot in (a) the FMR signal and (b) the normalized current measured in both samples.

In Figure 4.3, we plot the measured FMR signal $d\chi''/dH$, and the normalized dc current [5] j_{dc}/h_{rf}^2 for both samples [6] at low temperature $T = 7K$. We observe that the FMR signal which is proportional to the total absorbed power by our sample, has almost the same amplitude for both samples, whereas the linewidth of the FMR signal for the TiO_2 terminated STO sample is higher by ~ 1.7 times compared to that of the SrO-terminated STO reference sample. This can be ascribed to a higher loss of the transverse component of the magnetization due the presence of the 2DES at the interface. On the other hand, we

[5] Normalized by the microwave power
[6] Both Py/LAO(5u.c)/STO(001) samples with TiO_2 and SrO terminations for STO

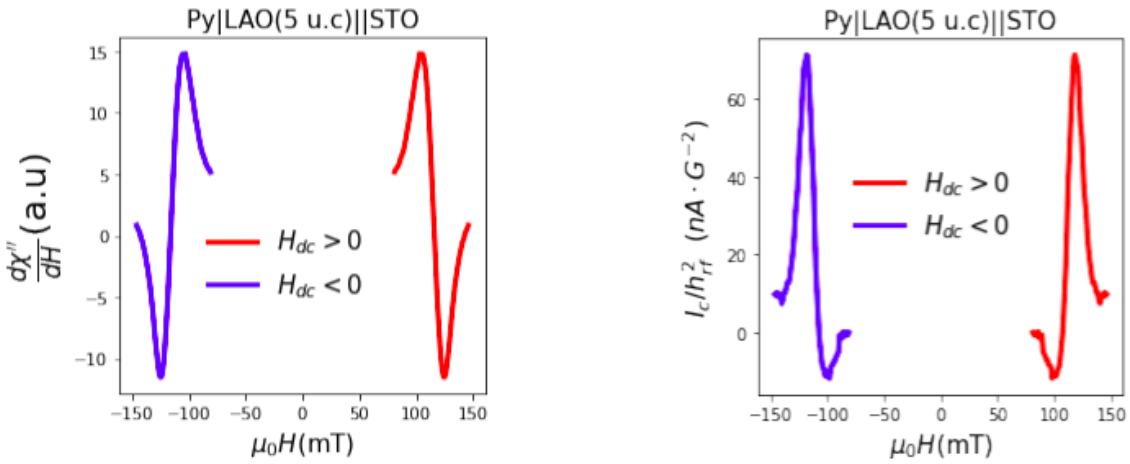

Figure 4.4: A comparison between the symmetry of the FMR signal and the normalized current upon a sign change for H_{dc}.

observe that the normalized dc current in the reference sample is smaller by a factor of ~ 10 compared to the signal measured for the TiO_2-terminated STO sample. Therefore, we attribute this to the effect of the 2DES at the interface, which absorbs the injected spin current and converts it into a charge current.

Moreover, upon changing the sign of the injected spin current we observe that the measured voltage in the TiO_2-terminated STO sample does not change sign (see Figure 4.4). This provides further evidence for the IEE origin of the effect because the measured signals are field derivatives, as seen in 3.23.

In order to gain more insight into the origin of the measured dc voltage in Py/LAO(5u.c)/STO, we have measured both samples upon changing the back-gate voltage V_g. We also need to inform the reader that a special procedure was followed in order to sweep the gate voltage V_g, which we will be discussed in more details in subsection 5.2.1 . We plot in Figure 4.5 , the normalized dc current along both directions for both samples[7] at low temperature, at $T = 77K$ and $T = 7K$. In the former case, the back-gate voltage V_g, was swept from $+300V$ to $-300V$. It appears, that the signal for the TiO_2-terminated STO sample at $T = 77K$ does not change in amplitude for all applied back-gate voltages. A similar behavior is displayed by the reference sample at $T = 7K$, with a smaller amplitude evidencing an additional contribution from the 2DES in the TiO_2-terminated STO sample. Furthermore, we observe a strong back-gate dependence of the normalized current for the TiO_2-terminated STO sample at $T = 7K$, in stark contradiction with the absence of variations in the signal measured by the reference sample, exhibiting the strong contribution of the 2DES whereby the IEE signal is generated.

[7]For both samples of Py/LAO(5u.c)/STO with both TiO_2 and SrO termination

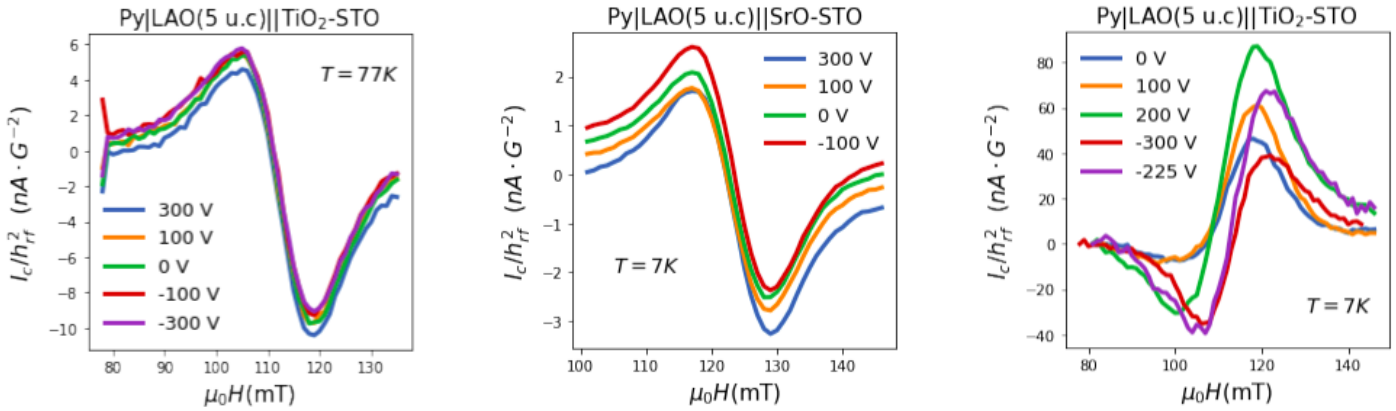

Figure 4.5: Gate dependence of the normalized current measured in two LAO|STO samples in the presence and absence of the 2DES at the interface, for two different temperatures $T = 77K$ and $T = 7K$.

4.1.2 Longitudinal Spin Seebeck measurement

A different way to perform spin injection in a sample of Py/LAO(5 u.c)/STO, relies on the longitudinal spin Seebeck Effect (LSSE), by which a longitudinal thermal gradient perpendicular ($\Delta_{\perp}T$) to the plane of the ferromagnetic layer (FM), creates a spin current flowing parallel to the direction of this gradient. The spin current then reaches the 2DES at the interface of LAO/STO, where it is converted into a charge current, as discussed in subsection 4.2.2 . In the following, we will simulate the temperature distribution induced by our light source, which will allow us to estimate the thermal gradient and thereby the generated spin current. In a second step, we will emphasize the benefits of this technique compared to the spin pumping experiment, where we will compare the later results obtained while pursuing those two approaches.

4.1.2.1 Thermal gradients

We used a longitudinal spin Seebeck effect (LSSE) geometry as shown in Figure 3.14 (ref), where the light source irradiation method was used as a model to compute the thermal gradient ∇T, in thin films. The created light-induced thermal gradient in the ferromagnetic layer (FM) produces a chemical potential gradient, which will give rise to a spin current along the ferromagnet's thickness carrying angular momentum parallel to the magnetization of the FM layer. Hence, it will be converted into a charge current by the ISHE/IEE effects. In order to estimate this light induced thermal gradient, we performed simulations by the finite element method (FEM)[25, 40]. Here, we present FreeFem++ simulations using a 2D heat transfer model, where the heat transport equation is given by:

$$Q = \rho C_p \frac{\partial T}{\partial t} + \Delta \cdot \mathbf{q} \tag{4.1}$$

where Q is the heat source given in (W/m^3), ρ is the density (Kg/m^3), C_p is the heat capacity $(J/Kg.K)$, T is the temperature (K), and **q** is the heat flux vector which depends on the thermal conductivity κ $(W/m.K)$ and the thermal gradient ($\mathbf{q} = -\kappa\Delta T$).

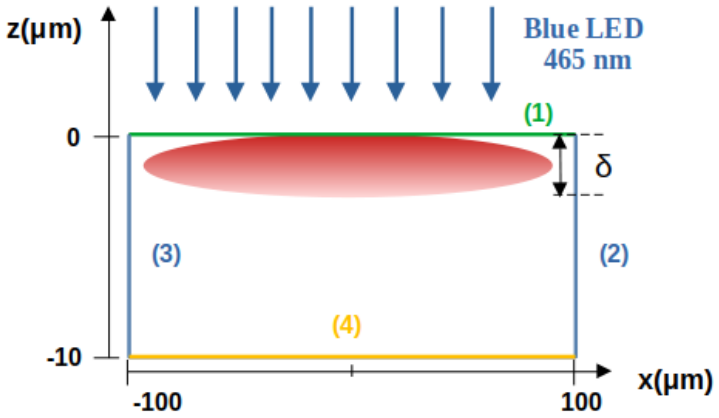

Figure 4.6: Schematics representing the various boundary conditions taken into account for our 2D simulations.

In this model, the dc light source[8] serves as a heat source, so that its term Q in equation 4.1, will depend on the material properties, as well as the geometry of the sample, so that its spatial distribution in the case of an incident light with a Gaussian profile, will be given by[40]:

$$Q = \frac{1-R}{\delta} \cdot e^{\frac{-z}{\delta}} \cdot \frac{2P}{\pi\omega_0^2} \cdot e^{\frac{-2r^2}{\omega_0^2}} \tag{4.2}$$

where λ is the optical penetration depth, R is the reflectivity coefficient given by the Fresnel equation, P is the light source power, ω_0 the spot size of the light beam, z the sample thickness, and r the width of the sample. Our 2D model is similar to that in [40], where the samples are simplified to 2D rectangles, with the width along the x coordinate and the depth along y (see Figure 4.6). We consider that the whole sample is irradiated by the light source which simplifies the heat source distribution to the following equation:

$$Q(y) = F \cdot \frac{1-R}{\delta} \cdot e^{\frac{-y}{\delta}} \tag{4.3}$$

where F stands for the fluence of the irradiated light on the surface of the sample (W/m^2). In addition, the surface boundary condition were chosen so that the irradiated area (1), as shown is Figure 4.6, is described by the equation:

$$\overrightarrow{n} \cdot (\kappa\Delta T) = q_0 + \alpha(T_{ext} - T) + \sigma\epsilon(T_{ext}^4 - T^4) \tag{4.4}$$

[8]See subsection 4.2.2.3 Chapter 4 for more details

where $\overrightarrow{n}$ is the normal vector to the interface, q_0 is the surface heat flux(W/m^2), α is the convection heat transfer coefficient $(W/m^2 \cdot K)$, σ is the Stefan-Boltzmann constant $(W/m \cdot K^4)$, ϵ is the emissivity, and T_{ext} is the external temperature (K). For these simulations, we considered two different samples of Py/LAO(5u.c)/STO and Ge/Py/LAO(5u.c)/STO, where all the relevant parameters are presented in Table 4.1.

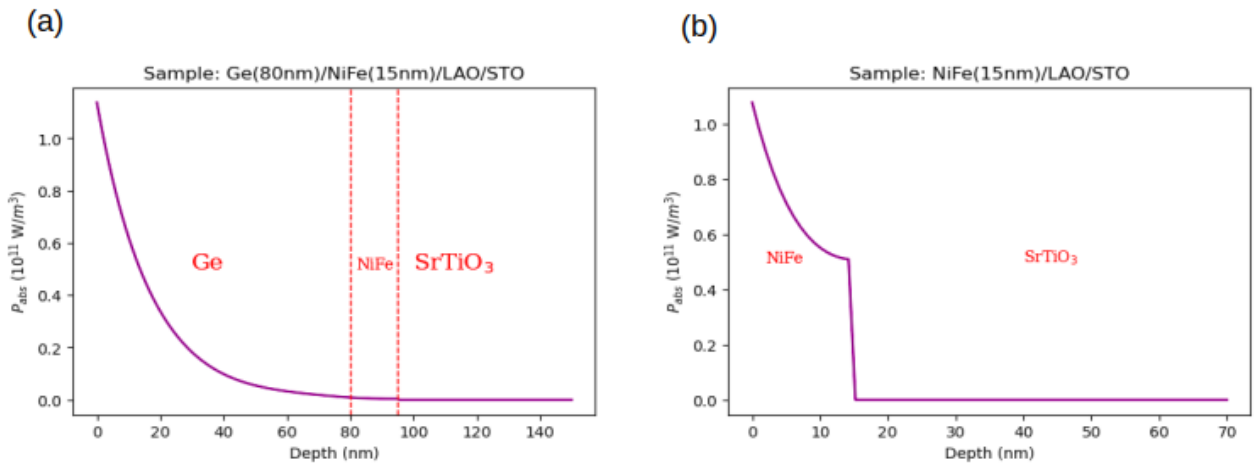

Figure 4.7: The Absorption profile for two samples of (a) Ge|NiFe|LAO|STO and (b) NiFe|LAO|STO illuminated by a $100mW$ d.c light source ($\lambda = 465nm$).

In Figure 4.7, we plot the absorption profiles, for both samples[9], using the various optical parameters presented in Table 4.2. We notice an exponential decay of the absorption profile for both samples across a characteristic penetration depth which can be estimated in the case of NiFe layer $\delta_{NiFe} \simeq 9.6nm$ and for Ge layer $\delta_{Ge} \simeq 16.5nm$ for an incident light at $\lambda = 465nm$.

Table 4.1: Thermal parameters used to perform the temperature gradient simulations at $T = 10K$

	Germanium	Permalloy	$SrTiO_3$
Thermal conductivity (W/cm·K)	12[27]	2.43[4]	0.07 [141]
Heat capacity (mJ/g·K)	1.65[48]	1.54[146]	4[97]
Density (g/cm^3)	5.5[65]	8.69[65]	4.81[65]
Thermal diffusivity (10^3cm^2/s)	1.32	0.18	0.004

For the heat transfer simulations, we considered a prism-shaped mesh for the whole sample with a resolution of $1nm$ along both x and z axis. Moreover, we considered a fixed temperature at the bottom of the STO, which is in contact with a heat sink at $T = 10K$ [10], we also neglected the contribution of the LAO layer in

[9] These results were obtained through calculations using a TMM package in Python
[10] We set a Dirichlet boundary condition to equation 4.1

the simulations of the temperature profile ΔT. In Figure 4.8, we show the calculated temperature profile ΔT, for both samples, at the center of the light spot along the normal to the surface of the film, as shown in Figure 4.6. We notice that ΔT is gradually diminishing inside both the Ge and NiFe layers, while it decreases linearly inside the STO substrate.

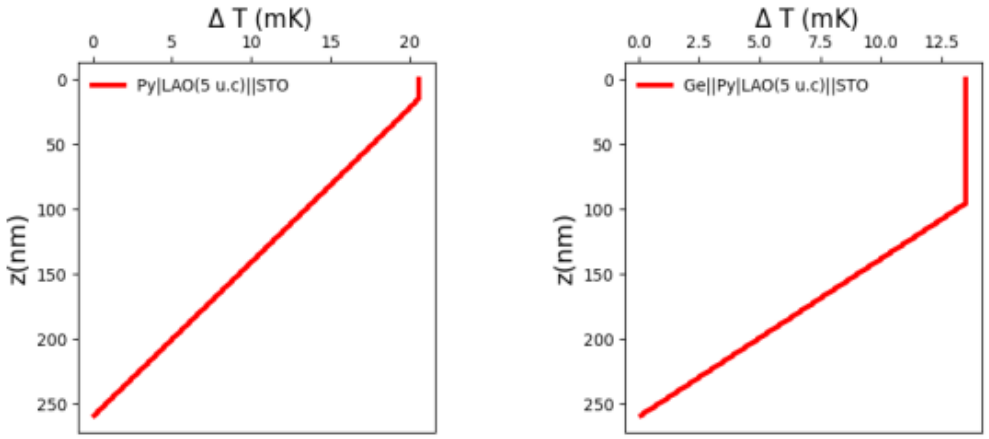

Figure 4.8: The simulated temperature profile for both samples of Ge|NiFe|LAO|STO and NiFe|LAO|STO, where $\Delta T = T - 10K$

The temperature difference between the top and the bottom of a 15 nm thick NiFe ΔT_{NiFe}, and a 95 nm thick Ge/NiFe bilayer $\Delta T_{Ge/NiFe}$, were calculated from the simulated parameters, which give $\Delta T_{NiFe} \simeq 0.1mK$ and $\Delta T_{Ge/NiFe} \simeq 0.4mK$, respectively. The absorbed heat increases by a factor of ~ 4 in Ge/NiFe bilayer compared to the bare NiFe layer.

In Figure 4.9, we plot a side view of the temperature profiles for both samples around the center of the light spot. We should also note that the calculation of ∇T across both samples are used to investigate the thermodynamic state at the samples interfaces which will be implemented for spin-to-charge conversion experiments.

Table 4.2: The optical constants at $\lambda = 465nm$[63]

	Germanium	Permalloy	$SrTiO_3$
Refractive index	4.1	2.3	2.52
Extinction coefficient	2.24	3.87	0

And before proceeding to comment on the results obtained for the gradients for both samples, we need to stress that the calculated gradients are taken as a normalized variation of $\Delta T = T$–$10K$ along both directions x & z, with respect to the dimension of the mesh size element[11]. In Figure 4.10, we plot the

[11]See Appendix D for more details

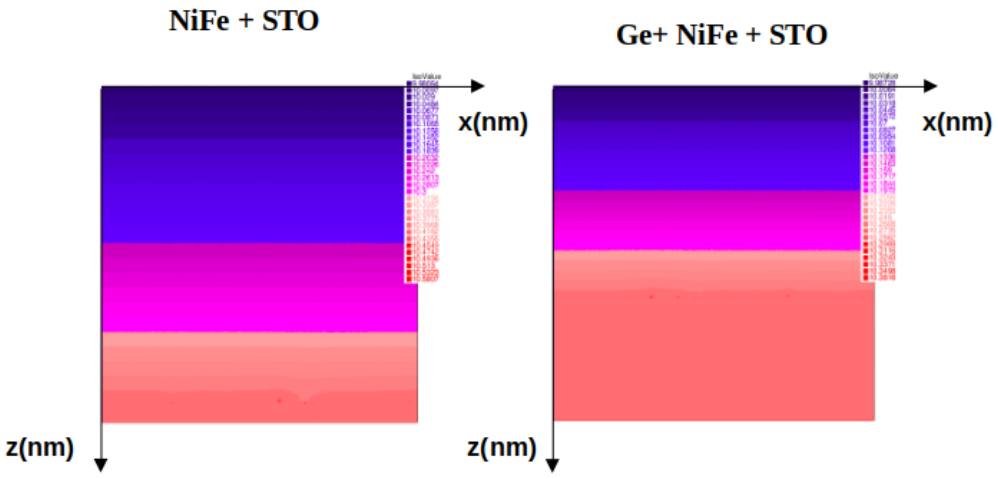

Figure 4.9: A profile of the temperature variations for both samples of Ge|NiFe|LAO|STO and NiFe|LAO|STO using a 2D simulation model, one should note that the stack order in this figure is reversed.

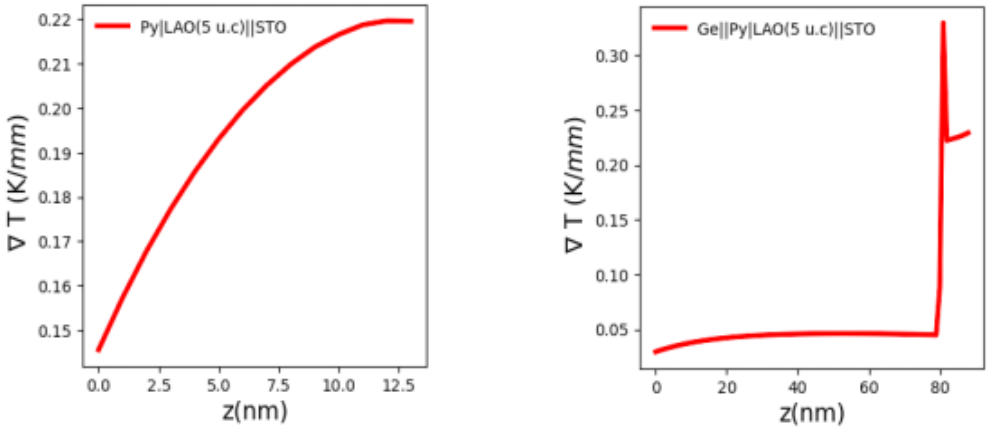

Figure 4.10: The simulated temperature gradient for both samples of Ge|NiFe|LAO|STO and NiFe|LAO|STO, around the interface between NiFe and LAO||STO

calculated thermal gradient profile ∇T for both samples, using the thermal parameters in Table 4.1. We notice that the thermal gradient increases in the NiFe layer, which can be estimated at the interface of the NiFe and STO layers to be equal to $|\nabla T_{NiFe}| = 0.21 K/mm$ for the sample without Ge capping layer, and $|\nabla T_{Ge/NiFe}| = 0.25 K/mm$ for the sample with Ge capping layer. This is within the range of previously reported values for thermal gradients in these conditions[52, 154].

In Figure 4.11, we plot the spin-to-charge conversion signal measured for both samples, whose Ge/P y amplitudes can be estimated to be equal to $V_{th}^{Py} \simeq 1.1 \mu V$ and $V_{th}^{Ge/Py} \simeq 2.32 \mu V$, respectively. Owing to the fact that the spin current is proportional to the temperature gradient as shown from the spin-drift diffusion model in equation 3.32, we can evaluate the spin Seebeck coefficient in both samples of LAO/STO to be $S_{SEE}^{Py} \simeq 1.04 \mu V/K$ and $S_{SEE}^{Ge/Py} \simeq 1.85 \mu V/K$, which is in agreement with previous experimental

results[61, 52]. We can also note that the amplitude of the measured spin-to-charge conversion signal in both samples agrees with the thermal gradient computation giving similar values for both samples.

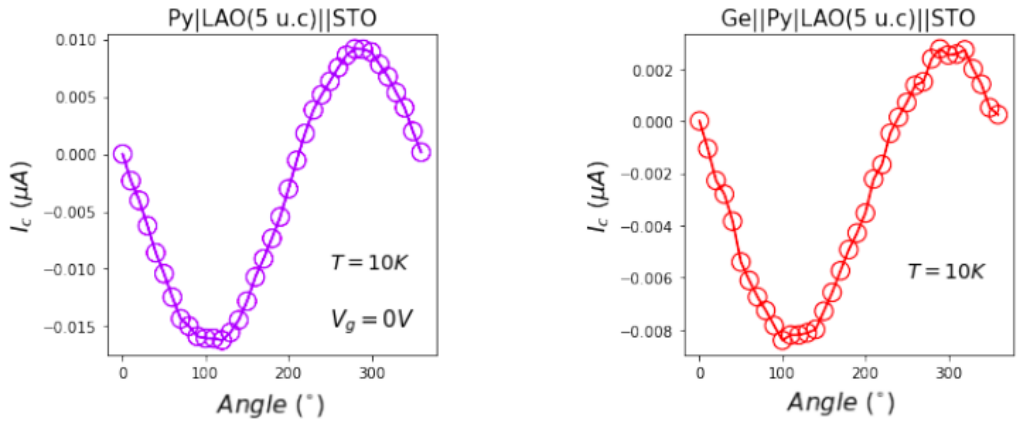

Figure 4.11: The charge current measured for both samples of Py|LAO|STO and Ge|Py|LAO|STO, while rotating the direction of $\overrightarrow{H_{dc}}$ in the plane of the sample.

In conclusion, as the profile of the light-driven thermal gradient is very difficult to experimentally measure, we have simulated it for both Py|LAO|STO and Ge|Py|LAO|STO samples. The results are consistent with the experimental spin-to-charge conversion measurements on both samples.

4.1.2.2 IEE signal without spurious effect

In this section we demonstrate the existence of longitudinal SSE in a thin film of NiFe, thanks to the thermal gradient inducing a spin flow parallel to it. In order to retrieve the contribution for the 2DES at the interface of LAO/STO, we compared the measured signals for two different samples of NiFe/LAO/STO and a reference sample of NiFe/LAO . In Figure 4.12 shows the measured signal along both geometries of our contacts, as sketched in Figure 3.20. In Figure 4.12 a $\&$ b, we plot the signal measured in the NiFe/LAO/STO sample at $T = 77K$, and a sample of NiFe/LAO at $T = 10K$. We notice that both signals have a similar amplitude, albeit slightly higher for the NiFe/LAO/STO sample, signaling that the voltage at $T = 77K$ is dominated by other spurious effects such as the Anomalous Nernst Effect (ANE), or intrinsic ISHE in the NiFe layer[126, 52]. In contrast, the signal at 10K for a sample of NiFe/LAO/STO shown in Figure 4.12 c, displays a much higher amplitude compared to the measured signal in the reference sample. This indicates that the measured variation in the signal at low temperature $T = 10K$ comes from the IEE of the 2DES at the interface.

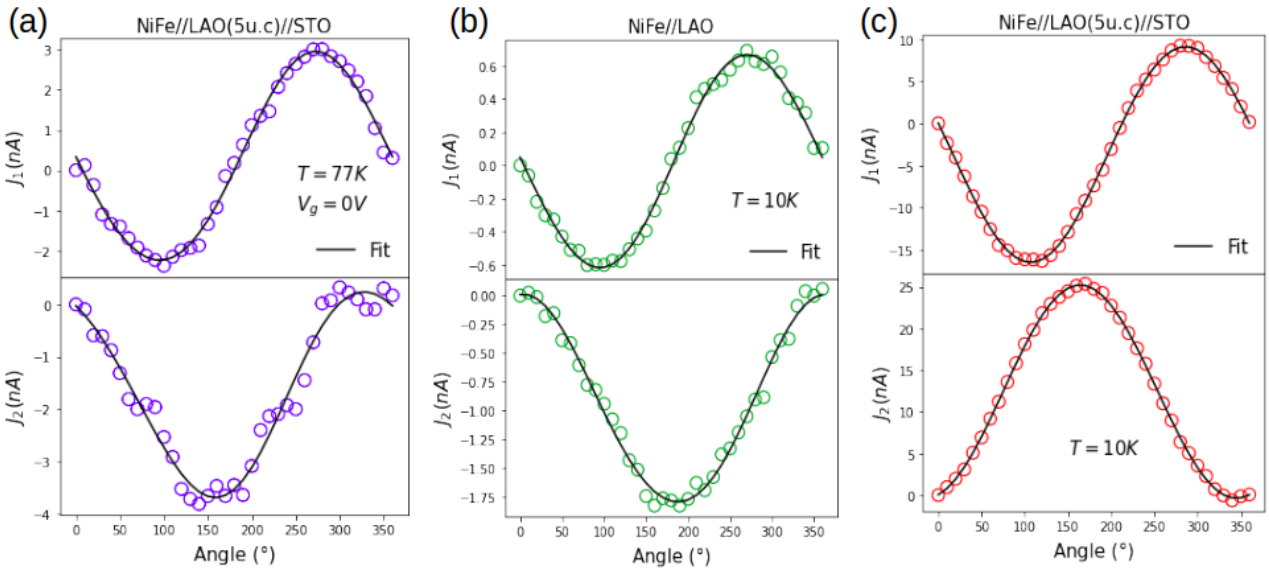

Figure 4.12: Measured current along both directions (1) and (2) in the spin Seebeck experiment, for different samples of Py|LAO(5u.c)|STO and Py|LAO and both $T = 77K$ and $T = 10K$.

In Figure 4.13, we plot the signals at $T = 10K$ for both the NiFe/LAO/STO and NiFe/LAO samples for different back-gate voltages where we observe clearly no variation in the signal of the reference sample, while we have a strong back-gate modulation of the signal in the NiFe/LAO/STO sample, thereby providing strong evidence for an IEE signal thanks to the SSE in the NiFe layer.

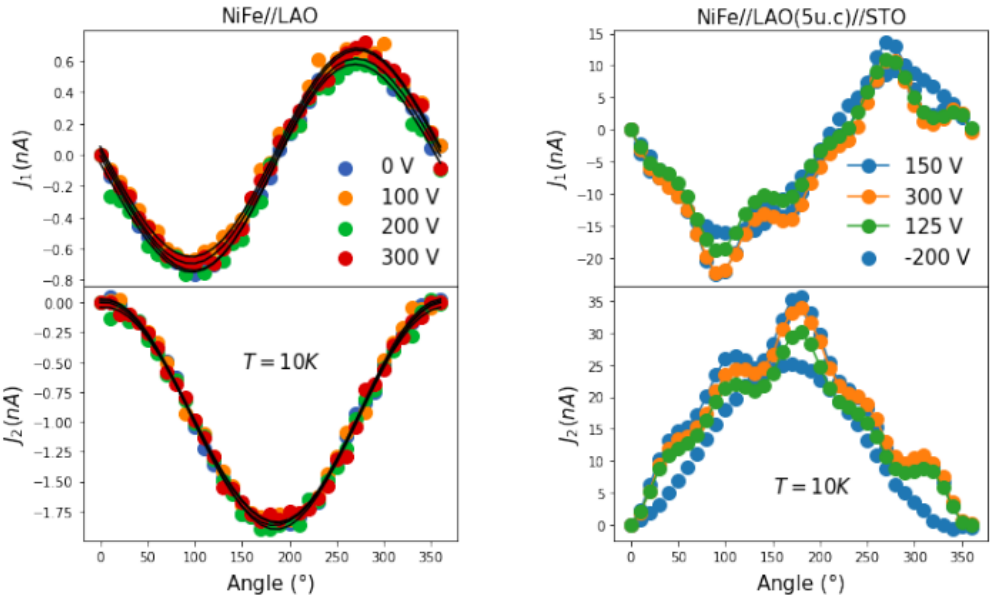

Figure 4.13: Gate-dependence of the measured current along both directions (1) & (2) for both samples of Py|LAO and Py|LAO(5u.c)|STO at $T = 10K$.

We should also emphasize that these SSE measurements do not display any significant AMR contribution to the signal, unlike the spin pumping experiment where the AMR contribution is always present. In addition,

this SSE measurements do not display any ac contribution to the spin current which can be rectified, and give rise to a non zero contribution to the conversion signal which can be very tricky to separate from the dc spin current contribution. Hence, the thermal spin current generation using SSE is well suited to the experiment. Nevertheless, the technique presents some drawbacks such as the ANE, but also some parasitic photoelectric effects coming from the substrate can add to the conversion signal, as shown in subsection 4.2.2 .

4.1.3 Temperature dependent IEE signal

To further clarify the nature of the measured signal, we performed temperature dependent measurements using spin pumping and SSE.

In Figure 4.14 a $\&$ b, we plot the amplitude of the normalized current measured for both $T = 7K$ and $T = 298K$. Similarly, in Figure 4.14 c $\&$ d, we plot the SSE signal at $T = 10K$ and $T = 298K$. We observe that in both cases the measured signal is larger at low temperature. In Figure 4.15, we plot the temperature dependence of the λ_{IEE}, we observe that $\lambda_{IEE} = 1nm$ at $T = 77K$ and decreases by a more that a factor of four at room temperature, which is in line with the results reported by Chauleau et al. and Ohya et al.[34, 110] where a strong decrease in the signal was observed when increasing the temperature. To understand the reason behind this, we need to recall that the spin-to-charge conversion signal in LAO/STO is proportional to the momentum relaxation time in the 2DES. This relaxation decreases upon increasing the temperature due to a decrease in the electron mobility in the 2DES, which is know to vary in a temperature activated fashion. However, the exact temperature dependence is hard to quantitatively analyze as several other parameters come into play such as the Rashba coefficient or the thickness of the 2D liquid at the interface.

4.2 Amplitude modulation of the IEE signal using back-gate voltage

In this section we present the results for the back-gate modulated IEE signal using both spin pumping and SSE experiments. In order to investigate the gate-dependence of the IEE signal we will first need to analyze it in the framework of magneto-transport experiments where we explore the evolution of the spin-orbit coupling and the momentum relaxation time by the application of an external electric field. Then, we will uncover the strong variation of the gate-modulated IEE amplitude, when rotating the direction of the spin degree of freedom.

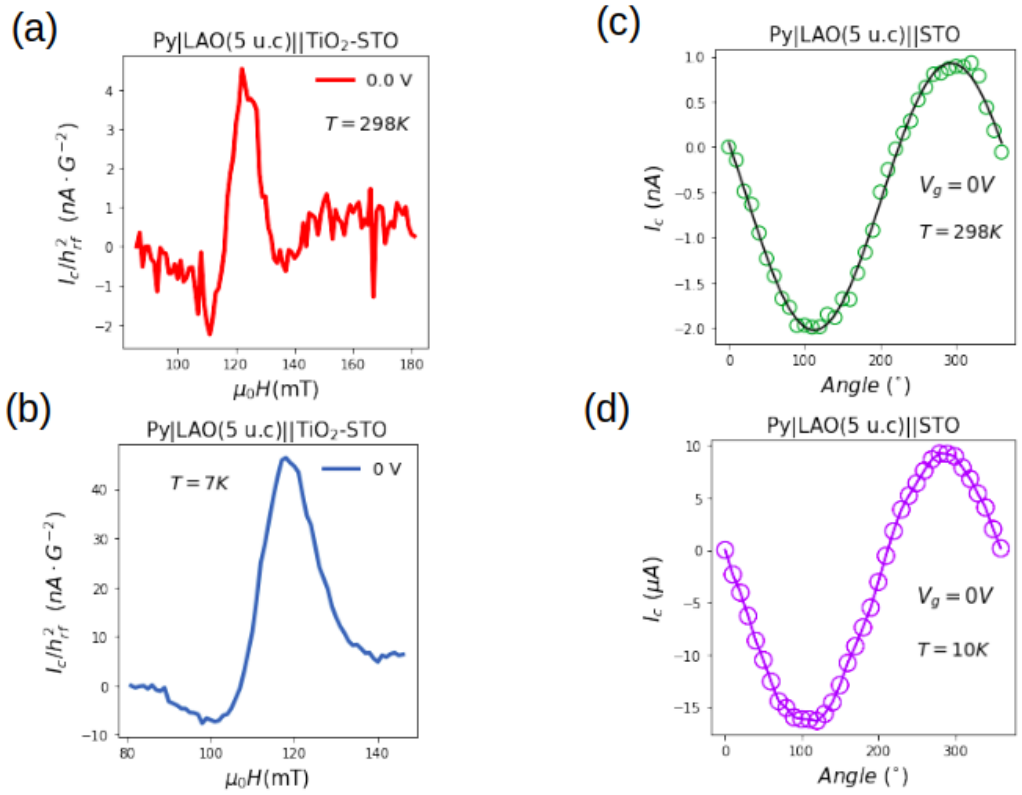

Figure 4.14: Temperature dependence of the IEE signal in Py|LAO(5u.c)|STO sample. We plot the normalized current measured in the spin pumping experiment for both (a) $T = 298K$, (b) $T = 7K$ as well as that in the spin Seebeck experiment at (c) $T = 298K$ and (d) $T = 10K$.

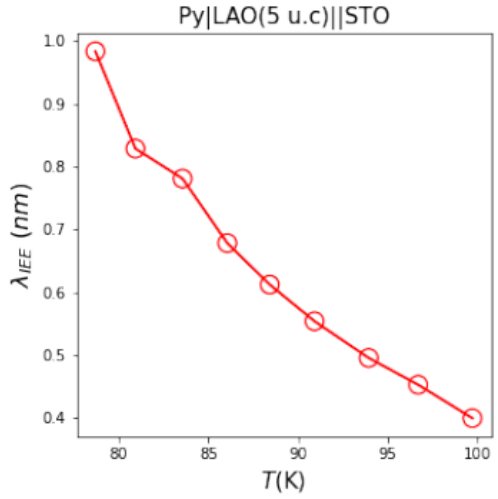

Figure 4.15: Temperature dependence of the Inverse Edelstein characteristic length λ_{IEE}.

4.2.1 Electrostatic gating in LAO/STO

Upon cooling the STO below $T < 37K$, Muller et al.[102] reported a quantum paraelectric/ferroelectric phase transition that they attributed to the coupled fluctuations of the phonon modes. This results in a large amplification of the the dielectric constant by at least two orders of magnitude compared to its value at room temperature, to reach at $T = 4K$ a value of $\epsilon_{STO} \sim 10^4$[46], as shown in Figure 4.16 a.

Thanks to this high dielectric constant, one can perform an electrostatic doping of the 2DES at the LAO/STO interface. This was shown by Thiel et al.[188] who have been one of the first research groups to report the possibility to perform an electrostatic modulation of the carrier density at the LAO/STO interface at low temperature $T = 4.2K$, as shown in Figure 4.16 b. By a simple approximation one can estimate the carrier density variation within the 2DES at the interface of LAO/STO, which can be expressed as :

$$\Delta n_c = \frac{\epsilon_0}{eL} \int_0^{V_g} \epsilon(V)\, dV \tag{4.5}$$

where $L = 0.5mm$ corresponds to the thickness of the STO substrate, $V_g = 300V$ is the maximum positive voltage applied to the sample. From equation 4.5, we obtain a carrier modulation of $\Delta n_c \approx 3 \cdot 10^{13} e^-/cm^2$, which is in the range of the reported carrier densities in LAO/STO $n_c^{LAO/STO} \sim 10^{13} e^-/cm^2$, demonstrating a strong electrostatic modulation of the carrier density in LAO/STO as it was shown from previous studies[188, 14].

One should also note that the electrostatic gating in LAO/STO needs to follow a special procedure, as demonstrated by the work of Biscaras et al[14] . In their study, they have shown that the back gate voltage has two different effects on the interface. The first one being the possibility to either dope or deplete the 2DES at the interface by either applying positive $\Delta V_g > 0$ or negative $\Delta V_g < 0$ back-gate voltage . The second effect, corresponds to the band tilting, which changes the conduction band profile in the STO substrate as shown in Figure 2.6. Moreover, an hysteresis effect has been observed in the sheet resistance of their sample of LAO/STO, upon the first polarization[12], as shown in Figure 4.16 b. One can observe that after the first polarization the carrier density is saturated[13] as shown in Figure 4.16 b. This can be explained simply by the fact that the Fermi level lies at the top of the the potential well and when increasing V_g, more electrons are added to the higher energy subbands at the top of the potential well, which will lead eventually to a leakage of the charge carriers into the substrate where they will be trapped. This explains the saturation of the carriers density resulting in an irreversible first polarization as seen in Figure 4.16 b.

[12] Where they swept the V_g to a maximum value of +200 V and minimum value of -200V[14]

[13] The sheet resistance decreases slightly then becomes saturated and independent of the back gate voltage

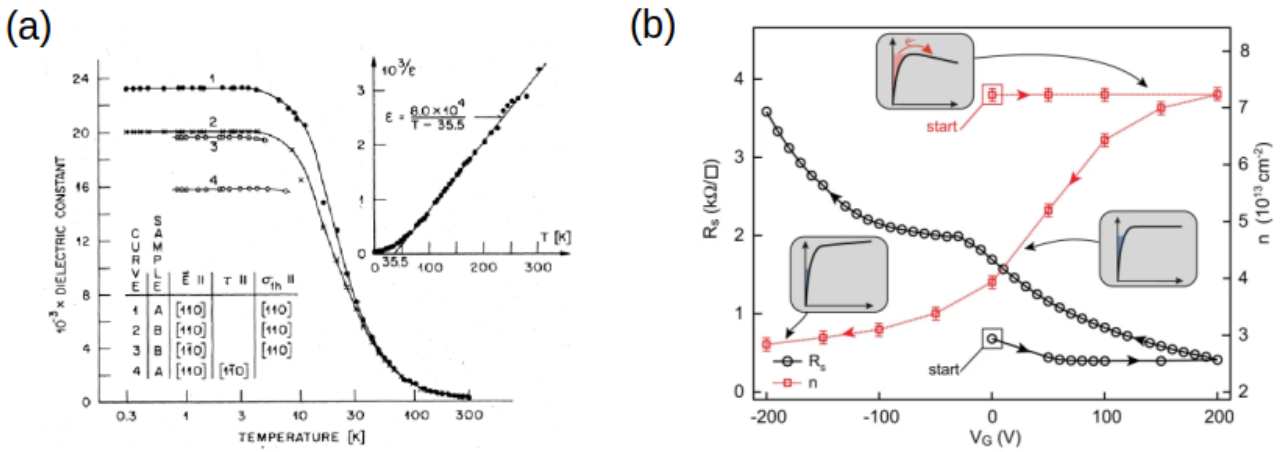

Figure 4.16: (a) Dielectric constant $\epsilon\prime$ of $SrTiO_3$ versus temperature (at low temperatures $T < 100K$), the figure in the inset represents the inverse of the dielectric susceptibility versus temperature.[46] (b) We plot the sheet resistance (left axis) and electron density (right axis) versus the back-gate voltage measured for a sample of LAO|STO upon the first polarization followed by a reversed sweep.[14]

Furthermore, we observe that the carrier density is decreasing when we decrease the backgate voltage which is in agreement with the removing of charge carriers from the potential well as described in Figure 4.16 b. Contrary to the first polarization this process is reversible, meaning that the 2DES can be either emptied $\Delta V_g < 0$ or filled $\Delta V_g > 0$ as long as the back gate voltage does not exceed the initial maximum back gate voltage set in the first polarization step .

Therefore, in order to avoid this irreversible effect[14], one needs to perform an initial step where the back gate voltage is swept to its maximum positive value[15], where a fraction of the electrons is lost into the substrate. During our spin pumping measurements, we have observed a similar effect when measuring the IEE signal in a sample of AlOx/NiFe/Cu/LAO/STO, where the first sweep corresponds to the first polarization which is irreversible, as shown in Figure 4.17. Applying subsequent multiple sweeps of the back gate voltage[16] after the first polarization we observe a reversibility of the IEE signal in agreement with the results shown by Biscaras et al[14].

4.2.2 A tunable IEE characteristic length

We start by analyzing the gate-dependence of the IEE signal for the spin pumping experiment. In Figure 4.18, we plot the FMR response at positive and negative H_{dc} and for different back-gate voltages V_g, we observe that neither the band width nor the resonance field change upon changing the voltage, meaning that the back-gate voltage has no effect on the properties of our ferromagnetic layer. In the lower panel, Figure 4.18,

[14] Also know as the "forming process"
[15] We set the maximum $V_g^{max} = 300V$
[16] Between +300 V and -300V

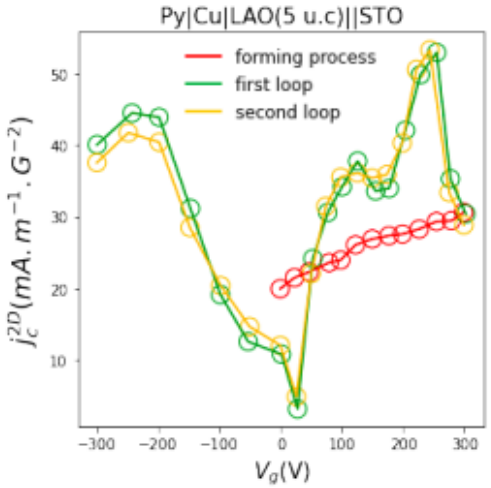

Figure 4.17: We plot the charge current density measured on a sample of Py|Cu|LAO(5.c)|STO verus the back-gate voltage upon first polarization followed by two consecutive sweeps

we uncover the normalized charge current, which was measured along both directions[17], for different back-gate voltages, and for positive and negative H_{dc}.

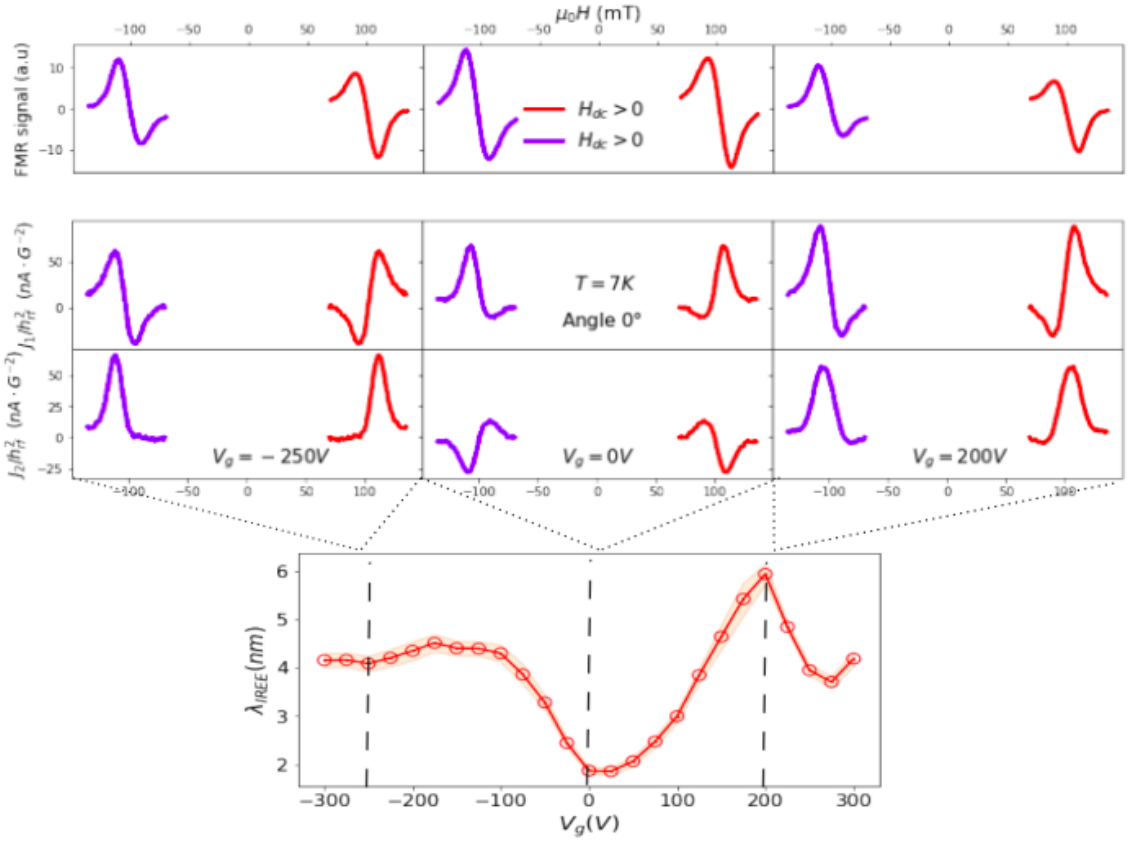

Figure 4.18: (Top:) the FMR signal and (middle) the normalized charge current along both directions (1) and (2), for both positive and negative H_{dc} and for for various back-gate voltages $V_g = -250V$, $V_g = 0V$, and $V_g = 200V$. The bottom figure shows λ_{IEE} versus back-gate voltage, where the three points related to the pannel above are marked by dashed lines.

[17] See the contacts geometry in Figure 4.18

Upon H_{dc} inversion the signal changes sign, while the amplitude stays about the same, in agreement with what we expect from a spin-to-charge conversion signal. We should also stress that our signal was normalized by the square of the rf field $|h_{rf}|^2$ itself proportional to the microwave power $P_{rf} \propto |h_{rf}|^2$, which allows us to compare between samples for various $|h_{rf}|^2$. We observe a variation in the amplitude of the normalized currents $J_1/|h_{rf}|^2$ and $J_2/|h_{rf}|^2$ upon changing the back-gate voltage. In order to analyze these results in term of the spin-to-charge conversion efficiency in LAO/STO, we need to estimate the IEE figure of merit, i.e. the characteristic length λ_{IEE} from the parameters calculated in equation 3.26. This yields $\lambda_{IEE} \simeq 6nm$ at $V_g = 200V$, which is at least 1 order of magnitude higher compared to Ag/Bi(111) with $\lambda_{IEE} \simeq 0.3nm$[199]. Interestingly, even though LAO/STO has a Rashba coefficient 1 order of magnitude lower, its momentum relaxation time is 2 orders of magnitude larger compared to Ag/Bi[199, 193, 200] (see Table 4.3) .

Table 4.3: A brief comparison between two different Rashba systems

	$\alpha_R(eV\cdot\text{m})$	$\tau(ps)$	$\lambda_{IEE}(nm)$
LAO/STO[193]	$3\cdot10^{-12}$	1.3	**6**
Ag/Bi[199]	$0.56\cdot10^{-10}$	$0.5\cdot10^{-2}$	**0.3**

It can also be compared to heavy metals, like Pt, where the effective characteristic length[18] in this case can be estimated as the product of the spin Hall angle and the spin diffusion length, which yields values typically $\lambda_{eff} < 1nm$ for Pt or Ta[56, 122]. In Figure 4.18, we observe that the IEE conversion efficiency λ_{IEE} can be tuned using a back gate voltage V_g, so that it varies from around $\lambda_{IEE} \simeq 6nm$ at $V_g = 200V$ to $\lambda_{IEE} \simeq 2nm$ at $V_g = 0V$.

Furthermore, the SSE measurements show a similar behavior. In Figure 4.19, we plot the photo-current response for different gate voltages V_g, where we observe a change in the amplitude, as well as, a deformation in the shape of our signal, at positive gate voltages $V_g > 0$. It is difficult to estimate λ_{IEE} form the spin drift-diffusion model for the LSSE experiment, due to the difficulty to measure experimentally the thermal gradient at the interface of LAO/STO. In order to analyze the variations of the SSE photo-current signal I_{SSE}, we plot in Figure 4.19 the amplitude of the I_{SSE} signal for various gate voltages V_g. We observe that the signal has a subtle back-gate dependence which yields a similar non-monotonic behavior compared to the previous results. It appears that the signal increases to a maximum value $I_{SSE} \simeq 50nA$ at around $V_g = 200V$, and it is minimum $I_{SSE} \simeq 3nA$ at around $V_g = -50V$. Thus, the amplitude variation of the

[18] See subsection 4.2.1.2.2 for more details

IEE signal [19] is larger than that previously measured.

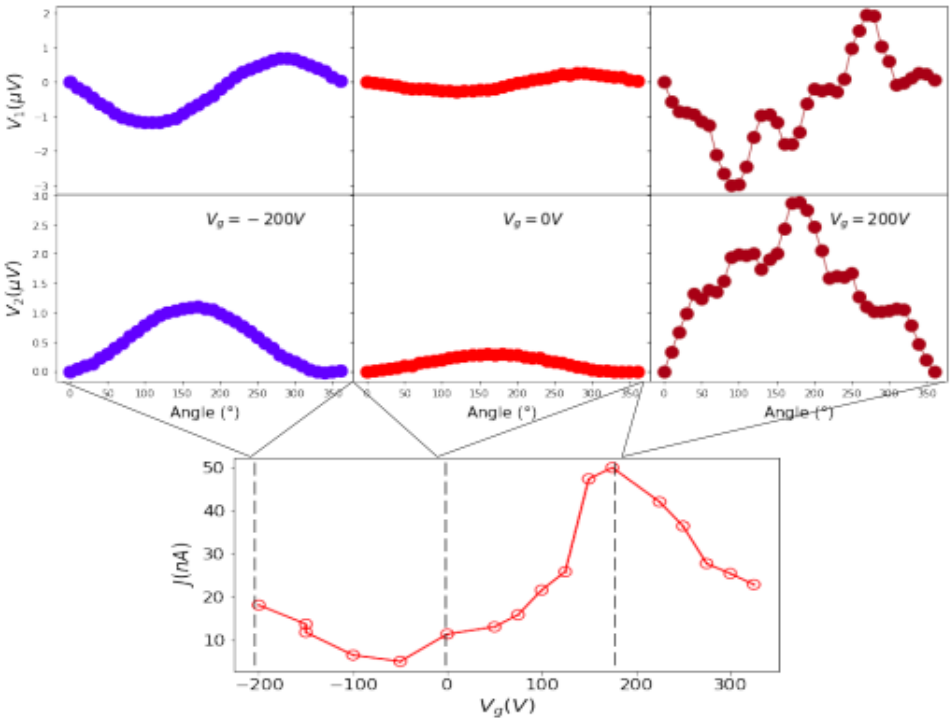

Figure 4.19: The top pannel: the thermal voltage measured for a sample of Py|LAO(5u.c)|STO along both directions (1) and (2) for different back-gate voltages $V_g = -200V$, $V_g = 0V$, and $V_g = 200V$. Bottom pannel: amplitude of the spin Seebeck current versus the back-gate voltage.

This highlights, the different contributions from the spurious effects such as AMR signals and ac spin current contributions for the spin pumping measurements, and the photoelectric effects in the LSSE experiments, but also to some subtleties related to different doping levels for different samples. These can be avoided by measuring the variation of the IEE signal with respect to the sheet conductivity of the 2DES at the interface, which was performed in various studies revealing a universal behaviour for the LAO/STO interface . In our case, it is difficult to evaluate the 2DES conductivity at the interface, due to the metallic layer of NiFe deposited on top of LAO/STO, that shunts our current bias in a four contact measurements and prevents us from measuring the 2DES response. We also plot in Figure 4.20, the anisotropy parameter ϵ_{ani} which is related to I_{SEE} through the following relation :

$$\epsilon_{ani} =< |I_{SEE}(\psi) - cos(\psi)| >_{\psi} \tag{4.6}$$

where ψ is the angle between the direction of $\overrightarrow{H_{dc}}$ and the orientation of the electrical contacts. Hence, from equation 4.6, one can identify ϵ_{ani} as the term which quantifies the deformation of the photo-current

[19] 5 times bigger in the LSSE experiment compared to the spin pumping experiment where is it 3 times bigger

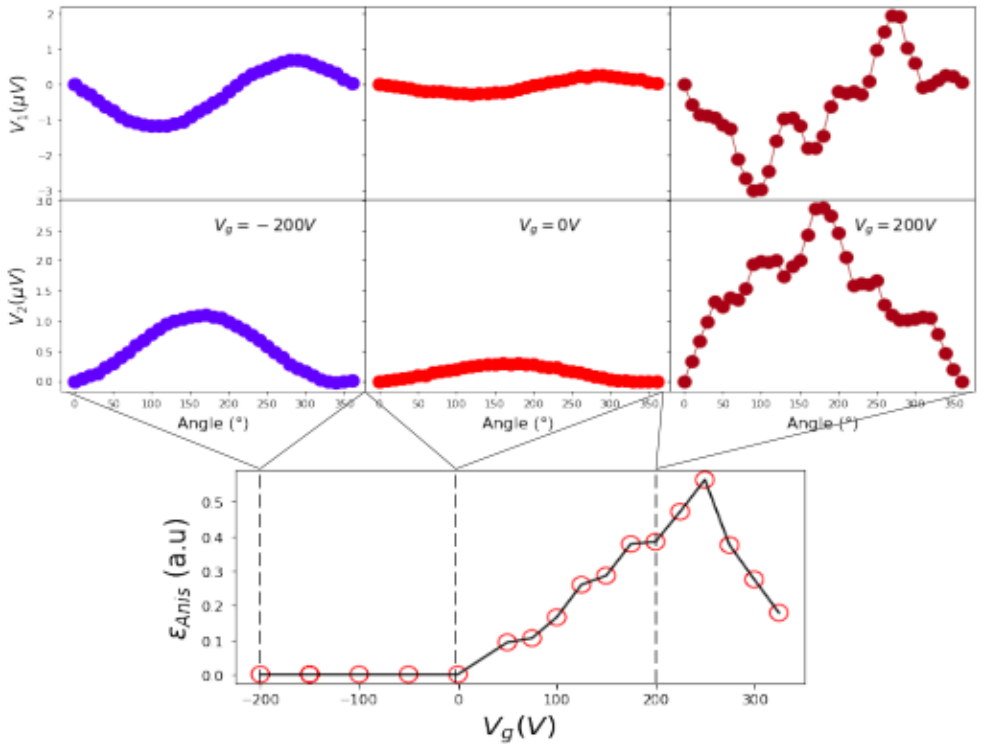

Figure 4.20: Similar to Figure 4.19 but in the bottom pannel we plot the anisotropy coefficient defined in equation 5.6 versus the back-gate voltage.

signal, with respect to the cosine-like shape of the signal which we observe at negative back-gate voltages $V_g < 0$. We notice that this parameter increases, upon applying a positive back-gate voltage $V_g > 0$, and it is maximum around $V_g = 250V$ before decreasing again for higher gate voltages $V_g > 250V$ .This non-trivial variation of the conversion efficiency of the IEE signal λ_{IEE} and the anisotropy parameter ϵ_{ani} with respect to the back-gate voltage V_g, will be discussed in the following sections.

4.2.3 Discussion

To gain more insight into the back-gate dependence of the IEE signal one needs to remember that λ_{IEE} is proportional to two quantities which are the momentum relaxation time τ and the Rashba coefficient α_R which both need to be estimated experimentally, in order to uncover the underlying variations of λ_{IEE} with respect to the back-gate voltage V_g.

4.2.3.1 A tunable Rashba coefficient and momentum relaxation time

As shown previously[20], when the spin precession is governed by the Rashba coupling, the D'yakonov Perel' spin relaxation mechanism dominates the extrinsic spin dephasing processes[21], then the IEE characteristic

[20] In Chapter 1 section 2.4.2
[21] While the Eliot-Yaffet can be neglected in this case

length λ_{IEE} is given by equation 1.30.

It is useful to recall here that in the magneto-transport measurements[193, 50], a weak localization regime arises due to the constructive interference of two coherent time-reversed electron paths in disordered systems, which reduces the conductance, whereas when applying an external magnetic field the quantum coherence of the two time-reversed paths is destroyed leading to an increase in conductance. However, in the presence of spin-orbit coupling, the two time-reversed paths experience opposite spin dephasing mechanisms, leading to a destructive interference, which increases the conductance, and this is known as the weak anti-localization regime. Upon applying an external magnetic field the spin coherence is destroyed leading to a negative magneto-conductance.

In the case of Rashba-split spin-orbit coupling, like in LAO/STO we also have a spatial inversion symmetry breaking at the interface. In this case, the electrons' spin will experience a precession motion around the effective Rashba field which is perpendicular to the electron motion, leading to the spin dephasing mechanism dominated by the electron scattering which randomizes the spin precession angles[22]. In Figure 2.5 a, we plot the results of the magneto-conductance for a sample of LAO/STO obtained by Caviglia et al.[193], when applying electrostatic doping, where it is observed that for a negative back-gate voltage $V_g < 0$ a weak localization regime dominates which corresponds to the depleted state, while a weak anti-localization regime starts appearing once we apply positive back-gate voltage $V_g > 0$, signaling spin-orbit coupling in the doped state. Caviglia et al.[193] have estimated the gate-dependence of the Rashba coefficient, the momentum scattering time and the D'yakonov-Perel' relaxation time, for different electrostatic dopings using the Maekawa-Fukuyama model[94][23], whose results are reproduced in Figure 4.21 .

In order to grasp the non trivial variation of the IEE signal, we can explain qualitatively this non-monotonic behavior of λ_{IEE}. From Figure 4.21, the elastic momentum relaxation time appears to decrease exponentially with respect to the back-gate voltage, which explains the decrease recorded in the IEE Figure 4.18 $\&$ 4.19. For positive back-gate voltages $V_g > 0$, the increase in the IEE signal can be attributed to the increase of the Rashba coefficient, as shown in Figure2.5 b. This simple qualitative analysis of the variation of λ_{IEE} can be quite interesting, despite showing some limitations, such as the simple monotonic increase in the Rashba coefficient without reaching a maximum value, as shown in our results Figure 4.18.

Other studies have shown a more complex variation for the Rashba coefficient, which has a more dome-like shape for positive back-gate voltages $V_g > 0$ as shown in the study performed by Vaz et al.[29], where they measured the bidirectional magneto-resistance response in LAO/STO upon electrostatic doping. Another

[22] See Chapter 1 section 2.4.2 for more details

[23] The Maekawa-Fukuyama model seems to be irrelevent at high doping levels so an additional parameter needs to be added to take into account for the classic conductance term.[68, 69]

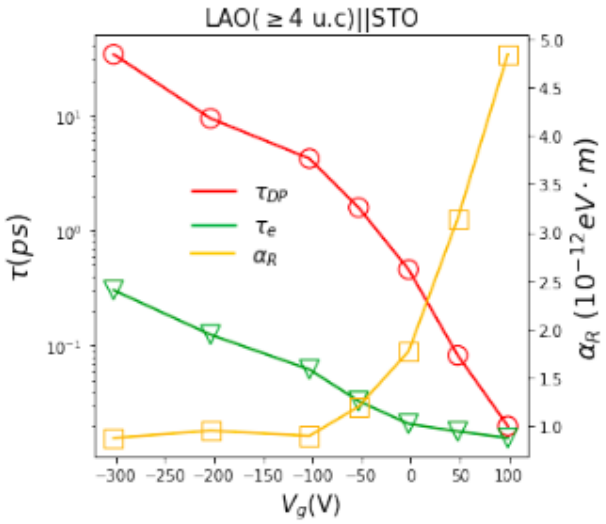

Figure 4.21: The gate-dependence of Rashba coefficient α_R, the momentum scattering time τ_e and the D'yakonov-Perel' relaxation time τ_{DP} for a sample of LAO($\geq 4u.c$)||STO.[193, 50]

interesting study by Liang et al.[92] showed a non-monotonic variation of α_R in LAO/STO for which a k-cubic contribution to the SOC in LAO/STO was introduced. These results tend to agree with measurements of IEE signal at positive gate voltages $V_g > 0$, but at negative back-gate voltages $V_g < 0$, Nakamura et al.[105] reported a linear decrease in the spin precession length with respect to the electron sheet carrier density in SrTiO3-based surface 2DES, where a simplified version of Maekawa-Fukuyama theory[24] was used to fit the magneto-transport measurements. To further clarify this non-monotonic behavior we need to turn to the complex band structure, that will be discussed in more details in the following section, and which is at play when it comes to the non-trivial variation in LAO/STO.

Hereinafter, we present the measurements of λ_{IEE} realized while mapping the angular dependence of the spin direction.

4.2.3.2 Varying the direction of the injected spins

To gain more insight in the non-monotonic variation of λ_{IEE}, we changed the direction of the injected spins, by rotating $\overrightarrow{H_{dc}}$ in the plane of the sample. In Figure 4.22, we plot the variation of λ_{IEE} for different spin angles, and for various electrostatic doping levels. We notice that for all spin angles, λ_{IEE} keeps the same non-monotonic behavior, whereas we observe a strong variation in the maximum amplitude around $V_g = 200V$ upon changing the spin angle. Furthermore, λ_{IEE} is almost unchanged for negative back-gate voltages $V_g < 0$, upon spin rotation. These observations, suggest that λ_{IEE} around $V_g = 200V$ has an anisotropic angular dependence with respect to the spin orientation, which is quite unexpected from the

[24] They used the Hikami-Larkin-Nagaoka model[58]

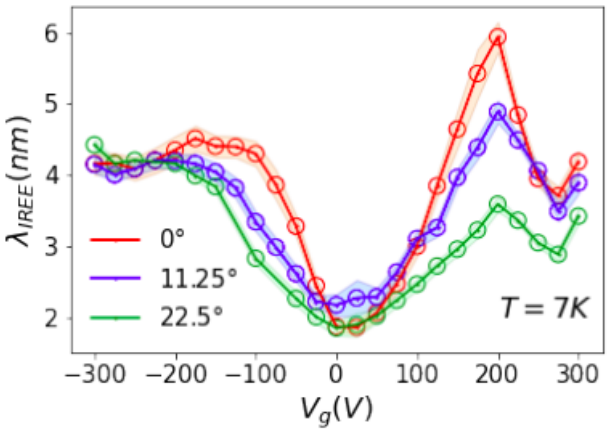

Figure 4.22: Backgate dependence of λ_{IEE} for three different angles of $\overrightarrow{H_{dc}}$.

classical picture of the Rashba spin-orbit coupling. These remarks suggest that a more complex physics is at play that needs further understanding in order to grasp the complete picture surrounding this non-trivial variation of λ_{IEE}. To clarify these subtleties, we will study the complex band structure of the 2DES at the LAO/STO interface, which governs this non-trivial gate dependence of λ_{IEE}. In addition, we present in the next section a complete angular dependence of the IEE signal in order to get a better understanding of the different phenomena at work.

4.3 Angular dependence of the IEE signal

In this section, we will show the results obtained by mapping the spin degree of freedom, to the IEE signal. First, for a standard k-linear Rashba spin-orbit coupling (see equation 1.23), one can deduce the following relation $J_c^{2D} \propto J_s^{3D} \times \boldsymbol{\sigma}$, where J_c^{2D} is the charge current density, J_s^{3D} is the spin current density, and $\boldsymbol{\sigma}$ the spin direction.

Although recent magneto-conductivity measurements have suggested the possibility of a k-cubic Rashba spin-orbit coupling for the d_{xz} and d_{yz} orbitals, first-principle calculations combined with the envelope function method have shown anisotropic non-parabolic spin-split subbands for the d_{xz} and d_{yz} orbitals, which cannot be explained by the simple k-cubic Rashba term[25]. Accordingly, a complete angular dependence of the IEE signal, is required in order to shed light on the complex orbital nature of the 2DEG at the interface of LAO/STO.

[25]In our case, the k-cubic Rashba term cannot be observed in our signal, because the sum over all k-dependent contributions with three-fold symmetry cancel perfectly each other giving a zero contribution to the charge current !

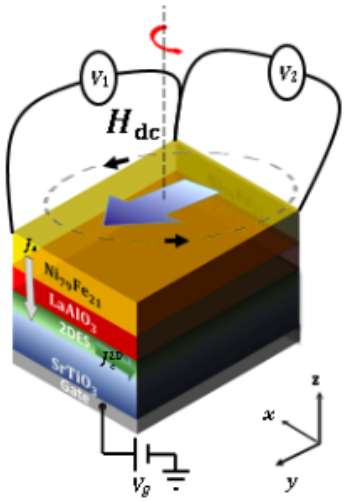

Figure 4.23: Sketch illustrating the contacts geometry on a sample of NiFe||LAO||STO heterostructure, while rotating the $\overrightarrow{H_{dc}}$ in the sample plane.

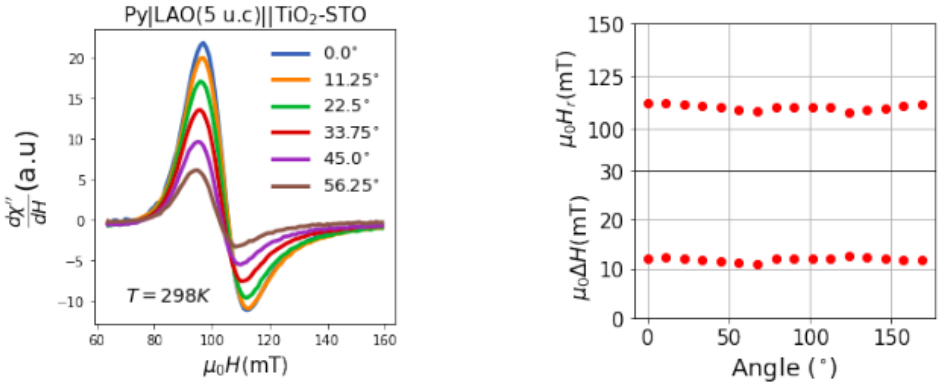

Figure 4.24: Left pannel: FMR signal for various directions of the spin. Right pannel: Resonance frequency and linewidth versus the angle of injected spins.

4.3.1 A non trivial angular dependence

In this subsection, we will present the total angular dependence of the IEE signal using both spin-pumping and SSE experiments. This complex dependence for different electrostatic doping levels will be combined with the non-trivial band structure obtained from the symmetry of the d orbitals. A more detailed analysis will follow, in order to understand the underlying physics behind the anatomy of the spin to charge conversion.

4.3.1.1 Angular dependence of the IEE signal

We will start by presenting the results obtained using the spin-pumping experiment, where $\overrightarrow{H_{dc}}$ have been rotated in the sample plane, as shown from Figure 4.23. We plot in Figure 4.25 a, the FMR response signal $d\chi''/dH$,and the normalized charge current along both contact directions, J_1 and J_2, for various

spin angles and for different back-gate voltages V_g. At first glance, we observe that the linewidth δH and the resonance field H_r of the FMR signal does not change upon changing the direction of the injected spins(see Figure 4.24), while the amplitude of $d\chi''/dH$ changes as a $cos(\theta)^2$ function [26], where θ is the angle between $\overrightarrow{H_{dc}}$ and $\overrightarrow{h_{rf}}$. In Figure 4.25 a, we plot the angular dependence of the FMR signal while rotating $\overrightarrow{H_{dc}}$ in the plane of the sample. In the case of J_1 and J_2, we notice a change in the amplitude while rotating the spin degree of freedom, accompanied with a sign change for both signals, upon a reversal of the magnetic field $\overrightarrow{H_{dc}}$, which is in agreement with the expected symmetry of the IEE signal.

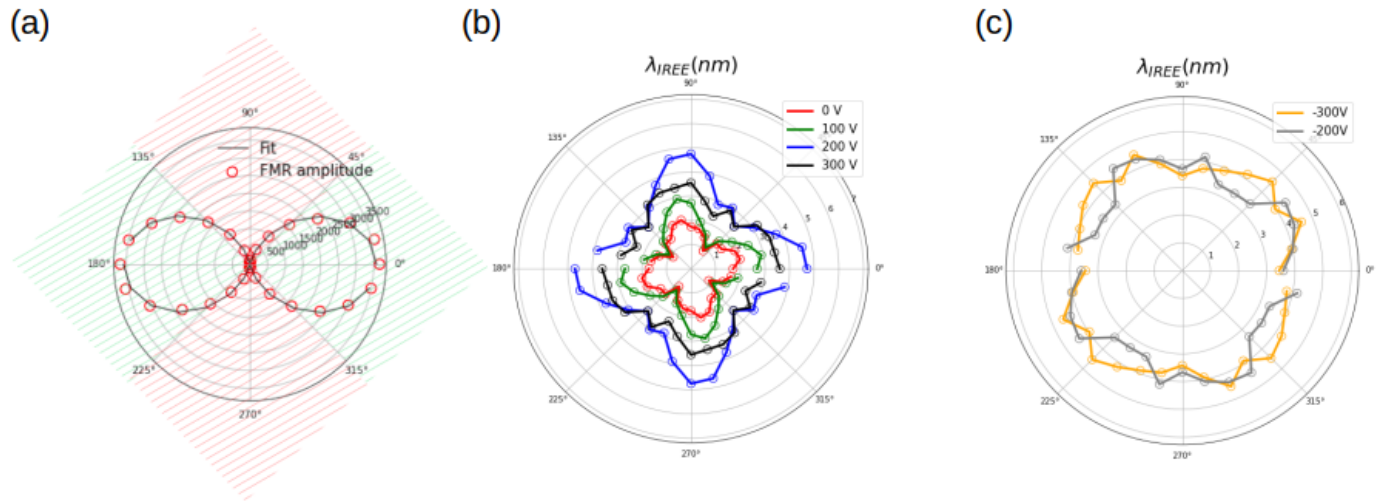

Figure 4.25: (a) Angular dependence of the FMR signal where the green hashed region corresponds to the selected quadrants used in the reconstruction of the total angular dependence of the IEE signal. We plot the angular dependence of λ_{IEE} for (b) $V_g > 0$ and (c) $V_g < 0$.

In order to reconstruct quantitatively the total angular dependence of the IEE signal, we need to normalize the IEE signal with respect to the FMR signal which is proportional to $d\chi''/dH \propto |h_{rf}|^2$, and goes to zero at $\theta = 90°$. Hence, to avoid dividing the IEE signal by zero, we performed our angular dependence measurements for two sample configurations, where the sample was rotated and measured in two different positions at $90°$ angle from each other, in order to avoid regions where $d\chi''/dH$ goes to zero, as shown in Figure 4.25, where we chose only the quadrants where $d\chi''/dH$ is maximum in amplitude. We plot in Figure 4.25 b & c, the total angular dependence of λ_{IEE} for various back-gate voltages V_g, while following the procedure detailed above.

Similarly, in the case of the SSE experiment, as shown in Figure 3.20, we have measured the IEE signal along both contacts directions, while rotating $\overrightarrow{H_{dc}}$ in the plane of the sample, for various back-gate voltages V_g. With this technique, we do not need to rotate the sample, which makes the thermal experiment much

[26] This angular dependence can simply be retrieved from equation 3.13 for both $\overrightarrow{H_{dc}}$ and $\overrightarrow{h_{rf}}$ lying in the sample plane

more flexible than the spin pumping one. In Figure 4.26, we plot the total angular dependence of the IEE signal for positive $V_g > 0$ and negative $V_g < 0$ electrostatic doping voltages.

Upon a first examination of the results shown in Figure 4.25 & 4.26, we observe that the IEE conversion signal displays a non-trivial angular dependence, which takes the shape of a four-fold symmetric signal at around $V_g = 200V$. In the following paragraph we will comment in more details about these results.

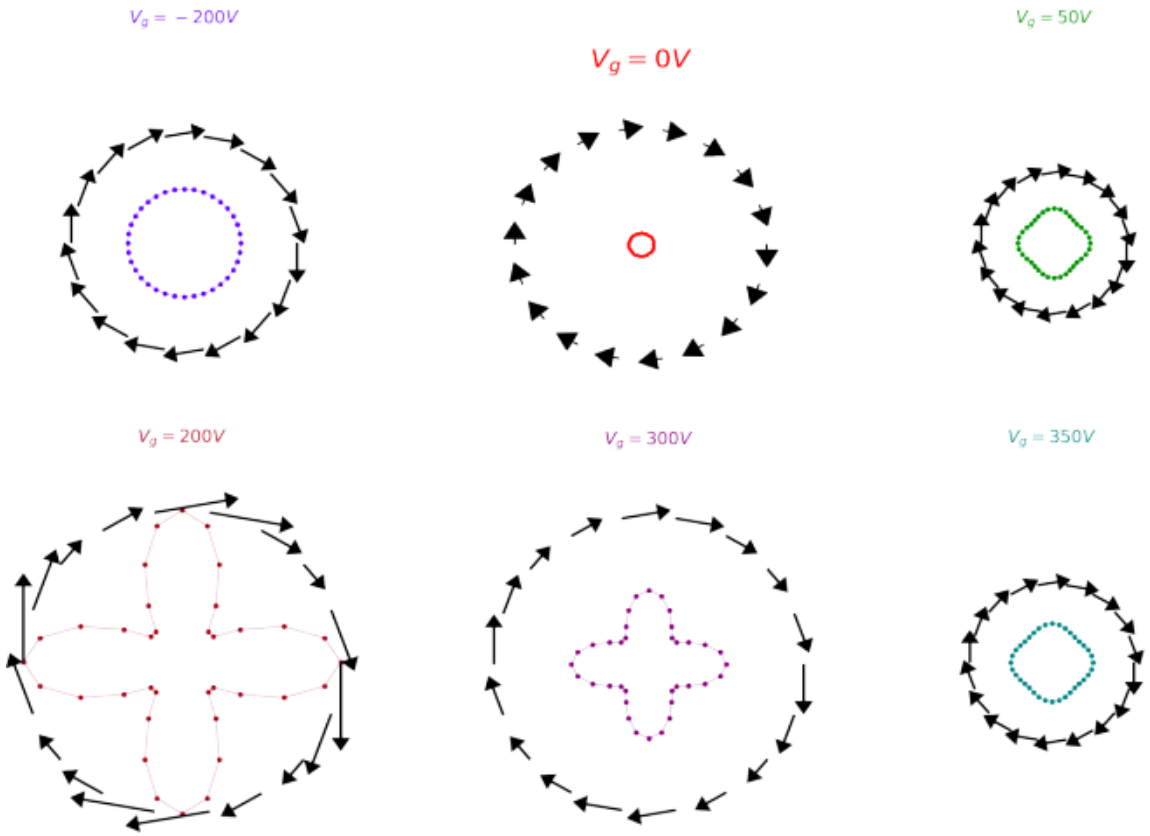

Figure 4.26: Angular dependence of the amplitude of charge current measured in the spin Seebeck experiment for various back-gate voltages. The arrows represent the direction of the measured charge current with respect to the direction of $\overrightarrow{H_{dc}}$.

4.3.1.2 Anisotropic variation of the IEE signal

From Figure 4.26, we notice that in the depleted state (negative $V_g < 0$) the photo-current signal displays an isotropic angular dependence, which is ascertained by the measurement in Figure 4.20 displaying a cosine(sine)-like shape for the signal. On the other hand, when we start applying a positive back-gate voltage $V_g > 50V$, the photo-current signal exhibits a non-trivial angular dependence. This behaviour peaks near $V_g = 200V$ where a four fold symmetric signal is clearly visible, which starts vanishing when applying back-gate voltages higher than $V_g > 300V$. Similar results where obtained for the spin pumping experiment as evidenced by measurements displayed in Figure 4.25, where we observe analogous angular dependence for

λ_{IEE}. It exhibits again the clear four fold symmetry at around $V_g = 200V$, which appears to be vanishing for higher back-gate voltages $V_g > 300V$, whereas for negative back-gate voltages $V_g < 0$, we have a similar isotropic dependence for λ_{IEE}.

This angular study sheds light on the complex multi-band effect which takes place in SrTiO3-based 2DES. In the papers of Bert et al.[8], and Li et al.[8], anistropic spin susceptibility have been reported experimentally which has been linked to an anisotropic Rashba spin-orbit coupling. This results in a different spin Hall conductivity σ_{SHC} from the k-linear case, as shown by Zhou et al.[173]

To further investigate this non trivial angular dependence of the IEE signal, we need to recall equation 1.30, which links λ_{IEE} to the Rashba coefficient α_R and the electron relaxation time τ_e. Hence, the non trivial angular dependence of λ_{IEE} is related to the subtleties associated with the angular dependence of the Rashba coefficient α_R and the momentum relaxation time τ_e. Thus, a more detailed study using first principles calculations may be needed in order to evaluate the different parameters at play.

4.3.2 Evidence for IEE using directional mapping

To gain further insight into the non trivial angular dependence of λ_{IEE}, we can plot the directional mapping of the IEE signal, knowing that we are measuring our IEE signal along two non-collinear directions[27], as shown in Figure 4.26. In the plot, the arrows represent the direction and the norm of the IEE current that was measured for different directions of $\overrightarrow{H_{dc}}$ and backgate voltage.

Furthermore, we observe that the IEE charge current for negative $V_g < 0$, has a constant modulus, in accordance with the isotropic angular dependence of λ_{IEE} obtained using a spin pumping experiment. A second remark has to do with the direction of the charge current with respect to $\overrightarrow{H_{dc}}$: we observe that $\overrightarrow{j_c^{IEE}}$ is always perpendicular to the direction of $\overrightarrow{H_{dc}}$. When applying positive back-gate voltage $V_g > 0$, we notice a change in the modulus of the charge current vector $\overrightarrow{j_c^{IEE}}$, when changing the direction of $\overrightarrow{H_{dc}}$, we observe that the modulus of the vector goes almost to zero along both $[110]$ and $[1-10]$ directions, at around $V_g = 200V$. Again, the direction of the charge current $\overrightarrow{j_c^{IEE}}$, seems to be orthogonal to the direction of H_{dc} for positive back-gate voltages $V_g > 0$.

To further clarify these findings, we need to recall equation 1.30 defining the charge current density with respect to the spin current density, which can be re-written as follow:

$$\overrightarrow{j_c^{IEE}} = \lambda_{IEE} \, (\overrightarrow{j_s} \times \boldsymbol{\sigma}) \tag{4.7}$$

[27] Along both $[100]$ and $[010]$ directions with respect to the sample crystalline axis.

This relation 4.7 shows that in the Rashba-Eldenstein picture, the charge current vector $\overrightarrow{j_c^{IEE}}$ is always perpendicular to the spin current vector $\overrightarrow{j_s}$. This is consistent with the experimental results, validating the nature of the measured signal which can be associated to the IEE.

These measurements allow us to confirm that in the depleted state ($V_g < 0$), the spin orbit interaction (SOI), is mainly due to a standard k-linear isotropic Rashba term (see equation 1.23). By contrast, for the doped state ($V_g > 0$), the Rashba splitting becomes very anisotropic[105]. However, one needs to keep in mind that in our case we cannot observe the k-cubic Rashba contributions due to a symmetry argument of the k-cubic Rashba coupling which gives a zero contribution in the measured direction of the charged current.

Nevertheless, in order to better understand the experimental results, we need to investigate the complex band structure of SrTiO3-based 2DES, in order to shed light on this non-trivial angular dependence.

4.3.3 A complex multi-band effect for STO based 2DES

As presented in Chapter 3 section 3.3.1 , the main ingredient for lifting the degeneracy of the t_{2g} triplet, which forms the conduction band minimum in LAO/STO, is the inversion symmetry breaking at the interface of LAO/STO, generating a perpendicular confining electric field $\overrightarrow{E_\perp}$. In this case, the 3d bands are split, as shown in Figure 2.11, into a light d_{xy} bands and heavy d_{yz} & d_{xz} bands. In the depleted state ($V_g < 0$), the Fermi energy E_f is located in the d_{xy} bands, which display a small spin-splitting, resulting from a low Rashba coefficient α_R, which was estimated by Caviglia et al.[193], to be of the order of $\alpha_R \simeq 3 \times 10^{-12} eV.m$.

When increasing the carrier density ($V_g > 0$), the Fermi energy E_f increases so that the d_{yz} & d_{xz} bands are becoming occupied, leading to an increase in spin-splitting and therefore of the Rashba coefficient α_R. It is also to be noted that at the band crossing of the d_{xy} and d_{yz} & d_{xz} bands, the Rashba coefficient α_R increases by at least one order of magnitude due to a strong orbital intermixing.[172]

4.3.3.1 Avoided band crossings

The Magneto-transport measurements reported a universal Lifshitz transition in several LAO/STO samples, corresponding to a transition from a d_{xy} single-band to a d_{yz} & d_{xz} multi-band regime, around a critical density estimated by Joshua et al.[75][28], to be $n_c \simeq 1.68 \times 10^{13} cm^{-2}$. On a sample of LAO/STO, similar transport measurements [29] were performed while changing the back-gate voltage, so that a carrier density

[28] In the rigid band structure approximation, where the potential well is unaffected by neither the external electric field, nor by the carrier density itself

[29] Which were realized at the Univertsity of Geneva[18]

of $n_e \simeq 9 \cdot 10^{13} cm^{-2}$ was reported at $V_g = +100V$, for a sample of LAO(5u.c)/STO.

In addition, a density variation of $\Delta n_e \simeq 3 \cdot 10^{13} cm^{-2}$, was reported while changing the back-gate voltage between $-100V$ and $+100V$, which corresponds to a variation of the Fermi energy of $\Delta E_f \simeq 30meV$. As shown in Figure 4.18, we have observed a non-monotonic variation of λ_{IEE}, which was attributed to a complex gate modulation of the Rashba coefficient α_R and the electron relaxation time τ_e. We can further investigate the gate modulation of λ_{IEE} by simply mapping its variation to the band structure.

Indeed, when applying a negative back-gate voltage $V_g < 0$, the 2DES at the interface of LAO/STO is in a depleted state, where the Fermi energy E_f, lies below the Lifshitz point $n_e < n_c$ and only the d_{xy} bands are occupied. Given that the d_{xy} bands display a weak Rashba coupling α_R, one would naively expect a small λ_{IEE}, though this ignores the fact that the momentum relaxation time τ_e is large and has a non-zero gate-dependence. Upon increasing the back-gate voltage, the momentum relaxation time τ_e decreases, while the Rashba coefficient α_R although small, has a weak energy dependence for d_{xy} bands, which explains the decrease in λ_{IEE} which is minimum at $V_g = 0V$. For positive back-gate voltages $V_g > 0$, the Fermi energy increases, and the heavy d_{yz} & d_{xz} orbitals are occupied. Furthermore, We observe that λ_{IEE} increases for positive back-gate voltages $V_g > 0$ signaling a higher Rashba splitting Δ_R for the heavier bands. In addition, we notice that λ_{IEE} reaches a maximum value around $V_g = +200V$, which corresponds to the Fermi level hitting the avoided band crossing region. There, a strong orbital mixing takes place, leading to a maximum spin-orbit strength as demonstrated by the calculations of Zhong et al.[172], where the spin splitting has a multi-orbital origin, rather different from the standard Rashba splitting (see Figure 2.13 b). Similarly , in Figure 4.27, Liang et al.[92] have shown similar results, where the spin splitting is maximum around $n_e \simeq 3.3 \cdot 10^{13} cm^{-2}$, which explains qualitatively the maximum value reported at $V_g = +200V$. In addition, when increasing the back-gate voltage even further we observe a decrease of λ_{IEE}, which can be attributed to the Fermi level E_f leaving the avoided band crossing region, and reaching the higher energy sub-bands with different contribution to α_R.

To summarize, we need to recall that λ_{IEE} not only depends on α_R, but also on τ_e which can change under electrostatic gating, leading to a more complex analysis of the variations of λ_{IEE}. It is also important to note that the interpretation of the observed α_R, expressed in equation 1.25, is nothing but the average of all spin splitting contributions for all the occupied bands leading to a much more complex analysis for α_R. Indeed, those subtleties need to be addressed, to further gain more insight about the complex behavior of λ_{IEE}. We will, in the next section, undertake a complete analysis of the angular dependence results for the IEE signal, aiming to better understand the non trivial multi-orbital effects underlying the complex behavior of α_R.

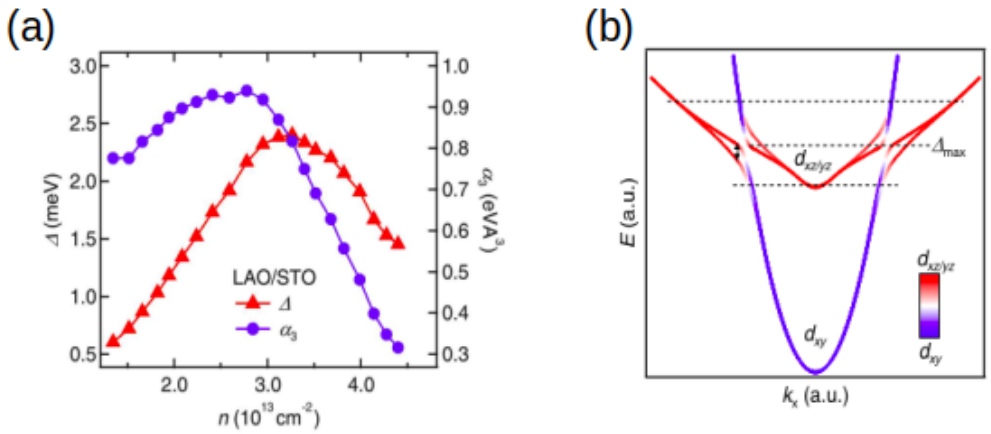

Figure 4.27: (a) Spin splitting Δ (left axis) and Rashba coefficient (right axis) versus the 2DES carrier density, for a LAO(11u.c)|STO sample .(b) Band structure of STO-based interfaces with the three lowest subbands d_{xy}, d_{xz} and d_{yz} in the presence of spin-orbit coupling.[92]

4.3.3.2 Anisotropic Rashba coefficient

In order to map the angular dependence of the IEE signal, let us now focus on Figure 4.26. We notice that at negative back-gate voltage $V_g < 0$, only the light d_{xy} bands are occupied. On the right panel in Figure 4.28, we plot the Fermi surface for the d_{xy} band, we notice that it contains two Fermi contours with opposite spin chiralities, where the spin degree of freedom is always perpendicular to the electron momentum. This is in accordance with the standard Rashba picture[30] and it is consistent with the results shown at negative back-gate voltage. When increasing the backgate voltage to positive values $V_g > 0$, the Fermi energy lies within the heavier bands d_{xz} and d_{yz}.

From the first-principles calculation, taking a six-band k.p Hamiltonian used within the envelope function method, Heeringen et al.[157] have found anisotropic non-parabolic spin-splitting for the heavy sub-bands d_{xz} and d_{yz}, as shown in Figure 4.29 a. These theoretical results agree with the magnetic torque magnetometry and transport measurements which were realized by Li et al.[90], from which he reported an anisotropic spin susceptibility. Similarly, we observe in Figure 4.28 that the IEE signal displays an anisotropic behavior similar to that reported by Zhou et al.[173] where first order perturbation theory leads to an effective Hamiltonian for the top pair of bands[31] :

$$H_{top}(\mathbf{k}) = \begin{pmatrix} \frac{|k|^2}{2m_{top}} & i\alpha_R^{top} k_- \\ -i\alpha_R^{top} k_+ & \frac{|k|^2}{2m_{top}} \end{pmatrix} \tag{4.8}$$

[30] Check equation 1.25

[31] Zhou et al. have derived an effective Hamiltonian from a quasi-degenerate perturbation theory up to a leading order in spin-orbit strength ξ, so that the (6×6) Hamiltonian can be divided into 3, (2×2) block matrices H_{top}, H_{middle} and H_{bottom}.[173]

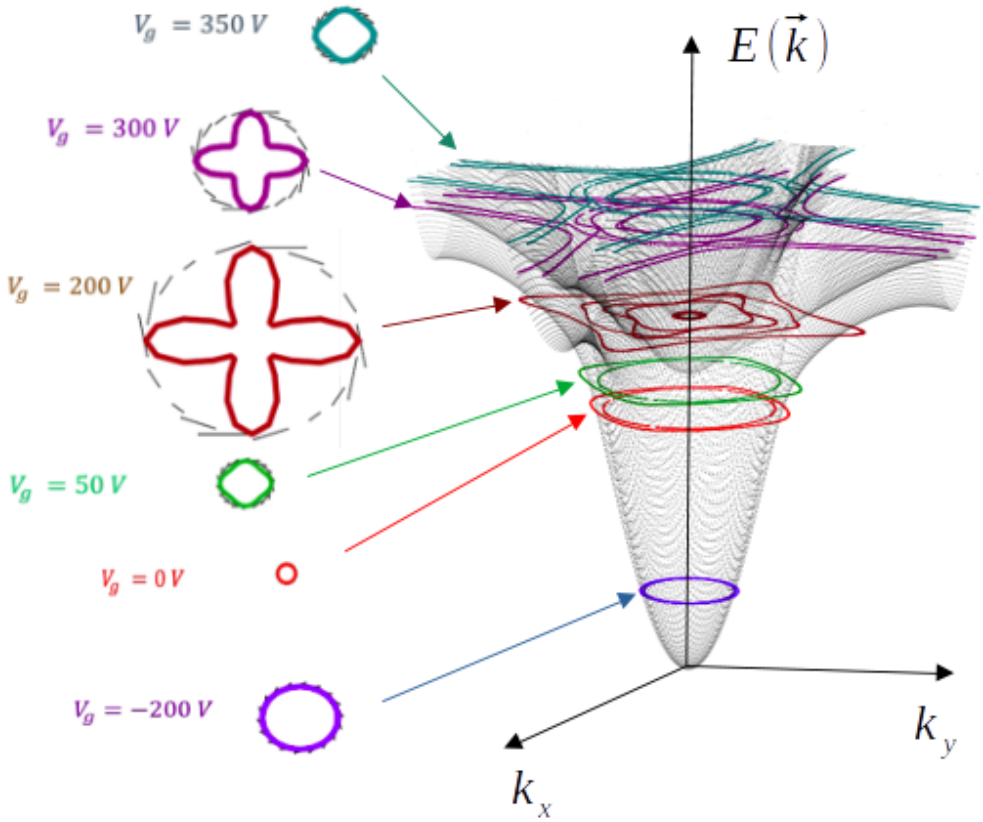

Figure 4.28: 3D band structure of the LAO|STO interface, where six different Fermi surfaces are mapped to the corresponding angular dependence of the IEE signal obtained from spin Seebeck measurements.

the middle pair of bands:

$$H_{middle}(\mathbf{k}) = \begin{pmatrix} \frac{|k|^2}{2m_{middle}} & i\alpha_R^{middle}(k_x^2 - k_y^2)k_+ \\ -i\alpha_R^{middle}(k_x^2 - k_y^2)k_- & \frac{|k|^2}{2m_{middle}} \end{pmatrix} \tag{4.9}$$

and the bottom pair of bands:

$$H_{bottom}(\mathbf{k}) = \begin{pmatrix} \frac{|k|^2}{2m_{bottom}} & i\alpha_R^{bottom}k_- \\ -i\alpha_R^{bottom}k_+ & \frac{|k|^2}{2m_{bottom}} \end{pmatrix} \tag{4.10}$$

where $k\pm = k_x \pm ik_x$, we notice that each pair of bands displays its own effective Rashba coefficient α_R^{top}, α_R^{middle} and α_R^{bottom} respectively, where the top and bottom bands exhibit a standard k-linear Rashba SOC while the middle bands exhibit an anisotropic Rashba SOC given by :

$$H_R^{ani} = (k_x^2 - k_y^2)(k \times \sigma) \cdot \vec{z} \tag{4.11}$$

This anisotropic spin-orbit coupling was also reported by Zhong et al.[172], where at the avoided crossing points, the multi-orbital effects lead to a four-fold symmetric Rashba coefficient, as shown in Figure 4.29 c.

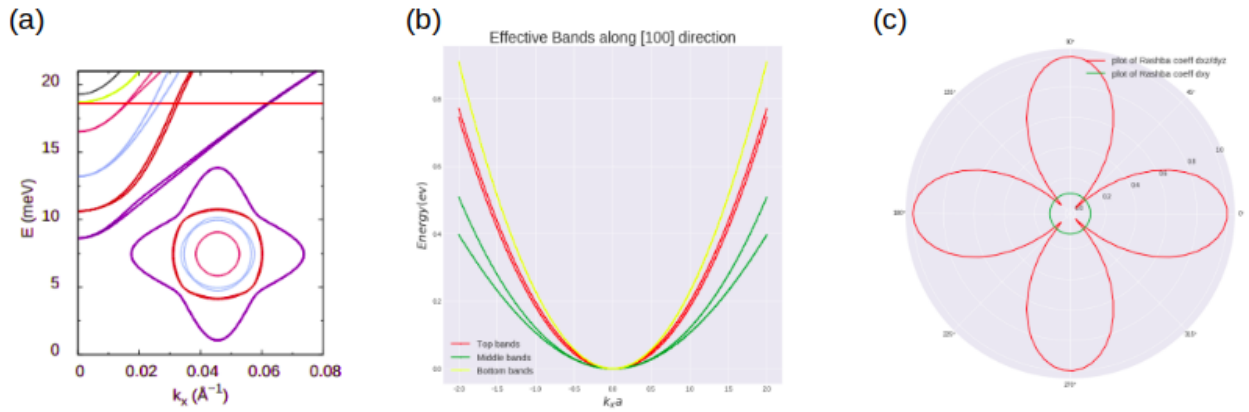

Figure 4.29: (a) Energy dispersion computed using a 6-band $\mathbf{k} \cdot \mathbf{p}$ Hamiltonian within the envelope function method, the figure in the inset corresponds to the Fermi contours at Fermi energy $E_f = 18.6meV$ (red line).[157] (b) Energy dispersion corresponding to the 6-band effective Hamiltonian derived by Zhou et al.[173] (c) Angular dependence of the Rashba coefficient for both the bottom bands (green curve) and middle bands (red curve) in the framework of the effective Hamiltonian.[172]

So to summarize, when increasing our back-gate voltage, the heavy bands d_{xz} and d_{yz}, will be occupied leading to anisotropic α_R, which we observe for $V_g > 0V$. At around 200V we observe a clear four-fold symmetric signal, similar to the shape of α_R, shown in Figure 4.29 c. Upon applying $V_g > 300V$, we notice that the anisotropy of the IEE signal decreases , due to the Fermi energy leaving the band crossing points

and reaching higher energy bands which have isotropic contribution to α_R. This is consistent with the results of Zhou et al.[173], who reports a standard k-linear Rashba SOC for the upper bands in his effective Hamiltonian. We also need to note that although this interpretation seems in accordance with the observed experimental results, the angular dependence of the IEE signal also depends on τ_e, whose possible angular dependence was not taken into account for this analysis.

4.3.3.3 Highly efficient Orbital Edelstein Effect in LAO|STO

Since electrons display both spin and orbital degrees of freedom, one would expect that the spin-to-charge conversion in LAO|STO should be driven by both the inverse spin and orbital Edelstein effects. However, the latter have often been ignored when discussing the Edelstein effect in Rashba systems. It appears that for the two dimensional electron gas at $SrTiO_3$ interfaces[32] the orbital Edelstein effect could exceed its spin counterpart by one order of magnitude. In the following, we will show both spin and orbital effects are necessary to account for our experimental results.

4.3.3.3.1 Orbital Edelstein effect in LAO|STO As shown previously[33], the strong contributions of the orbital Edelstein effect have been predicted to emerge from the wave packet self-rotation, taking place in helical and chiral crystals, as well as Rashba systems such as the surface of sp metals[226], noncentrosymmetric antiferromagnets[130], or oxide interfaces in particular the 2DES at the interface of LAO|STO[203] . Indeed, from first principles calculations, Johansson et al.[203] have shown that the orbital Edelstein effect is at least one order of magnitude higher than its spin counterpart in the 2DES at $SrTiO_3$-based interfaces, as illustrated in Figure 2.14 c. The dominating contribution of the orbital Edelstein effect can be linked to the non-compensation of the orbital moments in the inner and outer Fermi contours compared to their spin counterpart, due to the higher quantum numbers associated with the orbital degree of freedom.

Furthermore, the orbital contribution of the Edelstein effect does not change sign[34], contrary to the spin Edelstein effect. A similar conclusion can be drawn for the inverse effects[35], in virtue of the Onsager reciprocity theorem.[216]

It is also important to report, that the orbital and spin Edelstein effects display a maximum efficiency around $E_f \simeq -53meV$, as shown in Figure 2.14 a, which coincides with the first avoided crossing of the band structure of the 2DES at the STO interface. However, the origin of these maximum contributions in both

[32] Such as the interface between $LaAlO_3$ and $SrTiO_3$
[33] See section 2.5.2.3 Chapter 2
[34] For the desired energy range blow $E_f \simeq -20meV$, or at a higher back gate voltage unreachable in the experiment
[35] Inverse Spin and Orbital Edelstein effects

the spin and orbital Edelstein effects can be attributed to two different sources. In the case of the spin Edelstein effect, the maximum efficiency can be linked to the strong Rashba splitting induced by the orbital hybridization at the avoided band crossing which is accompanied by a large difference of the band-resolved spin densities of states. On the other hand, the maximum efficiency of the orbital Edelstein effect can be related to the large differences in the orbital moments of the Rashba-like split states, which can be seen in Figure 4.31.

4.3.3.3.2 Discussion From the experimental results shown in Figures 4.18 and 4.26, we report no sign reversal of the IEE signal with back-gate voltage V_g, as well as an extremely large angular anisotropy of the IEE signal around $V_g = 200V$, which was not reported in previous experimental findings. In fact the sign change of the IEE signal was first reported by Lesne et al.[200] (see Figure 4.30) who attributed such effect to the various orbitals contributions with opposite spin chirality. In addition to that, we report a strong in-plane anisotropy which is predicted by calculations to show a factor of 2.2 between IEE signals at 0° and 45°, whereas we measure a factor 6. So, it seems that some ingredient is missing to fully account for our data.

Indeed, as one may suspect we need to take into account the Inverse Orbital Edelstein effect. In fact, the orbital contribution should exist in our case due to the spin-orbit coupling in the permalloy layer, which converts some spin flow into an orbital angular momentum flow. Interestingly, considering only 8% of orbital contribution to the total IEE conversion efficiency χ_{xy}^{tot}, is enough to suppress the sign change stemming from the reverse spin chirality of some bands. In Figure 4.30, we plot the total conversion efficiency for both sets of measurements with spin pumping and spin Seebeck, which can be accounted for by taking respectively 8.2% and 7% of Orbital contributions of the total conversion efficiency[36] χ_{xy}^{tot}.

Furthermore, the angular dependence of the IEE signal can also be understood in the framework of these two contributions to the IEE signal. As a first consequence, this additional orbital contribution is mainly driven by a k-linear Rashba term even at $V_g > 200V$, so that a purely tangential IEE current is expected by the orbital effects which agrees with the experimental findings (see Figure 4.18 $\&$ 4.19). Moreover, the anisotropy of the orbital Edelstein effect signal around the avoided band crossing points ($V_g \sim 200V$) is greater and opposite to the one displayed by its spin counterpart[37] (see Figure 4.31). Thus, when adding 8% of the orbital Edelstein contribution to 92% of the pure spin contribution, one obtains an anisotropy factor of 5, which is rather close to the factor 6 observed in our measurements (see Figure 4.26). Hence, it

[36] The percentage of orbital versus spin contributions, is roughly equivalent to the ratio between the crystal field potential, allowing for the interaction between the lattice and the orbital angular momentum of the electron, and the spin-orbit strength.[54]

[37] It is around a factor of 3 as estimated from Figure 4.31

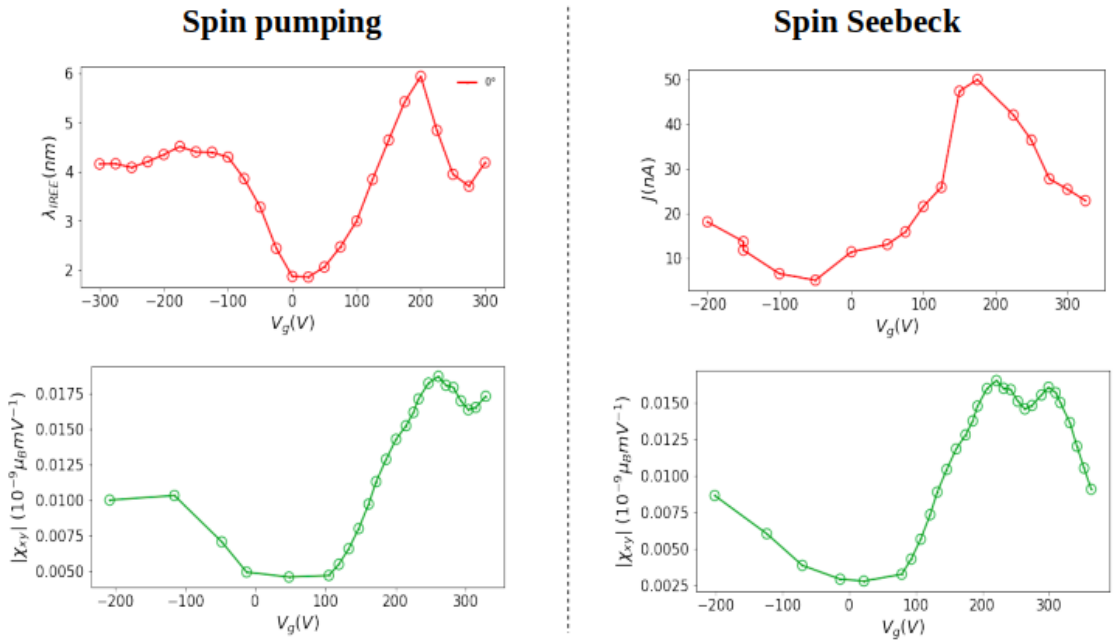

Figure 4.30: (Top left) gate-dependence of λ_{IEE} and (top right) charge current measured in the spin Seebeck experiment. Figures in the bottom represent the computed Edelstein efficiency extracted from Johansson et al.[203] considering 8.2% (bottom left) and 7% (bottom right) of orbital Rashba contributions along with the inelastic lifetimes from Fête et al.[175]

seems that the whole picture is consistent with our data.

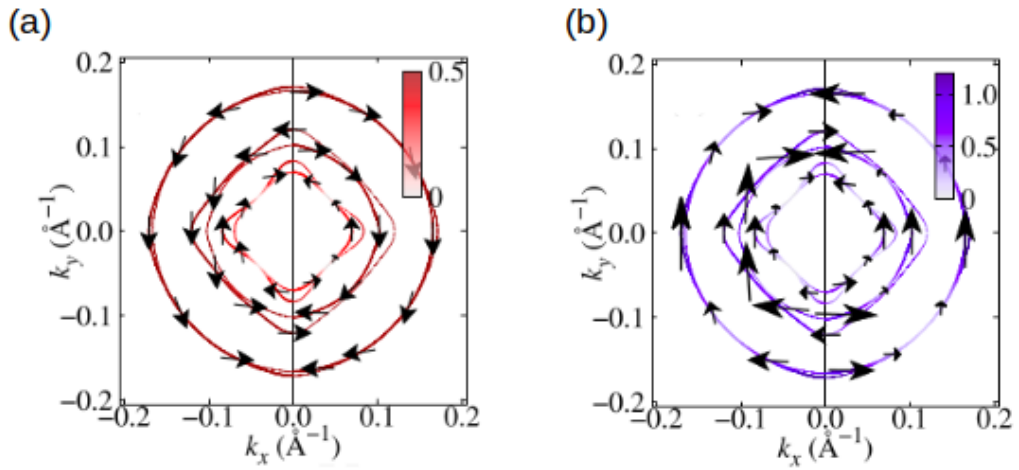

Figure 4.31: Evidence of the anisotropic spin and orbital splitting for $SrTiO_3$ based 2DES.(a) Spin texture and (b) orbital texture at $E_f = -53meV$.[203]

It is also important to note that the tunnel barrier can be detrimental to the filtering of the small orbital contributions. In particular, the amorphous nature of the AlO_x barrier which was used in previous studies where no orbital contribution was reported on the IEE signal. In contrast, we believe that our well crystallized 5 u.c thick LAO barrier transmits the orbital part much more efficiently.

4.3.4 The spin lifetime in LAO/STO

The large λ_{IEE} reported for LAO/STO is rather surprising, knowing that the Rashba splitting in LAO/STO interface was reported to be at least two orders of magnitude lower than that measured in Ag/Bi, albeit λ_{IEE} in LAO/STO is at least 1 order of magnitude higher than that measured in a sample of Ag/Bi, as shown previously[200, 199]. However, one should recall that $\lambda_{IEE} \sim \alpha_R \tau_e$, is also dependent on the carrier lifetime, which is estimated to be in the order of $\tau_e \sim 1ps$[175], at least two order of magnitude higher than Ag/Bi where $\tau_e \approx 10fs$.[199]

To gain further insight in this astonishing difference in the carriers relaxation rate between these different Rashba systems, one needs to investigate the transport properties of the conducing electrons at these Rashba interfaces. In the case of a perfectly isolated 2DES, only the electron scattering relaxation time should be considered, but because our 2DES is not perfectly isolated from its environment, electrons can leak out through the tunneling barrier into the adjacent metallic layer where these electrons will be scattered at much faster rate $\tau_e \sim 10fs$. In this picture, the effective carriers lifetime τ_{eff} is characterized by two different channels. The first being the escape time τ_{esc} through the tunneling barrier, and the second is the momentum relaxation in the 2DES τ_e resulting in the following expression for τ_{eff}:

$$\tau_{eff} = \frac{1}{\frac{1}{\tau_{esc}} + \frac{1}{\tau_e}} \tag{4.12}$$

In the case of a long escape time $\tau_{esc} \gg \tau_e$, only the electron scattered within the 2DES will participate into the carriers lifetime, which is the optimal situation. Whereas in the case of a short escape time $\tau_{esc} \ll \tau_e$, the carriers lifetime will be provided by the electron scattering time in the adjacent metallic layer. In this regard, the carriers life time in Ag/Bi interface will correspond to the latter case. Whilst, in the case of LAO/STO, the carriers escape lifetime is given by $\tau_{esc} = (RAe^2m)/(2\pi\hbar^2)$, which is estimated to be in the range[38] of $\sim 1ps$, which corresponds to the same order of magnitude as τ_e, which is estimated from transport measurement to be in the order of ~ 1 to 10 ps[175]. This approach explains quantitatively the long electron life time observed in LAO/STO.

Another important question is also of interest, which is related to the spin injection mechanism in LAO/STO, in our case the spin transparency of the LAO layer seems to be independent of the thickness of the LAO barrier[34], in stark contradiction with the spin tunneling paradigm, where the injected spin current would decay with the barrier thickness.

To further clarify this contradiction, we need to invoke the results shown by Reyren et al.[242] where a

[38] Given that $RA = \rho t_{LAO} \approx 25\Omega \cdot \mu m^2$ for a 5 u.c LAO layer

resonant tunneling in the LAO barrier was reported to amplify the spin accumulation signal, due localized states in LAO layer which are strongly coupled to the 2DES at the interface. Thus localized states in the LAO barrier can play an important role in the spin injection mechanism in LAO/STO where strongly coupled localized states in the insulating LAO barrier will participate into the spin injection mechanism, through exchange coupling .

Similarly, Cerqueira et al.[33] have demonstrated that coupled localized states in n-Si barrier can enhance the injected signal in the Pt layer compared to a system without the n-Si barrier. They even reported a very small variation in the ISHE signal when changing the thickness of the n-Si layer as shown in Figure 4.32, where similar results are observed for both thicknesses of $37nm$ and $124nm$. Thus, localized states in the LAO barrier can explain the discrepancy observed between our results and the simple tunneling model[39].

To summarize, the long relaxation lifetime of the carriers in LAO/STO can be attributed to the low carrier concentration in the 2DES which is quite isolated from the outside charge reservoirs, thanks to the insulating barrier of LAO. In addition, it should be noted that the spin injection mechanism through an insulating barrier of LAO can be explained by a chain of weakly coupled localized states, which can be promoted by defects or impurity present during the growth of the insulating barrier. In order to further investigate the electron relaxation rate at the interface of LAO/STO, we need to perform a new kind of measurement, using ultra-fast optical techniques, which will allow us to study the ultra-fast dynamics of the spin-to-charge conversion in LAO/STO, and also to give an estimation of the electron relaxation rate.

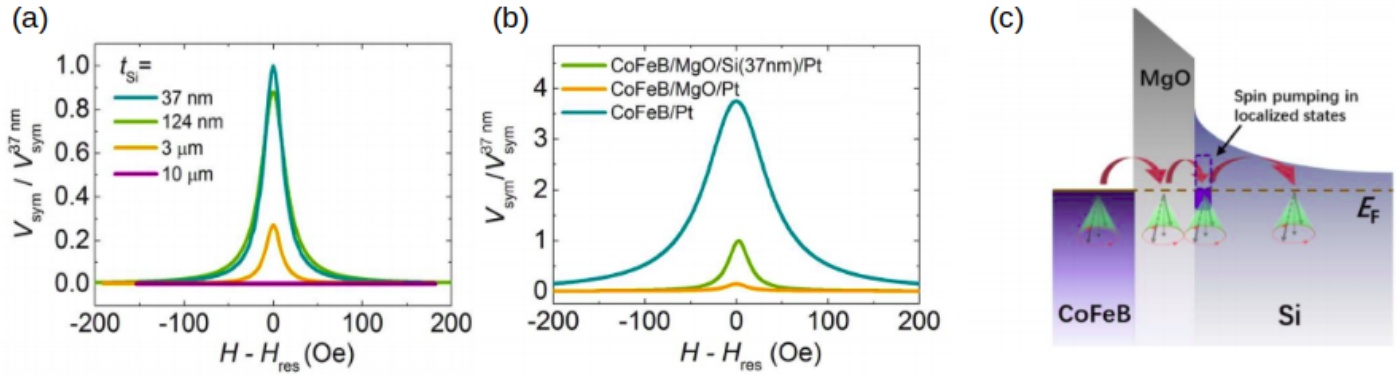

Figure 4.32: Spin pumping mechanism through localized states at a MgO|Si interface.(a) ISHE signal for different thicknesses of the n-Si interlayer.(b) Comparison of the ISHE signal for three different samples. (c) A sketch illustrating the spin injection mechanism through the localized states at the MgO|Si interface.[33]

[39]With an exponential decay for the injected spin current

4.4 Conclusion

To sum up, we have reported in this Chapter the possibility to modulate the IEE signal at the interface of LAO/STO, through electrostatic doping, as well as a strong anisotropy of the angular dependence of the spin-to-charge conversion signal. This is linked to a complex multi-band effect which is a salient feature of transition metal-oxides.

In addition, our measurements unravel the existence of a dominant orbital Eldelstein effect contribution to the IEE signal. In this regard, we have postulated an 8% orbital angular momentum injection which explains all the features of the back-gate and angular dependences of the IEE signal including its sign, its strong anisotropy and its directional dependence. Interestingly, we have been able to draw a link between the back-gate and angular dependences of the IEE signal and the band structure of LAO/STO. This is particularly visible when the chemical potential is near the avoided band crossings where the IEE signal displays a strong 4-fold symmetry.

Furthermore, it seems that the orbital part of the IEE signal, which is potentially the dominant contribution, could be much better harnessed in order to maximize the conversion efficiency. It is also important to note that the electron relaxation time in the 2DES at the LAO/STO interface, is of central importance in the strong spin-to-charge conversion efficiency recorded at the LAO/STO interface. In order to design the future highly efficient spin-to-charge converters, one needs to take into account the various parameters which can be exploited such as the anisotropy effects, the orbital contribution to the IEE signal and the spin relaxation rates. Obviously, much larger conversion efficiencies could be achieved if the orbital part of the incoming angular momentum, as well as the electron relaxation times can be maximized.

Chapter5

Time-resolved measurements of the spin-to-charge inter-conversion signal

Contents

5.1 Introduction

In this chapter we attempt to investigate the ultrafast dynamics of the spin-to-charge conversion process in LAO/STO. To do so, we need to generate a picosecond burst of a spin current matching the timescales behind the spin-to-charge conversion mechanism in LAO/STO[1], which is estimated to be around $\sim 1ps$ from magneto-transport experiments[193, 175]. However, we need an additional experimental method which will allow us to study the ultrafast dynamics behind the spin-to-charge conversion at the picosecond timescale in order to answer some fundamental questions related to the spin lifetime τ_s within the 2DES at

[1] See Chapter 5 section 5.3.4

LAO/STO interface, and to elucidate the various mechanisms at play when the spin is converted into a charge.

In this chapter we will present the first preliminary results in order to answer to these opened questions. First of all, because we want to study our systems at timescales which are very short ($\sim 1ps$), we rely on the high time resolution provided by ultrafast lasers($\sim 150fs$), which allow us to study the ultrafast dynamics behind the spin-to-charge conversion. In this context, this chapter will provide the first experimental findings using various methods in order to characterize the spin-to-charge conversion at different timescales. In the course of this Chapter we will present three optical methods used to detect a picosecond spin current burst which is generated by taking advantage of the ultrafast demagnetization mechanism.

In this regard, we will first investigate the ultrafast demagnetization process in a ferromagnetic layer which is the basic mechanism at the origin of the optically induced picosecond spin current burst. Secondly, we will introduce a first measurement technique allowing us to probe a picosecond spin current burst through the Magneto-Optical Kerr effect (MOKE). Then, we will present a second technique which relies on the generation of the Second Harmonic signal in order to probe the electric field in heavy metals thanks to the spin-to-charge conversion. Lastly, a third technique to detect spin currents at the picosecond timescale relies on the detection of THz radiations which can be generated through the spin-to-charge conversion mechanism in an adjacent layer.

5.2 Ultrafast demagnetization and Hot carrier injection

Following the absorption of a femtosecond optical pulse, a ferromagnetic material undergoes a process called ultrafast demagnetization, where the magnetization of the ferromagnetic layer drops rapidly in the $100fs$ time scale, and if we place an adjacent layer in contact of the ferromagnet, a fraction of the magnetization will be transferred to the adjacent layer. In this section, we will present both the local mechanisms which are associated with the demagnetization processes within the ferromagnet, and the non-local mechanism which can be tied to the transport of the hot carriers towards the adjacent layer.

Beaurepaire et al.[7] were the first to report the ultrafast demagnetization effect using nickel thin films, other ferromagnetic materials display behave similarly as shown by various later studies[26, 16, 96]. In order to understand the relaxation mechanisms of the electrons and spin systems during the ultra-fast demagnetization one needs to separate the thermalization and the coherent processes. The former relates to the three temperature model which includes three interacting reservoirs (electrons, spins, and the lattice) which thermalize at different time scales, so that the demagnetization process takes place after the charge

carriers relaxation time $\sim 50fs$. It appears that the thermalization process plays an important role in the demagnetization mechanism through the spin orbit coupling reported e.g. by Boeglin et al.[16] using XMCD measurements on CoPd film, as well as the exchange splitting between the majority and minority spin populations studied e.g. by Carley et al.[26] using angle-resolved photoemission spectroscopy on gadolinium . On the other hand , the coherent processes are associated with the laser pump which can influence the magnetic ordering in our ferromagnetic layer. Bigot et al.[10, 11] have demonstrated that these coherent processes can be understood in the framework of the coherent interaction between the photon field and the spins through the spin-orbit interaction. This modifies the magneto-optical response which was investigated using time-resolved magneto-optical Kerr effect measurements on nickel and CoPt samples.

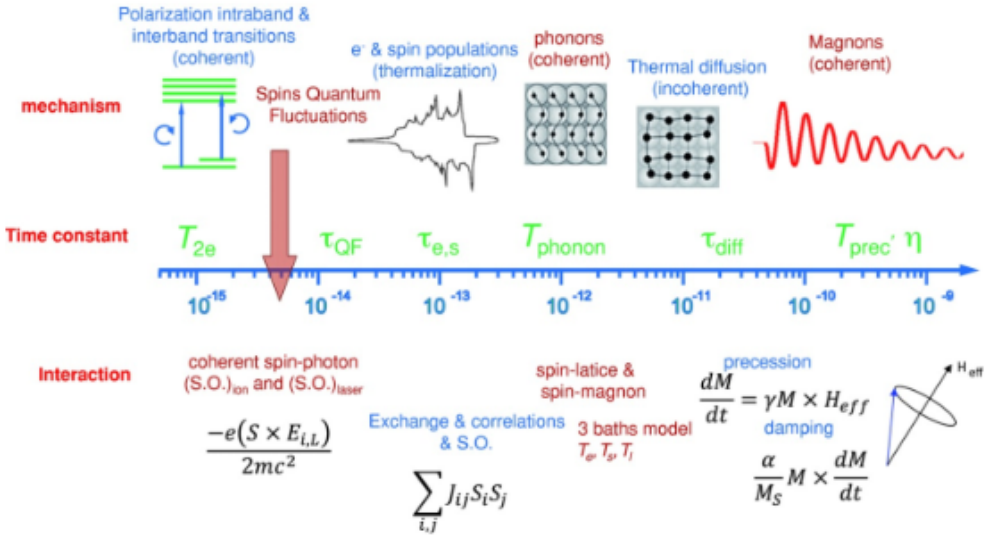

Figure 5.1: Various processes associated with the magnetization dynamics at different time scales.[11]

In Figure 5.1, we plot a sequence of various relaxation processes taking places at various time scales. Shortly after the laser excitation hits the ferromagnet, the electrons are selectively excited to higher energy bands, in a coherent process decaying very rapidly with a dephasing time around ~ 0.1 to $1fs$, and the uncertainty over the spin density distribution takes place due to quantum fluctuations. After that, the electrons relax to lower energy states, near the Fermi level, where they undergo inelastic scattering due to the Pauli exclusion principle this process can last around $\sim 100fs$. Later, the interaction between the electron, spin and phonon reservoirs transfer the energy to the lattice, leading to the longer time scale for the full demagnetization process around $\sim 1ps$. Finally, through elecron-magnon interactions the ferromagnetic layer is remagnetized with the typical timescale of the magnetization precession around $\sim 1ns$.

As we have seen previously, the ultrafast demagnetization process in a ferromagnetic layer creates ballistic spin polarized hot electron which exist for around $\sim 1fs$ after the first laser burst, shortly after they

transfer their angular momentum to the lattice through the electron-phonon coupling for the next $200fs$. Importantly, if one places a heavy metal layer[2] in contact with the ferromagnet, a portion of the angular momentum will be expelled form the FM into the metal and disappear due to fast spin relaxation mechanisms. At the same time, some of it will be converted into charge[3]. So by studying the demagnetization of the ferromagnetic layer one can deduce the amount and time scale of the spin population lost inside the heavy metal layer[42, 119]. It is also important to note that various mechanisms are behind the creation of non-equilibrium hot charge carriers upon the femtosecond laser excitation. In fact, these mechanisms can be separated into local electronic processes which occur inside the ferromagnetic layer and have been discussed previously[4], and non-local processes[6, 98] which correspond to various spin transport phenomena into the adjacent heavy metal layer through mechanisms such as conduction, heat diffusion or state-filling transport which corresponds to transfer of spin polarized excited states into the adjacent heavy metal layer as shown in Figure 5.2.

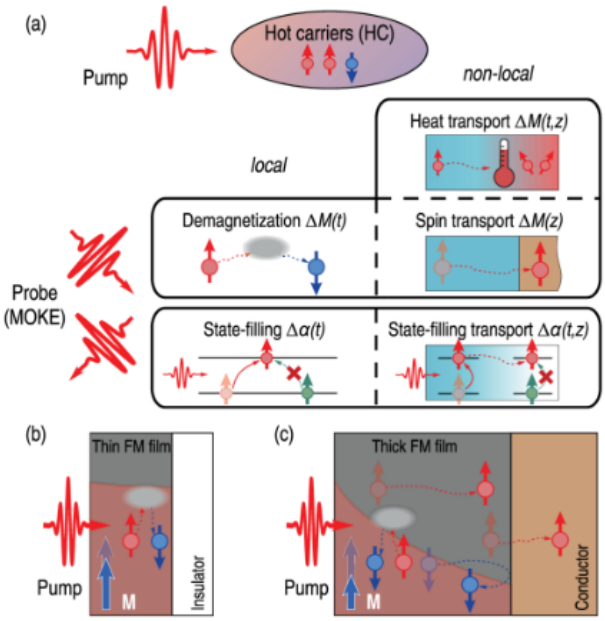

Figure 5.2: (a) Creation of hot carriers (HC) through both local and non-local electronic processes. Sketch of the effects of the femtosecond laser excitation on both (b) a FM/Insulating bilayer where only local processes exist and (c) a FM/Conducting bilayer where both local and non-local processes exist. The red shaded area corresponds to the laser profile inside the FM layer.[119]

To summarize, we have introduced here that the ultrafast demagnetization mechanism can be derived into various processes with various response times. In fact, it has been reported that at least 80% of the magnetization is transferred to the lattice trough electron-phonon coupling in the first $200fs$ after the

[2]It can be any highly efficient spin-to-charge conversion system.
[3]Either through the ISHE/IEE
[4]see chapter 6 section 6.1

laser burst[43]. In addition, thanks to the non-local mechanisms, a picosecond spin current can be injected within an adjacent layer, which was demonstrated in previous experiments[6, 98, 78]. In the case where the adjacent layer is a heavy metal, the injected picosecond burst will be converted into a charge current, thanks to the ISHE, which will be detected as a terahertz (THz) radiation, which was experimentally reported by Kampfrath et al. in Fe/Au heterostructures[78].

5.3 Time-resolved characterization of the Picosecond Spin Currents

5.3.1 Time-resolved MOKE experiment

The first method used to experimentally characterize the utrafast spin current relies on a time-resolved measurement of the magnetization of a ferromagnetic material at the time scale between $100fs$ to $1ns$, through the so-called Magneto-Optical Kerr Effect (MOKE) which will be introduced in the next section.

5.3.1.1 Magneto-optical Kerr effect

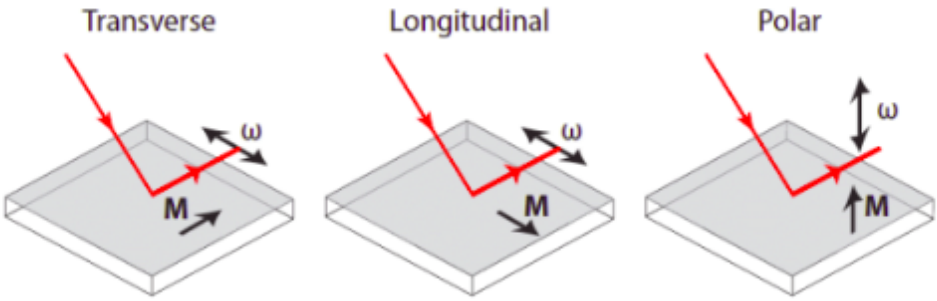

Figure 5.3: Various configurations of Magneto-Optical Kerr Effect (MOKE). **M** represents the magnetization of the ferromagnetic layer, while $\boldsymbol{\omega}$ represents the plane of incidence of the incoming light.

Due to the interaction between the laser light which is partly reflected on the surface of a ferromagnetic material and its magnetization, a change in the polarization as well as the intensity of the reflected signal is induced, This is mainly due to an anisotropic permittivity appearing in the the off-diagonal components of the permittivity tensor $\boldsymbol{\epsilon}$, so that the magneto-optical coupling is maximum when the magnetization is parallel to the propagation vector of the light[117]. This effect is known as the magneto-optical Kerr effect (MOKE) and it is very well suited to study the demagnetization of a ferromagnetic layer at the picosecond timescale through the analysis of the time-resolved Kerr rotation and ellipticity, which allows us to retrieve all relevant parameters related to the magnetization dynamics.[119]

5.3.1.2 Time-resolved MOKE experiment: experimental set up

The ultrafast demagnetization process can be investigated thanks to the time-resolved MOKE experiment which relies on a pump-probe measurement where the laser beam is split into a $70/30$ power ratio between the laser pump beam and the probe beam. In this case the pump beam is set at 200mW through the attenuators and $\lambda = 800nm$ and impinges at normal incidence to the surface of the sample (see Figure 5.4) with a fluence of $200\mu J/cm^2$, while a probe beam is sent on the sample at a 45° incident angle[5], with a fluence of $50\mu J/cm^2$. After being reflected on the surface of the sample, the light beam goes through either a half-waveplate or a quarter-waveplate[6] which allows for the measurement of TR-MOKE signal either in rotation or in ellipticity. Then, the light beam goes through a Wollaston prism[7] which allows for the separation of the light beam into ordinary and extraordinary light beams which are collected by a balanced photodiode that compares the intensity of those two light beams (see Figure 5.4).The laser beam is produced by Ti:sapphire laser beam (LIBRA) with a laser pulse of $150fs$ and $\lambda = 800nm$. In the case of the probe beam, its wavelength is converted to $\lambda = 400nm$ after passing through a β-BBO crystal, then it goes through a polarizer and attenuators in order to tune the polarization and the power of the incident light beam as shown in Figure 5.4. In order to study the static effect, the magnetic field is rotated in the plane of the sample, and rotation and ellipticity of the light polarization are analysed by the difference of intensity detected by the balanced photodetector between the two channels, which follows a sine curve, as shown in Figure 5.5. In order to perform time-resolved measurements, the time delay between the pump and the probe is adjusted through a delay stage at a constant magnetic field, as shown in Figure 5.4. The temporal evolution of the MOKE signalis then reconstructed by measuring the signal at various time delays. In fact, the MOKE signal is measured with a balanced detector connected to a lock-in amplifier locked on the frequency of the beam chopper set at 125 Hz, placed in the pump beam so that only the variations in the signal coming from the pump will be detected. Additionally, in order to retrieve the true demagnetization signal from the measurements one needs to subtract all non-magnetic contributions. This is achieved by subtracting the measured signal for two opposite directions preferably at maximum intensity i.e at 0° and 180°, to maximize the contrast of the signal. Moreover, the demagnetization signal is normalized by the amplitude of the MOKE signal in the absence of the pump. The MOKE signal shown in Figure 5.5 was measured using a lock-in amplifier which was synchronized with the frequency of the chopper on the incident laser beam equal to a harmonic of the repetition rate of 1 kHz (usually we chose

[5]Since the magnetization of thin film is in-plane, the MOKE signal is only sensitive to the parallel component of light with the in-plane magnetization.

[6]See Appendix E section e2 for more details

[7]See Appendix E section E1 for more details

125 Hz). We should also note that the amplitude of the measured MOKE signal at saturation was used to normalize the variations of demagnetization curve, as shown in Figure 5.5.

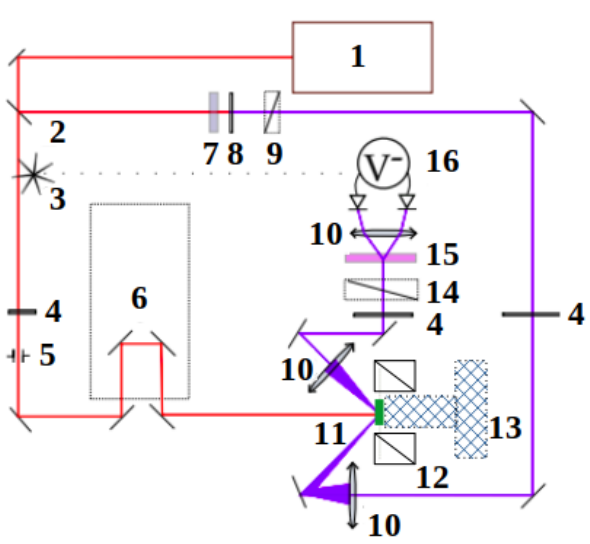

1. LIBRA
2. Beam Splitter 90/10
3. Light chopper
4. Attenuators
5. Diaphragm
6. Delay stage
7. BBO
8. High pass filters
9. Polarizer
10. Convergent lenses
11. Sample
12. Electromagnet
13. Cryostat
14. Waveplate (λ/2 or λ/4)
15. Wollaston prism
16. Balanced diode detector

Figure 5.4: A sketch illustrating a TR-MOKE experiment.(Adapted from [35])

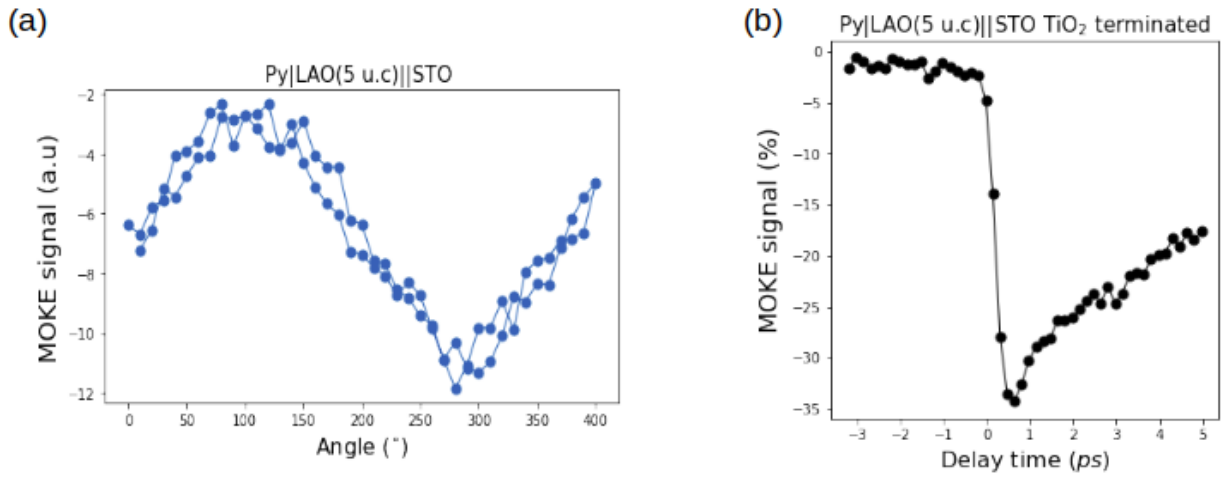

Figure 5.5: (a)MOKE signal measured in rotation on a sample of Py|LAO(5u.c)|STO for two scans of the magnetic field which was rotated in the plane of the sample.(b)Normalized TR-MOKE signal measured on a sample of Py|LAO(5u.c)|STO.

5.3.1.3 TR-MOKE measurements

In this section we will present various demagnetization curves obtained from various samples of Py|LAO(5u.c)|STO with and without the 2DES at the interface. Before digging into the experimental results we will first give a brief overview on the various parameters that can be retrieved from a demagnetization curve.

5.3.1.3.1 Fitting TR-MOKE curves The ultrafast demagnetization processes occur shortly after the laser pulse hits the sample, usually in less than 2 ps. After that , the sample slowly remagnetizes through typical magnetization precession processes in the nanosecond range most likely triggered by the ultrafast changes in the magnetic anisotropy field. In order to take into account those two effects, we can model our signal using the following equation:

$$\frac{\Delta M(t)}{M_0} = -A_d e^{-t/\tau_d} - A_p cos(2\pi\nu t + \phi) e^{-t/\tau_p} \tag{5.1}$$

where $\Delta M(t)/M_0$ is the relative variation of the MOKE signal, A_d is the maximum demagnetization, A_p is the amplitude of the precession, τ_d is the remagnetization time, τ_p is the damping time, ν is the frequency of the precession, and ϕ is the phase of the precession motion.

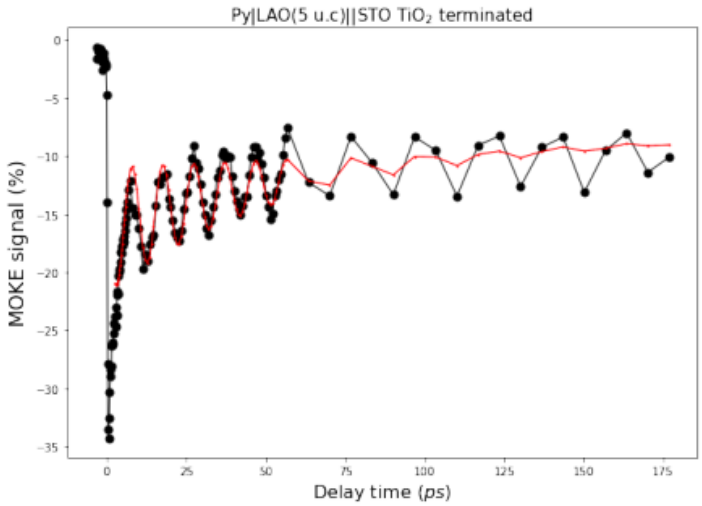

Figure 5.6: Normalized TR-MOKE signal measured on a sample of Py|LAO(5u.c)|STO.

In Figure 5.6, we plot the ultrafast demagnetization signal of a sample of Py|LAO(5u.c) | STO in rotation. We observe a rapid decrease in the magnetization in less than $< 1ps$ with a maximum demagnetization amplitude $A_d \simeq 35\%$ and a remagnetization time $\tau_d \simeq 800ps$ in the nanosecond time scale, as we would expect. Meanwhile, the precessional part of the signal seem to be less well reproduced by the fit due to the fact that model considers the norm of the magnetization to be constant, which is not the case in reality. So, we can retrieve the amplitude of the precession on the MOKE signal $A_p \simeq 10.8\%$, and the ferromagnetic frequency $\nu \simeq 13.6GHz$[8] .

[8]From Kittel's Formula (see section 4.2.1.1.2), we retrieve a frequency at $H = 1,5KOe$ equal to $\nu \simeq 12.6GHz$

5.3.1.3.2 TR-MOKE signal in LAO/STO samples The demagnetization curve of a sample of Py|LAO(5u.c)|STO has been measured by TR-MOKE, and was compared to two other samples of CoFeB|Pt and CoFeB|MgO|Pt, as shown in Figure 5.7. Those measurements reveal a similar magnetization drop for both Py|LAO(5u.c)|STO and CoFeB|Pt, whereas the sample of CoFeB|MgO|Pt displays a smaller drop of magnetization. Futhermore, in order to highlight the effect of the 2DES at the interface of LAO/STO we need to compare the TR-MOKE signal for two different samples of LAO/STO with and without the 2DES at their interface. In Figure 5.8, we plot the TR-MOKE signal for both samples of LAO/STO, which unveils a slightly higher drop in the magnetization in the case of TiO_2-terminated STO (35% magnetization drop) compared to that with SrO-terminated STO (30% magnetization drop). However, the remagnetization time for both samples seems to be in the same range at the nanosecond timescale. Furthermore, the spin coherence time exhibits a slightly higher value in the case of TiO_2-terminated STO ($\tau_p \simeq 50.4ps$) compared to SrO-terminated STO sample ($\tau_p \simeq 25ps$) at room temperature, as shown in Figure 5.8.

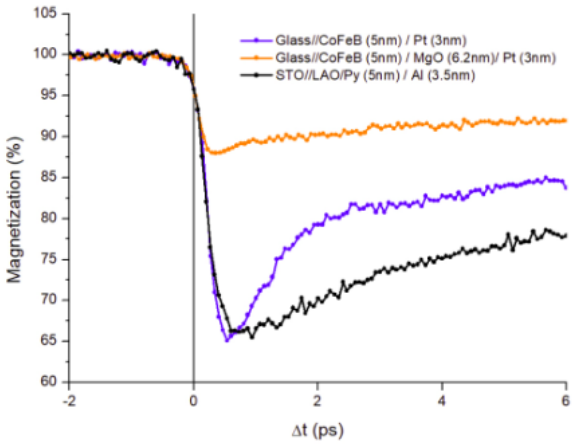

Figure 5.7: Comparison of the ultrafast demagnetization in three different samples.

5.3.1.4 Discussion of the TR-MOKE measurements

From Figure 5.8, we observe that the demagnetization in the LAO/STO sample with TiO 2 -terminated STO is higher than the one with SrO-terminated STO. This difference can be ascribed to the presence of the 2DES at the interface which seems to provide an additional spin reservoir leading to an increase in the demagnetization of the FM layer. However, the apparent larger damping of the FMR oscillations for the SrO-terminated sample is not consistent with the increased exchange (loss) of angular momentum with the 2DES.

We should also note that when comparing the three different curves as shown previously in Figure 5.7, one

can link the drop in the magnetization to the transfer of a spin population into the 2DES/HM layer, which is clearly evidenced by the small drop in the magnetization when an MgO barrier is separating the CoFeB layer from Pt layer, thus preventing the magnetization transfer from the ferromagnet to the HM layer. However, when comparing the remagnetization curves for both samples of Py|LAO|STO and CoFeB|Pt, we observe a much faster remagnetization in the latter case. This points to a quite different relaxation process between CoFeB|Pt and Py|LAO|STO very likely linked to the much larger spin relaxation time in the latter[193, 200].

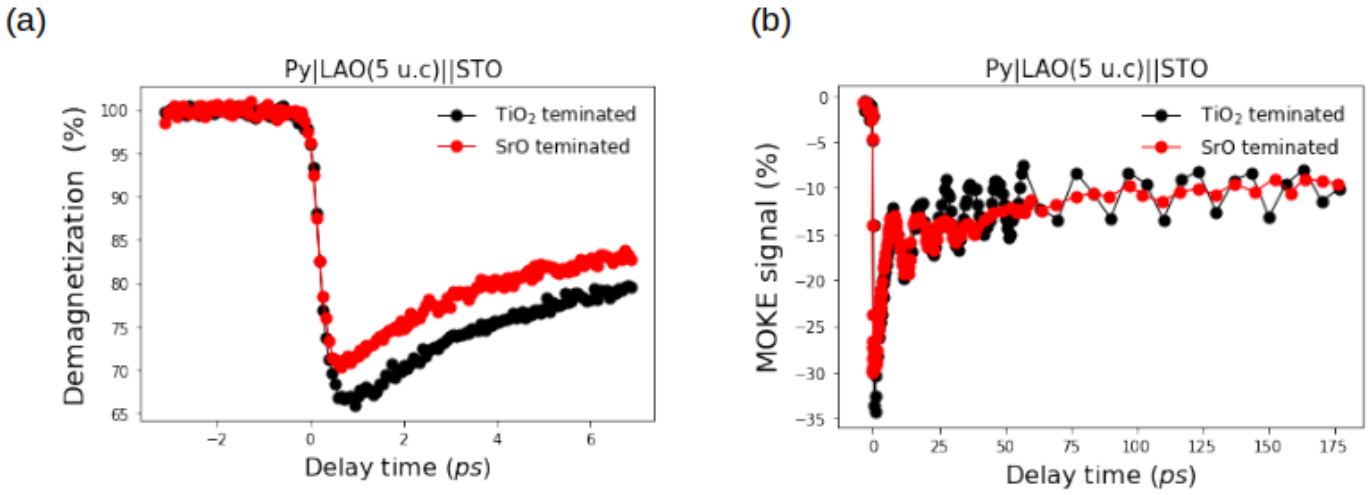

Figure 5.8: (a) Demagnetization curves and (b) TR-MOKE signal measured in two samples of Py|LAO(5u.c)|STO with both TiO_2 and SrO terminated STO at room temperature.

5.3.2 Time-resolved SHG experiment

5.3.2.1 Imaging of the electric field with Second Harmonic generation (SHG)

In the electric dipole approximation, a non-linear contribution to a leading order comes from the second harmonic term [9], which can be associated to either spatial or time symmetry breaking[41]. Since an in-plane electric field breaks the spatial symmetry, one can expect to measure a second harmonic signal emanating form the electric field generated through the spin-to-charge conversion of the picosecond spin current through the ultrafast demagnetization process. The experimental technique used to probe the electric field within the heavy metal layer relies on non-linear optics and the generation of higher harmonics of light and particularly the second harmonic generation at twice the frequency 2ω of the incoming light[149]. Hence, the incoming laser light at ω will couple to the in-plane electric field through the third order susceptibility tensor $\overline{\overline{\overline{\chi}}}$, generating an electric dipole $\mathbf{P^{2\omega}}$ at a frequency 2ω given by :

[9] Which is proportional to a third order electric susceptibility tensor $\overline{\overline{\overline{\chi}}}$, for which we give a detailed expression, in Appendix F, in the case of 4mm point group symmetry, which corresponds to the symmetry at the interface of LAO/STO.

$$\mathbf{P}^{2\omega} = \overline{\overline{\chi}}\mathbf{E}^{\omega}\mathbf{E}^{\omega}\mathbf{E}_{\text{ISHE}} \tag{5.2}$$

It is also important to note that the generated electric field $\mathbf{E}_{\text{ISHE}}$ due to spin-to-charge conversion can be at frequency Ω, so that the generated light will be emitted at frequency $|2\omega \pm \Omega|$[103]. However, if one considers a slowly varying electric field ($\Omega \ll \omega$), the generated light wave will still be seen as the second harmonic signal ($|2\omega \pm \Omega| \simeq 2\omega$).

5.3.2.2 Time-resolved SHG imaging: experimental set up

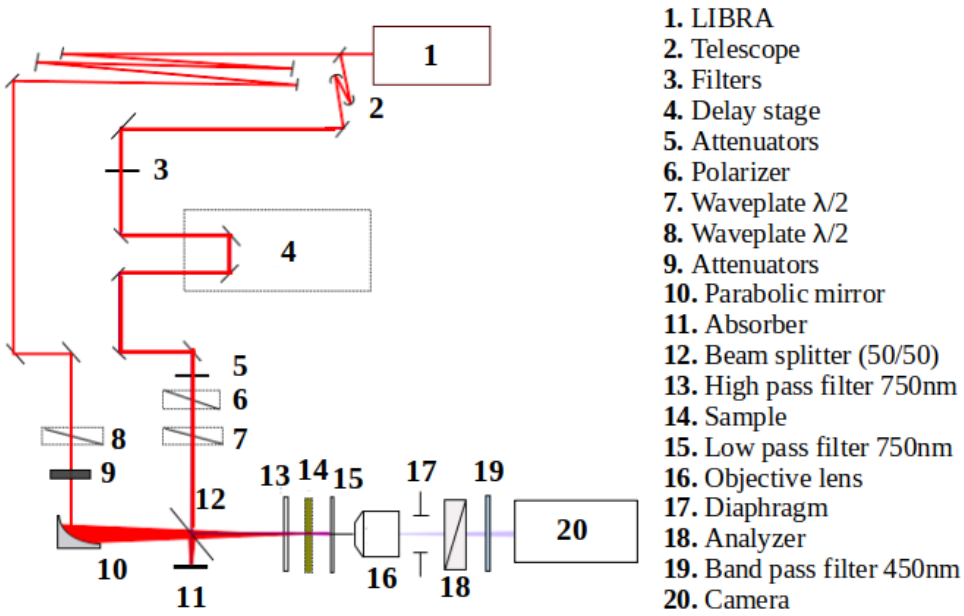

Figure 5.9: A sketch illustrating a TR-SHG experiment.(Adapted from [35])

In order to perform time-resolved imaging of the electric field at the interface of FM/HM samples, we have developed a pump-probe experiment. In our case, we set both the pump and the probe beams at the same wavelength $\lambda = 800nm$. The pump beam is sent through some filters and attenuators so that the power is set at $P = 200mW$ then it is focused on the sample by a parabolic mirror, as illustrated in Figure 5.4. At the same time, the probe beam is set at $P = 200mW$, delayed while going through a delay stage and sent to the sample by a 50/50 beam splitter (see Figure 5.9). The Second Harmonic signal generated by the sample is then collected by a camera after being filtered and focused[10], as shown in Figure 5.9.

[10]It is also interesting to note that the SHG signal measured by the camera is normalized with respect to the angular dependence of the laser intensity while varying the angle of the polarizer (see Figure 5.9).

5.3.2.3 Comparison between Pt, MgO and Cu

It is important to note that the second harmonic signal associated with the in-plane electric field due to the spin-to-charge conversion was never observed previously in the literature. Therefore, we will present in the following the preliminary results obtained by comparing three different well-known systems, which are CoFeB|Pt, CoFeB|Cu|Pt and CoFeB|MgO|Pt heterostructures.

Since we are measuring the TR-SHG signal using the pump and the probe beams at the same wavelengths ($\lambda = 800nm$), one would expect that at $t = t_0$ we will observe a maximum intensity signal corresponding to the cross-correlation of both laser beams, as shown in Figure 5.10 a. The highest signal is reported from the sample of CoFeB|Pt, where we observe a rapid decrease of the signal just after the first $200fs$ from $t = t_0$ which can be associated with the effect of the demagnetization on the CoFeB|Pt interface. Furthermore, we notice that the SHG signal emitted by a sample of CoFeB|Cu|Pt displays a similar shape with a lower amplitude compared to CoFeB|Pt. However, in the case of CoFeB|MgO|Pt, we observe that the SHG signal exhibits a different shape from to the other two samples, without the rapid demagnetization curve measured previously, and with a similar amplitude to the one reported in the sample with Cu spacer. Additionally, we report a cosine-like shape angular dependence of the SHG signal with respect to the magnetic field in a sample of CoFeB|Pt, which is illustrated in Figure 5.10 b, highlighting the magnetic nature of this interface signal. Furthermore, when measuring the angular dependence of the SHG signal while rotating the position of the analyzer (see Figure 5.10 c) we observe a strong change at 90° angle of the analyzer at $t = t_0$, which can be associated with the cross-correlation happening at $t = t_0$. In the next section, we will try to give a brief analysis of the aforementioned results.

5.3.2.4 Discussion of TR-SHG

It seems that the measured SHG signal has a magnetic nature, and from Figure 5.10 a, we can assume that its strength is linked to the CoFeB and Pt interface. In fact, the explanation of the measured signal seems to stem from the strong magneto-plasmonic effect at the interface of CoFeB and Pt[168, 144]. Indeed, when inserting a Cu or an MgO spacer layer between the CoFeB and Pt layers, we observe that the effect is considerably reduced. However, when inserting the MgO spacer, we also observe that the signal no longer displays the rapid demagnetization curve that can still be observed in the sample with the Cu spacer. This can be related to the fact that the MgO barrier does not allow for the spin to be transferred to the adjacent Pt layer contrary to Cu barrier.

To conclude, we can say that the measured SHG signal does not allow to clearly identify the built-in spin

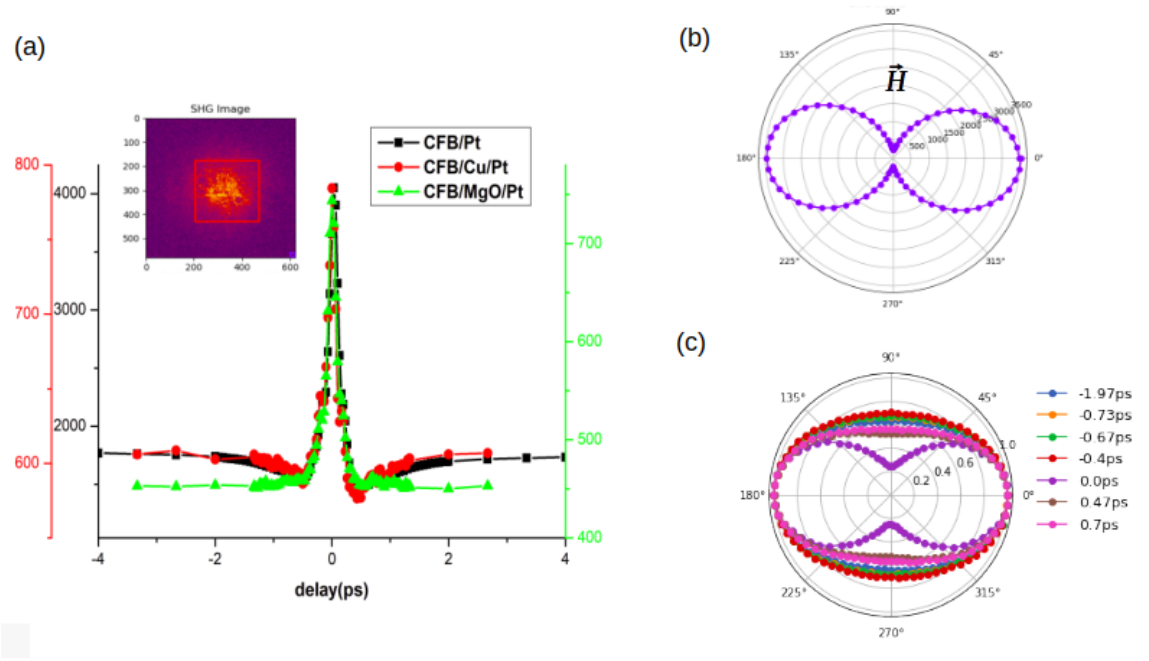

Figure 5.10: Comparison of TR-SHG signal for three different samples. (a) The TR-SHG signal for CoFeB|Pt, CoFeB|Cu|Pt and CoFeB|MgO|Pt. In the inset we plot the SHG image obtained using a form a CoFeB|Pt sample at $t = t_0$. (b) The magnetic angular dependence of the SHG signal, for a sample of CoFeB|Pt, at $t = t_0$ and where the polarizer and analyzer are set at perpendicular orientations. (c) The angular dependence of the SHG signal versus the orientation of the analyzer, for a sample of CoFeB|Pt, at various time delays, the polarizer was set at $90°$ angle.

accumulation at the interface, which is seemingly overwhelmed by the magneto-plasmonic effect in the case of CoFeB|Pt. Hence, further measurements need to be undertaken with different systems where magneto-plasmonic effects are absent, such as CoFeB|Ta or CoFeB|Au.[144]

5.3.3 Highly efficient THz emitters

The ultrafast demagnetization of a ferromagnetic layer allows for the transfer of the magnetization[11] to an adjacent layer which can convert the picosecond spin current into a charge current. This operates in the THz regime thanks to the femtosecond timescale response of the spin-orbit coupling. As we have shown previously[12], there are various systems which can fulfill this role such as heavy metals[36, 78, 136] or Rashba interfaces[125]. It appears that some of these highly efficient spin-to-charge converters can display a similar THz emitter performance as the state of the art ZnTe crystals[160], allowing for a wide range of applications. In the next sections, we will investigate the THz emission produced by a 2DES at the interface of LAO/STO, after a brief overview of the basic principles behind THz detection.

[11] Since the angular momentum is conserved.
[12] See Chapter 4 section 4.1

5.3.3.1 THz generation

By sending a laser pulse through a $15nm$ thick permalloy ferromagnetic layer, a picosecond spin current burst is produced and transferred to the 2DES at the interface of LAO/STO interface, as shown in Figure 5.11. Since the IEE effect relies on the spin-orbit coupling, one would expect a very fast spin-to-charge conversion inside the 2DES so that the generated charge current has a temporal variation in the terahertz regime, as shown in Figure 5.11.

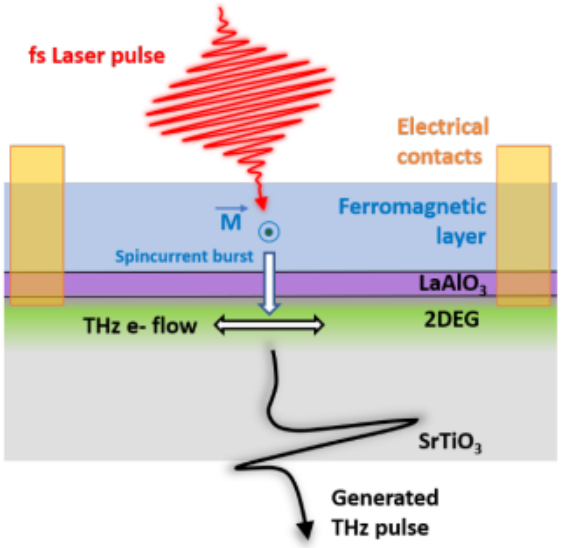

Figure 5.11: Schematics illustrating the mechanism behind the THz generation in an LAO/STO sample

5.3.3.2 THz generation: experimental set up

The THz radiation measurements were performed in the NOVA group at Institut des Molécules et Matériaux du Mans (IMMM) in collaboration with Vincent Juvé and Artem Levchuck, where they use an electro-optic sampling technique[148]. Hence, a piezoelectric crystal such as ZnTe is used in order to detect the THz emission thanks to the variations in the optical refractive indices when hit by a THz radiation. So the basic idea behind electro-optic sampling is to measure in a pump-probe fashion the electro-optical response of the piezoelectric crystal at various time delays. To do so, a laser beam ($P = 1W$) coming from Ti:sapphire laser with $100fs$ pulse duration and a repetition rate of 1KHz, is sent through a beam splitter where it is separated into pump and probe beams. The pump beam is used to hit the sample, placed inside a cryostat at $T = 10K$, in order to generate a THz radiation. It then goes through a Silicon beam splitter transparent only to the THz radiation, which is then collected by a parabolic mirror and sent onto the ZnTe crystal, as shown in Figure 5.12.

Meanwhile, the probe beam hits directly the ZnTe crystal after coming out of a delay stage in order to

perform time-resolved measurements at various time delays. Then, both the ordinary and the extraordinary components of the beam coming out of the ZnTe crytal are separated and measured by a balanced photodetector in order to reconstruct the Thz emission signal coming out of the samples.

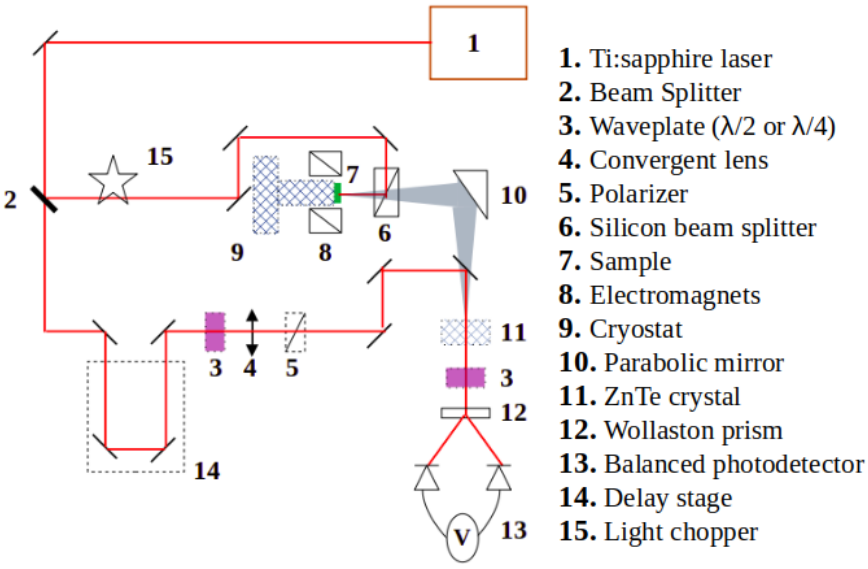

Figure 5.12: A sketch illustrating the THz detection set up.

5.3.3.3 Ultra-fast spin-to-charge interconversion at Rashba interfaces

In this section we will present results obtained when probing the spin-to-charge conversion signal at the interface of LAO/STO in the THz regime, in contrast to the spin pumping and spin Seebeck measurements presented in Chapter 5 which can only probe much longer time scales ($\sim 1ns$). In the present case, the THz radiation measurements can probe the signal at timescales between ~ 0.1 to $10ps$.

First, we will present the results obtained when measuring the THz radiations emitted by LAO/STO as a function of both backgate voltage and magnetization angle. Then, we will discuss these results, in the light of simulations of the temperature of the phonons and the electrons of our system.

5.3.3.3.1 THz measurements In Figure 5.13 a, we plot the electro-optical signal measured on ZnTe crystal thanks to the THz radiations emitted by a sample of Py|LAO(5u.c)|STO at $T = 10K$. We first notice that the THz radiation changes its polarization upon rotating the dc magnetic field to the opposite direction, as one may expect since the THz radiation at the interface is generated by the ultrafast spin current. In addition, the amplitude of the THz emitted by a sample of Py| LAO(5u.c)|STO is at least three orders of magnitude lower than that in CoFeB(5)|Pt. Meanwhile, the THz spectrum shows a broad emission spectrum centered around 1 THz for both samples, spanning until the cut off frequency of ZnTe

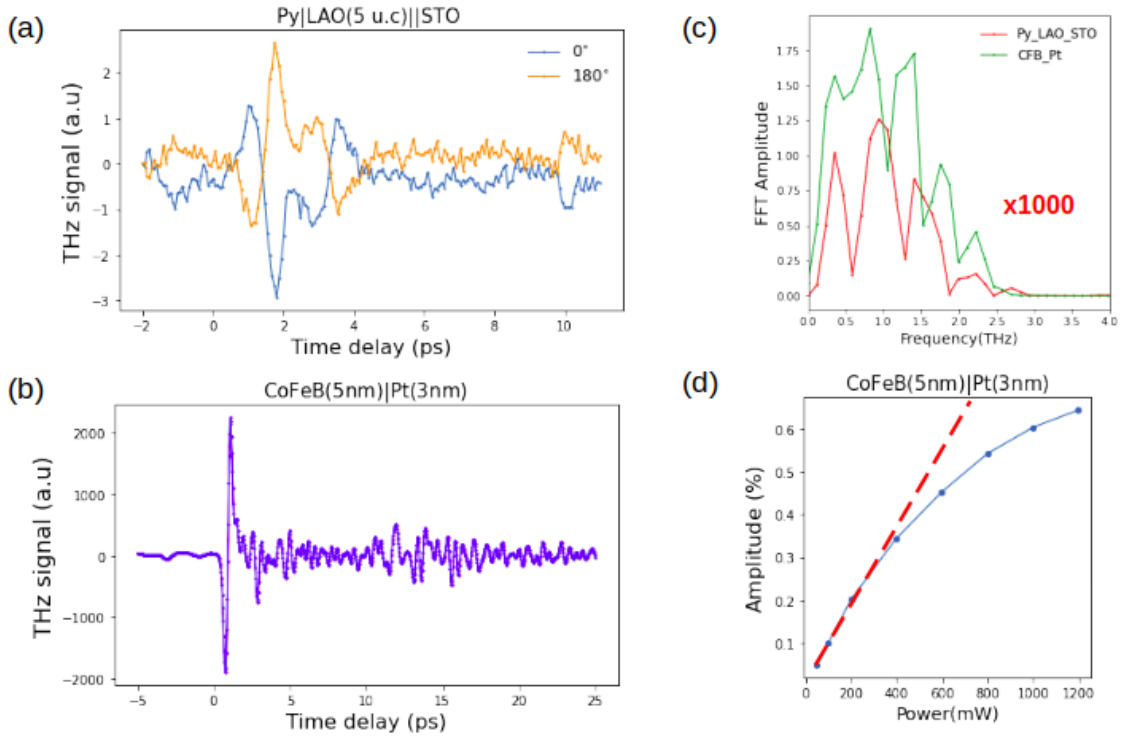

Figure 5.13: (a) THz signal measured in a sample of Py|LAO(5u.c)|STO at $0°$ and $180°$ angles of the magnetic field. (b) THz signal measured at room temperature in a sample of CoFeB|Pt. (c) FFT response of the measured THz signal. (d) Amplitude of the THz signal versus laser power.

at $\sim 3THz$[13].

Furthermore, we plot in Figure 5.14 the total angular dependence of the THz signal emitted by a sample of Py| LAO(5u.c)|STO for two perpendicular orientations of the ZnTe crystal while rotating the dc magnetic field produced by the electromagnet. The cosine(sine)-shape of the signal is as one would expect from an isotropic Rashba-split band. We should also note that the amplitude of the THz signal increases linearly with the power of the laser pump and saturates above $> 600mW$, as shown in Figure 5.13 d. In addition, we plot in Figure 5.14 a comparison between the THz signal at both room temperature and $T = 10K$, where we observe a similar shape and amplitude. Furthermore, upon varying the applied backgate voltage, we notice that the THz signal does not change. Similarly, the angular dependence of the signal at various backgate voltages does not change neither and displays the same cosine(sine)-shape as that observed at $V_g = 0V$ (see Figure 5.14). In this regard, the question that begs to be answered, is to find out if there is a THz contribution to the signal coming form the 2DES at the interface of LAO/STO ? And if no, why ?

The answer to this question lies on a simple comparison between two LAO/STO samples with and without the 2DES at the interface, through the modulation of the STO termination in contact with LAO. In

[13]The dips in the FFT are due to the absorption of water from the ambient atmosphere.[145]

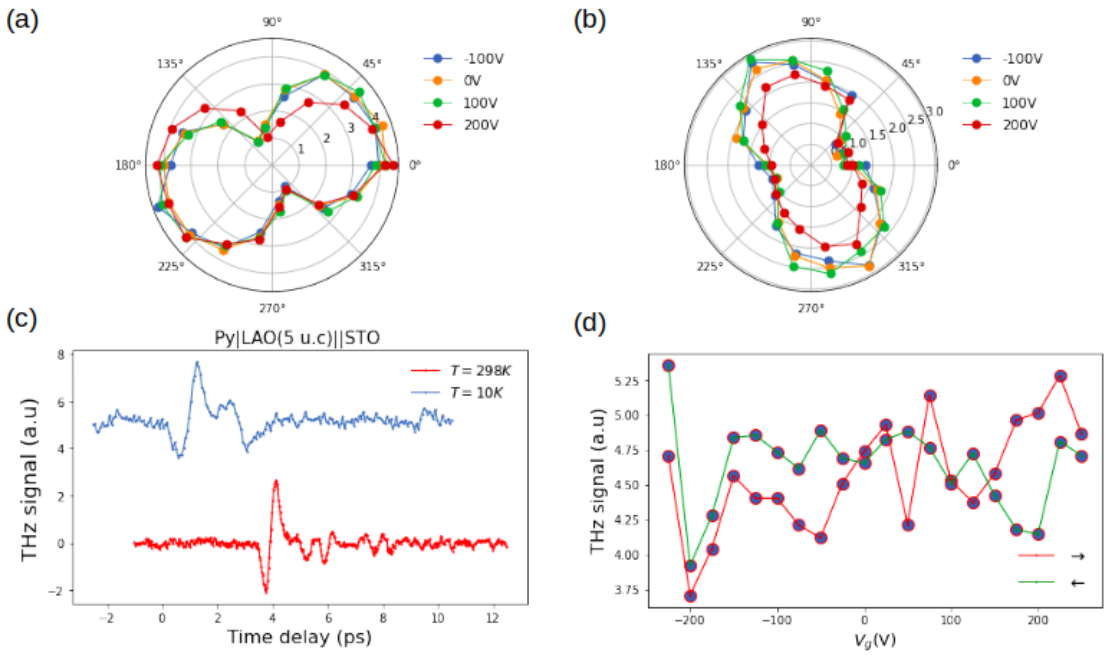

Figure 5.14: Angular dependence of the THz signal while rotating the direction of the magnetic field at various backgate voltages for both (a) $0°$ and (b) $90°$ angles of the orientation of the ZnTe crystal. (c) Comparison of the THz signal measured at $T = 298K$ and $T = 10K$. (d) Amplitude of the THz signal versus backgate voltage.

Figure 5.15, we observe that the THz signal displays almost the same amplitude in the presence and absence of the 2DES. So the key question we need to answer is why we do not observe the contribution of the 2DES in the THz signal. In this aim, we will present in the next section an argument based on the numerical simulations performed by Dang et al.[39]

5.3.3.3.2 Discussion In order to reproduce the THz signal detected in CoFeB|Pt, Dang et al.[39] have developed Finite Difference Time Domain (FDTD) simulations by using the Boltzmann transport equation for two spin channels in order to estimate the time and the spatial dependence of the population density of

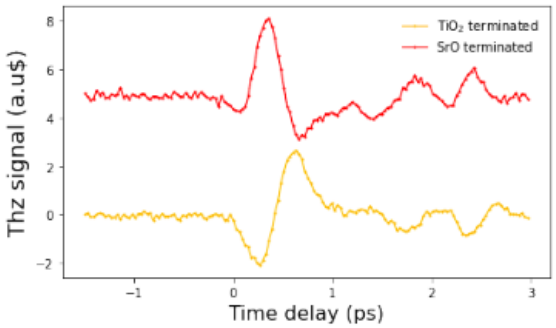

Figure 5.15: Comparison of the THz signal between two samples of LAO|STO, in the presence and absence of the 2DES at the interface.

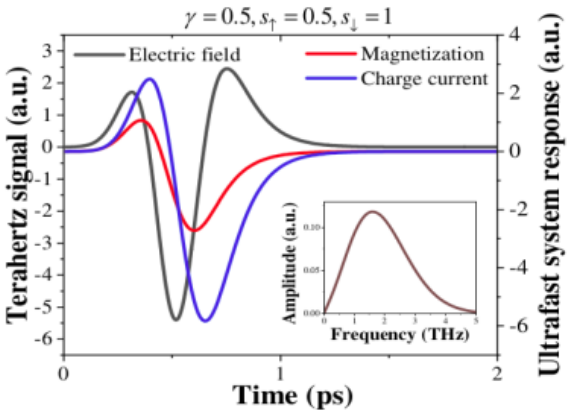

Figure 5.16: Time evolution simulations of the emitted terahertz signal (black), as well as, the charge current density (blue) and the out-of-equilibrium spin accumulation at the interface (red). Fourier transform of the terahertz signal is given in the inset.[39]

each spin channel. This also leads to the spin current density in order to simulate the out-of-equilibrium spin accumulation in HM at the interface of FM/HM, as well as the corresponding charge current generated within the HM layer. Thus, the computed THz signal agrees quite well with the experimentally measured THz radiation, as shown in Figure 5.16.

A simple interpretation of this numerical result comes from the fact that in the two spin channel model both spin populations are subject to two different Fermi velocities, within the FM layer. Upon transmission of both spin populations through the FM/HM interface the spin signal is converted instantaneously into a charge current[14] which displays a bipolar contributions corresponding to both majority and minority spin contributions separated in time due to the difference in their Fermi velocities. In a similar fashion, one would expect that in Py|LAO|STO the generated charge current will behave in the same way as in the case of CoFeB|Pt. However, some discrepancies between the two systems need to be appraised, and in particular the fact that the spin life time in LAO/STO is much longer that in the case of Pt. Hence, this will affect the overall response time of the conversion process within the 2DES, which will span for some picoseconds instead. This should lead to a wider temporal profile of the charge current which lead to a lower frequency electromagnetic radiation which will not be centered around the $\sim 1THz$ frequency, thus explaining in part why the 2DES contribution is not in the detected THz signal by the ZnTe crystal which has a lower cutoff frequency around 300 GHz. Additionally, another reason behind the small contribution of the 2DES to the THz signal may come from the fact that at the interface between the FM layer and the 2DES, lies a tunnel barrier of LAO, which can strongly reduce the transmission coefficient at the interface. This can play a crucial role when it comes to the peak-to-peak amplitude of the THz signal, so if the transmission rate is 3

[14]Thanks to very fast response time of the spin-orbit coupling which is below $1ps$.

orders of magnitude lower in Py|LAO|STO compared to the interface of CoFeB|Pt, then one would expect a much smaller contribution of the 2DES compared to the state of the art CoFeB|Pt samples, as shown experimentally.

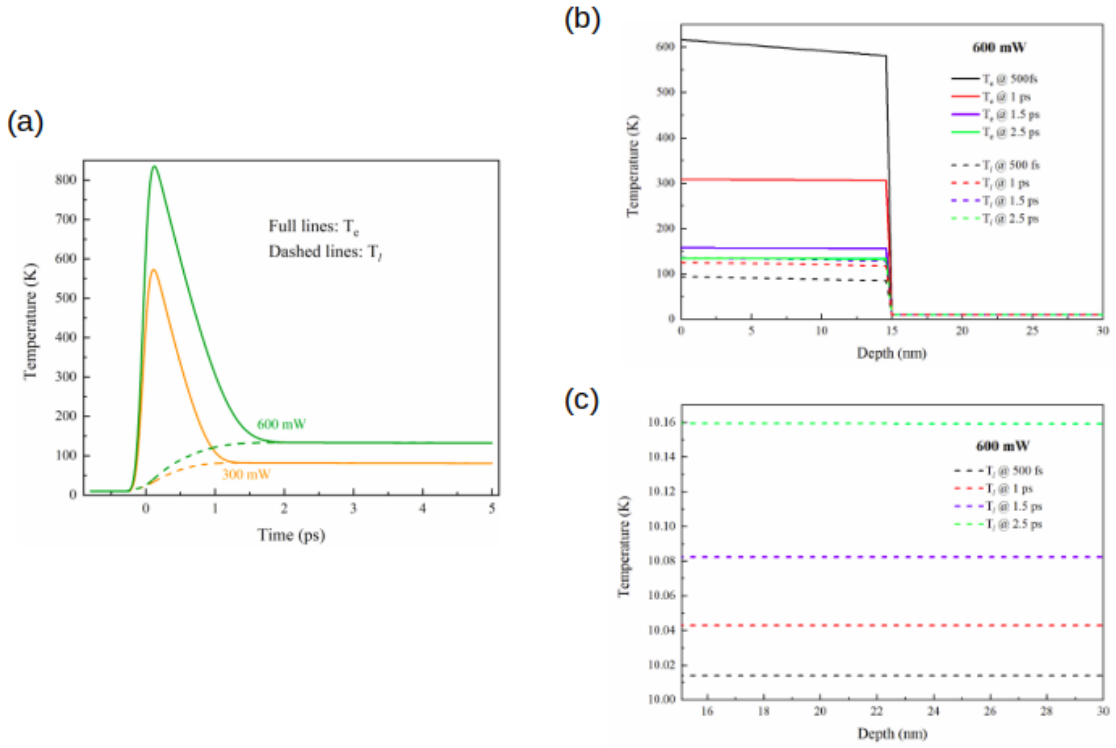

Figure 5.17: Two temperature simulations. (a) Time dependence of the electron temperature (solid line) and the phonon temperature (dashed line) at the center of the Permalloy layer, for two different laser powers $P = 300mW$ and $P = 600mW$. (b) Temperature profile inside the Py|LAO|STO sample at different time delays. (c) Zoom of the temperature of profile within the STO layer.

Additionally, in order to study the impact of the laser heating on our sample of Py|LAO(5u.c)|STO, we performed a two temperature model simulations, for both the phonon and electron temperatures, which was realized in collaboration with Otomalo et al., at the Institut des Molécules et Matériaux du Mans (IMMM). These simulations have demonstrated that the electron temperature inside the Py layer can reach temperature up to $T_e \simeq 800K$ after the first $100fs$ when the laser beam hits the sample, as shown in Figure 5.17. However, the temperature profile inside the STO layer shows that the temperature does not change a lot[15] compared to the temperature set by the cryostat $T = 10K$ (see Figure 5.17), and since the 2DES is trapped within the STO layer, we would expect a little effect from the laser heating on the 2DES[16] .

[15] $\Delta T = T - 10K \simeq 10.04K$ after 1 ps after the laser beam hits the sample

[16] For more details regarding the parameters chosen for the simulation see Appendix G

5.4 Conclusion

In this chapter we have presented three different optical techniques used to characterize the important mechanisms behind the spin-to-charge conversion at timescales between 0.1ps to 1ns. The TR-MOKE measurements have shown that the spin-to-charge mechanism within LAO/STO can be quite different from other systems such as CoFeB/Pt. It is also important to note, that the preliminary results of the TR-SHG measurements so far, do not give the expected electric field signal at the interface. Nevertheless, very important steps have been taken in order to measure the spin lifetime within LAO/STO 2DES, which can have very interesting impact on future applications in spin-orbitronics.

Furthermore, we have seen that the THz generation is a great way to characterize the spin currents at timescales between 0.3 – 3 ps range, allowing for the study of the spin-to-charge conversion mechanism at the picosecond timescale. However, it seems that in the case of LAO/STO the spin-to-charge signal is not centered around $1THz$ frequency unlike other systems like CoFeB/Pt, which we attribute to the longer spin lifetime within LAO/STO compared to other metallic compounds, where $\tau_s \sim 10fs$. Hence, these results seem to agree with the fact that the spin-to-charge conversion mechanism within LAO/STO is greatly associated with the long spin relaxation time which is behind the strong conversion efficiency λ_{IEE} in the DC regime. It is also important to note that the barrier interface of LAO can also reduce greatly the transmission rate of both spin channels within the 2DES, which can be quite detrimental to the amplitude of the generated THz radiation. Of course, this argument is also valid for the DC regime, but the combination of timescales between the different time regimes may play an important role. Nevertheless, it could be quite interesting in the future to perform the THz generation measurements with different LAO thicknesses in order to vary the transmission rate of the spin current through the tunnel barrier.

Chapter6

Conclusions and Future Perspectives

In this dissertation we have investigated the spin-to-charge conversion in the 2DES at the LAO/STO interface at different timescales through various experimental methods . In the following we give a brief summary of the main results obtained during my thesis, and then we conclude by giving a quick review of future perspectives that can be explored.

6.1 Summary of this thesis

In the first two **Chapters 1** $\&$ **2**, we have introduced the basic concepts behind spin-to-charge conversion using both spin and orbital degrees of freedom through the spin and orbital Edelstein effects. These two effects are particularly relevant for the 2DES present at the LAO/STO interface displaying a wide variety of exotic phenomena thanks to its complex band structure which was also analysed using a tight binding model.

In **Chapter 3**, we have presented the two main experimental methods, namely spin pumping and spin Seebeck effect, to study the spin-to-charge conversion signal. We have showed that both methods can be optimally used to bypass their intrinsic spurious effects affecting the measured signal.

In **Chapter 4**, we investigated the large spin-to-charge conversion in LAO/STO, using both experimental methods presented in **Chapter 3**. A large spin-to-charge conversion efficiency was recorded at low temperature with an inverse Edelstein length reaching $6nm$. In addition, we demonstrated the possibility to strongly tune the conversion efficiency using electrostatic doping with a backgate voltage. Furthermore, we have studied the angular dependence of the spin-to-charge signal with respect to the direction of the injected angular momentum, which showed a non-trivial symmetry that we mapped onto the band structure of LAO/STO presented in **Chapter 2**. We have also demonstrated that in addition to the spin,

The experimental measurements are consistent with an 8% proportion of this largely unexplored orbital contribution. A better harvesting of this effect could offer a huge boost to the conversion efficiencies from the Edelstein effect.

In **Chapter 5**, we explored the spin-to-charge conversion at timescales between 0.1 to 10ps using picosecond spin current bursts generated by laser-induced ultrafast demagnetization processes in ferromagnetic layers. Using magneto-optical Kerr effect measurements, we have evidenced some differences in demagnetization processes between LAO/STO with or without the presence of the interface 2DES. On the other hand, we measured the THz radiation emitted by a sample of Py/LAO/STO which was found to be at least 3 orders of magnitude smaller than that in CoFeB/Pt. We attribute this huge difference to the long electron relaxation time inside the 2DES at LAO/STO interface.

6.2 Future Perspectives & Discussion

The highly efficient spin-to-charge conversion in the 2DES at the LAO/STO interface, opens up exciting opportunities for various spinorbitronics applications. As we have seen previously, this spin-to-charge signal is driven by two effects which are the inverse spin and orbital Edelstein effects, relying on the injection of both spin and orbital degrees of freedom into the 2DES. From first principles calculations, it was postulated that the efficiency of the inverse orbital Edelstein effect can be at least one order of magnitude higher compared to its spin counterpart. However, since we are injecting only 8% of this orbital contribution, we need to think of a way to maximize it.

One possible way to inject a pure orbital angular moment within the 2DES relies on the use of light with a helical or twisted wavefront. Another interesting idea, would be to use a helical or a chiral crystal which can display a giant orbital angular momentum current through the direct orbital Edelstein effect. This orbital degree of freedom which was unexplored until recently, can have a tremendous impact on the future applications in oxide-electronics.

In this thesis, we also explored the injection of picosecond spin currents during the ultrafast demagnetization process in a magnetic layer into the 2DES at the LAO/STO interface. Different measurement methods have been presented, suggesting a long relaxation time within the 2DES. However, some work is still required in order to quantitatively estimate this relaxation time, as well as the amount of the ultrafast spin current generated. Importantly, one can think of a way to vary this electron relaxation time so that the spin-to-charge conversion efficiency can also be improved without the need for band gap engineering or chemical doping. A possible way forward is through the design of the tunnel barrier to set the electron

leakage into the adjacent ferromagnet. One can also imagine replacing the conducting ferromagnetic layer with a ferromagnetic insulator such as YIG or a demi-metal like LSMO. It is also possible to maximize the electron relaxation time, using electrostatic doping in $SrTiO_3$ -based 2DES. A compromise between the strength of the Rashba coupling as well as the electron relaxation time needs to be attained in order to maximize this spin-to-charge conversion efficiency, where different characteristics are required for the DC or THz regimes.

AppendixA

Auxiliary Calculations

A.1 Susceptibility tensor components

Each component of the susceptibility tensor can be separated into real and imaginary parts :

$$\chi = \chi' - i\chi'' \tag{A.1}$$

$$\chi_a = \chi'_a - i\chi''_a \tag{A.2}$$

$$\chi_\parallel = \chi'_\parallel - i\chi'' + \parallel \tag{A.3}$$

We get after linearizing equation 3.9:

$$\chi' = \frac{1}{D}\gamma M_0 \omega_H(\omega_H^2 - (1-\alpha)\omega^2) \tag{A.4}$$

$$\chi'' = \frac{1}{D}\gamma M_0 \omega_H(\omega_H^2 + (1+\alpha)\omega^2) \tag{A.5}$$

$$\chi'_a = \frac{1}{D}\gamma M_0 \omega_H(\omega_H^2 - (1+\alpha)\omega^2) \tag{A.6}$$

$$\chi''_a = 2\alpha\gamma M_0 \omega^2 \omega_H \tag{A.7}$$

$$\chi'_\parallel = \frac{-\gamma\lambda}{\omega^2 + (\frac{\lambda\omega_H}{M_0})^2} \tag{A.8}$$

$$\chi''_\parallel = \frac{-\gamma\lambda^2 \frac{\omega_H}{M_0}}{\omega^2 + (\frac{\lambda\omega_H}{M_0})^2} \tag{A.9}$$

$$\chi''_{\parallel} = \frac{-\gamma\lambda\omega}{\omega^2 + (\frac{\lambda\omega_H}{M_0})^2} \tag{A.10}$$

$$D = (\omega_H^2 - (1+\alpha^2)\omega^2)^2 + 4\alpha^2\omega^2\omega_H^2 \tag{A.11}$$

A.2 Inverse Spin Hall voltage

From the Valet-Fert spin diffusion model[156], one can retrieve the spin-diffusion equation :

$$D\frac{\partial^2(\mu_\uparrow - \mu_\downarrow)}{\partial^2 x} = \frac{(\mu_\uparrow - \mu_\downarrow)}{\tau_{sf}} \tag{A.12}$$

Upon choosing the right boundary conditions the solution to this differential equation is given by :

$$\Delta\mu = \frac{\Delta\mu(0)}{1 + e^{-2t}/\lambda_{sd}}(e^{-x/\lambda_{sd}} + e^{-2t/\lambda_{sd}} \cdot e^{x/\lambda_{sd}}) \tag{A.13}$$

where $\Delta\mu = \mu_\uparrow - \mu_\downarrow$, t is the normal metal thickness, and λ_{sd} is the spin diffusion length. Thus, we can define the spin current as a function of distance from the FM/NM interface as : :

$$J_s = -\sigma\frac{d\Delta\mu}{dx} \tag{A.14}$$

And by averaging equation A.14 across the whole film $< J_s >= \frac{1}{t}\int_O^t J_s(x)\,dx$, retrieve the following expression for the inverse spin Hall voltage :

$$V_{ISHE} = \theta_{SH}\frac{g_{\uparrow\downarrow}}{g_{\uparrow\downarrow} + g_{NM}}\frac{hLPfsin^2(\theta)}{2et_{NM}}\frac{(1 - e^{-t_{NM}/\lambda_{sd}})^2}{1 + e^{-2t_{NM}/\lambda_{sd}}} \tag{A.15}$$

where g_{NM} is the NM spin conductance given by:

$$g_{NM} = \frac{\sigma}{\lambda_{sd}}\frac{1 - e^{-2t_{NM}/\lambda_{sd}}}{1 + e^{-2t_{NM}/\lambda_{sd}}} \tag{A.16}$$

,P is the ellipticity correction factor which can be expressed as:

$$P = \frac{2\omega(\omega_M + \sqrt{\omega_M^2 + 4\omega^2})}{\omega_M^2 + 4\omega^2} \tag{A.17}$$

and θ is the precession angle given by :

$$tan(\theta) = \frac{M_t}{M_z} = \frac{2h_{rf}}{\Delta H} \tag{A.18}$$

AppendixB

Frequency-swept Ferromagnetic Resonance

In the case of a frequency-swept FMR experiment, the rf frequency f is swept using a microwave source, while the dc magnetic field $\mathbf{H_{dc}}$ is kept constant, so that the measurement is then repeated for a range of magnetic fields in order to retrieve the Kittel formula (see equation 3.16). Indeed, in order to extract the Gilbert damping coefficient α from the the frequency linewidth Δf, we need to convert the dependence of α on the field linewidth ΔH into the frequency linewidth Δf, by differentiating the Kittel equation (see equation 3.15), which relates both quantities :

$$\Delta f = \Delta H \frac{\partial f_{Kittel}(H_{eff})}{\partial H_{eff}}\Big|_{H_{eff}=H_{Kittel}(f)} \tag{B.1}$$

In the case of an out-of-plane magnetized film, Δf is a linear function of f_{res}, so that equation B.1 becomes:

$$\Delta f = 2\alpha f_{res} \tag{B.2}$$

While in the case of an in-plane magnetized film, equation B.1 yields an inverse square-root dependence of Δf, given by :

$$\Delta f = 2\alpha f_{res}\sqrt{1+(\frac{\gamma\mu_0 M_s}{2f_{res}})^2} \tag{B.3}$$

Hence, one would expect a very large frequency linewidth a low frequencies and then it decreases until hitting a minimum given by :

$$f_{\Delta f_{min},\|}\frac{\mu_0\gamma}{2}(\frac{\Delta H_0 M_s^2}{\alpha})^{\frac{1}{3}} \tag{B.4}$$

And above this frequency $f_{\Delta f_{min},\parallel}$ the linewidth increases slowly as shown in Figure B.1.

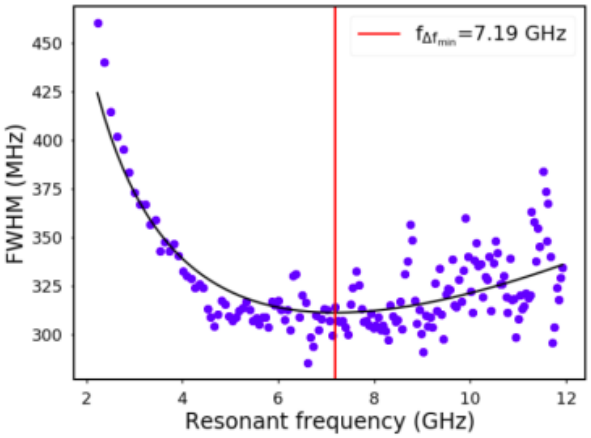

Figure B.1: The frequency linewidth Δf versus the resonance frequency f_{res} extracted using a frequency-dependent FMR measurement for various magnetic fields for a sample of 30 nm of Py in the in-plane configuration. The black curve corresponds to a the fit using the inverse square-root law (see equation B.3) . The red line indicates the position of the minimum frequency linewidth at $f_{\Delta f_{min},\parallel}$ (see equation B.4).[62]

AppendixC

Fitting parameters for the FMR signal

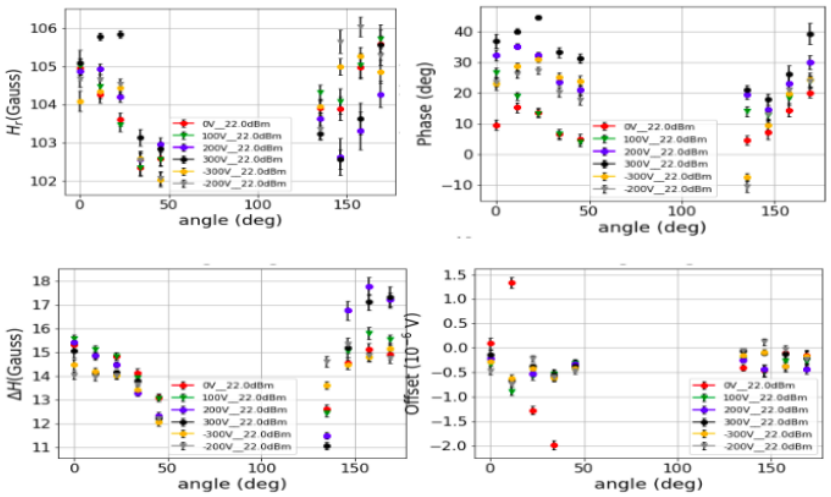

Figure C.1: Fitting parameters of the FMR signal versus the angle and various backgate voltages : 0V,100V,200V,300V,-300V,-200V.

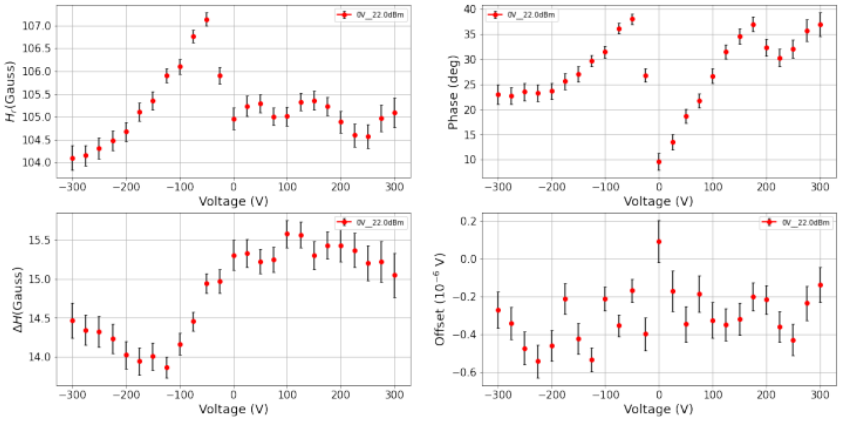

Figure C.2: Parameters of the FMR signal versus backgate voltages.

AppendixD

Finite Element Model for temperature simulations

The temperature simulation of a laser heating a sample with dimensions $5 \times 5 \times 0.5\ mm^3$ is solved using a numerical procedure which was developed using the open source FreeFem++ software. As a way of simplification, we present here only 2D simulations [1] of a transverse cut of the sample passing through the center of the LED along x & z axis. The 2D surface was treated using a prism shaped $1nm$ mesh size elements [2], as illustrated in Figure D.1.

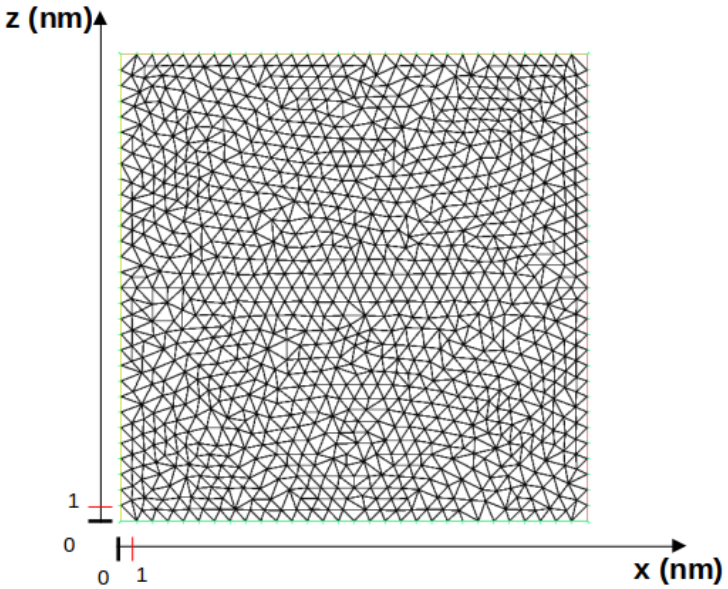

Figure D.1: A representation of the 2D triangle-shaped meshing of a 2D surface with dimensions 30×30 nm^2, with 1 nm resolution along both x & z axis .

In the heat equation 4.1, the convection was not taken into account for the lateral boundaries due to

[1] 3D simulations seems to give similar results
[2] Along both the x & z axis

contact with vacuum inside the cryostat see Figure 4.6. In addition to the surface (1) boundary condition which is expressed in equation 4.4, we fix the temperature at $T = 10K$ at the surface boundary condition (4), so that the bottom of the sample which is in contact with the cryostat is always at the same temperature.

However, in the case of the 3D model the whole volume of the sample is represented using prism-shaped mesh elements with a resolution of $1nm$ along all 3 axis as shown in Figure 4.6.

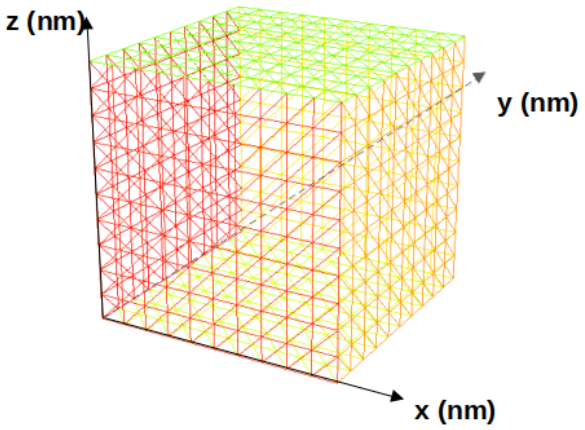

Figure D.2: A representation of the 3D prism-shaped meshing of a 3D volume with dimensions $10 \times 10 \times 10$ nm^3, with 1 nm resolution along both x, y & z axis .

Similarly to the 2D model, we plot in Figure D.3 the spatial variations of temperature in the 2D case in a subdomain with dimensions $100 \times 100 \times 100$ nm^3.

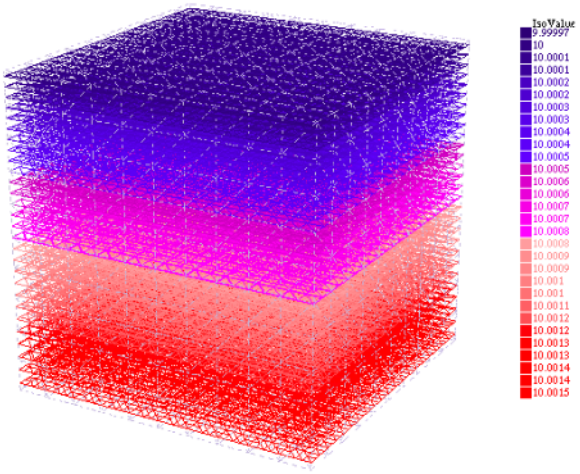

Figure D.3: The spatial variations of the temperature profile in the 3D model. The laser beam in this case is heating the sample from the bottom.

AppendixE

MOKE experiment

E.1 Wollaston prism

A Wollaston prism consists of two right triangle prisms with orthogonal optical axis cemented together. Hence, when sending a light beam into the Wollaston prism, the transmitted light is separated into two light beams with perpendicular polarization corresponding to the ordinary and extraordinary light beams. So when the incoming light has a circular polarization or a linear polarization along the diagonal of the prism then the two outgoing light beams from the Wollaston prism will display the same intensity.

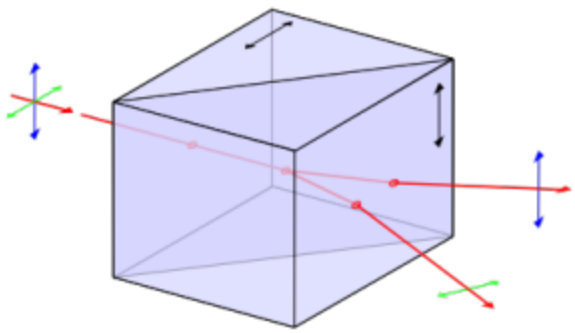

Figure E.1: A sketch illustrating a Wallaston prism

E.2 Waveplates $\lambda/2$ and $\lambda/4$

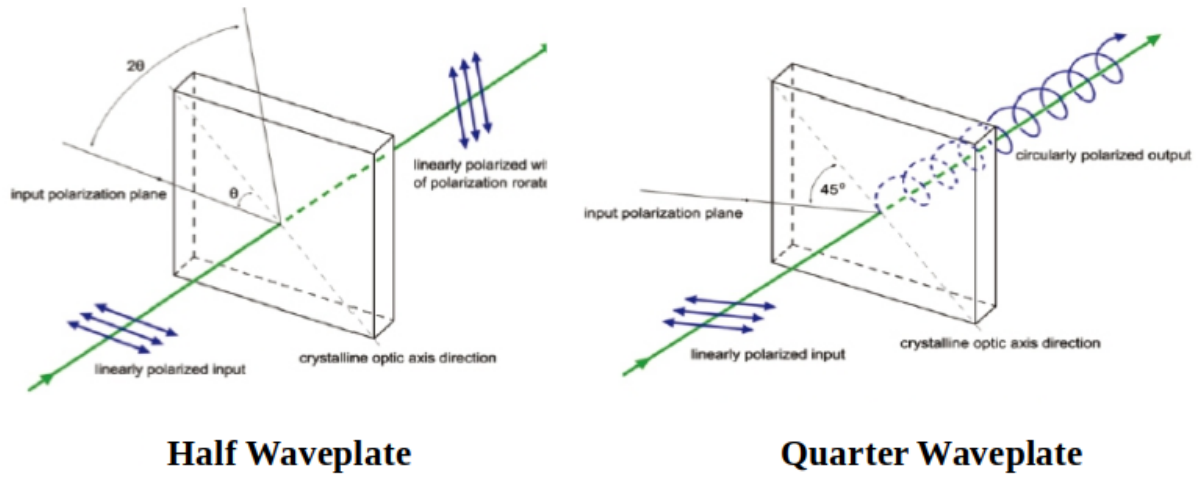

Figure E.2: Sketch illustrating both a half waveplate and a quarter waveplate.

A half waveplate rotates a linearly polarized light to any desired polarization, so that the rotation angle is twice the angle between the incident light and the optic axis.

A quarter waveplate transforms a linearly polarized light into an elliptically polarized light, so that in the special case when the incoming light has linear polarization at 45° angle the outgoing light will be circularly polarized.

AppendixF

2^{nd} order susceptibility tensor expression

The second order harmonic electric dipolar contribution, is given by :

$$P^{[2\omega]} = \underbrace{P^{(1)[2\omega]}}_{=0} + \underbrace{P^{(2)[2\omega]}}_{2^{nd}order} + \underbrace{P^{(\geq 3)[2\omega]}}_{Weak} \tag{F.1}$$

and if we focus on the second order term, it can be written as :

$$P_i^{(2)} = \sum_{i,j,k} \chi_{ijk}^{(2)} E_j E_k \tag{F.2}$$

and since $E_j E_k = E_k E_j$ for every k and j, we have $\chi_{ijk}^{(2)} = \chi_{ikj}^{(2)}$, so that the second order susceptibility tensor $\overline{\overline{\chi}}$ can written in a contracted form given by :

$$\overline{\overline{\chi}} = \begin{pmatrix} \chi_{11} & \chi_{12} & \chi_{13} & \chi_{14} & \chi_{15} & \chi_{16} \\ \chi_{21} & \chi_{22} & \chi_{23} & \chi_{24} & \chi_{25} & \chi_{26} \\ \chi_{31} & \chi_{32} & \chi_{33} & \chi_{34} & \chi_{35} & \chi_{36} \end{pmatrix} \tag{F.3}$$

so that :

$$P^{(2)} = \begin{pmatrix} \chi_{11} & \chi_{12} & \chi_{13} & \chi_{14} & \chi_{15} & \chi_{16} \\ \chi_{21} & \chi_{22} & \chi_{23} & \chi_{24} & \chi_{25} & \chi_{26} \\ \chi_{31} & \chi_{32} & \chi_{33} & \chi_{34} & \chi_{35} & \chi_{36} \end{pmatrix} \begin{pmatrix} E_1^2 \\ E_2^2 \\ E_3^2 \\ 2E_2E_3 \\ 2E_1E_3 \\ 2E_1E_2 \end{pmatrix} \tag{F.4}$$

Additionally, if we consider the 4mm symmetry at the interface of for example LAO|STO[1] the susceptibility tensor can be reduced to the following expression :

$$\overline{\overline{\chi}} = \begin{pmatrix} \chi_{11} & \chi_{12} & 0 & 0 & 0 & \chi_{16} \\ \chi_{21} & \chi_{22} & 0 & 0 & 0 & \chi_{26} \\ 0 & 0 & 0 & 0 & 0 & 0 \end{pmatrix} \tag{F.5}$$

where :

$$\chi_{11} = \chi_{xxxy} M_y \qquad \chi_{12} = \chi_{xyyy} M_y \qquad \chi_{21} = \chi_{yxxx} M_x$$
$$\chi_{21} = \chi_{yxxx} M_x \qquad \chi_{22} = \chi_{yyyx} M_x \qquad \chi_{26} = \chi_{yxyy} M_y$$

And according to Kirilyuk et al.[82] :

$$\begin{cases} \chi_{xyyy} = -\chi_{yxxx} \\ \chi_{xxxy} = -\chi_{yyyx} \\ \chi_{xxyx} = \chi_{xyxx} \end{cases}$$

so that the polarization components are given by :

$$\begin{cases} P_x^{(2\omega)}) = E_0^2 \ [\ \chi_{xxxy} M_y \cos^2(\phi) + \chi_{xyyy} M_y \sin^2(\phi) + 2\chi_{xxyx} M_x \cos(\phi)\sin(\phi) \ ] \\ P_y^{(2\omega)}) = -E_0^2 \ [\ \chi_{xyyy} M_x \cos^2(\phi) + \chi_{xxxy} M_x \sin^2(\phi) + 2\chi_{xxyx} M_y \cos(\phi)\sin(\phi) \ ] \end{cases}$$

where E_0 and ϕ are the amplitude and the phase of the electric field of light $\vec{E}$.

[1] No z component of the polarizarion and without the χ^{cr}

AppendixG

Temperature simulation parameters

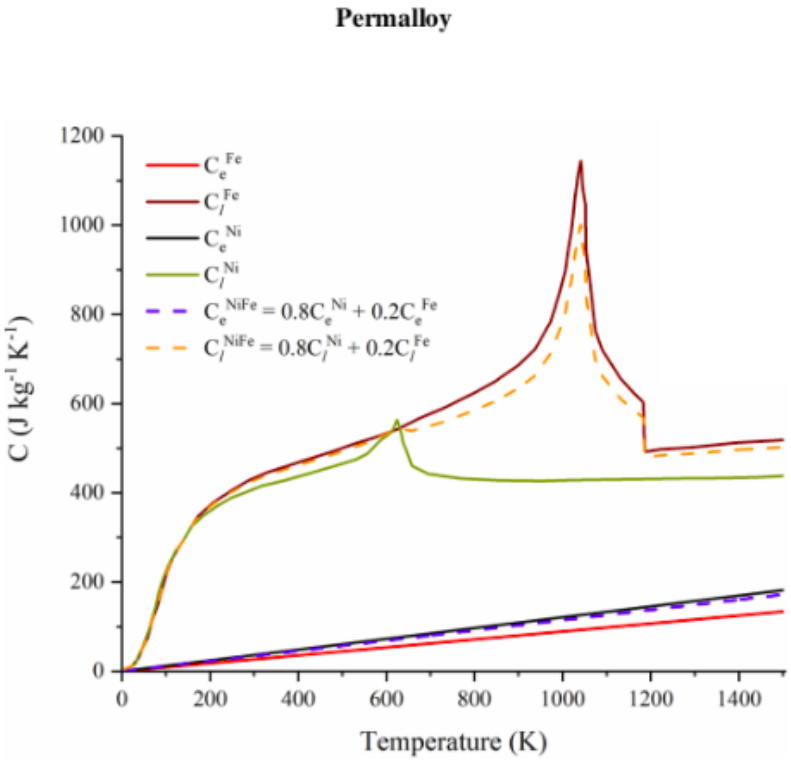

Figure G.1: Temperature dependence of the electron and the lattice heat capacity of Permalloy.[146]

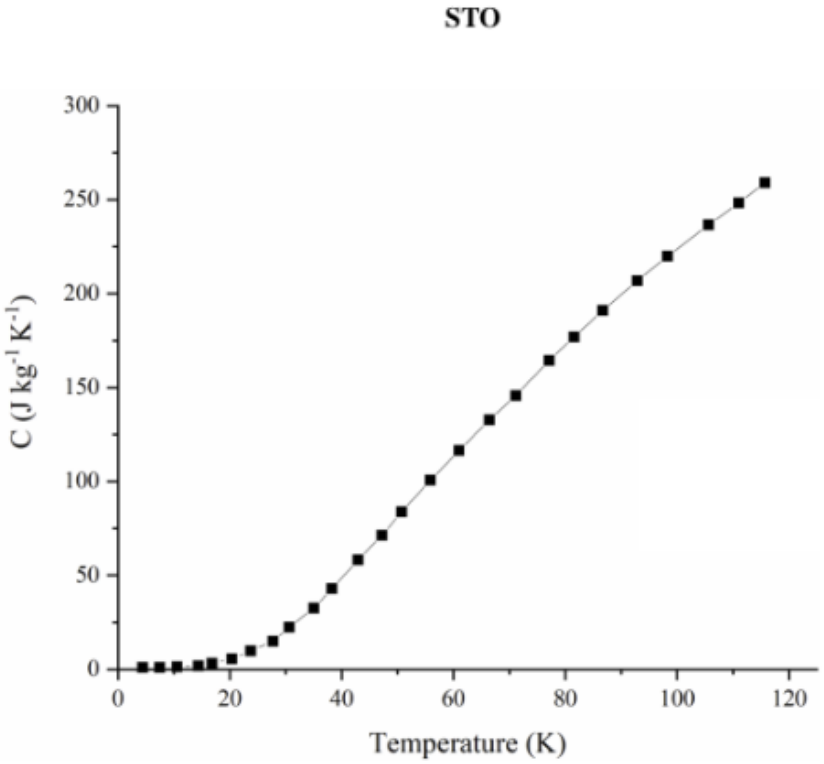

Figure G.2: Temperature dependence of the heat capacity of STO.[51]

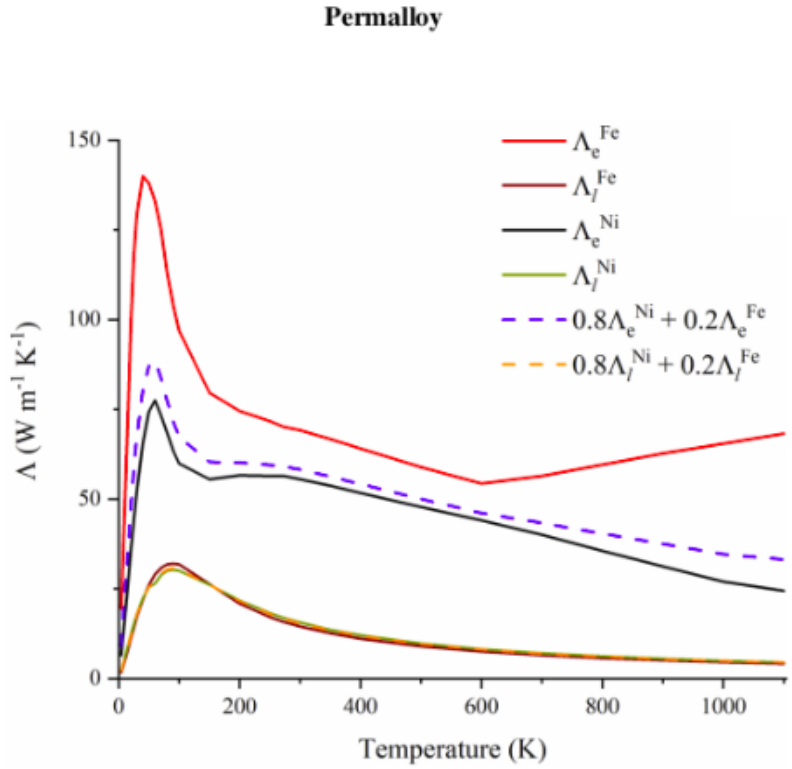

Figure G.3: Temperature dependence of the electron and lattice thermal conductivity of Permalloy, which were deduced by the weighted average.[59]

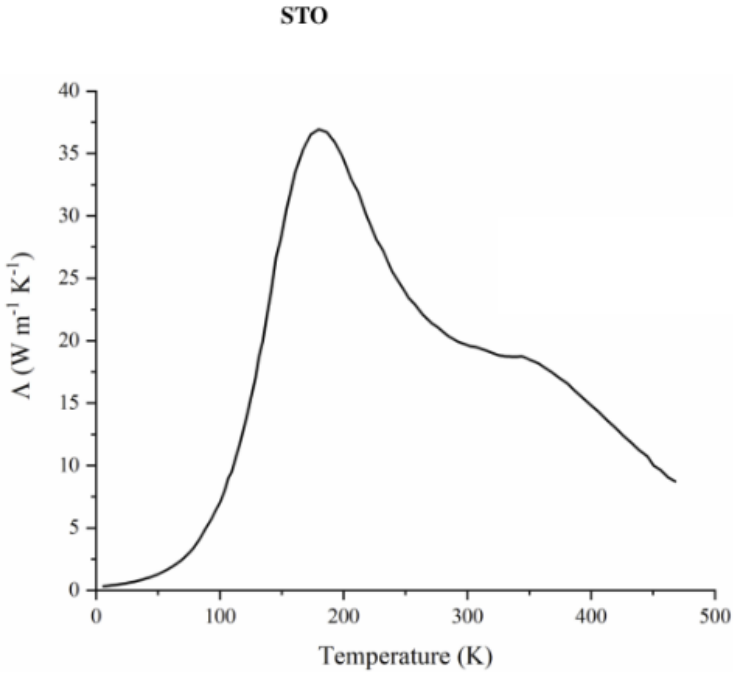

Figure G.4: Temperature dependence of the thermal conductivity of STO.[95]

AppendixH

Résumé en Français

H.1 Introduction à la spin-orbitronique

Depuis la découverte de l'effet de magnétorésistance géante par Albert Fert et Peter Grunberg[205, 211], une grande variété d'applications a vu le jour notamment dans le domaine des mémoires magnétiques. Jusqu'à présent, ceux-ci reposent sur le contrôle de l'aimantation dans les matériaux ferromagnétiques, par le biais de ce que l'on appelle le ≪ Spin-Transfer-Torque ≫ (STT)[244, 208], en utilisant l'injection d'un courant de spin polarisé pour appliquer un couple efficace sur l'aimantation. Cependant, un nouveau type de contrôle d'aimantation basé sur le couplage spin-orbite s'est avéré très efficace. Il permet d'effectuer une injection de spin efficace sans avoir besoin de matériaux ferromagnétiques[237, 235, 217], ainsi que la détection d'un courant de spin pur grâce à la conversion spin-charge qui peut avoir une grande variété d'applications[225, 232, 241]. Très récemment, un nouveau degré de liberté a également été étudié qui correspond au moment orbital quantifié des électrons, qui comme le spin peut jouer un rôle important dans le contrôle de l'aimantation[224]. De plus, les effets de conversion orbitale en charge seront discutés plus tard dans cette thèse[247].

Dans le premier chapitre, on introduit les concepts de base, tel que : le spin et le moment orbital d'un électron, les différents types de courants associés aux différents degrés de libértés d'un électron, à savoirs les courants de spin, d'orbital et de charge, ainsi que les différents mécanismes de conversion de ces différents types de courants dans des matériaux tel que les métaux lourds ou à l'interface entre deux matériaux différents. Dans ce dernier cas, nous avons étaillé la physique de la conversion spin-charge dans les gaz 2D en introduisant l'effet Edelstein direct et inverse pour le spin ainsi que le moment orbital [214, 249].

H.2 L'interface entre $LaAlO_3/SrTiO_3$

Les hétérostructures artificiellement fabriquées ont conduit à la découverte d'une variété de phénomènes émergents, grâce à l'ingénierie des paramètres d'ordres, conduisant à de nouvelles propriétés et fonctionnalités. Ces efforts ont ouvert la possibilité d'étudier un nouvel ensemble de phénomènes physiques à la frontière de deux matériaux différents, qui ont conduit à de grandes découvertes en physique des semi-conducteurs[181], et plus récemment, en physique des oxydes complexes[186]. Une première percée est venue de l'hétérointerface de deux oxydes pérovskites de $LaAlO_3$(LAO) et $SrTiO_3$(STO), qui se sont avérés héberger un système électronique à 2 dimensions au voisinage de leur interface[186]. Depuis lors, de multiples études ont été publiées à cet égard, démontrant l'existence d'une phase supraconductrice [190] . De plus, une autre propriété intéressante du 2DES, qui est le couplage Rashba dû à la brisure de la symétrie spatiale à l'hétérointerface a été démontrée très récemment[193], conduisant à la création d'un signal de conversion spin-charge dans l'interface LAO/STO , ouvrant la voie à de nouveaux dispositifs basés sur le spin[218, 246, 236]. Dans ce contexte, cette thèse suivra ces efforts et démontrera que ce système possède encore de nombreuses propriétés étonnantes.

La première partie de ce chapitre se concentrera sur les études expérimentales récentes concernant les propriétés émergentes de l'hétrointerface LAO/STO. Plus tard, nous discuterons des différents mécanismes en jeu, quand il s'agit de l'émergence de la conductivité à l'interface, ce qui nous donnera un indice sur son origine. Ensuite, une étude théorique de la structure électronique du 2DES à l'interface sera présentée afin de découvrir la structure de bande complexe qui est un point de repère pour les effets multi-bandes en jeu dans les oxydes métalliques complexes. Enfin, une revue rapide de la technique de dépôt laser pulsé utilisée pour la croissance de LAO/STO et les propriétés de caractérisation structurelle et de transport qui ont été réalisées en collaboration avec le groupe de Jean-Marc Triscone à Genève.

H.3 Conversion spin-charge dans $LaAlO_3/SrTiO_3$

Après la prédiction de l'effet Hall de spin direct et inverse par Dyakonov et al.[179], diverses études expérimentales ont démontré la possibilité de convertir un courant de spin en courant de charge, en particulier dans les métaux lourds comme le Pt, le Ta et l'Au qui affichent un grand angle de spin Hall, grâce au fort couplage spin-orbite atomique qui est supposé augmenter avec le numéro atomique Z comme $\sim Z^4$ dans le cas d'un atome de type hydrogène[122, 169, 109].

Récemment, un autre type de couplage spin-orbite a été découvert dans des systèmes 2D sans symétrie

d'inversion, en s'appuyant sur l'interaction de Rashba[1], qui découle d'une action conjointe du couplage de l'orbite, du spin et d'un champ électrique induit à l'interface de deux matériaux différents comme décrit par Byachkov et Rashba[214]. Divers systèmes Rashba ont montré une efficacité de conversion spin-charge prometteuse, comme les interfaces des semi-conducteurs dopés, comme AlGaN/GaN [91] ou InGaAs/InAlAs [84]), les surfaces des alliages métalliques, tels que Ag/Bi(111)[200], les interfaces des oxydes, tels que LAO/STO [199] ou plus récemment dans certains isolants topologiques, pour citer quelques uns α-Sn[124] et HgTe[108].

Dans ce chapitre, nous donnerons un aperçu de la variété des systèmes qui affichent une efficacité de conversion spin-charge très efficace, tels que les interfaces à base d'oxyde qui sont considérées comme l'un des meilleurs convertisseurs de la littérature, en particulier LAO /STO, qui affiche une variété de propriétés très intéressantes [2].

Dans un second temps, on introduit les deux permières techniques experimentales utilisées pour caractériser la conversion spin/charge dans le gaz 2D. La première technique repose sur le pompage de spin en utilisant le phénomène de résonance ferromagnétique, pour cela on a introduit brièvement la théorie de résonance ferromagnétique ainsi que le mécanisme d'injection des courants purs de spin dans le gaz 2D. La seconde technique repose sur l'utilisation de l'effet Seebeck de spin, que nous avons introduit en détail. Nous avons aussi discuté des différents effets parasites qui peuvent s'ajouter au signal de conversion spin-charge dans les deux cas, en proposant plusieurs méthode pour réduire ces effets parasites.

H.4 Dépendance angulaire et en tension de grille du signal de conversion spin-charge dans $LaAlO_3/SrTiO_3$

Nous avons rapporté dans ce chapitre la possibilité de moduler le signal IEE à l'interface LAO/STO, par du dopage électrostatique, ainsi qu'une forte anisotropie de la dépendance angulaire du signal de conversion spin-charge. Ceci est lié à un effet multibande qui est une caractéristique saillante des oxydes de métaux de transition. De plus, nos mesures révèlent l'existence d'une contribution dominante de l'effet Eldelstein orbital. À cet égard, nous avons postulé une injection de moment angulaire orbital de 8% qui explique toutes les caractéristiques des dépendances angulaires et en tension de grille du signal IEE, y compris son signe, sa forte anisotropie et sa dépendance directionnelle. Fait intéressant, nous avons pu établir un lien entre les dépendances angulaires et en tension de grille du signal IEE et la structure de bande de LAO/STO.

[1] Voir le chapitre 2 pour plus de détails
[2] Voir le chapitre 3 pour plus de détails

Ceci est particulièrement visible lorsque le potentiel chimique est proche des croisements de bandes où le signal IEE affiche une forte symétrie quadruple.

De plus, il semble que la partie orbitale du signal IEE, qui est potentiellement la contribution dominante, pourrait être beaucoup mieux exploitée afin de maximiser l'efficacité de conversion. Il est également important de noter que le temps de relaxation des électrons dans le 2DES à l'interface LAO/STO est d'une importance centrale dans la forte efficacité de conversion spin-charge enregistrée à l'interface LAO/STO. Afin de concevoir les futurs convertisseurs spin-charge hautement efficaces, il faut prendre en compte les différents paramètres pouvant être exploités tels que les effets d'anisotropie, la contribution orbitale au signal IEE et les taux de relaxation de spin. De toute évidence, des rendements de conversion beaucoup plus importants pourraient être obtenus si la partie orbitale du moment angulaire , ainsi que les temps de relaxation des électrons, pouvaient être maximisés.

H.5 Mesures résolues en temps du signal de conversion spin-charge

Dans ce chapitre, nous tentons d'étudier la dynamique ultrarapide du processus de conversion spin-charge dans LAO/STO. Pour ce faire, nous devons générer un courant de spin à l'échelle de la picoseconde ce qui correspond aux échelles de temps derrière le mécanisme de conversion spin-charge dans LAO/STO[3], qui est estimé à environ $\sim 1ps$[193, 175]. Cependant, nous avons besoin d'une méthode expérimentale qui nous permettra d'étudier la dynamique ultrarapide derrière la conversion spin-charge à l'échelle de la picoseconde afin de répondre à certaines questions fondamentales liées à la durée de vie du spin τ_s dans le 2DES à l'interface LAO/STO, et d'élucider les différents mécanismes en jeu lors de la conversion du spin en charge. Dans ce chapitre nous présenterons les premiers résultats préliminaires afin de répondre à ces questions ouvertes. Tout d'abord, parce que nous voulons étudier nos systèmes à des échelles de temps très courtes ($\sim 1ps$), nous nous appuyons sur la haute résolution temporelle fournie par les lasers ultrarapides ($\sim 150fs$), qui nous permettent d'étudier la dynamique ultrarapide derrière la conversion spin-charge. Dans ce contexte, ce chapitre fournira les premiers résultats expérimentaux utilisant diverses méthodes afin de caractériser la conversion spin-charge à différentes échelles de temps. Au cours de ce chapitre, nous présenterons trois méthodes optiques utilisées pour détecter une rafale de courant de spin qui est générée en tirant parti du mécanisme de démagnétisation ultrarapide.

À cet égard, nous étudierons d'abord le processus de démagnétisation ultrarapide dans une couche ferromagnétique qui est le mécanisme de base à l'origine de la création d'un courant de spin à l'échelle de la

[3]Voir chapitre 5 section 5.3.4

picoseconde. Dans un deuxième temps, nous introduirons une première technique de mesure permettant de sonder un courant de spin picoseconde à travers l'effet Kerr magnéto-optique (MOKE). Ensuite, nous présenterons une deuxième technique qui repose sur la génération du signal de seconde harmonique (SHG) afin de sonder le champ électrique dans les métaux lourds grâce à la conversion spin-charge. Enfin, une troisième technique pour détecter les courants de spin à l'échelle de la picoseconde repose sur la détection des rayonnements THz qui peuvent être générés par le mécanisme de conversion spin-charge dans une couche adjacente.

H.6 Conclusion & Perspectives

La conversion spin-charge est hautement efficace dans le 2DES à l'interface LAO/STO ce qui ouvre la voie vers diverses applications en spin-orbitronique. Comme nous l'avons vu précédemment, ce signal spin-charge est entraîné par deux effets qui sont les effets d'Edelstein inverse de spin et d'orbital, reposant sur l'injection de degrés de liberté de spin et d'orbital dans le 2DES. À partir des calculs de premiers principes, il a été postulé que l'efficacité de l'effet Edelstein inverse d'orbital peut être au moins un ordre de grandeur plus élevé que son homologue de spin. Cependant, comme nous n'injectons que 8% de cette contribution orbitalaire, nous devons réfléchir à un moyen de la maximiser.

Une façon possible d'injecter un moment angulaire orbital pur dans le 2DES repose sur l'utilisation de la lumière avec un front d'onde hélicoïdal ou tordu. Une autre idée intéressante serait d'utiliser un cristal hélicoïdal ou chiral qui peut afficher un courant de moment angulaire orbital géant grâce à l'effet Edelstein d'orbital direct. Ce degré de liberté d'orbital, inexploré jusqu'à récemment, peut avoir un impact considérable sur les futures applications en oxyde-électronique.

Dans cette thèse, nous avons également exploré l'injection de courants de spin à l'échelle de la picoseconde lors du processus de démagnétisation ultrarapide dans une couche magnétique dans le 2DES à l'interface LAO/STO. Différentes méthodes de mesure ont été présentées, suggérant un temps de relaxation long au sein du 2DES. Cependant, certains travaux sont encore nécessaires afin d'estimer quantitativement ce temps de relaxation, ainsi que la quantité de courant de spin ultrarapide généré. Surtout, on peut penser à un moyen de faire varier ce temps de relaxation des électrons afin que l'efficacité de conversion spin-charge puisse également être améliorée sans avoir besoin d'ingénierie de bande ou de dopage chimique. Une voie possible à suivre consiste à concevoir une barrière tunnel pour régler la fuite d'électrons dans la couche ferromagnétique adjacente. On peut aussi imaginer remplacer la couche ferromagnétique conductrice par un isolant ferromagnétique comme le YIG ou un demi-métal comme le LSMO. Il est également possible de

maximiser le temps de relaxation des électrons, en utilisant le dopage électrostatique dans le 2DES basé sur $SrTiO_3$. Un compromis entre la force du couplage Rashba ainsi que le temps de relaxation des électrons doit être atteint afin de maximiser cette efficacité de conversion spin-charge, où différentes caractéristiques sont requises pour les régimes DC ou THz.

Bibliography

[1] Adachi, hiroto, et al. "theory of the spin seebeck effect." reports on progress in physics 76.3 (2013): 036501.

[2] Arne brataas, yaroslav tserkovnyak, gerrit e. w. bauer, and bertrand i. halperin. spin battery operated by ferromagnetic resonance. physical review b, 66(6):060404, august 2002.

[3] Ast, christian r., et al. "giant spin splitting through surface alloying." physical review letters 98.18 (2007): 186807.

[4] Avery, a. d., et al. "thermal and electrical conductivity of approximately 100-nm permalloy, ni, co, al, and cu films and examination of the wiedemann-franz law." physical review b 92.21 (2015): 214410.

[5] Azevedo, a., et al. "spin pumping and anisotropic magnetoresistance voltages in magnetic bilayers: Theory and experiment." physical review b 83.14 (2011): 144402.

[6] Battiato, marco, karel carva, and peter m. oppeneer. "superdiffusive spin transport as a mechanism of ultrafast demagnetization." physical review letters 105.2 (2010): 027203.

[7] Beaurepaire, eric, et al. "ultrafast spin dynamics in ferromagnetic nickel." physical review letters 76.22 (1996): 4250.

[8] Bert, julie a., et al. "direct imaging of the coexistence of ferromagnetism and superconductivity at the laalo 3/srtio 3 interface." nature physics 7.10 (2011): 767-771.

[9] Bi, feng, et al. ""water-cycle" mechanism for writing and erasing nanostructures at the laalo 3/srtio 3 interface." applied physics letters 97.17 (2010): 173110.

[10] Bigot, jean-yves, mircea vomir, and eric beaurepaire. "coherent ultrafast magnetism induced by femtosecond laser pulses." nature physics 5.7 (2009): 515-520.

[11] Bigot, jean-yves, and mircea vomir. "ultrafast magnetization dynamics of nanostructures." annalen der physik 525.1-2 (2013): 2-30.

[12] Bihlmayer, g., et al. "the rashba-effect at metallic surfaces." surface science 600.18 (2006): 3888-3891.

[13] Bihlmayer, gustav, stefan blügel, and eugene v. chulkov. "enhanced rashba spin-orbit splitting in bi ag (111) and pb ag (111) surface alloys from first principles." physical review b 75.19 (2007): 195414.

[14] Biscaras, j., et al. "limit of the electrostatic doping in two-dimensional electron gases of laxo 3 (x= al, ti)/srtio 3." scientific reports 4.1 (2014): 1-7.

[15] Bistritzer, r., g. khalsa, and a. h. macdonald. "electronic structure of doped d 0 perovskite semiconductors." physical review b 83.11 (2011): 115114.

[16] Boeglin, christine, et al. "distinguishing the ultrafast dynamics of spin and orbital moments in solids." nature 465.7297 (2010): 458-461.

[17] Boona, stephen r., roberto c. myers, and joseph p. heremans. "spin caloritronics." energy environmental science 7.3 (2014): 885-910.

[18] Boselli, margherita. nanoscale investigations of the laalo3/srtio3 interface. diss. university of geneva, 2019.

[19] Bosu, s., et al. "spin seebeck effect in thin films of the heusler compound co 2 mnsi." physical review b 83.22 (2011): 224401.

[20] Brataas, arne, et al. "spin battery operated by ferromagnetic resonance." physical review b 66.6 (2002): 060404.

[21] Bristowe, n. c., p. b. littlewood, and emilio artacho. "surface defects and conduction in polar oxide heterostructures." physical review b 83.20 (2011): 205405.

[22] Bui, cong tinh, and francisco rivadulla. "anomalous and planar nernst effects in thin films of the half-metallic ferromagnet la 2/3 sr 1/3 mno 3." physical review b 90.10 (2014): 100403.

[23] Bui, cong tinh, et al. "planar nernst effect and mott relation in (in, fe) sb ferromagnetic semiconductor." journal of applied physics 123.17 (2018): 175102.

[24] Cancellieri, claudia, et al. "electrostriction at the laalo 3/srtio 3 interface." physical review letters 107.5 (2011): 056102.

[25] Cansever, h., et al. "characterization of continuous wave laser-induced thermal gradients in magnetic tunnel junctions integrated into microresonators via comsol simulations." ieee transactions on magnetics 55.7 (2019): 1-5.

[26] Carley, robert, et al. "femtosecond laser excitation drives ferromagnetic gadolinium out of magnetic equilibrium." physical review letters 109.5 (2012): 057401.

[27] Carruthers, j. a., et al. "the thermal conductivity of germanium and silicon between 2 an d 300 k." proceedings of the royal society of london. series a. mathematical and physical sciences 238.1215 (1957): 502-514.

[28] Castel, vincent, et al. "frequency and power dependence of spin-current emission by spin pumping in a thin-film yig/pt system." physical review b 86.13 (2012): 134419.

[29] Castro vaz, diogo. spin-to-charge current conversion in srtio3-based two-dimensional electron gases. diss. sorbonne université, 2018.

[30] Caviglia, a. d., et al. "electric field control of the laalo 3/srtio 3 interface ground state." nature 456.7222 (2008): 624-627.

[31] Caviglia, a. d., et al. "tunable rashba spin-orbit interaction at oxide interfaces." physical review letters 104.12 (2010): 126803.

[32] Cen, cheng, et al. "nanoscale control of an interfacial metal–insulator transition at room temperature." nature materials 7.4 (2008): 298-302.

[33] Cerqueira, carolina, et al. "evidence of pure spin-current generated by spin pumping in interface-localized states in hybrid metal–silicon–metal vertical structures." nano letters 19.1 (2018): 90-99.

[34] Chauleau, j-y., et al. "efficient spin-to-charge conversion in the 2d electron liquid at the lao/sto interface." epl (europhysics letters) 116.1 (2016): 17006.

[35] Chirac, theophile. new spintronic components based on antiferromagnetic materials. diss. université paris-saclay, 2019.

[36] Ciuciulkaite, agne, et al. "enhanced thz emission from spintronic fe/pt emitters through crystal growth optimization." arxiv preprint arxiv:2010.12457 (2020).

[37] Costache, m. v., et al. "electrical detection of spin pumping: dc voltage generated by ferromagnetic resonance at ferromagnet/nonmagnet contact." physical review b 78.6 (2008): 064423.

[38] Costache, m. v., et al. "electrical detection of spin pumping due to the precessing magnetization of a single ferromagnet." physical review letters 97.21 (2006): 216603.

[39] Dang, t. h., et al. "ultrafast spin-currents and charge conversion at 3 d-5 d interfaces probed by time-domain terahertz spectroscopy." applied physics reviews 7.4 (2020): 041409.

[40] Darif, mohamed, nadjib semmar, and france orléans cedex. "numerical simulation of si nanosecond laser annealing by comsol multiphysics." proceedings of the comsol conference 2008 hannover. 2008.

[41] Denev, sava a., et al. "probing ferroelectrics using optical second harmonic generation." journal of the american ceramic society 94.9 (2011): 2699-2727.

[42] Dewhurst, j. k., et al. "substrate-controlled ultrafast spin injection and demagnetization." physical review applied 10.4 (2018): 044065.

[43] Dornes, christian, et al. "the ultrafast einstein–de haas effect." nature 565.7738 (2019): 209-212.

[44] Dubroka, adam, et al. "dynamical response and confinement of the electrons at the laalo 3/srtio 3 interface." physical review letters 104.15 (2010): 156807.

[45] Egan, w. g., and h. j. juretschke. "dc detection of ferromagnetic resonance in thin nickel films." journal of applied physics 34.5 (1963): 1477-1484.

[46] Fang, xinyue. "phase transitions in strontium titanate." department of physics, university of illinois at urbana-champaign (2013).

[47] Fete, alexandre. magnetotransport experiments at the laalo 3/srtio 3 interface. diss. university of geneva, 2014.

[48] Flubacher, p., a. j. leadbetter, and j. a. morrison. "the heat capacity of pure silicon and germanium and properties of their vibrational frequency spectra." philosophical magazine 4.39 (1959): 273-294.

[49] Fête, alexandre, et al. "large modulation of the shubnikov–de haas oscillations by the rashba interaction at the laalo3/srtio3 interface." new journal of physics 16.11 (2014): 112002.

[50] Fête, alexandre, et al. "rashba induced magnetoconductance oscillations in the laalo 3-srtio 3 heterostructure." physical review b 86.20 (2012): 201105.

[51] Gallardo, m. c., et al. "low-temperature calorimetric study of srtio3." journal of physics: Condensed matter 14.8 (2002): 1881.

[52] Gamino, m., et al. "longitudinal spin seebeck effect and anomalous nernst effect in cofeb/non-magnetic metal bilayers." journal of magnetism and magnetic materials 527 (2021): 167778.

[53] Gilbert, thomas l. "a phenomenological theory of damping in ferromagnetic materials." ieee transactions on magnetics 40.6 (2004): 3443-3449.

[54] Go, dongwook, et al. "theory of current-induced angular momentum transfer dynamics in spin-orbit coupled systems." physical review research 2.3 (2020): 033401.

[55] Gurevich, a. g., and g. a. melkov. "magnetization oscillations and waves crc." new york 245 (1996).

[56] Hahn, christian, et al. "comparative measurements of inverse spin hall effects and magnetoresistance in yig/pt and yig/ta." physical review b 87.17 (2013): 174417.

[57] Herranz, gervasi, et al. "high mobility conduction at (110) and (111) laalo 3/srtio 3 interfaces." scientific reports 2.1 (2012): 1-5.

[58] Hikami, shinobu, anatoly i. larkin, and yosuke nagaoka. "spin-orbit interaction and magnetoresistance in the two dimensional random system." progress of theoretical physics 63.2 (1980): 707-710.

[59] Ho, c. y., et al. "thermal conductivity of ten selected binary alloy systems." journal of physical and chemical reference data 7.3 (1978): 959-1178.

[60] Hoffman, silas, koji sato, and yaroslav tserkovnyak. "landau-lifshitz theory of the longitudinal spin seebeck effect." physical review b 88.6 (2013): 064408.

[61] Holanda, j., et al. "longitudinal spin seebeck effect in permalloy separated from the anomalous nernst effect: Theory and experiment." physical review b 95.21 (2017): 214421.

[62] Holladay, samuel. frequency-swept ferromagnetic resonance characterization of permalloy thin films. technical report no. ucb/eecs-2018-53 university of california at berkeley, 2018.

[63] https://refractiveindex.info/.

[64] https://www.researchgate.net/figure/Polar-catastrophe-scenarioa-shows-the-origin-of-the-p
fig2_332138751.

[65] https://www.rsc.org/periodic-table/element/.

[66] Huang, b.-c. et al. mapping band alignment across complex oxide heterointerfaces. physical review letters 109, 246807 (2012).

[67] Huang, s. y., et al. "intrinsic spin-dependent thermal transport." physical review letters 107.21 (2011): 216604.

[68] Hurand, s., et al. "field-effect control of superconductivity and rashba spin-orbit coupling in top-gated laalo 3/srtio 3 devices." scientific reports 5.1 (2015): 1-9.

[69] Hurand, simon. contrôle de la supraconductivité à l'interface d'oxydes laalo3/srtio3 par effet de champ électrique. diss. paris 6, 2015.

[70] Iguchi, ryo, et al. "concomitant enhancement of the longitudinal spin seebeck effect and the thermal conductivity in a pt/yig/pt system at low temperatures." physical review b 95.17 (2017): 174401.

[71] Jaworski, c. m., et al. "observation of the spin-seebeck effect in a ferromagnetic semiconductor." nature materials 9.11 (2010): 898-903.

[72] Jiang, yeping, et al. "landau quantization and the thickness limit of topological insulator thin films of sb 2 te 3." physical review letters 108.1 (2012): 016401.

[73] Johnson, mark, and r. h. silsbee. "spin-injection experiment." physical review b 37.10 (1988): 5326.

[74] Johnson, mark, and r. h. silsbee. "thermodynamic analysis of interfacial transport and of the thermomagnetoelectric system." physical review b 35.10 (1987): 4959.

[75] Joshua, arjun, et al. "a universal critical density underlying the physics of electrons at the laalo 3/srtio 3 interface." nature communications 3.1 (2012): 1-7.

[76] Juretschke, h. j. "electromagnetic theory of dc effects in ferromagnetic resonance." journal of applied physics 31.8 (1960): 1401-1406.

[77] Kalabukhov, a. s., et al. "cationic disorder and phase segregation in laalo 3/srtio 3 heterointerfaces evidenced by medium-energy ion spectroscopy." physical review letters 103.14 (2009): 146101.

[78] Kampfrath, tobias, et al. "terahertz spin current pulses controlled by magnetic heterostructures." nature nanotechnology 8.4 (2013): 256-260.

[79] Khalsa, guru, and a. h. macdonald. "theory of the srtio 3 surface state two-dimensional electron gas." physical review b 86.12 (2012): 125121.

[80] Kim, younghyun, roman m. lutchyn, and chetan nayak. "origin and transport signatures of spin-orbit interactions in one-and two-dimensional srtio 3-based heterostructures." physical review b 87.24 (2013): 245121.

[81] King, p. d. c., et al. "quasiparticle dynamics and spin–orbital texture of the srtio 3 two-dimensional electron gas." nature communications 5.1 (2014): 1-7.

[82] Kirilyuk, andrei, and theo rasing. "magnetization-induced-second-harmonic generation from surfaces and interfaces." josa b 22.1 (2005): 148-167.

[83] Kittel, charles. "on the theory of ferromagnetic resonance absorption." physical review 73.2 (1948): 155.

[84] Koga, takaaki, et al. "rashba spin-orbit coupling probed by the weak antilocalization analysis in inalas/ingaas/inalas quantum wells as a function of quantum well asymmetry." physical review letters 89.4 (2002): 046801.

[85] Ky, vu dinh. "planar hall and nernst effect in ferromagnetic metals." physica status solidi (b) 22.2 (1967): 729-736.

[86] Laczkowski, p., et al. "large enhancement of the spin hall effect in au by side-jump scattering on ta impurities." physical review b 96.14 (2017): 140405.

[87] Laczkowski, piotr, et al. "evaluation of spin diffusion length of auw alloys using spin absorption experiments in the limit of large spin-orbit interactions." physical review b 92.21 (2015): 214405.

[88] Landau, l. a. l. e., and evgeny lifshitz. "on the theory of the dispersion of magnetic permeability in ferromagnetic bodies." perspectives in theoretical physics. pergamon, 1992. 51-65.

[89] Li, chengjian, et al. "formation of two-dimensional electron gas at amorphous/crystalline oxide interfaces." scientific reports 8.1 (2018): 1-9.

[90] Li, lu, et al. "coexistence of magnetic order and two-dimensional superconductivity at laalo 3/srtio 3 interfaces." nature physics 7.10 (2011): 762-766.

[91] Li, m., et al. "effect of well thickness on the rashba spin splitting and intersubband spin–orbit coupling in algan/gan/algan quantum wells with two subbands." solid state communications 151.24 (2011): 1958-1961.

[92] Liang, haixing, et al. "nonmonotonically tunable rashba spin-orbit coupling by multiple-band filling control in srtio 3-based interfacial d-electron gases." physical review b 92.7 (2015): 075309.

[93] Liu, z. q., et al. "origin of the two-dimensional electron gas at laalo 3/srtio 3 interfaces: the role of oxygen vacancies and electronic reconstruction." physical review x 3.2 (2013): 021010.

[94] Maekawa, sadamichi, and hidetoshi fukuyama. "magnetoresistance in two-dimensional disordered systems: effects of zeeman splitting and spin-orbit scattering." journal of the physical society of japan 50.8 (1981): 2516-2524.

[95] Martelli, valentina, et al. "thermal transport and phonon hydrodynamics in strontium titanate." physical review letters 120.12 (2018): 125901.

[96] Mathias, stefan, et al. "probing the timescale of the exchange interaction in a ferromagnetic alloy." proceedings of the national academy of sciences 109.13 (2012): 4792-4797.

[97] Mccalla, eric, et al. "low-temperature specific heat of doped srti o 3: Doping dependence of the effective mass and kadowaki-woods scaling violation." physical review materials 3.2 (2019): 022001.

[98] Melnikov, alexey, et al. "ultrafast transport of laser-excited spin-polarized carriers in au/fe/mgo (001)." physical review letters 107.7 (2011): 076601.

[99] Meyer, sibylle, et al. "observation of the spin nernst effect." nature materials 16.10 (2017): 977-981.

[100] Miyasato, t., et al. "crossover behavior of the anomalous hall effect and anomalous nernst effect in itinerant ferromagnets." physical review letters 99.8 (2007): 086602.

[101] Müller, k. alex, and h. burkard. "srti o 3: An intrinsic quantum paraelectric below 4 k." physical review b 19.7 (1979): 3593.

[102] Müller, k. alex. "macroscopic quantum phenomena." ferroelectrics 183.1 (1996): 11-24.

[103] Nahata, ajay, and tony f. heinz. "detection of freely propagating terahertz radiation by use of optical second-harmonic generation." optics letters 23.1 (1998): 67-69.

[104] Nakagawa, naoyuki, harold y. hwang, and david a. muller. "why some interfaces cannot be sharp." nature materials 5.3 (2006): 204-209.

[105] Nakamura, hiroyuki, takaaki koga, and tsuyoshi kimura. "experimental evidence of cubic rashba effect in an inversion-symmetric oxide." physical review letters 108.20 (2012): 206601.

[106] Niimi, y., et al. "extrinsic spin hall effect induced by iridium impurities in copper." physical review letters 106.12 (2011): 126601.

[107] Niimi, y., et al. "giant spin hall effect induced by skew scattering from bismuth impurities inside thin film cubi alloys." physical review letters 109.15 (2012): 156602.

[108] Noel, p., et al. "highly efficient spin-to-charge current conversion in strained hgte surface states protected by a hgcdte layer." physical review letters 120.16 (2018): 167201.

[109] Noel, paul. dynamical spin injection and spin to charge current conversion in oxide-based rashba interfaces and topological insulators. diss. université grenoble alpes, 2019.

[110] Ohya, shinobu, et al. "efficient intrinsic spin-to-charge current conversion in an all-epitaxial single-crystal perovskite-oxide heterostructure of l a 0.67 s r 0.33 mn o 3/laal o 3/srti o 3." physical review research 2.1 (2020): 012014.

[111] P. w. tasker, journal of physics c: Solid state physics 12, 4977 (1979).

[112] Park, jin-hong, et al. "orbital chirality and rashba interaction in magnetic bands." physical review b 87.4 (2013): 041301.

[113] Park, seung ryong, et al. "orbital-angular-momentum based origin of rashba-type surface band splitting." physical review letters 107.15 (2011): 156803.

[114] Pauli, s. a., et al. "evolution of the interfacial structure of laalo 3 on srtio 3." physical review letters 106.3 (2011): 036101.

[115] Polder, d. v. i. i. i. "viii. on the theory of ferromagnetic resonance." the london, edinburgh, and dublin philosophical magazine and journal of science 40.300 (1949): 99-115.

[116] Pu, yong, et al. "mott relation for anomalous hall and nernst effects in ga 1 x mn x as ferromagnetic semiconductors." physical review letters 101.11 (2008): 117208.

[117] Pustogowa, u., w. hübner, and k. h. bennemann. "theory for the nonlinear magneto-optical kerr effect at ferromagnetic transition-metal surfaces." physical review b 48.12 (1993): 8607.

[118] Ramaswamy, rajagopalan, et al. "extrinsic spin hall effect in cu 1 x pt x." physical review applied 8.2 (2017): 024034.

[119] Razdolski, ilya, et al. "analysis of the time-resolved magneto-optical kerr effect for ultrafast magnetization dynamics in ferromagnetic thin films." journal of physics: Condensed matter 29.17 (2017): 174002.

[120] Reinle-schmitt, m. l., et al. "tunable conductivity threshold at polar oxide interfaces." nature communications 3.1 (2012): 1-6.

[121] Reyren, nicolas, et al. "superconducting interfaces between insulating oxides." science 317.5842 (2007): 1196-1199.

[122] Rojas-sánchez, j-c., and a. fert. "compared efficiencies of conversions between charge and spin current by spin-orbit interactions in two-and three-dimensional systems." physical review applied 11.5 (2019): 054049.

[123] Rojas-sánchez, j-c., et al. "spin pumping and inverse spin hall effect in germanium." physical review b 88.6 (2013): 064403.

[124] Rojas-sánchez, j-c., et al. "spin to charge conversion at room temperature by spin pumping into a new type of topological insulator: -sn films." physical review letters 116.9 (2016): 096602.

[125] Rongione, e., et al. "ultrafast spin-charge conversion in rashba states probed by terahertz time-domain emission spectroscopy." 2020 45th international conference on infrared, millimeter, and terahertz waves (irmmw-thz). ieee, 2020.

[126] Rousseau, o., and m. viret. "interaction between ferromagnetic resonance and spin currents in nanostructures." physical review b 85.14 (2012): 144413.

[127] Rödel, tobias chris, et al. "universal fabrication of 2d electron systems in functional oxides." advanced materials 28.10 (2016): 1976-1980.

[128] Sagasta, edurne, et al. "tuning the spin hall effect of pt from the moderately dirty to the superclean regime." physical review b 94.6 (2016): 060412.

[129] Saitoh, e., et al. "conversion of spin current into charge current at room temperature: Inverse spin-hall effect." applied physics letters 88.18 (2006): 182509.

[130] salemi antiferromagnet - google scholar. https://scholar.google.com/scholar?hl=en&as_sdt=0%2C5&q=salemi+antiferromagnet&btnG=&oq=salemi+antiff.

[131] Salluzzo, m., et al. "orbital reconstruction and the two-dimensional electron gas at the laalo 3/srtio 3 interface." physical review letters 102.16 (2009): 166804.

[132] Sangiao, soraya, et al. "control of the spin to charge conversion using the inverse rashba-edelstein effect." applied physics letters 106.17 (2015): 172403.

[133] Scheiderer, p., et al. "surface-interface coupling in an oxide heterostructure: Impact of adsorbates on laalo 3/srtio3." physical review b 92.19 (2015): 195422.

[134] Schreier, michael, et al. "sign of inverse spin hall voltages generated by ferromagnetic resonance and temperature gradients in yttrium iron garnet platinum bilayers." journal of physics d: Applied physics 48.2 (2014): 025001.

[135] Segal, y., ngai, j. h., reiner, j. w., walker, f. j. ahn, c. h. x-ray photoemission studies of the metal-insulator transition in laalo 3 /srtio 3 structures grown by molecular beam epitaxy. physical review b 80, 241107(r) (2009).

[136] Seifert, tom, et al. "terahertz spin currents and inverse spin hall effect in thin-film heterostructures containing complex magnetic compounds." spin. vol. 7. no. 03. world scientific publishing company, 2017.

[137] Shalom, m. ben, et al. "tuning spin-orbit coupling and superconductivity at the srtio 3/laalo 3 interface: a magnetotransport study." physical review letters 104.12 (2010): 126802.

[138] Siemons, wolter, et al. "origin of charge density at laalo 3 on srtio 3 heterointerfaces: Possibility of intrinsic doping." physical review letters 98.19 (2007): 196802.

[139] Sing, m., et al. "profiling the interface electron gas of laalo 3/srtio 3 heterostructures with hard x-ray photoelectron spectroscopy." physical review letters 102.17 (2009): 176805.

[140] Song, qi, et al. "observation of inverse edelstein effect in rashba-split 2deg between srtio3 and laalo3 at room temperature." science advances 3.3 (2017): e1602312.

[141] Suemune, yasutaka. "thermal conductivity of batio3 and srtio3 from 4.5 to 300 k." journal of the physical society of japan 20.1 (1965): 174-175.

[142] Takizawa, m., et al. "electronic charges and electric potential at laalo 3/srtio 3 interfaces studied by core-level photoemission spectroscopy." physical review b 84.24 (2011): 245124.

[143] Tamai, anna, et al. "spin-orbit splitting of the shockley surface state on cu (111)." physical review b 87.7 (2013): 075113.

[144] Temnov, vasily v. "ultrafast acousto-magneto-plasmonics." nature photonics 6.11 (2012): 728-736.

[145] Thrane, l., et al. "thz reflection spectroscopy of liquid water." chemical physics letters 240.4 (1995): 330-333.

[146] Thurnay, kalman. thermal properties of transition metals. no. fzka–6095. forschungszentrum karlsruhe gmbh technik und umwelt (germany). inst. fuer neutronenphysik und reaktortechnik, 1998.

[147] Tikhonov, konstantin s., jairo sinova, and alexander m. finkel'stein. "spectral non-uniform temperature and non-local heat transfer in the spin seebeck effect." nature communications 4.1 (2013): 1-6.

[148] Tomasino, a., et al. "wideband thz time domain spectroscopy based on optical rectification and electro-optic sampling." scientific reports 3.1 (2013): 1-8.

[149] Trassin, morgan, et al. "probing ferroelectric domain engineering in bifeo3 thin films by second harmonic generation." advanced materials 27.33 (2015): 4871-4876.

[150] Tserkovnyak, yaroslav, et al. "nonlocal magnetization dynamics in ferromagnetic heterostructures." reviews of modern physics 77.4 (2005): 1375.

[151] Tusche, christian, alexander krasyuk, and jürgen kirschner. "spin resolved bandstructure imaging with a high resolution momentum microscope." ultramicroscopy 159 (2015): 520-529.

[152] Uchida, k., et al. "observation of the spin seebeck effect." nature 455.7214 (2008): 778-781. .

[153] Uchida, k., et al. "thermal spin pumping and magnon-phonon-mediated spin-seebeck effect." journal of applied physics 111.10 (2012): 103903.

[154] Uchida, ken-ichi, et al. "observation of longitudinal spin-seebeck effect in magnetic insulators." applied physics letters 97.17 (2010): 172505.

[155] Uchida, ken-ichi, et al. "spin seebeck insulator." nature materials 9.11 (2010): 894-897.

[156] Valet, t., and a. fert. "theory of the perpendicular magnetoresistance in magnetic multilayers." physical review b 48.10 (1993): 7099.

[157] Van heeringen, l. w., et al. "theoretical models of rashba spin splitting in asymmetric srtio 3-based heterostructures." physical review b 95.15 (2017): 155134.

[158] Vaz, d. c. magnetotransport properties of metal/laalo 3 /srtio 3 heterostructures. master's thesis, faculdade de ciências e tecnologia, universidade nova de lisboa (2015).

[159] Velmre, enn. "thomas johann seebeck (1770-1831)." estonian journal of engineering 13.4 (2007).

[160] Vidal, sébastien, et al. "optimized terahertz generation via optical rectification in znte crystals." josa b 31.1 (2014): 149-153.

[161] Vonsovski, sergueï vasilievitch, ed. ferromagnetic resonance. israel program for scientific translations, 1964.

[162] Wang, h. l., et al. "scaling of spin hall angle in 3d, 4d, and 5d metals from y 3 fe 5 o 12/metal spin pumping." physical review letters 112.19 (2014): 197201.

[163] Wang, yi, et al. "room-temperature giant charge-to-spin conversion at the srtio3–laalo3 oxide interface." nano letters 17.12 (2017): 7659-7664.

[164] Warusawithana, m. p., et al. "laalo 3 stoichiometry is key to electron liquid formation at laalo 3/srtio 3 interfaces." nature communications 4.1 (2013): 1-9.

[165] Willmott, p. r., et al. "structural basis for the conducting interface between laalo 3 and srtio 3." physical review letters 99.15 (2007): 155502.

[166] Wu, b. w., et al. "longitudinal spin seebeck effect in a half-metallic l a 0.7 s r 0.3 mn o 3 film." physical review b 96.6 (2017): 060402.

[167] Yaji, koichiro, et al. "rashba spin splitting of l-gap surface states on ag (111) and cu (111)." physical review b 98.4 (2018): 041404.

[168] Yamane, haruki, et al. "magneto-plasmonics on perpendicular magnetic nanostructures consisting of a copt layer and noble-metal grains." journal of applied physics 124.8 (2018): 083901.

[169] Yamanoi, kazuto, et al. "signature of spin-dependent seebeck effect in dynamical spin injection of metallic bilayer structures." journal of physics: Materials 3.1 (2019): 014005.

[170] Yoshino, t., et al. "universality of the spin pumping in metallic bilayer films." applied physics letters 98.13 (2011): 132503.

[171] Yu, liping, and alex zunger. "a polarity-induced defect mechanism for conductivity and magnetism at polar–nonpolar oxide interfaces." nature communications 5.1 (2014): 1-9.

[172] Zhong, zhicheng, anna tóth, and karsten held. "theory of spin-orbit coupling at laalo 3/srtio 3 interfaces and srtio 3 surfaces." physical review b 87.16 (2013): 161102.

[173] Zhou, jianhui, wen-yu shan, and di xiao. "spin responses and effective hamiltonian for the two-dimensional electron gas at the oxide interface laalo 3/srtio 3." physical review b 91.24 (2015): 241302.

[174] Zhu, lijun, daniel c. ralph, and robert a. buhrman. "highly efficient spin-current generation by the spin hall effect in au 1 x pt x." physical review applied 10.3 (2018): 031001.

[175] alexandre fête - google scholar. https://scholar.google.com/citations?user=IQvdUMEAAAAJ&hl=fr. (Accessed on 11/04/2020).

[176] Elliott, r _ j, theory of the effect of spin-orbit coupling on magnetic resonance in some semiconductors. *Physical Review*, 96(2):266, 1954.

[177] Yafet, y, g factors and spin-lattice relaxation of conduction electrons. In *Solid state physics*, volume 14, pages 1–98. Elsevier, 1963.

[178] Ando, kazuya, et al., possibility of orienting electron spins with current. *Soviet Journal of Experimental and Theoretical Physics Letters*, 13:467, 1971.

[179] Dyakonov, m. i., and v. i. perel., spin relaxation of conduction electrons in noncentrosymmetric semiconductors. *Soviet Physics Solid State, Ussr*, 13(12):3023–3026, 1972.

[180] Beuneu, francois and monod, philippe, the elliott relation in pure metals. *Physical Review B*, 18(6):2422, 1978.

[181] Alferov, zh i. the history and future of semiconductor heterostructures. *Semiconductors*, 32(1):1–14, 1998.

[182] Ganichev, s. d., et al. spin-galvanic effect. *Nature*, 417(6885):153–156, 2002.

[183] Ganichev, sergey d., et al.experimental separation of rashba and dresselhaus spin splittings in semiconductor quantum wells. *Physical review letters*, 92(25):256601, 2004.

[184] Kato, yuichiro k., et al., observation of the spin hall effect in semiconductors. *science*, 306(5703):1910–1913, 2004.

[185] Nishimura, jun, et al. "controlled carrier generation at a polarity-discontinued perovskite heterointerface.". *Japanese journal of applied physics*, 43(8A):L1032, 2004.

[186] Ohtomo, a., and h. y. hwang. "a high-mobility electron gas at the laalo 3/srtio 3 heterointerface.". *Nature*, 427(6973):423–426, 2004.

[187] Saitoh, e., et al., conversion of spin current into charge current at room temperature: Inverse spin-hall effect. *Applied physics letters*, 88(18):182509, 2006.

[188] Thiel, stefan, et al. "tunable quasi-two-dimensional electron gases in oxide heterostructures.". *Science*, 313(5795):1942–1945, 2006.

[189] Basletic, m., et al. "mapping the spatial distribution of charge carriers in laalo 3/srtio 3 heterostructures.". *Nature materials*, 7(8):621–625, 2008.

[190] Caviglia, ad and gariglio, stefano and reyren, nicolas and jaccard, didier and schneider, t and gabay, m and thiel, stefan and hammerl, german and mannhart, jochen and triscone, j-m, electric field control of the laalo 3/srtio 3 interface ground state. *Nature*, 456(7222):624–627, 2008.

[191] Copie, o., et al. "towards two-dimensional metallic behavior at laalo 3/srtio 3 interfaces.". *Physical review letters*, 102(21):216804, 2009.

[192] Kontani, hiroshi, et al. giant orbital hall effect in transition metals: Origin of large spin and anomalous hall effects. *Physical review letters*, 102(1):016601, 2009.

[193] A. d. caviglia, al., tunable rashba spin-orbit interaction at oxide interfaces. *PHYSICAL REVIEW LETTERS*, 104(126803), 2010.

[194] Cheng, j. l., wu, m. w. fabian, j., theory of the spin relaxation of conduction electrons in silicon. *Physical Review Letters*, 104(016601), 2010.

[195] Studer, m., et al. role of linear and cubic terms for drift-induced dresselhaus spin-orbit splitting in a two-dimensional electron gas. *Physical Review B*, 82(23):235320, 2010.

[196] Ando, kazuya, et al. inverse spin-hall effect induced by spin pumping in metallic system. *Journal of applied physics*, 10(109):103913, 2011.

[197] Bert, julie a., et al. "direct imaging of the coexistence of ferromagnetism and superconductivity at the laalo 3/srtio 3 interface.". *Nature physics*, 7(10):767–771, 2011.

[198] Fabian, jaroslav and wu, mw, spin relaxation and spin dynamics in semiconductors. *Handbook of Spin Transport and Magnetism*, 1, 2011.

[199] Sánchez, jc rojas, et al. spin-to-charge conversion using rashba coupling at the interface between non-magnetic materials. *Nature communications*, 4(1):1–7, 2013.

[200] E. lesne, al. highly efficient and tunable spin-to-charge conversion through rashba coupling at oxide interfaces. *Nature materials*, 15:1261–1266, December 2016.

[201] Mendes, j. b. s., et al. dirac-surface-state-dominated spin to charge current conversion in the topological insulator (bi 0.22 sb 0.78) 2 te 3 films at room temperature. *Journal of physics C: Solid state physics*, 96(18):180415, 2017.

[202] Go, dongwook, et al. intrinsic spin and orbital hall effects from orbital texture. *Soviet Physics Solid State*, 121(8):086602, 2018.

[203] Johansson, annika, et al. spin and orbital edelstein effects in a two-dimensional electron gas: Theory and application to srtio 3 interfaces. *Physical Review Research*, 3(1):013275, 2021.

[204] A. G. Aronov and Yu B. Lyanda-Geller. Nuclear electric resonance and orientation of carrier spins by an electric field. *Soviet Journal of Experimental and Theoretical Physics Letters*, 50:431, 1989.

[205] Mario Norberto Baibich, Jean Marc Broto, Albert Fert, F Nguyen Van Dau, Frédéric Petroff, P Etienne, G Creuzet, A Friederich, and J Chazelas. Giant magnetoresistance of (001) fe/(001) cr magnetic superlattices. *Physical review letters*, 61(21):2472, 1988.

[206] J George Bednorz and K Alex Müller. Possible high t c superconductivity in the ba- la- cu- o system. *Zeitschrift für Physik B Condensed Matter*, 64(2):189–193, 1986.

[207] Luc. Berger. Side-jump mechanism for the hall effect of ferromagnets. *Physical Review B*, 2(11):4559, 1970.

[208] Luc Berger. Emission of spin waves by a magnetic multilayer traversed by a current. *Physical Review B*, 54(13):9353, 1996.

[209] Kerry Bernstein, Ralph K Cavin, Wolfgang Porod, Alan Seabaugh, and Jeff Welser. Device and architecture outlook for beyond cmos switches. *Proceedings of the IEEE*, 98(12):2169–2184, 2010.

[210] Sayantika Bhowal and Sashi Satpathy. Intrinsic orbital moment and prediction of a large orbital hall effect in two-dimensional transition metal dichalcogenides. *Soviet Physics Solid State*, 101(12):121112, 2020.

[211] Grünberg Binasch, Peter Grünberg, F Saurenbach, and W Zinn. Enhanced magnetoresistance in layered magnetic structures with antiferromagnetic interlayer exchange. *Physical review B*, 39(7):4828, 1989.

[212] David C Brock and Gordon E Moore. *Understanding Moore's law: four decades of innovation*. Chemical Heritage Foundation, 2006.

[213] Yu A. Bychkov. Properties of 2d electron gas with lifted spectral degeneracy. *JETP lett.*, 39(2):78–81, 1984.

[214] Yu A Bychkov and Emmanuel I Rashba. Oscillatory effects and the magnetic susceptibility of carriers in inversion layers. *Journal of physics C: Solid state physics*, 17(33):6039, 1984.

[215] Ming-Che Chang and Qian Niu. Berry phase, hyperorbits, and the hofstadter spectrum. *Physical review letters*, 75(7):1348, 1995.

[216] Bernard D. Coleman and Clifford Truesdell. On the reciprocal relations of onsager. *The Journal of Chemical Physics*, 33(1):28–31, 1960.

[217] Martin Collet, Xavier De Milly, O d'Allivy Kelly, Vladimir V Naletov, Rozenn Bernard, Paolo Bortolotti, J Ben Youssef, VE Demidov, SO Demokritov, Jose Luis Prieto, et al. Generation of coherent spin-wave modes in yttrium iron garnet microdiscs by spin–orbit torque. *Nature communications*, 7(1):1–8, 2016.

[218] Supriyo Datta and Biswajit Das. Electronic analog of the electro-optic modulator. *Applied Physics Letters*, 56(7):665–667, 1990.

[219] Robert H Dennard, Fritz H Gaensslen, Hwa-Nien Yu, V Leo Rideout, Ernest Bassous, and Andre R LeBlanc. Design of ion-implanted mosfet's with very small physical dimensions. *IEEE Journal of Solid-State Circuits*, 9(5):256–268, 1974.

[220] M. I. Dyakonov and V. I. Perel. Spin relaxation of conduction electrons in noncentrosymmetric semiconductors. *Soviet Physics Solid State*, 13(12):3023–3026, 1972.

[221] Victor M. Edelstein. Spin polarization of conduction electrons induced by electric current in two-dimensional asymmetric electron systems. *Solid State Communications*, 93(3):233–235, 1990.

[222] Richard P Feynman, Robert B Leighton, and Matthew Sands. *The Feynman lectures on physics, Vol. I: The new millennium edition: mainly mechanics, radiation, and heat*, volume 1. Basic books, 2011.

[223] Aaron D Franklin, Mathieu Luisier, Shu-Jen Han, George Tulevski, Chris M Breslin, Lynne Gignac, Mark S Lundstrom, and Wilfried Haensch. Sub-10 nm carbon nanotube transistor. *Nano letters*, 12(2):758–762, 2012.

[224] Kevin Garello, Can Onur Avci, Ioan Mihai Miron, Manuel Baumgartner, Abhijit Ghosh, Stéphane Auffret, Olivier Boulle, Gilles Gaudin, and Pietro Gambardella. Ultrafast magnetization switching by spin-orbit torques. *Applied Physics Letters*, 105(21):212402, 2014.

[225] Kevin Garello, Farrukh Yasin, Sébastien Couet, Laurent Souriau, Johan Swerts, S Rao, Simon Van Beek, Wonsub Kim, Enlong Liu, Shreya Kundu, et al. Sot-mram 300mm integration for low power and ultrafast embedded memories. In *2018 IEEE Symposium on VLSI Circuits*, pages 81–82. IEEE, 2018.

[226] Dongwook Go, Jan-Philipp Hanke, Patrick M Buhl, Frank Freimuth, Gustav Bihlmayer, Hyun-Woo Lee, Yuriy Mokrousov, and Stefan Blügel. Toward surface orbitronics: giant orbital magnetism from the orbital rashba effect at the surface of sp-metals. *Scientific reports*, 7(1):1–10, 2017.

[227] et al. Herschbach, Christian. Insight into the skew-scattering mechanism of the spin hall effect: Potential scattering versus spin-orbit scattering. *Physical Review B*, 88(22):205102, 2013.

[228] JE Hirsch. Spin hall effect. *Physical review letters*, 83(9):1834, 1999.

[229] James A Hutchby, George I Bourianoff, Victor V Zhirnov, and Joe E Brewer. Extending the road beyond cmos. *IEEE circuits and devices magazine*, 18(2):28–41, 2002.

[230] Iu B. Lianda-Geller Ivchenko, E. L. and G. E. Pikus. Photocurrent in quantum well structures with optical orientation of free carrier. *Pisma v Zhurnal Eksperimentalnoi i Teoreticheskoi Fiziki*, 50:156–158, 1989.

[231] Chenglong Jia and Jamal Berakdar. Electrically controlled persistent spin currents at the interface of multiferroic oxides. *Physical Review B*, 80(1):014432, 2009.

[232] Tobias Kampfrath, Marco Battiato, Pablo Maldonado, G Eilers, J Nötzold, Sebastian Mährlein, V Zbarsky, Frank Freimuth, Yuriy Mokrousov, Stefan Blügel, et al. Terahertz spin current pulses controlled by magnetic heterostructures. *Nature nanotechnology*, 8(4):256–260, 2013.

[233] Alexey A Kovalev, Yaroslav Tserkovnyak, Karel Vỳbornỳ, and Jairo Sinova. Transport theory for disordered multiple-band systems: Anomalous hall effect and anisotropic magnetoresistance. *Physical Review B*, 79(19):195129, 2009.

[234] Yu V. Nazarov Levitov, L. S. and G. M. Eliashberg. Magnetoelectric effects in conductors with mirror isomer symmetry. *Sov. Phys. JETP*, 61(1):133–137, 1985.

[235] Luqiao Liu, Chi-Feng Pai, Y Li, HW Tseng, DC Ralph, and RA Buhrman. Spin-torque switching with the giant spin hall effect of tantalum. *Science*, 336(6081):555–558, 2012.

[236] Sasikanth Manipatruni, Dmitri E Nikonov, Chia-Ching Lin, Tanay A Gosavi, Huichu Liu, Bhagwati Prasad, Yen-Lin Huang, Everton Bonturim, Ramamoorthy Ramesh, and Ian A Young. Scalable energy-efficient magnetoelectric spin–orbit logic. *Nature*, 565(7737):35–42, 2019.

[237] Ioan Mihai Miron, Kevin Garello, Gilles Gaudin, Pierre-Jean Zermatten, Marius V Costache, Stéphane Auffret, Sébastien Bandiera, Bernard Rodmacq, Alain Schuhl, and Pietro Gambardella. Perpendicular switching of a single ferromagnetic layer induced by in-plane current injection. *Nature*, 476(7359):189–193, 2011.

[238] Naoto Nagaosa Murakami, Shuichi and Shou-Cheng Zhang. Dissipationless quantum spin current at room temperature. *Physical Review B*, 301(5638):1348–1351, 2003.

[239] Shuichi. Murakami. Intrinsic spin hall effect. *Springer, Berlin, Heidelberg*, 2(11):197–209, 2005.

[240] Naoto Nagaosa, Jairo Sinova, Shigeki Onoda, Allan H MacDonald, and Nai Phuan Ong. Anomalous hall effect. *Reviews of modern physics*, 82(2):1539, 2010.

[241] VT Pham, L Vila, G Zahnd, P Noël, A Marty, and JP Attané. Cross-shaped nanostructures for the study of spin to charge inter-conversion using spin-orbit coupling in non-magnetic materials. *Applied Physics Letters*, 114(22):222401, 2019.

[242] N Reyren, M Bibes, E Lesne, J-M George, C Deranlot, S Collin, A Barthélémy, and H Jaffrès. Gate-controlled spin injection at laalo 3/srtio 3 interfaces. *Physical Review Letters*, 108(18):186802, 2012.

[243] V Scagnoli, U Staub, Y Bodenthin, RA De Souza, M García-Fernández, M Garganourakis, AT Boothroyd, D Prabhakaran, and SW Lovesey. Observation of orbital currents in cuo. *Science*, 332(6030):696–698, 2011.

[244] John C Slonczewski. Current-driven excitation of magnetic multilayers. *Journal of Magnetism and Magnetic Materials*, 159(1-2):L1–L7, 1996.

[245] J. Smit. The spontaneous hall effect in ferromagnetics. https://scholar.google.com/scholar?hl=en&as_sdt=0%2C5&q=Smit%2C+J.+The+spontaneous+hall+effect+in+ferromagnetics+II.+Physica+24%2C+39%E2%80%9351+%281958%29.&btnG=. (Accessed on 10/03/2021).

[246] Satoshi Sugahara and Junsaku Nitta. Spin-transistor electronics: An overview and outlook. *Proceedings of the IEEE*, 98(12):2124–2154, 2010.

[247] T Tanaka, Hiroshi Kontani, Masayuki Naito, T Naito, Dai S Hirashima, K Yamada, and J Inoue. Intrinsic spin hall effect and orbital hall effect in 4 d and 5 d transition metals. *Physical Review B*, 77(16):165117, 2008.

[248] Sergio O Valenzuela and M Tinkham. Direct electronic measurement of the spin hall effect. *Nature*, 442(7099):176–179, 2006.

[249] Taiki Yoda, Takehito Yokoyama, and Shuichi Murakami. Orbital edelstein effect as a condensed-matter analog of solenoids. *Nano letters*, 18(2):916–920, 2018.

[250] Takehito Yokoyama Yoda, Taiki and Shuichi Murakami. Current-induced orbital and spin magnetizations in crystals with helical structure. *Scientific reports*, 5(1):1–7, 2015.

Titre: Conversion spin-charge dans les états d'interface Rashba dans $LaAlO_3/SrTiO_3$

Mots clés: Couplage spin-orbit, conversion spin-charge, 2DES, Interaction Rashba

Résumé: Un domaine émergent de la spintronique, appelé spin-orbitronique, permet l'interconversion entre les courants de charge et de spin via le couplage spin-orbit (SOC) dans les matériaux non magnétiques, reliant le degré de liberté de spin au degré de liberté orbital ce qui résulte en une diffusion des électrons de spins différents dans des directions préférentielles. Récemment, un nouveau type de SOC a été découvert en s'appuyant sur l'interaction de Rashba, qui découle d'une action conjointe du SOC et d'un potentiel électrique qui apparait dans les systèmes d'électrons bidimensionnels (2 DES) existant aux interfaces de deux matériaux différents. Un système prometteur pour étudier la conversion de spin-charge est l'interface entre deux isolants comme l'interface entre $LaAlO_3$ /$SrTiO_3$ (LAO/STO) , où un 2DES est créé en raison d'une discontinuité polaire à l'interface. Ce 2 DES à l'interface LAO/STO montre une très forte interaction Rashba dû à la brisure de la symétrie d'inversion. Il semble qu'en raison de la constante diélectrique élevée de STO à des températures inférieures à 30K, nous sommes en mesure d'ajuster l'interaction Rashba à l'aide d'un champ électrique. Dans ce travail j'ai mesuré une forte efficacité de conversion spin-charge dans LAO/STO ce qui peut s'expliquer par la nature orbitalaire de la conversion spin-charge dans le 2DES, que j'ai pu régler grâce à un dopage électrostatique. Dans une deuxième partie, j'ai montré que l'efficacité de conversion en LAO/STO peut être anisotrope du fait des effets multibandes qui apparaîssent notamment dans les oxydes de métaux de transition. Enfin, j'ai étudié la dynamique de la conversion spin-charge en LAO/STO, grâce à la désaimantation ultrarapide d'une couche ferromagnétique, en utilisant différentes méthodes optiques pour caractériser les courants de spin et de charge.

Title: Spin-to-charge conversion at the $LaAlO_3/SrTiO_3$ interface Rashba state

Keywords: Spin-orbit coupling, spin-to-charge conversion, 2DES, Rashba interaction

Abstract: An emerging field of spintronics, called spin-orbitronics, enables the inter-conversion between charge and spin currents through the spin-orbit coupling (SOC) in non-magnetic materials, which links the spin degree of freedom to the orbital degree of freedom resulting in a preferential directional scattering for electrons of different spins. Recently, a new type of SOC have been discovered relying on the Rashba interaction,which stems for a joint action of the SOC and an electrical built-in potential in two-dimensional electrons systems (2 DES) existing at interfaces of two different materials. A promising system to study the spin to charge conversion is the interface between two band gap insulators like the interface between $LaAlO_3$ /$SrTiO_3$ (LAO/STO) , where a 2DES is created due a polar discontinuity at the interface. This 2 DES at the interface of LAO/STO shows a very strong Rashba spin-orbit interaction raising from the breaking of the inversion symmetry. It appears that due to the high dielectric constant in STO below 30K, we are able to tune our Rashba splitting using an electric field. In this work I measured a strong spin-to-charge conversion efficiency in LAO/STO thanks to the orbital nature of the spin-to-charge conversion in the 2DES, which I was able to tune thanks to an electrostatic doping. In a second part, I showed that the conversion efficiency in LAO/STO can be anisotropic due to the interplay of a complex multiband effect that appears in particular in transition metal-oxides. Finally, I studied the dynamics of the spin-to-charge conversion in LAO/STO, thanks to the ultrafast demagnetization of a ferromagnetic layer, using various optical method to characterize the spin and charge currents.

Université Paris-Saclay
Espace Technologique / Immeuble Discovery
Route de l'Orme aux Merisiers RD 128 / 91190 Saint-Aubin, France